The preparation and characterization of multi-component systems in drug pre-formulation

By: Alexios Ivan Vicatos

Dissertation Presented for the Degree of Master of Science

In the Department of Chemistry

University of Cape Town

Supervisor: Professor Mino R. Caira

April 2018

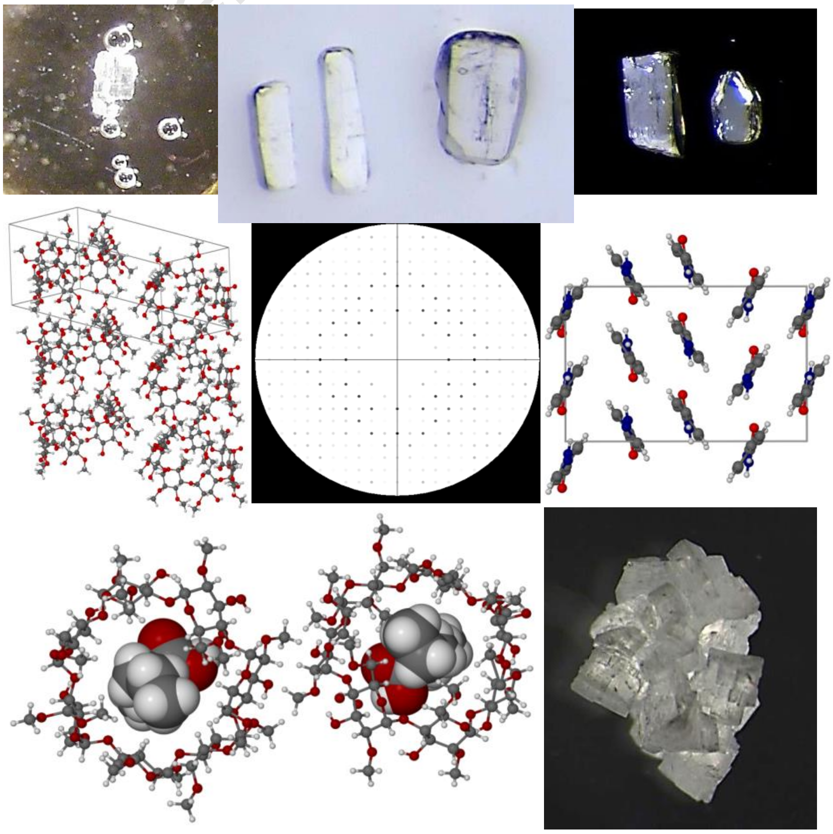

Acknowledgements

1. I am eternally thankful for the knowledge that I have acquired from my supervisor, Professor Mino R. Caira, during this Master’s dissertation. His superb supervision, endless support, patience, generosity and mentorship were most appreciated.
2. Dr Hong Su, Dr Clive Oliver and Dr Nabanita Chatterjee Samanta for single crystal data collection.
3. The Supramolecular Group for their generous support and assistance wherever necessary.
4. The David and Elaine Potter Fellowship for providing financial support over the two consecutive years.
5. My family and friends for their emotional and encouraging support.
6. Grant Bräsler and Tertia Visser, (my organ and piano lecturers respectively), for their support and encouragement.

Glossary

General

API:	Active pharmaceutical ingredient
CD:	Cyclodextrin
LAG:	Liquid-assisted grinding
GRAS:	Generally recognized as safe

Chemical compounds

α-CD:	α-Cyclodextrin
β-CD:	β- Cyclodextrin
γ-CD:	γ- Cyclodextrin
DMB:	Heptakis(2,6-di-*O*-methyl)-β-cyclodextrin
TMB:	Heptakis(2,3,6-tri-*O*-methyl)-β-cyclodextrin
TMA:	Hexakis(2,3,6-tri-*O*-methyl)-α-cyclodextrin
HPBCD:	Hydroxypropyl β-cyclodextrin
RAMEB:	Randomly methylated β-cyclodextrin

Cyclodextrin complexes

α-CD·VAL:	A α-CD – valproic acid inclusion complex
β-CD·VAL:	A β-CD – valproic acid inclusion complex
γ-CD·VAL:	A γ-CD – valproic acid inclusion complex
DMB·VAL:	A DMB – valproic acid inclusion complex
TMB·VAL:	A TMB – valproic acid inclusion complex
TMA·VAL:	A TMA – valproic acid inclusion complex

Crystallographic terms

ASU:	Asymmetric unit
CFOM:	Combined figure of merit
s.o.f.:	Site-occupancy factor
U_{iso}:	Isotropic thermal parameter
CSD:	Cambridge Structural Database

Solvents

DMSO-d_6:	Deuterated dimethyl sulfoxide
DMSO:	Dimethyl sulfoxide
EtOH:	Ethanol

Abstract

The supramolecular derivatisation, *via* co-crystallization and cyclodextrin (CD) inclusion of three active pharmaceutical ingredients (APIs), was attempted with the aim of generating new solid forms with potential pharmaceutical application. The APIs under investigation included allopurinol (used for the treatment of gout and kidney stones), 6-thioguanine (used to treat acute myelogenous leukaemia) and valproic acid (for treatment of epilepsy and bipolar disorders). Allopurinol and 6-thioguanine were fairly intractable, yielding very limited results following co-crystallization trials with a series of co-formers. However, a new polymorph of one of the co-formers, namely isonicotinamide, was discovered serendipitously and thoroughly characterized using thermal analysis and single crystal X-ray diffraction. Phase solubility studies with a variety of CDs showed that the poor aqueous solubility of allopurinol and 6-thioguanine was not significantly modified in the presence of CD solutions. However, a more accurate aqueous solubility value for 6-thioguanine was achieved, namely 0.078 ± 0.003 $mg.cm^{-3}$ at 25 ^{o}C.

Six new CD complexes of valproic acid (VAL) were isolated by kneading and/or co-precipitation methods and characterized by thermal analysis, powder X-ray diffraction and spectroscopic (^{1}H NMR and FT-IR) techniques. The six CD complexes (with host-guest stoichiometries in parentheses) included α-CD·VAL (2:1), β-CD·VAL (1:1), γ-CD·VAL (4:3), DMB·VAL (1:1), TMB·VAL (1:1) and TMA·VAL (1:1). The α-CD·VAL, β-CD·VAL, and γ-CD·VAL complexes were assessed for their ability to alter the aqueous solubility of the drug at 23 ^{o}C. The S_{CD}/S_o ratios for these CD complexes (S_{CD} being the solubility of VAL in the form of the CD complex and S_o the solubility of pure VAL) were 0.39, 0.42 and 0.41 respectively and thus CD complexation reduced the aqueous solubility of valproic acid. Single crystal X-ray structures of four of the CD-valproic acid complexes were determined, those with native CDs featuring fully disordered guest molecules, while those with permethylated α-CD and dimethylated β-CD revealed the modes of inclusion of the drug unequivocally.

Table of contents

Chapter 1: Introduction

Chapter 2: Experimental Methods

Chapter 3: Supramolecular Derivatisation of Allopurinol

Chapter 4: Supramolecular Derivatisation of 6-Thioguanine

Chapter 5: Supramolecular Derivatisation of Valproic Acid

Chapter 6: Conclusions

Chapter 1

Introduction

1.1) Overview

A wide variety of active pharmaceutical ingredients (APIs), either established or previously discarded, have potent bioactivity, yet with the disadvantage of inadequate physicochemical properties. Examples of such properties include insufficient aqueous solubility, hygroscopicity and low dissolution rate, poor compressibility, low thermal stability, low bioavailability, high volatility, low resistance to oxidation, hydrolysis, light and heat, and vile odours or tastes.[1-3] Despite technological advances and the increase in research, development and funding for the discovery of new pharmaceutical drugs, there has been a steady decline in the number of new drugs being produced. This decline has been apparent for the last sixty years and is associated with the increasing amount of financial investments and innovation required to produce each new drug.[4] As a result of this decline, alternative methods have been discovered and implemented in order to overcome the shortage in new pharmaceuticals. These methods involve changing the solid form of established or discarded pharmaceuticals by modifying their properties, which thus may improve the physicochemical properties of the API in question.[3]

1.2) Improving the physicochemical properties of an active pharmaceutical ingredient (API)

The traditional approach for improving the physicochemical properties of an API was to create a new formulation with a combination of extreme pH conditions, organic solvents and surfactants, which would often result in irritation and other side effects depending on the components used.[3] In recent years, more advanced methods of improving the physicochemical properties of an API have been studied and have subsequently replaced the traditional form of API adaptation. These include co-crystallization and the formation of cyclodextrin (CD) inclusion complexes with a particular API.[1,3,5] Both of these methods are preferred, and offer advantages such as improved aqueous solubility, dissolution rate, reduced hygroscopicity, compressibility, stabilisation, as well as disguising the taste of the API and reducing its volatility. In addition, the bioactivity of the respective API is not compromised during application of either of these methods.[1,3,5] In order to understand how the physicochemical properties of an API are improved, a chemical understanding of both co-crystals and CD inclusion complexes is necessary. For this reason, the chemistry of both co-crystallization and CD inclusion complexation is discussed in detail below.

1.3) Co-crystals

A co-crystal is defined as "a multiple component crystal in which all components are solid under ambient conditions when in their pure form. These components co-exist as a stoichiometric ratio of a target molecule and a neutral molecular co-crystal former(s)".[6] From a pharmaceutical perspective, the co-crystal comprises two neutral molecules where the one molecule is an API and the other is the co-crystal co-former.[1,7] Pharmaceutical co-formers are typically "Generally Recognized As Safe" (GRAS) compounds which are pharmaceutically acceptable for human consumption and they do not compromise the bioactivity of the API. There is a wide range of compounds which are classified as GRAS, for example, oxalic acid, malonic acid, succinic acid, adipic acid, nicotinamide, ascorbic acid and saccharin.[8] However, in some cases the co-former may be another drug other than the API in question, for example theophylline, theobromine, caffeine, and phenazine.[1,9]

1.3.1) Bonding in co-crystals

The bonding in co-crystals involves non-covalent interactions, which include combinations of hydrogen bonds, ionic bonds, π-π stacking and van der Waals interactions.[10] Co-crystals are often produced between molecules, regardless of their shape or size, which have complementary hydrogen bond functionalities in order to form a particular synthon. Synthons are defined as "structural units within supermolecules which can be formed and/or assembled by known or conceivable intermolecular interactions".[11] Examples of ring synthons involving hydrogen bonding in the 1:1 co-crystal of trans-1,4-cyclohexanedicarboxylic acid and 4,4′-bipyridine can be seen in Figure 1.1 on the following page.

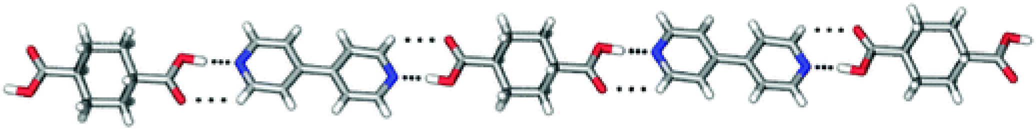

Figure 1.1: The non-covalent, hydrogen bond interactions in the 1:1 co-crystal of trans-1,4-cyclohexanedicarboxylic acid and 4,4′-bipyridine.[12]

1.3.2) Conditions for co-crystal formation

There are multiple variables that determine whether a co-crystal will form from a particular API and co-former. These include API and co-former molar ratio, solvent, crystallization technique, and the pressure and temperature of the system.[1] In addition, a co-crystal will only form if the co-crystal is thermodynamically more stable than the individual crystals of each component.[1,13-14] During co-crystallization no covalent bonds are either broken or formed and consequently the bioactivity of the API is not affected.[1,9,15-16] As a result of these non-covalent interactions in co-crystals, the latter have a different crystal structure from the original components which formed the respective co-crystal. Therefore, co-crystallization can produce a wide range of new solid forms of either established drugs or previously discarded drugs. These products have the potential to improve the physicochemical properties of the untreated drug.[1]

1.3.3) Co-crystallization – a pharmaceutical perspective

From a pharmaceutical perspective, co-crystallization offers the opportunity to produce new varieties of a given API, which in turn improve the physicochemical properties of the native drug.[17] These properties include insufficient aqueous solubility, hygroscopicity and low dissolution rate, poor compressibility (which can prevent tablet formation), and low thermal stability, reflected in a low melting point.[1,18] In addition, a further advantage of co-crystallization is that it extends the patent life of known drugs. The implication of this is that the time it would usually take to develop a new drug for commercial use (approximately 13.5 years) can be drastically reduced by modifying or improving the properties of known drugs already in use. Thus, this process allows the increasing demand for treatments to be met at a much earlier stage and to be safely feasible for human use.[19]

1.3.4) Co-crystals versus salts

For many years it has been known that salts of bioactive compounds are suitable as pharmaceuticals owing to their relatively high aqueous solubility. However, co-crystals have the added advantage that their formation does not depend on the presence of inherent acid and base functionalities in their components. This is in contrast to pharmaceutically acceptable salts, as the number of molecules that can be ion-paired to form salts is limited. As a result, the advantage of co-crystallization is that it allows for a much wider spectrum of components to be used to create new solid forms of the drug.[1,20]

1.4) Cyclodextrin (CD) inclusion complexes

CD inclusion complexation with a particular API can also improve the physicochemical properties of an API, but it involves a different preparative methodology in comparison to co-crystallization.[3] CDs are cyclic oligosaccharides which consist of multiple glucopyranose units linked together by α-(1,4) bonds.[3,21] CDs are formed by an intramolecular transglycosylation reaction as a result of the degradation of starch by a CD glucanotransferase enzyme.[3,22] The native CDs include α-CD, β-CD and γ-CD which consist of 6, 7 and 8 glucopyranose units respectively. The structure of a CD is toroidal in shape with a hydrophobic, non-polar cavity at the interior and a hydrophilic exterior.[3,23] X-ray studies have indicated that the secondary hydroxyl groups, which are located at C_2 and $C_{3,}$ are situated at the wider end of the toroidal shape while the primary hydroxyl groups, which are located at $C_{6,}$ are situated at the opposite, narrower end of the toroidal structure. This can be observed in Figure 1.2. In addition, the ether-like (glycosidic) oxygen atoms and non-polar C_3 and C_5 hydrogen atoms are directed towards the interior of the toroidal-shaped molecule (Figure 1.2).[3]

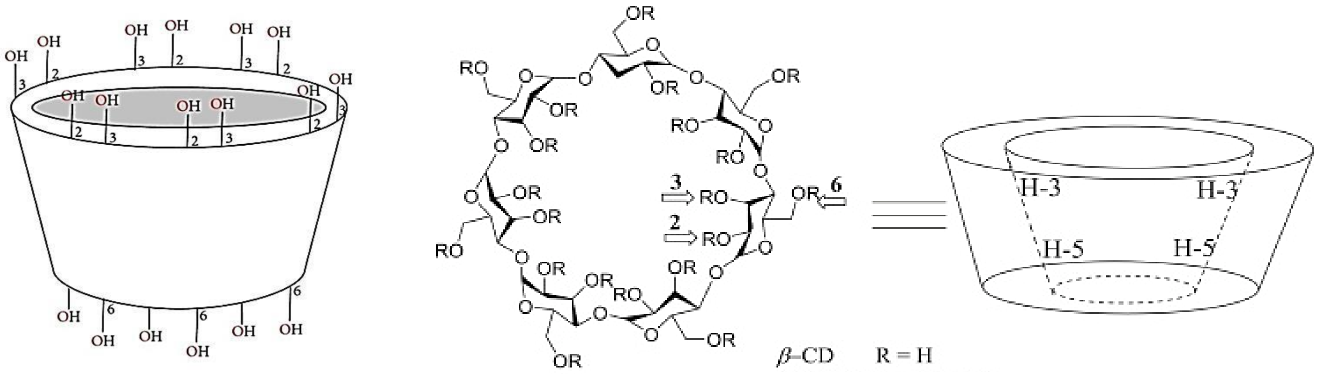

Figure 1.2: The left-hand image displays the O2 and O3 hydroxyl groups on the wider secondary rim, while the O6 hydroxyl groups are on the narrower primary rim. The central image displays the glycosidic oxygen atoms pointing towards the interior of the toroidal-shaped β-CD molecule. The right-hand image is a schematic diagram of β-CD, which displays two (of the seven) pairs of H3 and H5 atoms that are directed towards the interior of the cavity.[24-25]

1.4.1) The formation of a cyclodextrin (CD) inclusion complex

The formation of solid inclusion complexes is one of the most important features of CDs in the pharmaceutical industry. The interior of a CD acts as a cavity which can accommodate guest molecules. This cavity of the CD creates a microenvironment in which a correctly sized, non-polar guest molecule can enter in order to form an inclusion complex.[3,26] This can be observed in Figure 1.3. The binding strength of the CD complex is dependent on how well the guest molecule fits into the CD cavity. In solution, the guest molecule is not necessarily permanently situated in the CD cavity, but rather a dynamic equilibrium ($CD{\cdot}G \rightleftharpoons CD + G$) exists between the free host and free guest molecule, and the CD complex. Furthermore, it is not a requirement that the entire guest molecule should be situated inside the CD cavity, and successful CD inclusion complexation can also be achieved when only a hydrophobic residue of the guest molecule enters the cavity of the CD molecule.[3,27-28] As with the formation of co-crystals, during the formation of a CD inclusion complex, no covalent bonds are formed or broken.[3,29] CD inclusion complexation is an enthalpy-favoured reaction where the cavity releases enthalpy-rich water molecules. The hydrophobic guest molecules displace the water molecules from the hydrophobic cavity in order to attain non-polar···non-polar interactions between the CD cavity and guest molecules. This results in a decrease in the ring strain of a CD and thus the CD inclusion complex is in an overall more stable, lower energy state.[3,22] In summary, there are two main factors which result in the formation of a CD inclusion complex. The first factor is determined by the relative sizes between the CD cavity and the guest molecule. The second factor is the thermodynamic favourability of the complexed state relative to the separate components.[3]

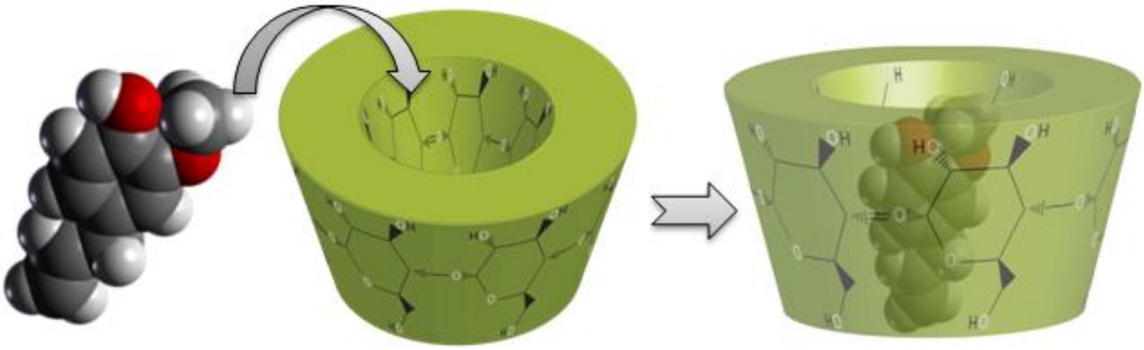

Figure 1.3: A diagram illustrating how a guest molecule fits inside the cavity of a CD molecule.[30]

1.4.2) The lower energy state and equilibrium of cyclodextrin (CD) inclusion complexes

There are four factors which contribute to this previously mentioned lower energy state of the CD inclusion complex. These include: polar water molecules being displaced from the hydrophobic cavity; an increase in hydrogen bond formation when the displaced water enters the bulk aqueous medium of the solvent; reduced repulsive interactions between the aqueous solution and guest molecules; and an increase in the hydrophobic interactions when the guest molecule enters the CD cavity.[3] CD inclusion complexation involves a double equilibrium process, whereby the initial equilibrium is reached rapidly as a result of the enthalpy-driven factors mentioned above. However, the second equilibrium takes longer to reach, as it involves fine conformational changes of the guest molecule inside the CD cavity in order to exploit the van der Waals forces that are present.[3]

1.4.3) The molecular geometry of a cyclodextrin (CD)

The molecular geometry of the CD molecule is often distorted, initially with crystallisation and furthermore with complexation, owing to the change in the electrostatic environment with the advent of the guest molecule.[31] As a result, geometrical parameters (based on an idealised O4-polygon drawn within the CD molecule) were defined within the macrocycle in order to quantify such distortions (Figure 1.7).[31-32] These geometrical parameters include the parameter l that measures the distance from each O4 atom to the centroid of the O4-polygon, the parameter D that measures the consecutive O4···O4 distances of the O4-polygon, the parameter Φ that measures O4A(n-1)···O4A(n)···O4A(n+1) angles of the O4-polygon, and the parameter d that measures the torsion angles O4A(n)···O4A(n+1)···O4A(n+2)···O4A(n+3) of the O4-polygon.

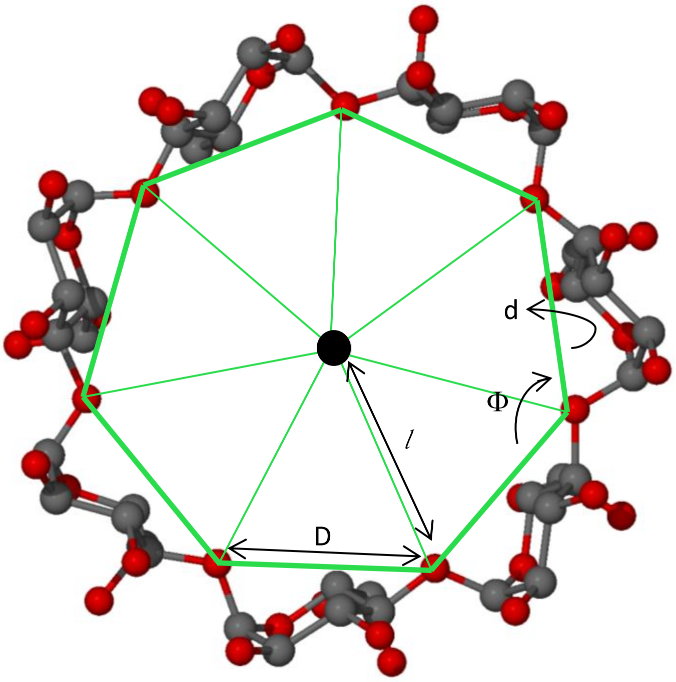

Figure 1.7: Principal parameters defining the geometry of the O4-polygon in β-CD.

Furthermore, the value D_3 (which is not directly related to the O4-polygon) measures the O···O distances of the O2(n)-H···O3(n-1) / O2(n)···H-O3(n-1) hydrogen bonds between consecutive glucose units. In addition, the parameter α measures the deviation from planarity of the O4-polygon, which is achieved by comparing the deviation of each O4 atom from the O4 mean plane (Figure 1.8a). Lastly, the value τ_2 is defined by the acute angle between the O4 mean plane and a second plane that passes through the O4, C4, C1 and O4′ atoms of each glucose unit. This angle measures the inclination of each glucose unit relative to the mean O4 plane (Figure 1.8b).

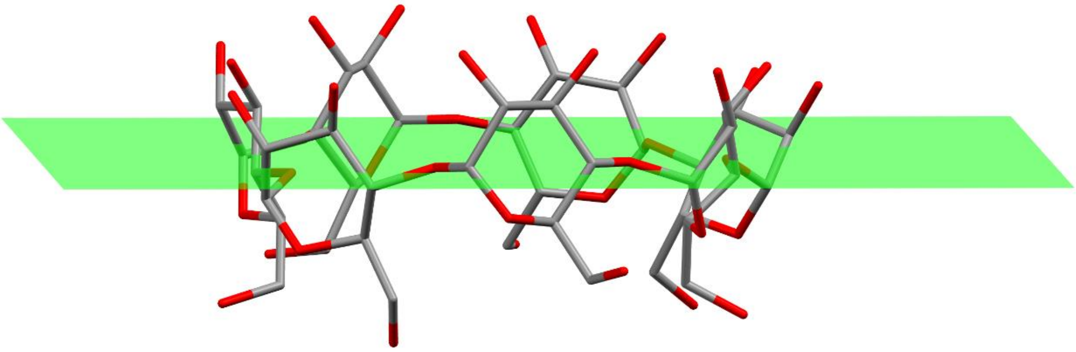

Figure 1.8a: The O4 mean plane of the O4-heptagon in β-CD.

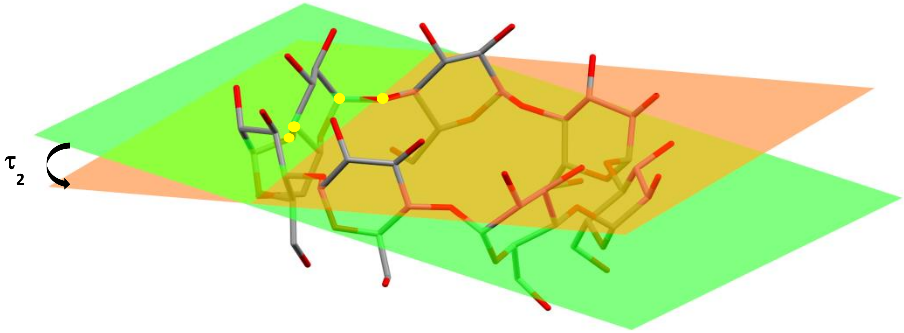

Figure 1.8b: The angle τ_2 is indicated by the acute angle between the O4 mean plane and a second plane that passes through the O4, C4, C1 and O4′ atoms of a glucose unit.

1.4.4) Cyclodextrins (CDs) – a pharmaceutical perspective

From a pharmaceutical perspective, CDs have the ability to enhance the delivery of drugs through a biological membrane. A CD inclusion complex achieves this by retaining the hydrophobic drug molecule in the aqueous medium. The majority of drugs based on CD formulation are delivered orally. In this case the aqueous medium is the gastrointestinal (GI) fluid and the biological membrane of interest is the GI tract. The CD molecule remains in the aqueous medium and is eventually degraded by enzymes, while the drug molecule diffuses through the membrane into the bloodstream.[3,33] Thus, CDs have a wide range of applications in the pharmaceutical industry. For example, CD inclusion complexes can aid in managing liquid APIs, which can be transformed into solids as CD inclusion complexes, and can thus allow tablet formation of the respective API to be produced. This can sometimes also result in an improved bioavailability (due to the hydrophilic exterior of the CD molecule), which would thus result in a lower dosage of the drug being administered. The stability of an API can also be improved *via* CD inclusion complexation, as it improves the resistance of the API to oxidation, hydrolysis, light and heat.[3] Furthermore, CD complexation can protect various organs in the human body, should the untreated API cause irritating effects during administration. Lastly, bitter tastes or vile odours of various APIs can also be disguised by forming CD inclusion complexes, which can result in a more acceptable administration of the drug from the point of view of the patient.[3] Possible guest molecules that can form CD inclusion complexes from a pharmaceutical perspective include drugs from many classes.[3,28]

1.5) General aims and objectives

The aim of this Master's project was to synthesize, characterise and isolate pharmaceutical supramolecular derivatives of APIs which may display modified properties, *via* co-crystallization and cyclodextrin inclusion complexation. Consequently, these supramolecular derivatives would be further investigated for their potential to alter the aqueous solubility of the native APIs. The APIs under investigation included allopurinol (used for the treatment of gout, kidney stones and certain cancers), 6-thioguanine (used for the treatment of leukaemia) and valproic acid (used for the treatment of epilepsy and bipolar disorders). The structures of these APIs can be seen in Figure 1.9. All three of these pharmaceutical drugs are currently in use and available commercially. In addition, they have the potential to form hydrogen bonds, which is the main criterion for co-crystallization.[1] Furthermore, they were selected as a result of their low aqueous solubility, which is the major shortcoming of these drugs in terms of bioavailability. A detailed description of each API is provided below, with a summary of their selected properties in Table 1.1.

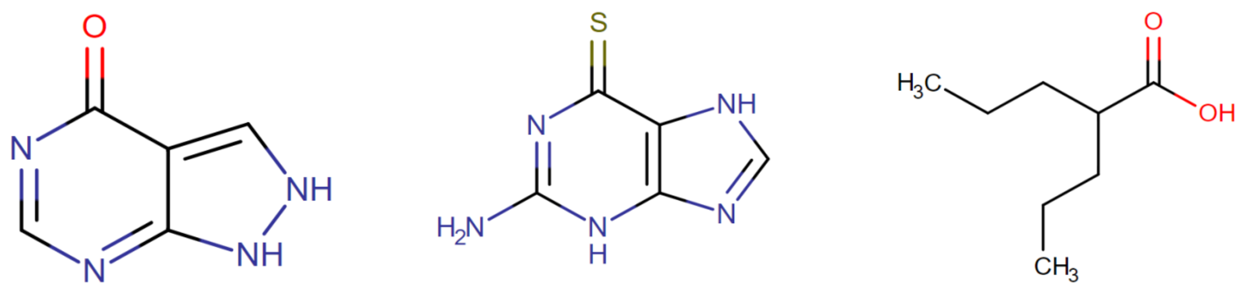

Figure 1.9: The molecular structures of allopurinol, 6-thioguanine and valproic acid (left to right).[34-36]

Table 1.1: Selected properties of the APIs.[34-40]

Property	**Allopurinol**	**6-Thioguanine**	**Valproic acid**
Molecular formula	$C_5H_4N_4O$	$C_5H_4N_5S$	$C_8H_{16}O_2$
Molar mass ($g.mol^{-1}$)	136.112	167.193	144.211
Aqueous solubility ($mg.cm^{-3}$)	0.480 – 0.569 (25 °C)	< 1 (22.5 °C)	1.3 (not stated °C)/ <1 (22.2 °C)
Melting point (°C)	350	> 360	–

1.5.1) Allopurinol

Allopurinol (systematic name 1H-pyrazolo[3,4-d]pyrimidin-4-ol)[37] is classed as a xanthine oxidase inhibitor and it is used for the prevention of gout attacks, the treatment of kidney stones and the excessive production of uric acid.[41] It is administered orally twice per day in the form of a pill and it is used to treat the above mentioned conditions by decreasing the levels of uric acid production in the human body.[41] The mechanism of action of allopurinol operates by inhibiting the activity of the enzyme xanthine oxidase, which produces uric acid through the oxidation of the oxypurines, hypoxanthine and xanthine. Consequently, serum and urinary uric acid levels can be controlled in the body.[34,42]

The literature values for the aqueous solubility of allopurinol are 0.48 $mg.cm^{-3}$ at 25 °C,[43] and 0.569 $mg.cm^{-3}$ at 25 °C,[40] and 80 – 90 % of the drug is absorbed in the gastrointestinal tract.[34] Therefore, the major shortcoming of this drug is its aqueous solubility. As a result, an improved aqueous solubility would be of pharmaceutical interest, as it could potentially reduce the cost of the drug, since less of the active ingredient would be required.

1.5.2) 6-Thioguanine

The drug 6-thioguanine (systematic name 2-amino-6-mercaptopurine)[38] is currently used to treat acute myelogenous leukaemia and it is administered orally; however, the dosage depends on the weight of the patient and on whether this medication is part of a combination therapy. For example, the dosage for adults is 2 mg.kg^{-1} per day for single agent therapy, and if no improvement is observed after four weeks, then the dosage may be increased cautiously to 3 mg.kg^{-1} per day.[44]

6-Thioguanine is categorised as an antimetabolite,[44] and therefore it would be more feasible to gain an overall understanding of the background with regard to the mode of action of an antimetabolite, in order to contextualise the mechanism of action for this drug. Antimetabolites contain either purine- or pyrimidine-based functionalities (in this case 6-thioguanine contains a purine functional group) and they have similar structures to the naturally occurring enzyme molecules used in DNA reproduction. As a result, the antimetabolites are ‘disguised’ as the naturally occurring enzyme molecules and diffuse into the cell and are thus transformed into analogues of cellular nucleotides. Consequently, they then prevent any of the naturally occurring enzymes from being incorporated into the cell during the S phase of the cell’s life cycle, which would be critical for DNA synthesis and replication of the cell.[45-46]

In the context of 6-thioguanine, it is metabolised *via* the enzyme hypoxanthine-guanine phosphoribosyltransferase (HGPRTase), and converted to the corresponding ribosenucleoside 6-thioguanine monophosphate (6-TGMP).[47-48] High concentrations of 6-TGMP accumulate (approximately 0.1 mM),[47] even after therapeutic doses, which prevents many natural enzymes from being involved in the purine-based biosynthesis of the cell. Furthermore, 6-TGMP is converted into 6-thioguanine diphosphate (6-TGDP) and 6-thioguanine triphosphate (6-TGTP) *via* the enzyme phosphorylation. The three derivatised ribosenucleosides, 6-TGMP, 6-TGDP, 6-TGTP (collectively named 6-thioguanine nucleotides (6-TGN)) are all cytotoxic. This toxicity occurs *via* the incorporation of the 6-TGNs into the cell during its S-phase, which thus prevents the growth and division of the cell.[47-48]

6-Thioguanine is classed as ‘insoluble’ since less than 1.0 mg dissolves in 1 cm^3 of water at 22.5 °C.[38] Consequently, an improved aqueous solubility would be of interest and this could also enhance the bioavailability of the drug.

1.5.3) Valproic acid

The drug, valproic acid (systematic name, 2-propylpentanoic acid),[39] is currently used as an anticonvulsant, primarily to treat epilepsy and bipolar affective disorder.[36,49] The drug is administered orally in the form of a gelatine tablet, in a liquid formulation, or as a powder.[36] The mechanism of action as a therapeutic anticonvulsant is not well understood and consequently several theoretical explanations for this exist.[36,49-50] Valproic acid dissociates into the ion, valproate, in the gastrointestinal tract. One theory suggested that the valproate ion causes an increase in the concentration of gamma-aminobutyric acid (GABA) in the brain.[36] The valproate ion prevents enzymes from catabolising GABA and therefore an increased concentration of GABA is observed. The function of GABA is to inhibit neurotransmission and thus an increase in concentration will amplify this effect.[36] A second theory for the mechanism of action proposed that valproic acid can block the voltage sensitive sodium channels and thereby reduce repetitive neuronal firing.[36,51]

Valproic acid is also currently under investigation for other pharmaceutical therapies, as it has also displayed various anti-cancer and anti-HIV activities.[36,52] In this case results have indicated that valproic acid appears to inhibit the *in vitro* activity of the enzyme histone deacetylase 1 (HDAC1) by binding to its catalytic centre.[36,49,52] According to Göttlicher *et al.,*[52] animal experiments have displayed reduced growth in cancerous tumours following treatment with valproic acid.[52] In addition, HIV requires the activity of HDAC1 in order to remain in infected cells. The results from a study performed in 2005 indicated that the combination of valproic acid with highly active antiretroviral therapy can result in the HIV infection being reduced by 75 % in the patient.[36] Another study conducted in 2008 also provided evidence for the treatment of HIV-1 with valproic acid as a HDAC1 inhibitor.[53]

Sodium valproate is an alternative, derivatised form of valproic acid that is currently available commercially. It has a high aqueous solubility of 2.0×10^3 $mg.cm^{-3}$ at 20 ^oC,[54] as opposed to pure valproic acid which is quoted as having a solubility “less than 1 $mg.cm^{-3}$ at 22.2 ^oC”,[39] and 1.3 $mg.cm^{-3}$ (temperature not specified)[36,39]. In addition, a study reported that sodium valproate slightly lowered the number of gastrointestinal side effects;[55] however, despite this advantage there was a significant amount of controversy around the financial cost of sodium valproate.[55-56] According to Schwartz, *et al.* it is approximately 120 times the cost of valproic acid at $1162.80 per patient per year,[55] and these authors also maintain that this high cost does not warrant the use of sodium valproate as a replacement for the acid form, despite the fewer reported side effects.[55-56]

As a result, further supramolecular derivatisation is warranted for valproic acid, which could render improved solubility, lower costs and less frequent pre-absorption side effects. Therefore, co-crystallization and CD inclusion complexation of this drug were considered worthy of investigation by the author of this dissertation.

1.6) Specific objectives

Thus, the objectives of this project were to synthesize co-crystals with each individual drug (namely allopurinol, 6-thioguanine and valproic acid) and a series of corresponding co-formers. In addition, the synthesis of CD inclusion complexes with all three APIs was to be attempted with the native CDs (namely α-CD, β-CD and γ-CD) and the methylated CDs (namely DMB, TMB and TMA). The intended syntheses anticipated the growth of single crystals of the desired products for further analytical studies. In addition, such products would be assessed for their drug solubility enhancement value. Lastly, phase solubility studies with γ-CD, RAMEB and HPBCD were also intended to be performed with allopurinol and 6-thioguanine in order to assess the possible solubility enhancement of the respective APIs in aqueous solution.

1.7) References

1) Sekhon, B. S. *Ars Pharmaceutica,* **2009**, *50*, 99.

2) Mirza, S.; Miroshnyk, I.; Heinämäki, J.; Yliruusi, J. *Dosis*, **2008**, *24*, 90.

3) Del Valle, M. *Process Biochem.*, **2004**, *39*, 1033.

4) Scannell, J. W.; Blanckley, A.; Boldon, H.; Warrington, B. *Nat. Rev. Drug Discov.,* **2012**, *11*, 191.

5) Upadhyay, N.; Shukla, T. P.; Mathur, A.; Manmohana, J. S. K. *Int. J. Pharm.,* **2011**, *8*, 144.

6) Shan, N.; Zaworotko, M. J. *Drug Discov. Today,* **2008**, *13*, 440.

7) Vishweshwar, P.; McMahon, J. A.; Bis, J. A.; Zaworotko, M. J. *J. Pharm. Sci.,* **2006**, *95*, 499.

8) Karki, S.; Friščić, T.; Fábián, L.; Laity, P. R.; Day, G. M.; Jones, W. *Adv. Mater.,* **2009**, *21*, 3905.

9) Sun, C. C.; Hou, H. *Cryst. Growth Des.*, **2008**, *8*, 1575.

10) Aakeröy, C. B.; Salmon, D. J. *CrystEngComm,* **2005**, *7*, 439.

11) Rao, C. N. R.; Jones, W. *Supramolecular Organization and Material Design;* Cambridge University Press: London, 2008.

12) Bhogala, B. R.; Basavoju, S.; Nangia, A. *CrystEngComm,* **2005**, *7*, 551.

13) Issa, N.; Karamertzanis, P. G.; Welch, G. W. A.; Price, S. L. *Cryst. Growth Des*., **2009**, *9*, 442.

14) Karamertzanis, P. G.; Kazantsev, A. V.; Issa, N.; Welch, G. W. A.; Adjiman, C. S.; Pantelides, C. C.; Price, S. L. *J. Chem. Theor. Comput.,* **2009**, *5*, 1432.

15) Zaworotko, M. *Acta Cryst*., **2008**, *A64*, C11.

16) Jayasankar, A.; Somwangthanaroj, A.; Shao, Z. J.; Rodríguez-Hornedo, N. *Pharm. Res.,* **2006**, *23*, 2381.

17) Remenar, J. F.; Morissette, S. L.; Peterson, M. L.; Moulton, B.; MacPhee, J. M.; Guzmán, H.; Almarsson, O. *J. Am. Chem. Soc.,* **2003**, *125*, 8456.

18) Peterson, M. L.; Hickey, M. B.; Zaworotko, M. J.; Almarsson, O. *J. Pharm. Sci.,* **2006**, *9*, 317.

19) Paul, S. M.; Mytelka, D. S.; Dunwiddie, C. T.; Persinger, C. C.; Munos, B. H.; Lindborg, S. R.; Schacht, A. L. *Nat. Rev. Drug Discov*., **2010**, *9*, 203.

20) Serajuddin, A. T. M. *Adv. Drug Deliv. Rev*., **2007**, *59*, 603.

21) Jinpeng, B. Y.; Huanxin, Z.; Jin, Z. *Molecules,* **2011**, *16*, 3010.

22) Szejtli, *J. Chem. Rev.,* **1998**, *98*, 1743.

23) Singh, R.; Bharti, N.; Madan, J.; Hiremath, S. N. *J. Pharm. Sci. Technol.,* **2010**, *3*, 171.

24) Savjani, K. T.; Gajjar, A. K.; Savjani, J. K. *ISRN Pharm.*, **2012**, *2012*, 1.

25) Liu, L.; Xu, J.; Zheng, H.; Li, K.; Zhang, W.; Li, K.; Zhang, H. *Dyes Pigments*, **2017**, *139*, 737.

26) Loftsson, T.; Brewster, M. E. *J. Pharm. Sci.,* **1996**, *85*, 1017.

27) Muñoz-Botella, S.; Del Castillo, B.; Martyn, M. A. *Ars. Pharm.,* **1995**, *36,* 187.

28) Schmid, G. *Trends Biotechnol.,* **1989**, *7*, 244.

29) Chadha, R.; Kashid, N.; Saini, A. *J. Sci. Ind. Res. India,* **2004**, *63*, 211.

30) Van der Rohe, M. *Thoughts for Food*. <http://thoughtsforfoodandbeyond.com/category/food-technology/> (Accessed 28 July 2016).

31) Harata, K. *Chem. Rev.*, **1998**, *98,* 1803.

32) Saenger, W.; Jacob, J.; Gessler, K.; Steiner, T.; Hoffman, D.; Sanbe, H.; Koizumi, K.; Smith, S. M.; Takaha, T. *Chem. Rev.,* **1998**, *98*, 1787.

33) Uekama, K.; Adachi, H.; Irie, T.; Yano, T.; Saita, M.; Noda. K. *J. Pharm. Pharmacol.,* **1992**, *44*, 119.

34) Drugbank. *Allopurinol*. <https://www.drugbank.ca/drugs/DB00437> (Accessed 8 February 2016).

35) Drugbank. *Tioguanine*. <https://www.drugbank.ca/drugs/DB00352> (Accessed 8 February 2016).

36) Drugbank. V*alproic acid*. <https://www.drugbank.ca/drugs/DB00313> (Accessed 8 February 2016).

37) Pubchem. *Allopurinol*. <https://pubchem.ncbi.nlm.nih.gov/compound/allopurinol> (Accessed 8 February 2016).

38) Pubchem. *6-Thioguanine*. <https://pubchem.ncbi.nlm.nih.gov/compound/6-Thioguanine> (Accessed 8 February 2016).

39) Pubchem. *Valproic acid*. <https://pubchem.ncbi.nlm.nih.gov/compound/valproic_acid> (Accessed 8 February 2016).

40) Yalkowsky, S. H.; He, Y.; Jain, P. *Handbook of Aqueous Solubility Data*; CRC Press: Boca Raton, London, New York, 2003, p. 137.

41) MedlinePlus. *U.S. National Library of medicine*. <www.nlm.nih.gov/medlineplus/druginfo/meds/a682673.html>, 2012 (Accessed 8 February 2016).

42) Pacher, P.; Nivorozhkin, A.; Szabó, C. *Pharmacol. Rev.,* **2006**, *58*, 87.

43) O'Neil, M. J. (ed.). *The Merck Index - An Encyclopedia of Chemicals, Drugs, and Biologicals;* Whitehouse Station, NJ: Merck and Co., Inc.: 2006, p. 283.

44) Drugs.com. Know more. Be sure. *Thioguanine*. <https://www.drugs.com/pro/thioguanine.html>, December 1984 (Revised March 2010; Accessed 7 February 2016).

45) Parker, W. B. *Chem. Rev.,* **2009**, *109*, 2880.

46) Das-Bradoo, S.; Bielinsky, A. *Nature Education*, **2010**, *3*, 50.

47) Nelson, J. A.; Carpenter, J. W.; Rose, L. M.; Adamson, D. J. *Cancer Res.*, **1975**, *35*, 2872.

48) Wikipedia. *Tioguanine*. <https://en.wikipedia.org/wiki/Tioguanine>, June 2006 (Revised February 2016; Accessed 8 February 2016).

49) Williams, R. S. B.; Cheng, L.; Mudge, A. W.; Harwood, A. J. *Nature*, **2002**, *417*, 292.

50) Kelly, K. M.; Gross, R. A.; Macdonald, R. L. *Neurosci. Lett.*, **1990**, *116*, 233.

51) Willow, M.; Kuenzel, E. A.; Catterall, W. A. *Mol. Pharmacol.,* **1984**, *25*, 228.

52) Göttlicher, M.; Minucci, S.; Zhu, P.; Krämer, O. H.; Schimpf, A.; Giavara, S.; Sleeman, J. P.; Lo Coco, F.; Nervi, C.; Pelicci, P. G.; Heinzel, T. *EMBO J.*, **2001**, *20*, 6969.

53) Castor, T. P. (2010), *US20100166806A1*, United States, Patent Application Publication.

54) Pubchem. *Sodium Valproate*. <https://pubchem.ncbi.nlm.nih.gov/compound/Sodium_valproate> (Accessed 17 March 2017).

55) Schwartz, T. L.; Massa, J. L.; Gupta, S.; Al-Samarrai, S.; Devitt, P.; Masand, P. S. *J. Clin. Psychiat.,* **2000**, *2*, 45.

56) Sawyer, W. T.; Carson, S. W.; Early, J. J. *Am. J. Health-Syst. Ph.,* **1997**, *54*, 1716.

Chapter 2

Experimental Methods

2.1) Materials

2.1.1) Active Pharmaceutical Ingredients (APIs)

The APIs, which consisted of allopurinol ($C_5H_4N_4O$), 6-thioguanine ($C_5H_5N_5S$) and valproic acid ($C_8H_{16}O_2$) were purchased from Sigma-Aldrich Chemie Gmbh (Steinheim, Germany).

2.1.2) Cyclodextrins (CDs)

β-Cyclodextrin (β-CD; $C_{42}H_{70}O_{35}$), hexakis(2,3,6-tri-*O*-methyl)-α-cyclodextrin (TMA; $C_{54}H_{96}O_{30}$), heptakis(2,6-di-*O*-methyl)-β-cyclodextrin (DMB; $C_{56}H_{96}O_{35}$), heptakis(2,3,6-tri-*O*-methyl)-β-cyclodextrin (TMB; $C_{63}H_{112}O_{35}$), randomly methylated β-cyclodextrin (RAMEB; $(C_{42}H_{70-n}O_{35})(CH_3)_n$, where n = 12) and hydroxypropyl β-cyclodextrin (HPBCD; $(C_{42}H_{70-n}O_{35})(C_3H_7O)_n$, where n = 4.5) were purchased from Cyclolab (Budapest, Hungary). α-Cyclodextrin (α-CD; $C_{36}H_{60}O_{30}$) and γ-cyclodextrin (γ-CD; $C_{48}H_{80}O_{40}$) were purchased from Wacker, Biosolutions (Halle, Germany).

2.1.3) Co-formers

The co-formers used in co-crystallization experiments were purchased from Sigma-Aldrich Chemie Gmbh (Steinheim, Germany) and Acros Organics (New Jersey, USA). The co-formers are listed in the Appendix under section 1, Table 1.1, p. 2.

2.2) Co-crystal screening

2.2.1) Virtual co-crystal screening

The first phase of the co-crystal screening included a qualitative computer-based investigation. This investigation firstly involved observing the type of supramolecular synthons that occurred between the API molecules in their own crystals. Secondly, it assessed different molecular fragments of the APIs for their potential to form stable, hydrogen bonded supramolecular ring synthons with carboxylic acid and amide functional groups. The frequency for the formation of these various hydrogen bonded ring synthons was noted and thus indicated which co-formers to select preferentially. This analysis was performed with the Cambridge Structural Database (CSD) in Conquest,[1] where the structures were imported into X-SEED,[2] and Mercury.[3]

2.2.2) Dry co-grinding

The second phase of the co-crystal screening involved dry co-grinding experiments. This process involved adding the API and one co-former into a mortar and grinding the mixture with a pestle. Equimolar quantities of the API and co-former were mixed and the time allocated to perform these experiments was 15 minutes, unless stated otherwise. These experiments were performed in order to assess whether a new crystalline phase could be synthesized after dry co-grinding the API with the co-former.

2.2.3) Liquid-assisted grinding (LAG)

This process involved the same experimental set-up and method as the dry co-grinding experiment, except that small measured volumes of organic solvent were added into the mortar during the co-grinding process.

2.2.4) Co-precipitation

The third phase of the co-crystal screening involved co-precipitation experiments. This process incorporated the separate dissolution of the API and the co-former in an equimolar ratio (unless stated otherwise) with a common solvent, while stirring at a constant temperature. The temperature used to dissolve both components was dependent on the organic solvent used. Once both the API and co-former were dissolved, each solution was filtered into a common vial with a nylon 0.45 µm microfilter. The resulting solution was subjected to varying conditions to allow co-precipitation to occur, as described below.

Slow cooling: This method of co-precipitation allowed the saturated solution, which contained the API and co-former, to cool slowly without any evaporation taking place. The individual solutions of the API and co-former were filtered into a common vial. The vial was subsequently sealed and placed in a Dewar flask, which had been filled with water and pre-heated to the temperature at which the solutions were dissolved.

Slow evaporation: This procedure involved allowing the solvent to evaporate slowly in order to permit the dissolved product to precipitate. Therefore, once the individual solutions of the API and co-former were filtered into a common vial, the vial was sealed with parafilm, subsequently punctured with a few pin-sized holes and left on the laboratory bench in order to allow evaporation to take place over a controlled, extended period.

2.3) Cyclodextrin inclusion

2.3.1) Kneading

This technique involved mixing the API and CD in a mortar and kneading them with a small amount of Milli-Q® water[4] for 30 – 40 minutes. Kneading experiments were performed with both the native CDs and methylated CDs. However, with the experiments that involved the latter class of host compounds, only a miniscule measured volume of water was added at five minute intervals, owing to their high aqueous solubility.

2.3.2) Co-precipitation

Co-precipitation experiments with the native and methylated CDs involved different methods of preparation. As a result, each will be described separately.

Native cyclodextrins (CDs): The co-precipitation experiments that involved the native CDs, namely α-CD, β-CD and γ-CD, were performed by dissolving the CD in water at 70 °C while stirring at a continuous rate. The volume of water was dependent on the type of CD used and the respective mass, and thus the volume is specifically stated for each experiment.

In the case where the API was a solid (for example, allopurinol and 6-thioguanine), the API in powder form was added very slowly to the aqueous CD solution. In contrast, where the API was a liquid (for example, valproic acid), the API was added dropwise to the aqueous CD solution. The resultant solution was left to stir for a period varying between 3 and 6 hours, unless stated otherwise. Thereafter, the solution was filtered using a nylon 0.45 µm microfilter and complex crystals were allowed to co-precipitate either through slow cooling or slow evaporation.

Methylated cyclodextrins (CDs): These methylated CDs, namely TMA, DMB and TMB, were dissolved in water at room temperature while stirring at a constant rate. Once again, the volume of water was dependent on the type of CD used and its respective mass, and thus the volume is specifically stated for each experiment. Miniscule amounts of the API were added slowly to the solution of the methylated CD. Subsequently, temperature cycling was employed which entailed repetitive cycles of heating the stirring solution to 70 ^{o}C and then suddenly cooling it to 4 ^{o}C. The aim of this process was to promote inclusion complexation of the API with the methylated CD. The solution was then filtered into a clean vial with a 0.45 µm nylon microfilter and the vial was then sealed and placed in the oven at 60 ^{o}C in order to allow complex crystallization to occur.

2.4) Powder X-ray Diffraction (PXRD)

Powder X-ray diffraction (PXRD) patterns were recorded for the co-ground, kneaded and co-precipitated materials, as well as for their respective reactants. This was performed in order to assess whether unique crystalline products had formed and was achieved by comparing the PXRD pattern of the co-ground, kneaded or co-precipitated material with the PXRD pattern of each individual reacting component. This analysis was performed at room temperature using a D8 Advance diffractometer using CuKα_1 radiation (λ = 1.5406 Å) with an X-ray generator set at 30 kV and 40 mA. The sample preparation involved grinding the material into a very fine crystalline powder in order to minimise the effect of preferred orientation. This sample was subsequently placed onto a silicon zero background sample holder. The scanning range was 4^{o} – 40^{o} 2θ with a step size of 0.0164^{o} and a primary beam path slit of 0.6 mm.

2.5) Single Crystal X-ray Diffraction (SCXRD) analysis

Crystals of adequate quality, obtained from co-precipitation experiments, were analysed using a single crystal four-circle X-ray diffractometer in order to determine the structural properties of the crystal. The crystals were removed from the mother liquor and immediately coated in Paratone oil[5] to prevent the loss of solvent molecules that may have been included in the crystal structure. Where necessary, the crystals were cut to an appropriate size and subsequently placed on the diffractometer for analysis. Initially, a unit cell measurement was performed at room temperature. This technique established the unit cell parameters of the single crystal in question and consequently these were compared with the parameters of all the crystal structures reported in the CSD.[1] This confirmed whether the single crystal under analysis was new, in which case a full data-collection was performed in order to determine the crystal structure. The instruments that were used to perform unit cell determinations were the Bruker KAPPA APEX II DUO single crystal X-ray diffractometer and the ENRAF Nonius FR 590 KappaCCD diffractometer. However, full data-collections were only performed on the Bruker KAPPA APEX II DUO instrument, owing to its superior detector sensitivity. Subsequently, the collected data sets were read into the program XPREP[6] which determined the respective space groups, and the structures were solved with the direct methods program SHELXS-97,[7] (or SHELXD-97,[7] for more complex structures). Thereafter the structures were refined by full-matrix least-squares techniques with SHELXL-97,[7] implemented in the X-SEED[2] interface.

A few of the CD inclusion complex structures were solved by the method of isomorphous replacement. This process involved identifying a CD inclusion complex from the CSD with very similar unit cell parameters and a common space group. The atomic co-ordinates of the selected complex were placed in the .ins file of the new CD inclusion complex. Subsequently, all the guest atoms, the water molecules, as well as the O6 atoms on the CD molecule (that can freely rotate), were deleted. Thus, only the rigid skeleton of the CD molecule remained as the trial model and it was thereafter refined isotropically and the remaining atoms of the new CD inclusion complex could be placed from subsequent difference Fourier maps. Once the structure of the host molecule was settled, the difference electron density ($\Delta\rho$) peaks of the guest molecule were assigned, and refined initially isotropically and thereafter anisotropically.

Oxygen atoms of the water molecules in the CD inclusion complexes were identified by measuring the distances between the oxygen atoms on the CD molecule and unassigned $\Delta\rho$ peaks and gauging whether they were in the range expected for O···O distances associated with O-H···O hydrogen bonds. The $\Delta\rho$ peaks of height ~2.0 e Å^{-3} or greater, were then assigned as water O atoms with a full site-occupancy, as they displayed acceptable isotropic thermal parameters (U_{iso}) after refinement. However, candidate oxygen atoms with $\Delta\rho$ less than 2.0 e Å^{-3} were pre-set to have constrained U_{iso} values equal to the average of those for the fully-occupied water oxygen atoms, and their individual site-occupancies were treated as variables. Furthermore, several water oxygen atoms were disordered over two positions, such that the distance between the disorder components was less than 2.5 Å. In the final cycles of refinement, the fully-occupied water oxygen atoms were treated anisotropically, while their disordered counterparts were refined isotropically.

2.6) ^{1}H Nuclear Magnetic Resonance (^{1}H NMR) Spectroscopy

Proton NMR experiments were conducted in order to quantify the host-guest stoichiometric ratios of the CD inclusion complexes. The samples of pure inclusion complexes were dissolved in deuterated dimethyl sulfoxide (DMSO-d_6) at 20 °C. These experiments were performed on the Bruker Ultrashield 400 Plus spectrometer and the data were analysed using the program 1D NMR processor.[8]

2.7) Fourier Transform Infrared (FT-IR) Spectroscopy

FT-IR experiments were conducted in order to observe specific frequency shifts for CD inclusion complexes. This was achieved by analysing the natural vibrational frequencies of the bonds in the compounds. This technique was employed to compare the FT-IR spectra of the starting materials with the FT-IR spectrum of the CD inclusion complex. The samples were pressed between sodium chloride windows and the spectra were thereafter recorded on the PerkinElmer Spectrum Two instrument.

2.8) Thermal analysis

Three different thermal techniques were employed in order to analyse the changes in the physical properties of the compounds as a function of temperature. The methods used were hot stage microscopy (HSM), thermal gravimetric analysis (TGA) and differential scanning calorimetry (DSC).

2.8.1) Hot Stage Microscopy (HSM)

HSM was performed in order to correlate the thermal events from the TGA and DSC analyses with a visual representation of these thermal events. The experiment involved placing the crystals on a glass slide and coating them with silicone oil. The analysis was viewed through a Nikon SMZ-10 stereoscopic microscope fitted with a Linkam THM600 hot stage and Linkam TP92 temperature control unit. The images at various temperatures were captured by a real-time Sony Digital Hyper HAD colour video. The captured images were viewed with the Soft Imaging Program AnalySIS.[9] A temperature range of 23 °C – 400 °C was used to analyse the crystals with a standard heating rate of 10 K.min^{-1}, unless stated otherwise.

2.8.2) Thermal Gravimetric Analysis (TGA)

The TGA was used to measure the percentage weight loss as a function of temperature. The data obtained supplied information with regard to the number of water molecules present in the CD inclusion complexes. In addition, the thermal stability of the inclusion complex could be established. The samples prepared for the TGA experiment had a mass of between 0.9 mg and 3.5 mg and were pre-dried on filter paper prior to the experiment. The analysis took place in an open aluminium pan under dry nitrogen gas with a constant flow rate of 60 $cm^3.min^{-1}$. The samples were heated at a constant rate of 10 $K.min^{-1}$ to a maximum temperature of 400 °C. This experiment was performed on the TA-Q500, with Universal Analysis 2000 software.[10]

2.8.3) Differential Scanning Calorimetry (DSC)

The DSC technique was used to analyse the energy difference between an empty reference pan and a pan containing the sample. The DSC detects the changes in energy between the two pans while they are heated at a constant rate. These energy changes are represented as either endothermic or exothermic deviations from the baseline. The endothermic and exothermic events can be associated with thermal events, for example, polymorphic transitions, dehydration, recrystallization, melting and decomposition.

The samples prepared for the DSC experiment were pre-dried on filter paper and had a mass that ranged between 1.0 mg and 3.0 mg and were subsequently placed in a crimped aluminium pan that was vented. The analysis took place under dry nitrogen gas with a constant flow rate of 60 $cm^3.min^{-1}$. The samples were heated at a constant rate of 10 $K.min^{-1}$ to a maximum temperature of 250 °C, unless stated otherwise. These experiments were performed on two different machines. The polymorph of isonicotinamide was analysed on the DSC-Q200 apparatus (TA Instruments) with Universal Analysis 2000 software,[10] while the CD inclusion complexes with valproic acid were analysed on the DSC XP-10 instrument (THASS: Thermal Analysis & Surface Solutions GmbH, Friedberg, Germany) with the software package Differential Scanning Calorimeter, version 3.3.0.7 (D).[11]

Owing to the sensitivity of the DSC machines, it was not possible to take any samples to decomposition, and thus no comparison with respect to decompositions recorded on the TGA or HSM instruments could be made.

2.9) Solubility analysis

2.9.1) Phase solubility analysis with allopurinol and 6-thioguanine

The CDs that were selected for the phase solubility study were γ-CD, HPBCD and RAMEB. A predetermined mass of each CD was dissolved in water in a separate volumetric flask and stirred for 72 hours. Thereafter, ten solutions of varying CD concentrations ranging from 10 % - 100 %, were prepared for each chosen CD. An excess amount of API was added to each solution and stirred vigorously for 72 hours at 25 ^{o}C, after which the solutions were subsequently filtered with 0.45 µm nylon microfilters. Thereafter, 0.1 cm^3 of each solution was diluted to 5 cm^3 (in order to be within the linear range of the UV-vis instrument) and the respective UV-vis absorbance readings were recorded. Three absorbance readings were recorded for each solution and averaged. These entire experiments were performed in duplicate and the results were averaged as they correlated within an acceptable range. The UV-vis absorbance readings were measured on a UV Cary 60 spectrophotometer (Agilent Technologies, Santa Clara, California, USA).

2.9.2) Solubility determination *via* mass increments for the native CD inclusion complexes with valproic acid

Solubility investigations were conducted using a method of adding pre-weighed incremental amounts of valproic acid CD inclusion complexes (namely α-CD·VAL, β-CD·VAL and γ-CD·VAL) into 3.0 cm^3 of water. The resultant suspension was stirred at a constant rate for 72 hours at 25 ^{o}C. An estimation of the aqueous solubility was established visually, its value being recorded as the range between those measured for solutions containing the penultimate and the final masses of CD inclusion complex added, since the final amount resulted in saturation. The aim of this method was not to achieve high accuracy, but rather to serve as a guideline for a reasonable estimation of an approximate solubility enhancement factor. Unfortunately, a more accurate determination was not possible with UV-vis spectrophotometric analysis, because the λ_{max} value of valproic acid (< 200 nm) was out of the readable range.

2.10) References

1. Bruno, J.; Cole, J. C.; Edgington, P. R.; Kessler, M.; Macrae, C. F.; McCabe, P.; Pearson, J.; Taylor, R. *Acta Cryst*., **2002**, *B58*, 389.
2. Barbour, L. J. X-SEED, *A graphical interface to SHELX,* University of Missouri, Columbia, U.S.A, **1999**.
3. Macrae, C. F.; Bruno, I. J.; Chisholm, J. A.; Edgington, P. R.; McCabe, P.; Pidcock, E., Rodriguez-Monge, L.; Taylor, R.; van de Streek, J.; Wood, P. A. *Appl. Cryst.*, **2008**, *41*, 466.
4. Milli-Q water, Millipore Corporation, Billerica, Massachusetts, USA.
5. Paratone N oil, Exxon Chemical Co., Texas, USA.
6. XPREP, *Data Preparation and Reciprocal Space Exploration*. Version 2.0, Bruker Analytical X-ray Systems, **1999**.
7. Sheldrick, G. M. *Acta Cryst*., **2008**, *A64*, 112.
8. Advanced Chemistry Development, Inc. (ACD/Labs*). ACD/NMR Processor Academic Edition,* Version 12.01. (Copyright, **1997 – 2010**).
9. Soft Imaging System GmbH, Digital Solutions for Imaging and Microscopy, Version 3.1 for Windows (Copyright, **1987 – 2000**).
10. Universal Analysis 2000 (TA Instruments-Waters LLC), Version 4.5A for Windows 2000/XP/Vista (Copyright, **1998 – 2007**).
11. Differential Scanning Calorimeter (DSC XP-10), Version 3.3.0.7 (D) (Copyright **2003**).

Chapter 3

Supramolecular Derivatisation of Allopurinol

3.1) Introduction

Various methods of supramolecular derivatisation have been performed on allopurinol.[1-2] According to one article, six different products were synthesized, which include solid dispersions (co-evaporates) of allopurinol with urea, with sodium salicylate and with β-CD, as well as the co-crystallized products of allopurinol with urea, sodium salicylate and β-CD.[1] The co-evaporates were prepared in 1:1 and 1:2 stoichiometric ratios of the drug to the host/carrier. However, the crystallization process involved dissolving allopurinol in dimethyl sulfoxide (DMSO) and adding a 5 % w/v aqueous solution of urea and sodium salicylate respectively, and a 1.9 % w/v aqueous solution of β-CD.[1] No crystal structures were obtained for these derivatised products, as their particle sizes ranged between 60 and 120 μm after filtering and drying under vacuum. Nevertheless, the results indicated varying levels of increased drug release rate relative to untreated allopurinol, with the exception of the crystallized product of allopurinol with 1.8 % w/v β-CD. This product resulted in a slower release rate of the drug in comparison to its native form.[1]

Furthermore, β-CD inclusion complexes were synthesized with allopurinol in its neutral and anionic form in equimolar ratios.[2] These complexes were analysed through NMR diffusion experiments where the resulting structures were theoretically calculated using a computational model (Parameterized Model number 3). The conclusion was that the anionic form of allopurinol had a greater attraction to the cavity of the β-CD molecule than the neutral form.[2]

With regard to co-crystallization, the authors of two studies have claimed to have produced co-crystals with allopurinol;[3-4] however, the published research did not provide convincing evidence for the isolation of allopurinol co-crystals. With regard to the first study, published in 2014,[3] the authors claimed that co-crystals of allopurinol and benzoic acid, as well as allopurinol and D-tartaric acid, had been synthesised in 1:1 stoichiometric ratios.[3] In addition, the authors indicated that an improved aqueous solubility of allopurinol was achieved *via* these products. However, the only evidence that the authors presented for the formation of co-crystals was that the powder X-ray diffraction (PXRD) pattern of the product material was different from the sum of the PXRD patterns of the starting materials in each case.[3] However, the difference in PXRD patterns can only indicate that one has obtained different material from that of the physical mixture of the starting materials, and therefore the product could instead be polymorphs of either starting material, or a salt, or a co-crystal. In other words, a PXRD analysis is not solely definitive to claim the synthesis of co-crystals. To characterise both products, further experimentation, such as a ^{1}H NMR study, would need to be performed in order to determine the stoichiometry of a product synthesised *via* co-precipitation. In addition, if a single crystal of adequate quality were to be grown, then a single crystal X-ray diffraction analysis could be performed in order to determine the structure of the product. This would indicate the bonding connectivity of the molecules and it would be possible to determine whether a salt or co-crystal had formed by measuring the relevant bond lengths.[5] Therefore, it is evident that the results of this research are inconclusive.

The authors of a second study, which is from a book published in 2012, also claimed to have synthesised co-crystals of allopurinol.[4] Unfortunately, due to a lack of access it was not possible to obtain the full text of this document. As a result, the co-formers of the putative co-crystals remain unknown. However, the title of the publication stated that the only method of preliminary characterisation was PXRD. The shortcoming of using this technique in isolation has already been alluded to above.

As a result, there appeared to be a significant amount of interest in forming supramolecular derivatives with allopurinol, and therefore it would be worth investigating this field. The author of this Master's dissertation will attempt to re-synthesize the claimed co-crystals of allopurinol[3] (in order to attempt to characterise them fully), as well as to synthesize additional co-crystals of allopurinol. CD-inclusion complexation will also be attempted with the native CDs, which include α-CD, β-CD and γ-CD. However, a different methodology from that provided in the literature[1] will be employed, the rationale being the attempted isolation of single crystals for further analysis. Furthermore, DMSO, used in the previous study,[1] will be avoided owing to the fact that it has a large affinity for CD cavities and it is often used to displace guest molecules from inclusion complexes. In addition, preparation of CD inclusion complexes will also be attempted with the derivatised CDs, namely, the methylated CDs, which include DMB, TMB and TMA. Lastly, the host compounds γ-CD, HPBCD and RAMEB will also be investigated during phase solubility experiments for their ability to enhance the solubility of allopurinol in aqueous solution.

3.2) Co-crystal screening

3.2.1) Virtual co-crystal screening

Initially, a computational investigation of potential co-crystal formation between allopurinol and the series of co-formers available in the laboratory, was launched. These co-formers are listed in Table 1.1 in the Appendix under section 1, p. 2. There are three factors that are generally considered during the co-former selection process; these are the possible supramolecular synthons (which involve hydrogen bonding) that might occur between the API and the co-former, the ΔpK_a value between the two components, and lastly the solubility of the co-former. The investigation primarily involved analysing the hydrogen bonding supramolecular synthons that could form with allopurinol. This was the fundamental criterion, because in the absence of hydrogen bonding between allopurinol and the co-former, the ΔpK_a value and the solubility of the co-formers become null and void. The ΔpK_a value would only indicate the potential to form either a co-crystal or a salt,[6] while the solubility of the co-former would generally only influence the solubility of the drug within the co-crystal. Therefore, it was imperative first to establish the potential formation of hydrogen bonding between allopurinol and various co-formers. All the co-formers in the laboratory possessed a significantly higher aqueous solubility than allopurinol and thus had the potential to be a solubility enhancer.[7-8] Therefore, the co-formers that indicated the highest potential to form supramolecular synthons were most desirable at this stage.

As a result, an investigation took place with the use of the Cambridge Crystallographic Database (CSD)[9] in order to identify likely supramolecular synthons that could form with allopurinol. Initially, the molecular structure was obtained from the CSD and viewed in X-SEED[10] in order to identify the supramolecular synthons that form within the crystal packing of pure allopurinol. A complex dual ring system was evident, where one of the rings involved two allopurinol molecules, and the other ring involved three allopurinol molecules. The 8-membered dimeric ring system that involved only N-H···N hydrogen bonds (Figure 3.1) was described as $R_2^2(8)$ (as designated with graph-set notation[11]). These H-bonds are inversion-related with a unique N···N distance of 2.88 Å and N-H···N angle of 164°. The 10-membered trimeric ring system shares one of the hydrogen bonds with the dimeric ring system to produce a $R_3^3(10)$ arrangement. This ring system involves two N-H···N hydrogen bonds, as well as a C-H···O hydrogen bond. The N···N distance of 2.87 Å and the N-H···N angle of 163° confirm that this is a classical hydrogen bond. Furthermore, the C-H···O bond has a C···O distance of 3.21 Å (slightly shorter than the sum of the van der Waals radii of C and O, *viz*. 3.22 Å) and the angle subtended at the hydrogen atom is 164°.

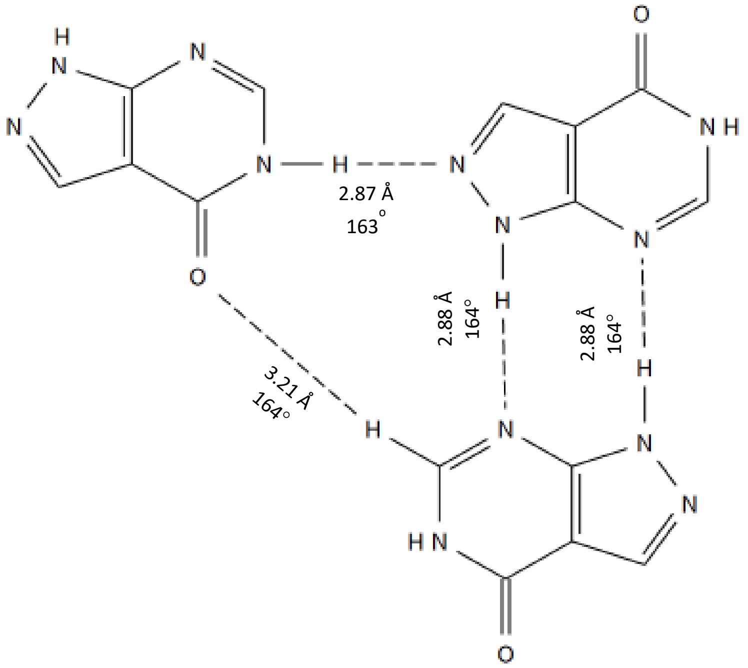

Figure 3.1: The hydrogen-bonded motif of allopurinol which displays the formation of dual dimeric and trimeric ring synthons.

A comprehensive study was conducted in the CSD and viewed in Mercury,[12] where molecular fragments of the allopurinol molecule were assessed for their potential to form stable, hydrogen bonded, ring synthons with other molecules. There are nine tautomers of allopurinol, which are displayed in Figure 3.2, and therefore the selected molecular fragments of allopurinol had to account for this tautomerism. Furthermore, Figure 3.3 identifies the potential hydrogen bonding sites of the allopurinol molecule, which are circled in red.

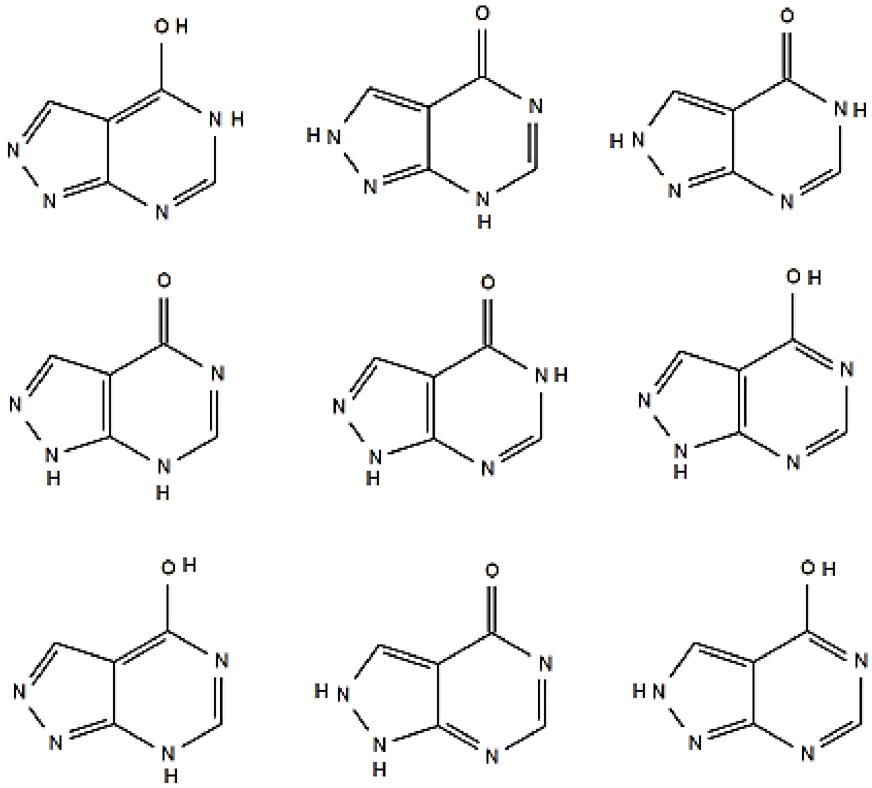

Figure 3.2: The tautomers of allopurinol.

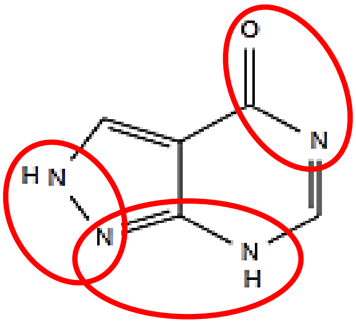

Figure 3.3: The potential hydrogen bonding sites (circled in red).

Consequently, the selected molecular fragments of allopurinol, which accounted for all the possible tautomers, are displayed in Figure 3.4. With reference to these molecular fragments, the atoms denoted as X accounted for any atom, and the respective X-C or X-N bonds were assigned as 'any' (i.e. single, double, aromatic). In addition, the bonds in the various N-C-N molecular fragments (3a – 3c) were also denoted as 'any' in order to account for the multiple tautomers of the molecule.

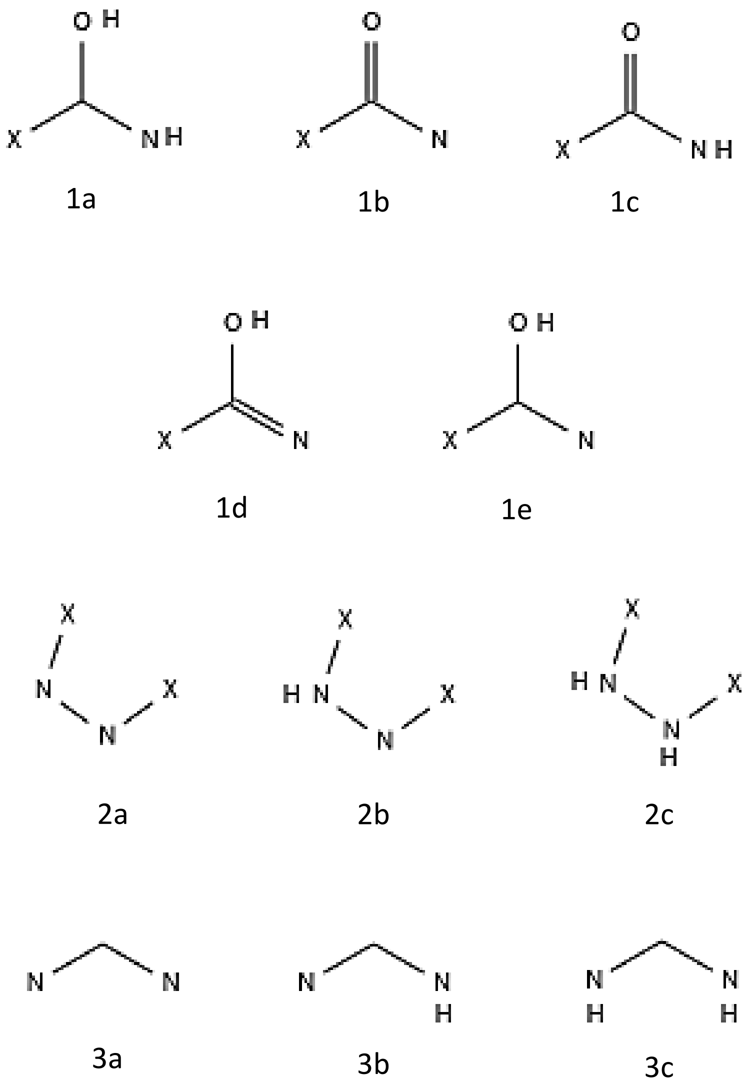

Figure 3.4: The various molecular fragments of allopurinol, which accounted for the possible tautomers. Atom X represents any atom, while the bond orders in C-X (1a-1e), N-X (2a-2c) and C-N (3a-3c) were unrestricted.

The available co-formers that could potentially form ring synthons were those that contained carboxylic acid and amide functional groups. Consequently, hydrogen bonds were drawn to form a ring synthon between the carboxylic acid functional group of a co-former, and the nitrogen and oxygen atoms (or just the nitrogen atoms) of each allopurinol molecular fragment. This process was repeated for each allopurinol molecular fragment with the amide functional group in place of the carboxylic functional group. In addition, the hydrogen bond lengths were pre-set in the CSD to have a O···N, O···O or N···N length that ranged between 2.5 and 3.2 Å.

This method allowed the relevant functionalities of the allopurinol molecule to be assessed for the frequency of forming ring synthons with carboxylic acid and amide functional groups from potential co-formers in the laboratory. Any results that did not display a realistic bonding scenario, particularly within the molecular fragments of allopurinol where the bonds were denoted as ‘any’, were not retained.

The results indicated that the amide functional group had a much higher frequency for forming ring synthons than the carboxylic acid functional group. This was particularly the case with the tautomeric fragment 1c (Figure 3.5), which accounted for 96 % of the amide ring synthon frequency. The remaining tautomeric fragments that engaged in ring synthons with the amide functional group were 1d, 1e, 3b and 3c (Figure 3.4). In addition, the tautomeric fragments 1c and 3b were involved in a fair frequency of hydrogen bonded ring synthons with the carboxylic acid group and several were also observed to occur with the tautomeric fragment 2b (Figure 3.4).

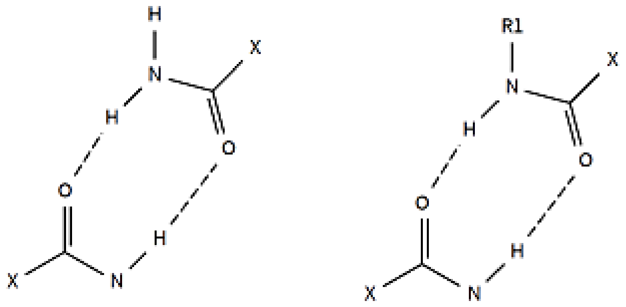

Figure 3.5: The most frequently occurring hydrogen bonded ring synthons, which involved the molecular fragment 1c (at the bottom) and either a primary or secondary amine (at the top). The atom X represents any atom and R1 is any organic moiety.

It is important to note that this investigation did not take into account the frequency of formation of synthons other than those involving rings. As mentioned previously, the purpose of this investigation was to establish the frequency for the formation of stable ring synthons between a potential co-former and the allopurinol molecule. As a result, the co-formers that were selected contained the functional groups from either amides or carboxylic acids. Isonicotinamide and nicotinamide were selected not only because they are amides, but also because they are known to be more successful in forming co-crystals. D-tartaric acid and benzoic acid were also selected in order to confirm and extend the analysis by Alatas *et al.*,[3] who claimed that it was possible to form co-crystals with allopurinol and these two co-formers separately. In addition, piperazine was also included, since it has the potential to form synthons of type C (‘chain’ synthon). As a result, the list of selected co-formers is displayed in Table 3.1.

Table 3.1: The selected co-formers for co-crystallization screening experiments with allopurinol.

Number	Selected co-former
1	Benzamide
2	Benzoic acid
3	Fumaric acid
4	Glutaric acid
5	Isonicotinamide
6	Maleic acid
7	Nicotinamide
8	Piperazine
9	Propionamide
10	D-Tartaric acid
11	Urea

3.2.2) Co-grinding, co-precipitation and recrystallization screening experiments

The majority of the experimental co-crystal screening attempts did not produce successful results that could be analysed further. However, a new polymorph of one of the co-formers, isonicotinamide, was formed serendipitously during attempted co-crystallization between this co-former and allopurinol. Owing to its novelty and the widespread use of this co-former in co-crystal research, a complete physicochemical analysis of the new crystal form was undertaken and is documented later in this chapter under section 3.2.3, pp. 36 – 74. A comprehensive analysis and detailed discussion of the remaining results, that either indicated preliminary degrees of success or those that were unsuccessful, have been placed in the Appendix under section 2, pp. 3 – 14. These partially successful results only included successful dry co-grinding experiments of allopurinol and isonicotinamide, allopurinol and piperazine, as well as allopurinol and maleic acid. An example of one of these successful dry co-grinding results is evident in Figure 3.6 which shows the PXRD patterns of allopurinol, piperazine and the PXRD pattern of the new crystalline phase in green (Figure 3.6).

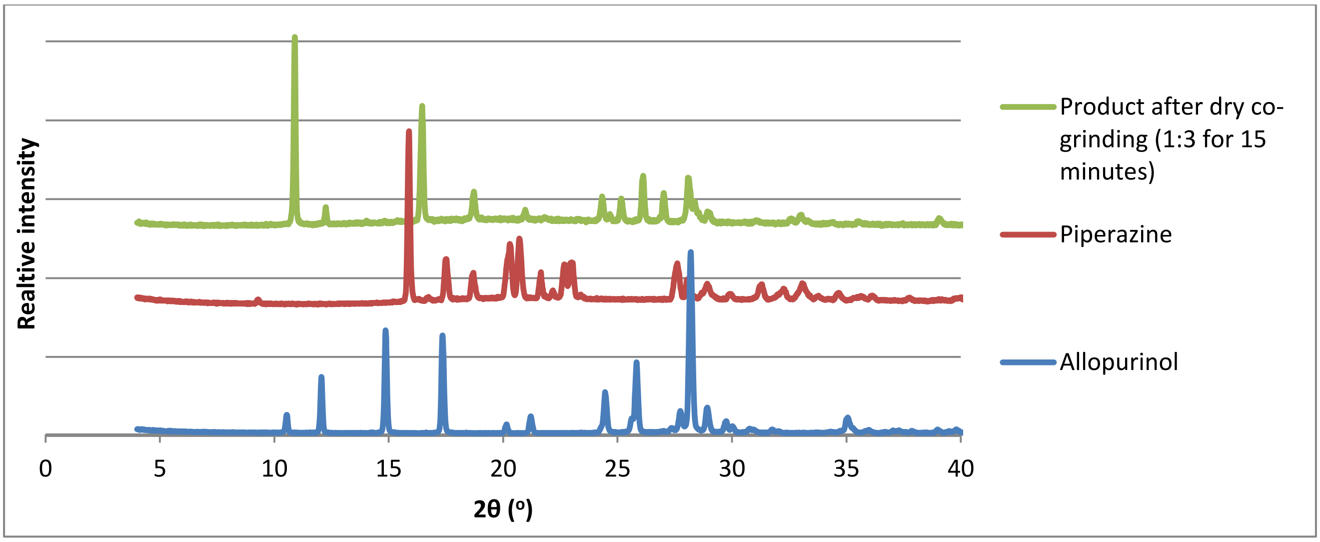

Figure 3.6: PXRD patterns of allopurinol, piperazine, and the product obtained by dry co-grinding the two components in a 1:3 molar ratio for 15 minutes.

The various co-grinding and co-precipitation experiments that were performed with the eleven selected co-formers included the following. With regard to the co-grinding experiments with allopurinol, these included dry co-grinding and LAG experiments with the respective solvents ethanol (EtOH), ethyl acetate, hexane, DMSO and chloroform. Furthermore, with regard to the co-precipitation experiments, these were performed with the solvents, namely chloroform (*via* slow evaporation in equimolar ratios), and DMSO (*via* slow evaporation, as well as *via* slow cooling in equimolar ratios), with all eleven co-formers. Another set of experiments was also performed with DMSO, which incorporated the three co-formers that indicated successful dry co-grinding results (namely isonicotinamide, piperazine and maleic acid) in an assortment of different stoichiometric ratios which were prepared for slow evaporation. Lastly, recrystallization experiments were attempted, where a variety of solvents was used, with the successful dry co-ground products. None of these experiments produced successful results, other than those that have already been mentioned above. Figure 3.7 illustrates an example of a PXRD pattern with allopurinol and D-tartaric acid, which displays a physical mixture of the two components, instead of a new crystalline phase.

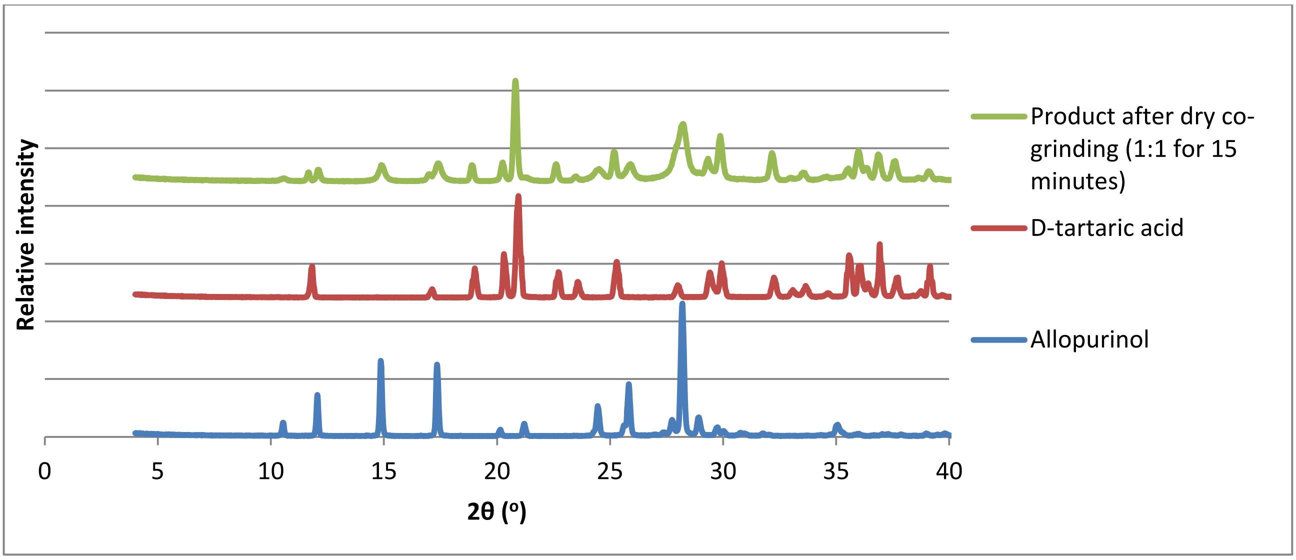

Figure 3.7: PXRD patterns of allopurinol, D-tartaric acid, and the product of dry co-grinding these components in a 1:1 molar ratio for 15 minutes.

It is of interest to note that all the co-grinding experiments that were performed with allopurinol and D-tartaric acid, and allopurinol and benzoic acid, were unsuccessful, despite the fact that Alatas *et al.*[3] claimed to have synthesized new materials *via* these methods. There are two possible explanations for this occurrence; either product formation is dependent on the grinding pressure applied,[13] or the authors were mistaken with regard to their PXRD interpretation.

In conclusion, the co-grinding experiments with allopurinol and isonicotinamide, allopurinol and piperazine, as well as allopurinol and maleic acid, did produce new material; however, it was not possible to characterise this material any further. The reported methodology for generating the claimed co-crystals by Alatas *et al.*,[3] of allopurinol and benzoic acid, as well as allopurinol and D-tartaric acid, was repeated, but it was not possible to form the product that they had claimed. Instead a physical mixture of the two components resulted. The co-precipitation results did not produce co-crystals, although a new polymorph of isonicotinamide was discovered (this is described in detail in the subsequent section). The virtual co-crystal screening analysis indicated that possible stable ring synthons could occur between the allopurinol molecule and a co-former, which could conceivably result in the formation of either a co-crystal or a salt. However, physical and chemical properties, such as the high melting point and low solubility of the API, could have prevented the formation of these desired multi-component systems.

3.2.3) A new polymorph of isonicotinamide

Another polymorph of isonicotinamide was discovered serendipitously during an attempt to co-crystallize allopurinol with isonicotinamide[a] in chloroform. It was initially identified from a unit cell analysis, where its cell dimensions were unique in comparison to the other five known polymorphs of isonicotinamide. As a result, a full intensity data-collection was performed and the crystal structure was solved and confirmed to be a unique polymorph. This new crystal modification of isonicotinamide will be referred to as polymorph 6.

Single crystal X-ray diffraction (SCXRD) analysis of polymorph 6

This particular SCXRD analysis could not be performed with the conventional methods that utilise the automation of technology. This was due to the fact that the space group assignment required manual determination through the careful examination of the intensity-weighted reciprocal lattice and that a pseudo-centre of inversion exists in the asymmetric unit (ASU) of polymorph 6. As a result, this analysis indicated the importance of applying first principle methods, and the importance of not relying on the automation of technology in solving a crystal structure.

Data-collection and space group determination

The unit cell parameters did not match those of either allopurinol or any known polymorphs of isonicotinamide and thus a full set of intensity data was collected. The original unit cell parameters were a = 7.9929(9) Å, b = 9.888(1) Å, c = 15.162(2) Å, $\alpha = \beta = \gamma = 90^{\circ}$, V = 1198.3(4) Å^3.

The space group of polymorph 6 was determined manually by inspecting the reciprocal lattice, since XPREP[14] failed to determine a possible space group. Initially the crystal system was established to be orthorhombic, as the intensity-weighted reciprocal lattice displayed *mmm* symmetry. The following conditions limiting possible reflections were initially identified, as listed in Table 3.2.

---

[a] The form of isonicotinamide that was used in this experiment was polymorph 1. The crystallographic data for all the polymorphs of isonicotinamide are defined in a table below.

Table 3.2: The conditions limiting possible reflections for the crystal of polymorph 6.

Number	Conditions limiting possible reflections	Deduction
1	hkl: none	Primitive lattice
2	0kl: k = 2n	b-glide plane perpendicular to the a-axis
3	h0l: l = 2n	c-glide plane perpendicular to the b-axis
4	hk0: none	-
5	h00: h = 2n *(apparent)*	Screw axis parallel to the a-axis
6	0k0: k = 2n	Redundant condition (from 2 above)
7	00l: l = 2n	Redundant condition (from 3 above)

This specific combination of conditions limiting possible reflections did not define any particular space group. However, very faint reflections with h = 2n + 1 were observed in the reciprocal lattice along the axial line h00 where the zero intensity positions for a screw axis were expected to be located. As a result, the condition for a screw axis to be present parallel to the a-axis became null and void. Removal of this false condition gave rise to two possible space groups, which were determined from the *International Tables for Crystallography*,[15] namely Pbcm (No. 57, centrosymmetric) and $Pbc2_1$ (non-centric), where $Pbc2_1$ can be transformed into the standard setting, $Pca2_1$ (No. 29). Table 3.3 displays the final unit cell parameters of polymorph 6 after the transformation had been applied, along with the unit cell parameters of the other five known polymorphs of isonicotinamide. Selection of the correct space group is described below.

The program XPREP could not determine either of these two possible space groups, because the ‘condition’ that limited the possible reflections h00: h = 2n was false. The intensities of these very weak reflections fell below the $I > 3\sigma(I)$ value for observed reflections, which is the program’s default value. As a result, XPREP could not register the presence of these reflections and thus was unable to assign a possible space group. In order to prove this assumption of program failure, the intensity values of a few of the very weak h00 reflections with h = 2n + 1 were artificially increased above the $I > 3\sigma(I)$ threshold in the hkl file, and thereafter XPREP was able to assign the two space group possibilities, namely Pbcm and $Pca2_1$.

Table 3.3: Selected crystal data for polymorphs 1 – 6 of isonicotinamide.[9, 16-18]

Polymorph	**a (Å)**	**b (Å)**	**c (Å)**	**α (°)**	**β (°)**	**γ (°)**	**Volume (Å^3)**	**Space group**	**Temp. (K)**	**Refcode**
1	10.176(1)	5.7319(6)	10.034(1)	90	98.042(3)	90	579.5(1)	$P2_1/c$	173	EHOWIH01
2	15.735(3)	7.998(1)	9.885(3)	90	105.59(1)	90	1198.2(5)	$P2_1/c$	173	EHOWIH02
3	10.1603(7)	7.3231(5)	15.8720(6)	90	90.0	90	1180.95(1)	Pbca	173	EHOWIH03
4	11.0819(6)	7.9976(4)	9.9850(5)	90	94.048(1)	90	882.75(8)	Pc	100	EHOWIH04
5	5.192(1)	9.466(3)	12.259(3)	90	91.217(7)	90	602.4(3)	$P2_1/c$	300	EHOWIH05
6	9.888(1)	7.9929(9)	15.162(2)	90	90	90	1198.3(4)	$Pca2_1$	173	–

Structure solution and refinement

The decision for the selection of the correct space group from the two possibilities (Pbcm and $Pca2_1$) further complicated this analysis. The combined figure of merit (CFOM) for the centrosymmetric space group Pbcm was 3.22, while the CFOM for the non-centrosymmetric space group $Pca2_1$ was 4.51. Thus, the space group with the lower CFOM was pre-selected by XPREP. However, attempted structure solution in Pbcm using direct methods failed. In order to understand the reason for this failure, one must take note of the fact that there are eight molecules in the unit cell (Z = 8). The centrosymmetric space group Pbcm has eight equivalent positions in the unit cell, while the non-centrosymmetric space group $Pca2_1$ has only four equivalent positions in the unit cell. As a result, the asymmetric unit (ASU) in the space group $Pca2_1$ would have two isonicotinamide molecules in the ASU. On attempting to solve the structure in $Pca2_1$ using SHELXS-97,[19] a solution was readily obtained, yielding two molecules in the ASU, as displayed in Figure 3.8. Close inspection of the relative orientations of these molecules revealed that they are related by a pseudo-inversion centre. The presence of this pseudo-inversion centre resulted in the $|E^2-1|$ value being 0.895, which is closer to the theoretical value for centrosymmetric structures, (0.968, as opposed to 0.736 for non-centrosymmetric structures). Following successful refinement of the structure in the space group $Pca2_1$, a check on the space group symmetry using the program PLATON[20] indicated this space group as being correct with 100 % correlation.

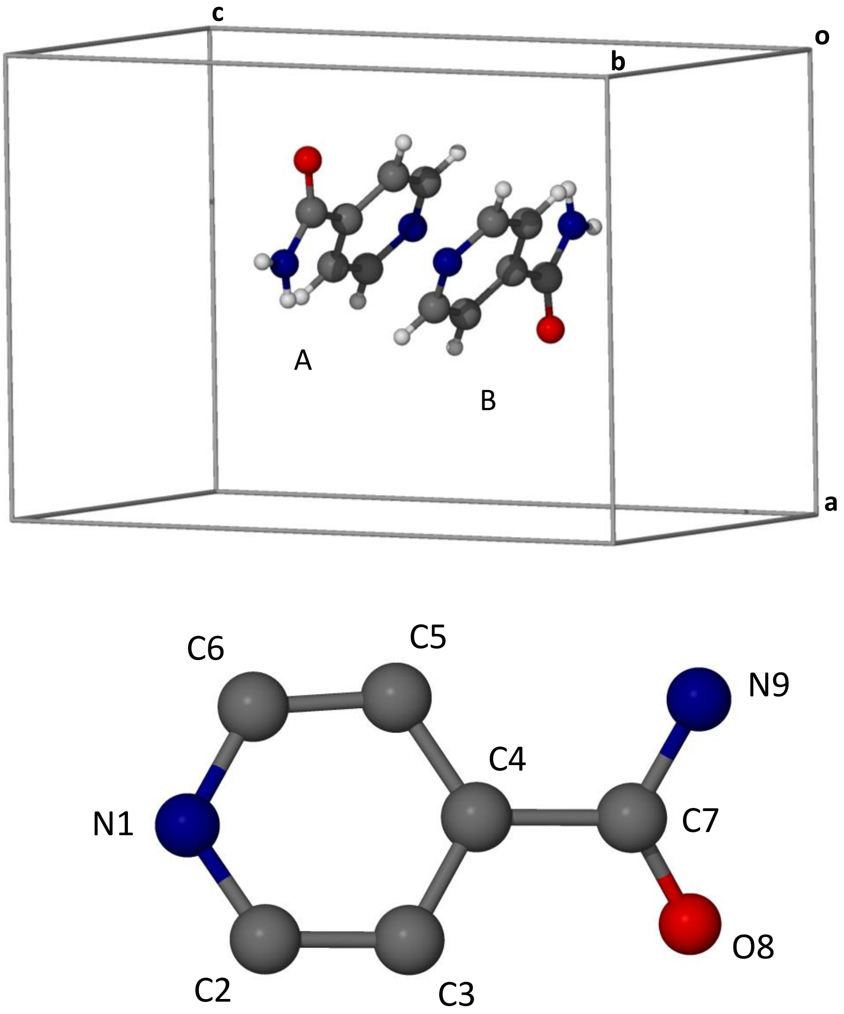

Figure 3.8: The asymmetric unit (ASU) comprises two independent isonicotinamide molecules labelled A and B. The numbering scheme of isonicotinamide is indicated below the ASU.

After the structure solution was obtained, the non-hydrogen atoms were all designated and refined isotropically and thereafter anisotropically, once the isotropic thermal parameters (U_{iso}) had converged. The hydrogen atoms were first located in the difference Fourier map and subsequently placed in idealised positions in a riding model and refined isotropically with U_{iso} values 1.2 times those of their parent atoms. The crystal data and refinement parameters are listed in Table 3.4.

Table 3.4: The crystal data and refinement parameters for polymorph 6.

Parameter	**Value**
Molecular formula	$C_6H_6N_2O$
Formula weight (g.mol^{-1})	122.13
Temperature (K)	173(2)
Wavelength (Å)	0.71073
Crystal system	Orthorhombic
Space group	$Pca2_1$
a (Å)	9.888(1)
b(Å)	7.9929(9)
c(Å)	15.162(2)
α (°)	90
β (°)	90
γ (°)	90
Volume (Å^3)	1198.3(2)
Z	8
Calculated density (g.cm^{-3})	1.354
μ (mm^{-1})	0.096
F (000)	512
Crystal size (mm)	0.200 x 0.270 x 0.400
θ-range scanned (°)	2.69 – 27.80
Index range	h: -13, 13; k: -10, 10; l: -19, 19
No. of reflections collected	22107
No. of unique reflections	2870
Data completeness (%)	99.8
Data/restraints/parameters	2870/1/163
S (Goodness-of-fit on F^2)	1.035
Final R indices R_1, wR_2, [$I > 2\sigma(I)$]	0.0532, 0.1415
R Indices, all data (R_1, wR_2)	0.0564, 0.1456
Largest diff. peak and hole (e. Å^{-3})	0.63, -0.23

Intramolecular and intermolecular structural features

Several structural features were assessed for molecules A and B in the crystal structure, which include the planarity of the aromatic rings, the angle of intersection of these two planes, possible π-π stacking and an overlay of molecules A and B.

The aromatic rings for both molecules A and B were confirmed to be planar within the expected range of deviation. For molecule A, the deviations of the atoms from the least-squares plane ranged between -0.004(2) Å and 0.005(3) Å for atoms C4A and C3A respectively, while, for molecule B, the deviations were between -0.007(3) Å and 0.004(3) Å for atoms C3B and N1B respectively. Furthermore, the plane of intersection of the aromatic rings of molecules A and B was $0.6(1)^{o}$, which further confirmed the fact that these two molecules are pseudo-centrosymmetrically related.

In addition, there was no evidence for adequate π-π stacking occurring between the aromatic rings of either molecule A or B. The centroid···centroid distances between various aromatic rings ranged between 4.324(2) Å and 5.902(2) Å, which is too large for π-π stacking to occur.

The results from the overlay of molecule A with the inverse of molecule B, further confirmed that they are pseudo-centrosymmetrically related. The results for the best fit of the two moieties indicated that the weighted RMS-FIT value was 0.015 Å and the un-weighted value was 0.013 Å.

Hydrogen bond interactions

There are four independent H-bond motifs that occur in the crystal structure of polymorph 6. Figure 3.9 displays these H-bonds in the ASU, and their distances and geometrical characteristics have been itemised in Table 3.5.

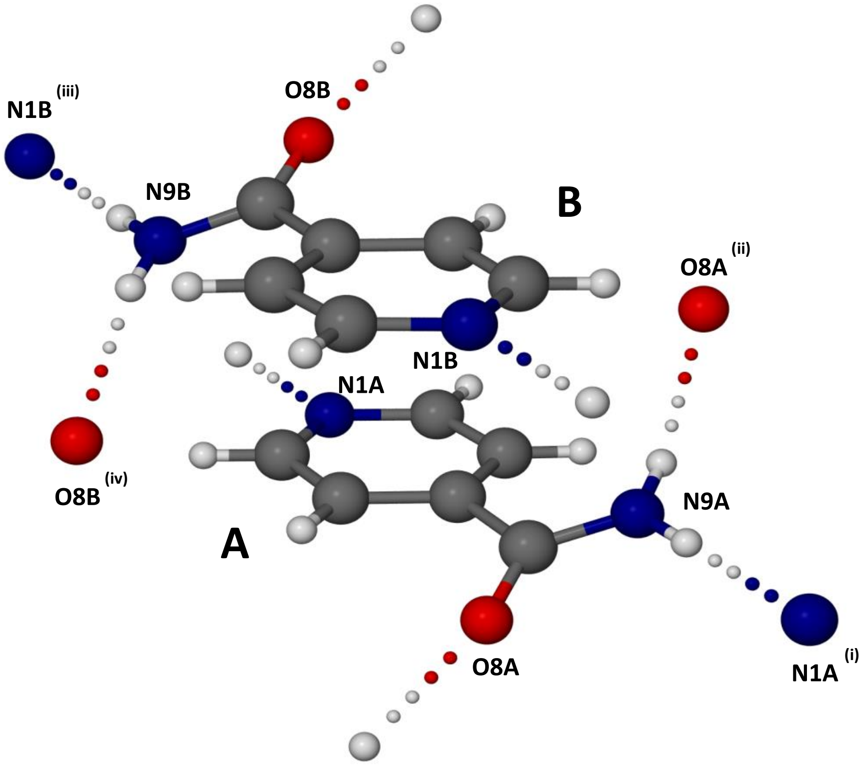

Figure 3.9: The H-bond motifs in the ASU of polymorph 6.

Table 3.5: Intermolecular hydrogen bond interactions for polymorph 6.

Hydrogen Bond	D···A Distance (Å)	Angle (°)[a]	Symmetry operator[b]
N9A – H9A2···N1A	2.975(3)	179	x,1+y,z (i)
N9A – H9A1···O8A	2.954(3)	156	½+x,2-y,z (ii)
N9B – H9B2···N1B	2.980(3)	175	x,-1+y,z (iii)
N9B – H9B1···O8B	2.935(3)	158	-½+x,1-y,z (iv)

[a] No e.s.d. was reported for the D-H···A angle, since the H atoms were placed in idealised positions.

[b] The symmetry operator refers to the hydrogen bond acceptor atom.

Crystal Packing

Figure 3.10 displays the packing arrangement of polymorph 6 viewed down the a-axis (left), b-axis (centre) and c-axis (right).

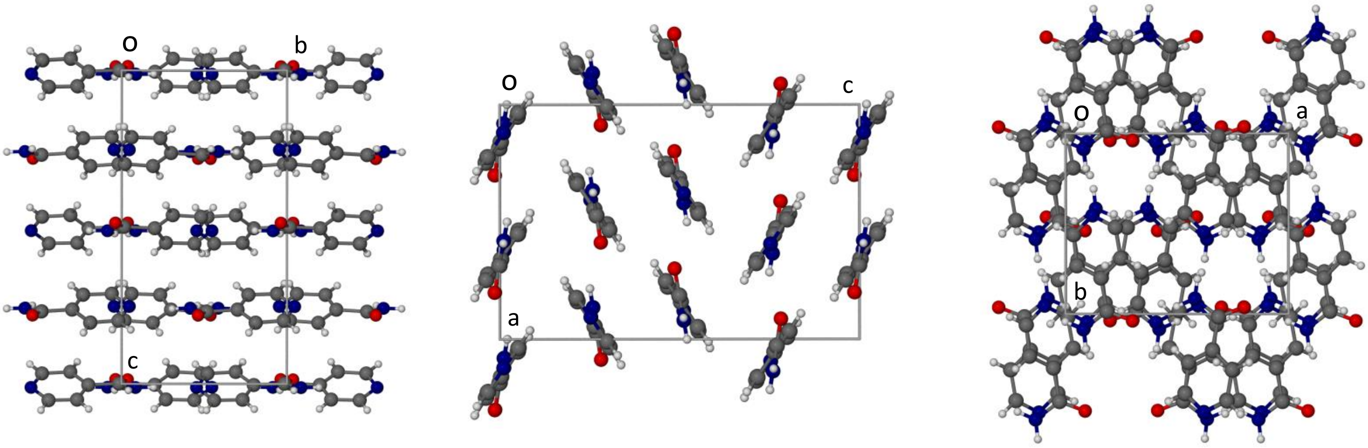

Figure 3.10: The packing arrangement of polymorph 6 viewed down the a-axis (left), b-axis (centre), and c-axis (right).

Polymorphic comparison

A polymorphic comparison was performed for all six forms of isonicotinamide which involved assessing their respective molecular conformations, as well as their crystal packing features.

Consequently, the torsion angles around the C4-C7 bond of all the polymorphs of isonicotinamide were compared, since this is the only significant bond that represents a conformational degree of freedom. The results are displayed in Table 3.6, and it indicated that all the torsion angles are unique for each polymorph except for polymorphs 2 and 6.

Table 3.6: The C3-C4-C7-O8 torsion angle magnitudes of the polymorphs of isonicotinamide.

Polymorph	**Torsion angle magnitude (°)**
Polymorph 1	30.5(2)
Polymorph 2 *(molecule A)*	24.0(3)
Polymorph 2 *(molecule B)*	25.4(3)
Polymorph 3	30.9(3)
Polymorph 4 *(molecule A)*	25.8(2)
Polymorph 4 *(molecule B)*	23.4(2)
Polymorph 4 *(molecule C)*	28.3(2)
Polymorph 5	19.6(2)
Polymorph 6 *(molecule A)*	24.2(4)
Polymorph 6 *(molecule B)*	25.6(4)

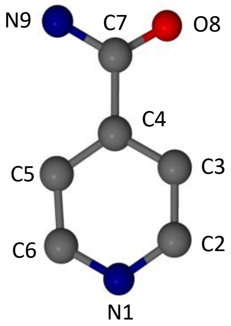

The ASU of polymorph 6 was compared with the corresponding two molecular entities from each of the other polymorphs of isonicotinamide through a structural overlay study. This test also indicated that all of the polymorphs were significantly different, except for polymorph 2 which appeared to be similar to polymorph 6. However, another study was subsequently performed where the molecular packing arrangement of these two similar crystal structures was compared over a longer range. Figures 3.11 – 3.13 display the overlays of polymorph 6 (pink) and polymorph 2 (green). Initially, the comparison of these similar polymorphs was established with the two unit cells orientated according to Figure 3.11, with the view down the b-axis, and with the two polymorphs being aligned to overlap at the left-hand side. With regard to this projection, a distinct difference can be observed over an extended range (from left to right) where polymorph 6 and polymorph 2 begin to separate vertically. Figure 3.12 displays the projection of Figure 3.11 rotated 90° around the c-axis of the orthorhombic polymorph, polymorph 2 then being viewed down the c-axis and polymorph 6 down the a-axis. This projection confirmed that there was a direct overlap between the two polymorphs in this direction and as a result, this is consistent with the fact that only a vertical separation occurred between the two polymorphs over an extended range in Figure 3.11. Similarly, Figure 3.11 was rotated by 90° around the a-axis of the orthorhombic polymorph in order to generate the projections displayed in Figure 3.13a and 3.13b, where polymorph 6 is viewed down the a-axis. The figures for the two polymorphs were separated for visual purposes and only the areas boxed in red were compared in order to conduct an adequate molecular comparison. This particular projection indicated that there was no overlap over the entire extended range and it can be observed that polymorph 6 has extended vertically in comparison to polymorph 2 by observing the height difference from the black reference line at the top of Figure 3.13b. There are some similarities with regard to the molecular arrangements between the two polymorphs, and this is particularly apparent in the space-filling image (Figure 3.13b). However, the most significant differences within the areas boxed in red are that polymorph 6 contains a small periodic void, whereas polymorph 2 does not.

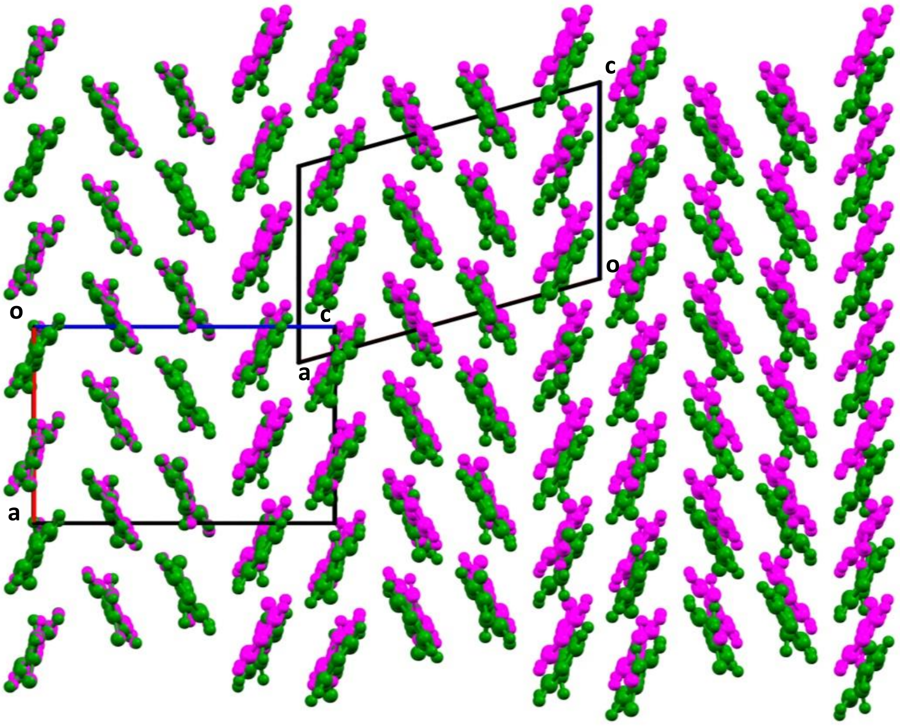

Figure 3.11: The molecular overlay of polymorph 2 (green) and polymorph 6 (pink) viewed down the b-axis.

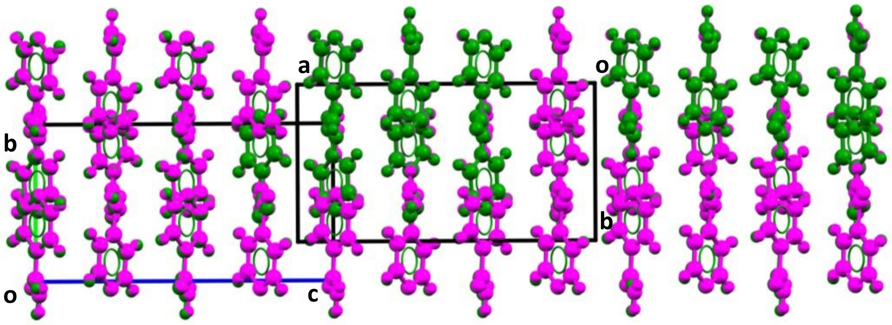

Figure3.12: The molecular overlay of polymorph 2 (green) and polymorph 6 (pink), derived from Figure 3.11 by a 90^o rotation around the c-axis of the orthorhombic polymorph.

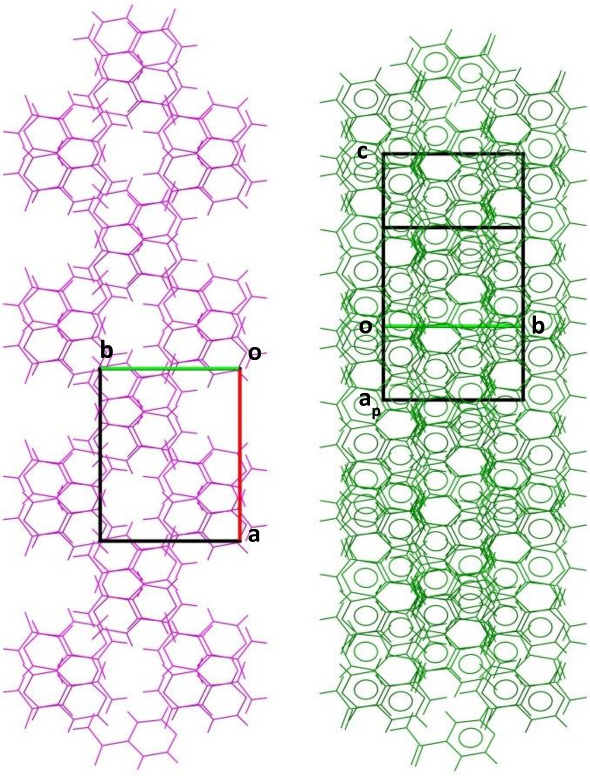

Figure 3.13a: A wireframe representation of the molecular overlay of polymorph 2 (green) and polymorph 6 (pink), derived from Figure 3.11 by a 90^{o} rotation around the a-axis of the orthorhombic polymorph.

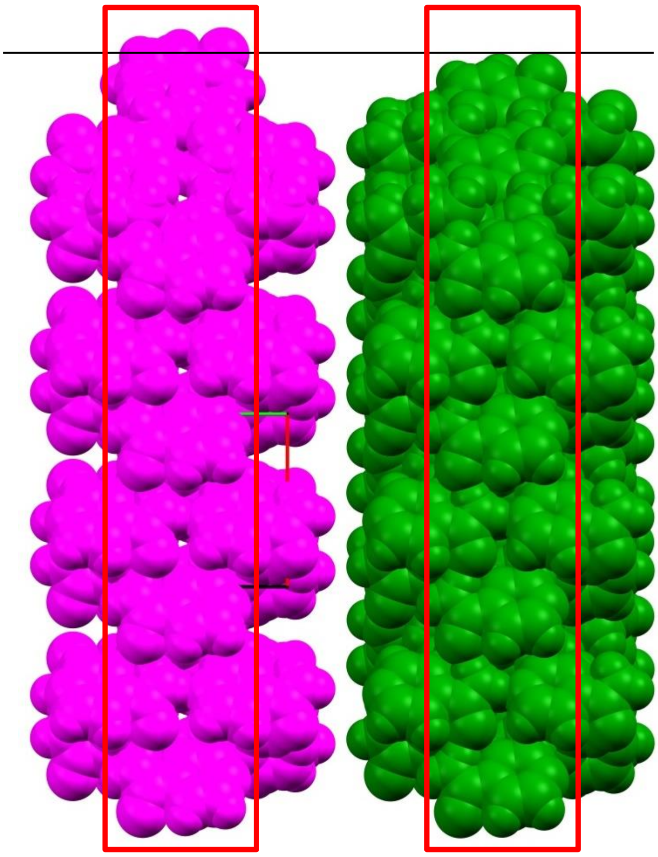

Figure 3.13b: A space-filling representation of the molecular overlay of polymorph 2 (green) and polymorph 6 (pink), derived from Figure 3.11 by a 90^{o} rotation around the a-axis of the orthorhombic polymorph.

It is noteworthy that the intensity data for polymorph 2 and polymorph 6 were collected at the same temperature. As a result, the very significant differences between the two PXRD patterns of the respective polymorphs, calculated from their single crystal X-ray data at 173 K, confirm that they are distinct crystalline phases (Figure 3.14).

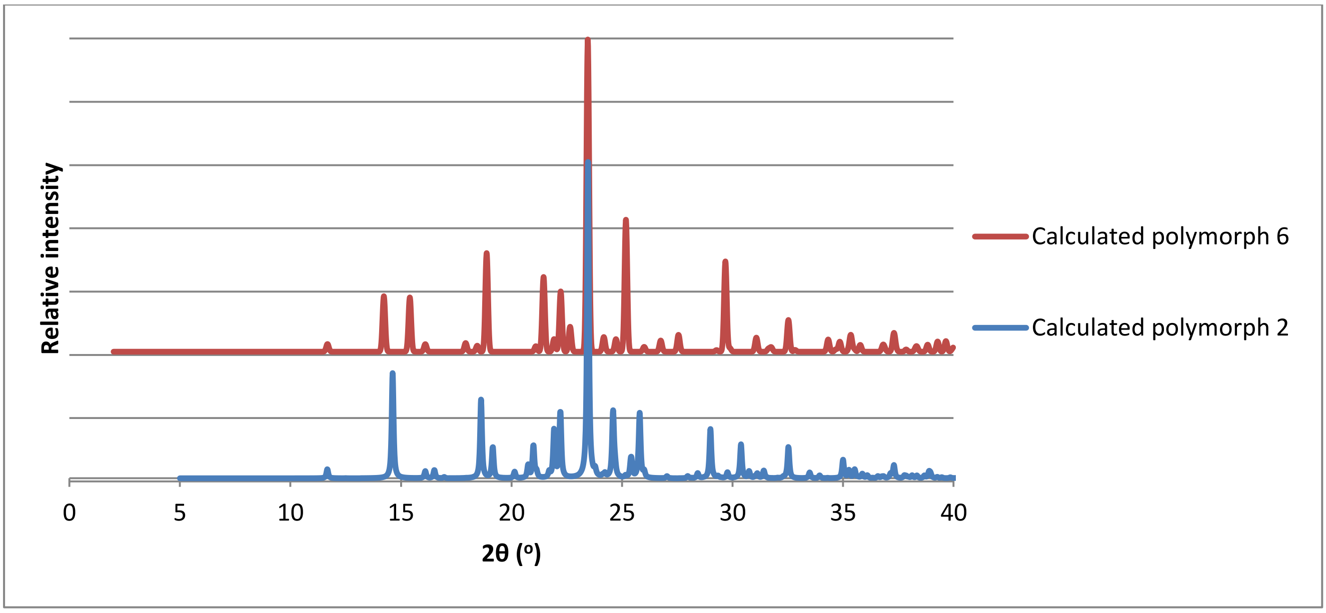

Figure 3.14: The calculated PXRD patterns of polymorph 2 and polymorph 6.

Furthermore, upon closer inspection of the unit cells of polymorphs 2 and 6, the molecular packing arrangements are significantly different. Polymorph 2 displays a packing arrangement B′A′AB around a centre of inversion (Figure 3.15), while the molecular packing arrangement of polymorph 6 followed an alternating ABAB packing arrangement (Figure 3.15). As a result, the SCXRD analysis confirmed the uniqueness of polymorph 6.

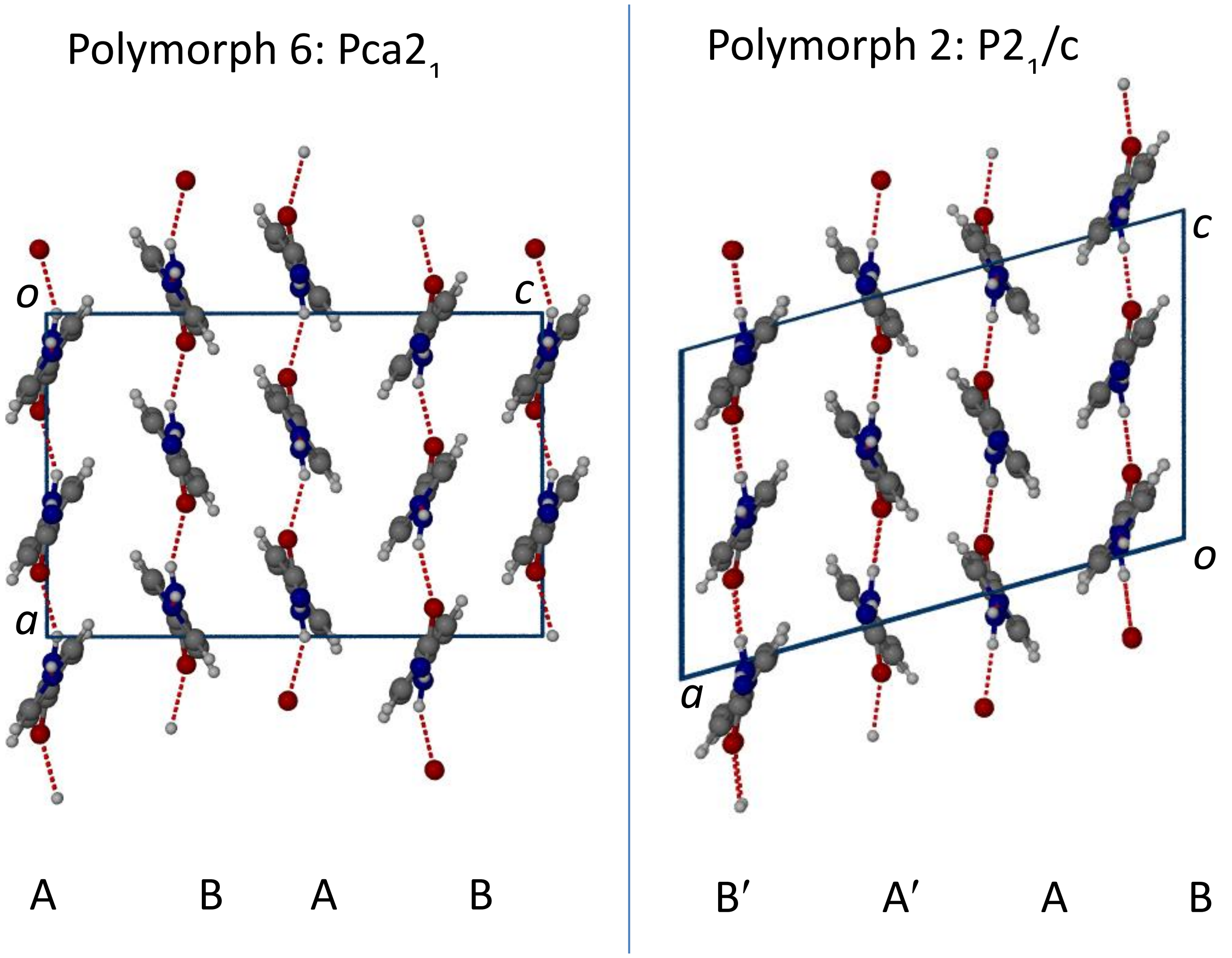

Polymorph 6: $Pca2_1$

Polymorph 2: $P2_1/c$

Figure 3.15: The packing arrangements of polymorph 6 (left) and polymorph 2 (right). Both polymorphs have Z′ = 2 molecules (designated A and B). The designation 'A', for example, indicates that the row above it contains only molecules of type A.

Further experimentation was performed in order to attempt to characterise polymorph 6 and compare it to the other five known polymorphs. This new polymorph did not correspond to the new crystalline phase obtained in the dry co-grinding experiments of allopurinol and isonicotinamide (polymorph 1). This is evident in the results shown in Figure 3.16, where the PXRD pattern of the product of dry co-grinding allopurinol and isonicotinamide (molar ratio 1:1) for 35 minutes, did not correspond to the PXRD patterns of either the original reagents or to the calculated PXRD pattern of polymorph 6.

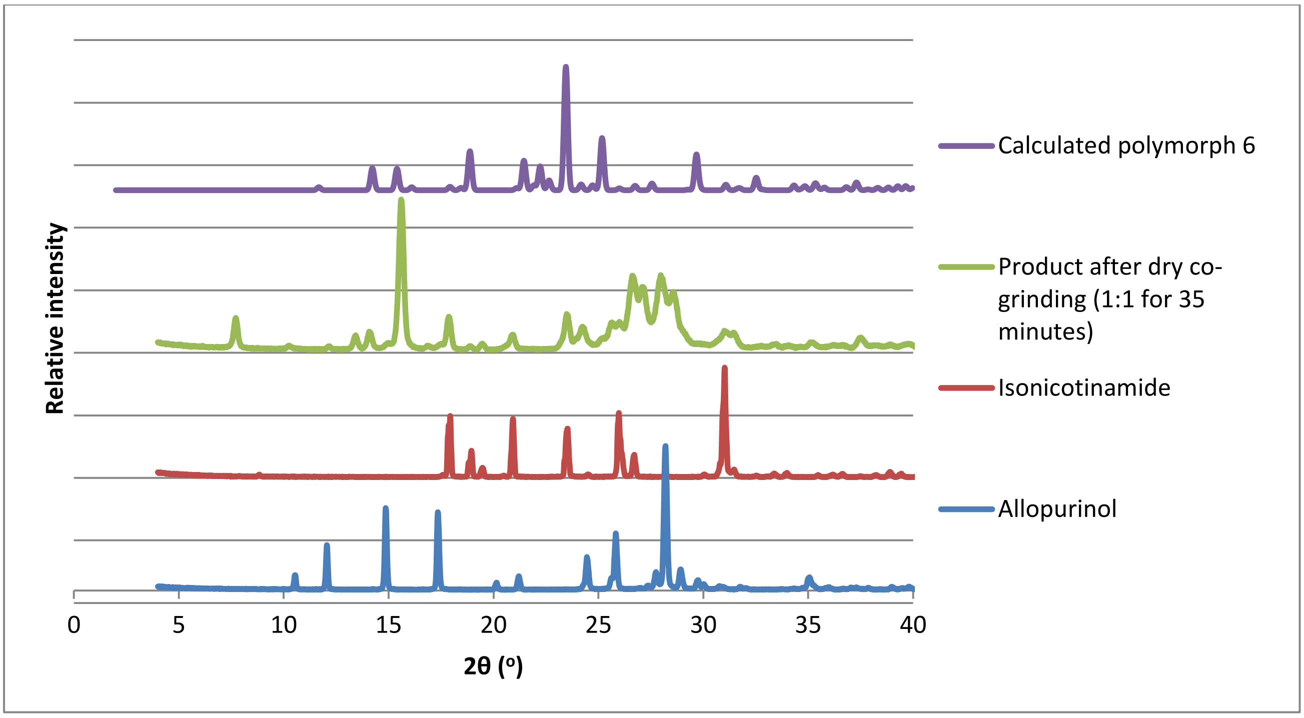

Figure: 3.16: PXRD patterns of allopurinol, isonicotinamide (polymorphic form 1), the product of dry co-ground allopurinol and isonicotinamide (1:1) for 35 minutes, and the calculated trace for polymorph 6.

Polymorph 6 crystallized alongside the five other known polymorphs of isonicotinamide. The observation from the SCXRD analysis indicated that polymorph 6 and polymorph 3 appeared to crystallize in major amounts at the specific time of analysis, while the remaining polymorphs appeared to be present in a lesser quantity. It is important to note that this observation only takes into consideration the crystals that were of an adequate quality for SCXRD experiments. In addition, this observation was also time-dependent, since it was later reported by the author of this dissertation, that the polymorphs appear to transform over time. At the time of writing, the most reliable method for the isolation of polymorph 6 was in the presence of the API, namely allopurinol, as allopurinol initially appeared to act as a template for its formation.[21] In addition, the method of preparation was very quantity-specific and any deviations or variations caused the new polymorph either to form in a lesser quantity and inferior crystal quality, or not to form at all.

Furthermore, the use of allopurinol (which apparently behaved as a template) for the isolation of polymorph 6, was especially important if the crystallization was being performed for the first time in a laboratory. This deduction arose since there could have been a possibility that once polymorph 6 was synthesized in a specific laboratory, the air was thereafter seeded with it. This is similar to what occurred with the HIV drug, ritonavir.[22] Towards the end of this investigation of polymorph 6, it was possible to produce it by recrystallizing isonicotinamide either from isopropanol, acetone or acetonitrile, without the templating influence of allopurinol.[b] Aakeröy *et al.* had already used acetone as a recrystallizing solvent for the possible formation of new polymorphs.[16] However, since Eccles *et al.* did not report the existence of polymorph 6, one can conclude that either they were unable to discover it owing to a polymorphic transition of this form to another form having taken place, or that the subsequent formation of polymorph 6 in different organic solvents without allopurinol is dependent on an initial crystallization with allopurinol in order to seed the laboratory.[18,22]

Polymorph preparation

The initial preparative method involved dissolving equimolar amounts of allopurinol (5 mg; 0.0367 mmol) and isonicotinamide (4.486 mg; 0.0367 mmol) in separate, clean vials. Approximately 2 cm^3 of chloroform was used to fully dissolve the isonicotinamide and 6 cm^3 of chloroform was used to dissolve as much of the allopurinol as possible. The isonicotinamide solution and the suspension of allopurinol were tightly sealed and stirred for 12 hours at 35 ^{o}C. Subsequently, they were filtered into a common, clean vial (even though very little of the allopurinol had dissolved)[23] and left for slow evaporation. This method produced the first batch of crystals in which polymorph 6 was discovered.

A more refined preparative method was subsequently discovered, which produced more reliable crystals in terms of single crystalline quality and quantity. This variation involved increasing the amount of chloroform used to dissolve more of the allopurinol from 6 cm^3 to 20 cm^3. The rationale behind this was to allow more allopurinol into the system during the crystallization of polymorph 6 and thus it might allow the allopurinol to act as a more effective template, which could increase the amount of desired polymorph. In addition, a larger volume of chloroform during slow evaporation would result in a slower precipitation process, which could allow for an improved, single crystalline quality. Owing to the high volatility of chloroform, only six holes were punctured into the parafilm that sealed the vial during slow evaporation.[c] This also allowed the solution to evaporate slowly

---

[b] Polymorph 6 appeared to crystallize as the major form with isopropanol in comparison to acetone and acetonitrile.

[c] Furthermore, the parafilm was not stretched over the vial opening, as it was observed that the chloroform vapour reacted with the parafilm and produced large holes in any thin areas.

over two weeks, a period which appeared to yield the best quality and highest quantity of crystals of polymorph 6.

Further variations in this methodology were attempted, with no success. These included: lowering the mass of allopurinol since not all of it had dissolved in the chloroform and thus was technically 'wasted';[23] stirring the individual chloroform and allopurinol solutions for a shorter period of time; attempting to produce polymorph 6 without the presence of allopurinol in the chloroform; attempting to produce polymorph 6 by adding the unfiltered allopurinol-chloroform solution into the filtered solution of isonicotinamide; and lastly, scaling up the quantity of the overall mass used while preserving the equimolar ratio.

The refined preparative method, as described above, successfully produced over fifteen vials, each of which contained single crystals of polymorph 6, along with the other five known polymorphs. However, in the final attempts to reproduce single crystals of polymorph 6 towards the end of the investigation, difficulties were experienced. Even though the method was followed meticulously, the quality of the synthesized crystals was inadequate for SCXRD analysis. However, it is important to state that along with the fifteen batches that produced high-quality single crystals of polymorph 6, there were additional vials that contained specimens of poorer crystalline quality. The latter included a crystalline, helical tape morphology, and a powdery residue of isonicotinamide. Thus, it was these two poorer morphological forms that were continuously obtained during the later attempts at isolating polymorph 6 with chloroform and allopurinol.

Morphology

The morphology of polymorph 6 appeared to be unique, as displayed in Figure 3.17a (with reference to the crystal on the right-hand side of the micrograph). This morphology was characterised by the shape of a bullet-head, where the bottom half of the crystal had a rectangular side which tapers midway to form a triangular point at the top. This was in contrast to polymorph 3, which as mentioned previously, was initially found to crystallize in approximately the same quantity as polymorph 6. Polymorph 3, as depicted in the left-hand crystal (Figure 3.17a), had a more rectangular morphology, where the shorter sides of the rectangular crystal were not parallel. This correlated with the morphology as described in the PhD thesis of Li.[24] The bullet-head shaped crystals of polymorph 6 crystallized together by means of a type of radial conglomerate, where the bullet-head tips all pointed towards a common focal point. This conglomerate of crystals separated when touched by a needle that was employed to assess the crystals for multiple SCXRD unit cell measurements. All the crystals with this unique morphology were determined to be polymorph 6 by means of unit cell determinations. However, other crystals having a more rectangular, or even an irregular shape, also yielded the unit cell parameters of polymorph 6 within acceptable limits, as measured by the respective χ and mosaicity values (Figure 3.17b). This could be as a result of the fact that the majority of the crystals crystallized on the sides of the vial during their formation and consequently the crystals could have been unintentionally shattered when they were removed with a spatula (in spite of the care taken to remove them). Therefore, the bullet-head shaped crystals appeared to represent the general morphology of polymorph 6, since these crystals all separated from each other without being damaged.

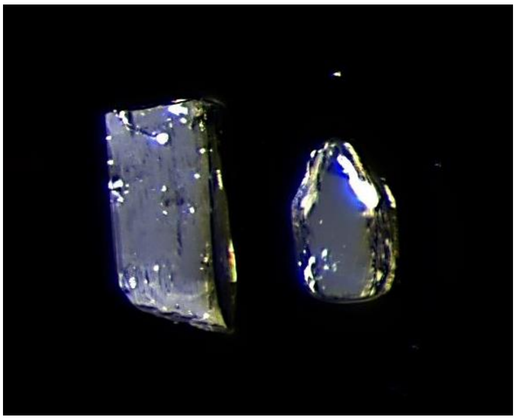

Figure 3.17a: Polymorph 3 (left) and polymorph 6 (right). This micrograph displays the bullet-head shaped morphology of polymorph 6.

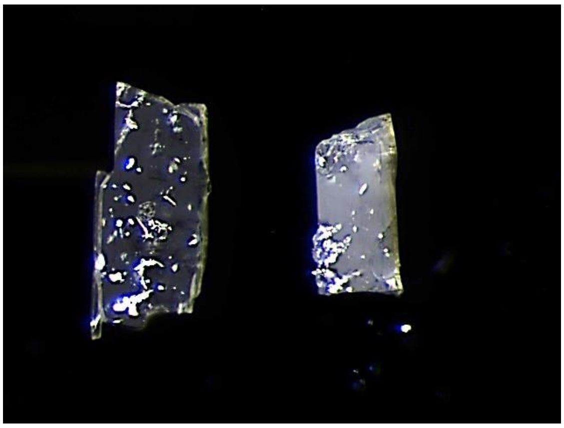

Figure 3.17b: Polymorph 3 (left) and polymorph 6 (right). This micrograph indicates that other morphological forms of polymorph 6 could also exist.

Even though polymorph 6 appeared to be distinctive from a morphological perspective in comparison to the other polymorphs, a unit cell assessment was performed for each crystal investigated, since, as mentioned above, specimens with other morphologies were also determined to correspond to crystals of polymorph 6. Approximately only one-fifth of the crystals collected for further experimentation displayed this unique bullet-head morphology. As a result, crystals having the other morphologies, which most likely occurred from crystal shattering, were also collected for further experimentation. In addition, despite the tedious task of individually separating and analysing the single crystals of this new polymorph by means of unit cell determinations, it provided a very accurate confirmation that the resulting sample was polymorphically pure.

Unfortunately, no preparative method had yet been found to produce polymorph 6 exclusively and as a result, this separation method was imperative to guarantee purity.

Powder X-ray diffraction (PXRD): experimental and calculated PXRD pattern comparison

Obtaining a reliable experimental PXRD pattern of polymorph 6 was exceedingly challenging, and unfortunately it was not achieved. This was due to the fact that polymorph 6 did not crystallize in a pure form. As mentioned previously, there were the five other polymorphs of isonicotinamide also present, along with polymorph 6, in the vial after co-precipitation. This was also verified in the experimental PXRD pattern which analysed the whole co-precipitated product from the vial and thus indicated the presence of all six polymorphs, as displayed in Figure 3.18. This experimental PXRD pattern contains peaks from all six polymorphs, although with varying intensities in comparison to the individually calculated PXRD patterns of each polymorph. Furthermore, there were very slight shifts in the 2θ-positions between corresponding peaks in the experimental and calculated PXRD patterns. This was owing to the fact that the SCXRD data of the different polymorphs were collected at various temperatures in the range 100 – 173 K, as well as at 300 K (for polymorph 5), whereas the experimental PXRD pattern recorded by the author was obtained at room temperature (294 K). In addition, the experimental PXRD pattern contained at least one zero intensity peak for each polymorph in comparison to the calculated PXRD patterns.

Despite the fact that the experimental PXRD pattern is a superposition of all six polymorphic forms, each peak can be assigned to the polymorph(s) to which it corresponds. These assignments are presented in Table 3.7.

Table 3.7: The 2θ-positions from the experimental PXRD pattern that correlate with the 2θ-positions of calculated PXRD patterns of each polymorph.

Polymorph	**2θ-positions (^{o})**
1	17.5, 21.0, 23.0, 24.0, 25.5, 26.5, 30.0 and 33.0
2	11.5, 14.7, 16.0, 18.5, 19.0, 19.1, 23.0, 24.5, 25.5, 28.5, 29.5, 30.5, 32.5, 35.0 and 37.5
3	14.2, 17.5, 19.0, 21.5, 22.1, 24.3, 26.5, 27.0, 30.0, 31.0, 33.0, 33.5 and 37.2
4	14.1, 19.0, 19.5, 21.2, 22.0, 23.0, 24.0, 24.5, 25.8, 26.5, 29.0, 30.0, 31.0, 32.5, 33.2 and 35.0
5	11.5, 14.5, 19.0, 21.8, 24.0, 29.0, 30.5, 33.2, 35.0, 35.5, 37.5, 38.5 and 39.0,
6	11.5, 14.2, 15.2, 17.8, 19.0, 21.2, 21.8, 23.0, 24.0, 24.5, 25.5, 26.5, 29.5, 30.5, 32.2, 35.2, 37.0, 38.5 and 39.0

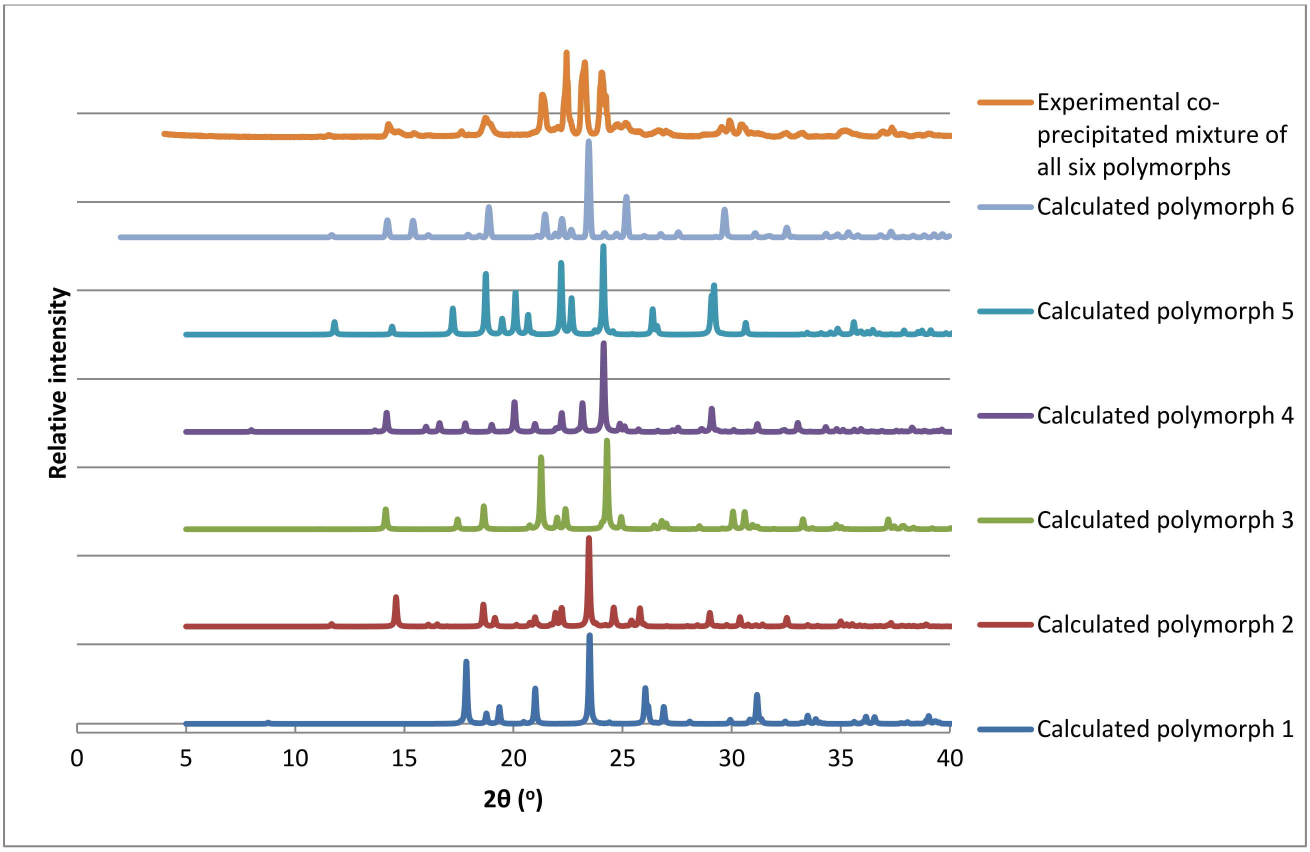

Figure 3.18: Calculated PXRD patterns of the six polymorphs of isonicotinamide and the experimental PXRD pattern of the co-precipitated mixture that contained all of these forms.[9,16-18]

In order to obtain a PXRD pattern of pure polymorph 6, this new crystal form had to be separated from the other polymorphs. Approximately 1.8 mg of pure polymorph 6 was harvested (before it became challenging to reproduce polymorph 6), and confirmed to be polymorphically homogeneous *via* SCXRD unit cell determinations. The experimental PXRD pattern [Figures 3.19a (original trace) and 3.19b (intensity-enhanced trace)] was of very poor quality, as it indicated preferred orientation of the crystallites, even though the sample was lightly ground into a fine powder. Consequently, there is the appearance of the high intensity peak at 23.0°, with all the remaining peaks being dwarfed to a noise level. Even though this was the case, it was still possible to attempt to correlate almost all of the 'very low' intensity peaks with the calculated PXRD pattern of polymorph 6, albeit with approximately half a degree of offset on average. This half a degree offset could be due to the fact that the experimental PXRD pattern was recorded at 294 K, while the calculated PXRD pattern was recorded at 173 K. These peaks are at the 2θ-positions 11.5°, 14.5°, 19.0°, 22.5°, 24,5°, 25.5°, 32.5°, 35.0° and 36.8°. However, this correlation is not very reliable, since at such a low signal-to-noise ratio of those 'low intensity peaks', the results do become questionable. This unreliability could further explain why some of the peaks were missing and why there was an additional peak at the 2θ-position of 15.0°, which was not represented in the calculated PXRD pattern of polymorph 6.

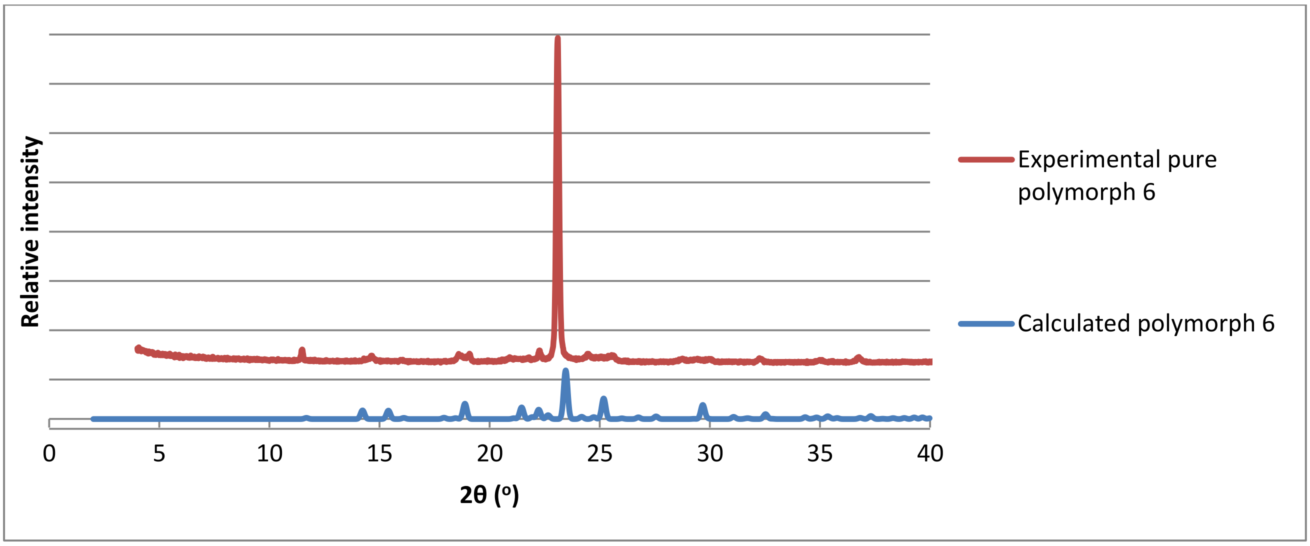

Figure 3.19a: The experimental PXRD pattern of pure polymorph 6 and the calculated PXRD pattern of polymorph 6.

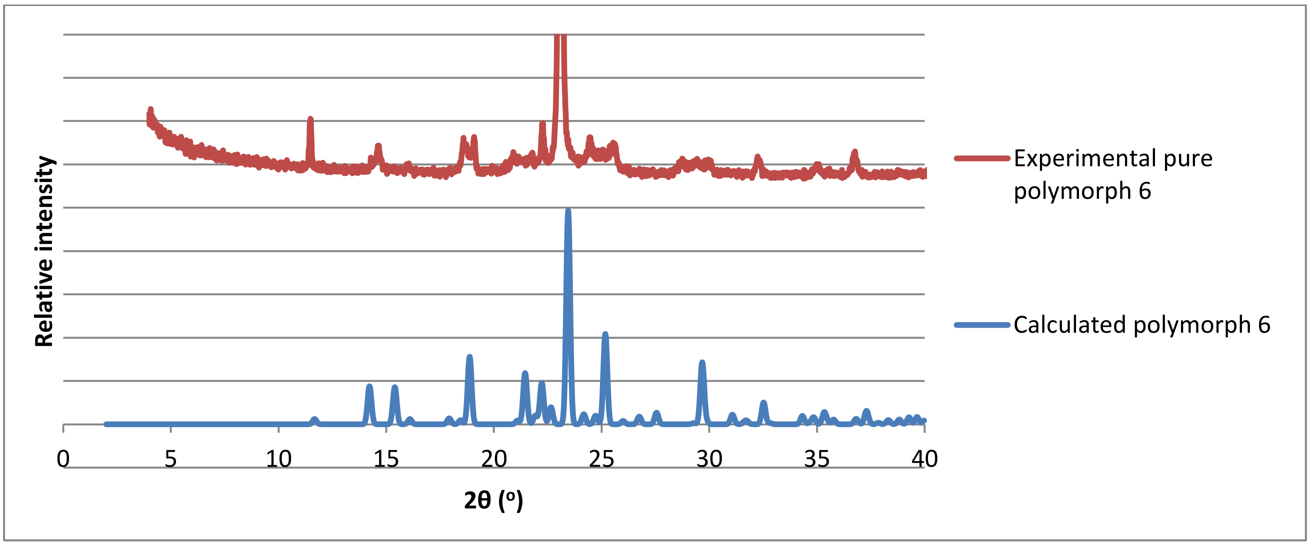

Figure 3.19b: Intensity-enhanced representations of the PXRD patterns shown in Figure 3.19a.

The crystal structure of polymorph 6 provided a reason to account for the most intense peak at 2θ = 23.0° in the calculated PXRD pattern of polymorph 6. This reason did not account for the extreme intensity of preferred orientation [which is displayed in the experimental PXRD pattern of pure polymorph 6 (Figure 3.19a and 3.19b)], since this could be caused by factors such as the crystal morphology and the level of grinding. The packing diagram of the unit cell viewed down the b-axis (Figure 3.20) displays a significant number of atoms from the isonicotinamide molecule, which are positioned in the close vicinity of the (004) planes. This resulted in significant constructive interference for the (004) reflection and thus gave rise to the most intense peak at 23.0° in the calculated PXRD pattern of polymorph 6.

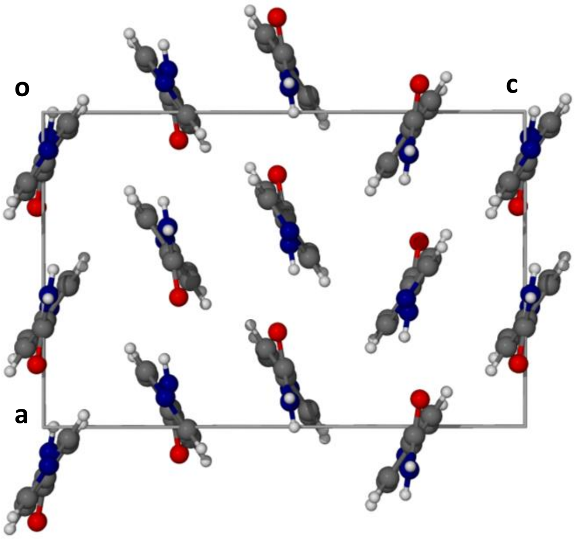

Figure 3.20: The unit cell of polymorph 6 which displays a significant number of atoms that straddle the (004) planes.

Obtaining a more substantial mass of polymorph 6 was no longer possible through physical separation that was intended to improve the quality of the experimental PXRD pattern. However, an alternative option for improving the signal-to-noise ratio of the experimental PXRD pattern would be to record the pattern from 4° to 22° and from 24° to 40°, thus eliminating the peak suffering maximum preferred orientation. By collecting two separate PXRD patterns on either side of the peak at 23.0°, it should be possible to merge the patterns together and compile a 'pseudo-single' PXRD pattern of polymorph 6. This would merely indicate whether the experimental PXRD pattern displayed the same 2θ peak positions as the calculated pattern. However, it would not be possible to compare the relative intensities accurately, as the peak of highest intensity had been eliminated. Unfortunately, these experimental PXRD pattern results were unsatisfactory, as displayed in Figure 3.21. The PXRD pattern from 4° to 22° 2θ displayed a very high signal-to-noise ratio with only one peak at 11.5°. In addition, the other low intensity peaks that were present in the full experimental PXRD pattern of polymorph 6 up to 22° were not present in this pattern ranging from 4° to 22°. This could either be due to the fact that those peaks were merely undefined noise in the full experimental PXRD pattern, or it could indicate that the sample was becoming amorphous over time. If the latter applied, the possible reason could have been due to the two separate PXRD patterns ranging from 4° to 22° and 24° to 40° having been recorded 5 weeks after the full PXRD experimental pattern of polymorph 6 was obtained. Lastly, the PXRD pattern ranging from 24° to 40° 2θ displayed only noise.

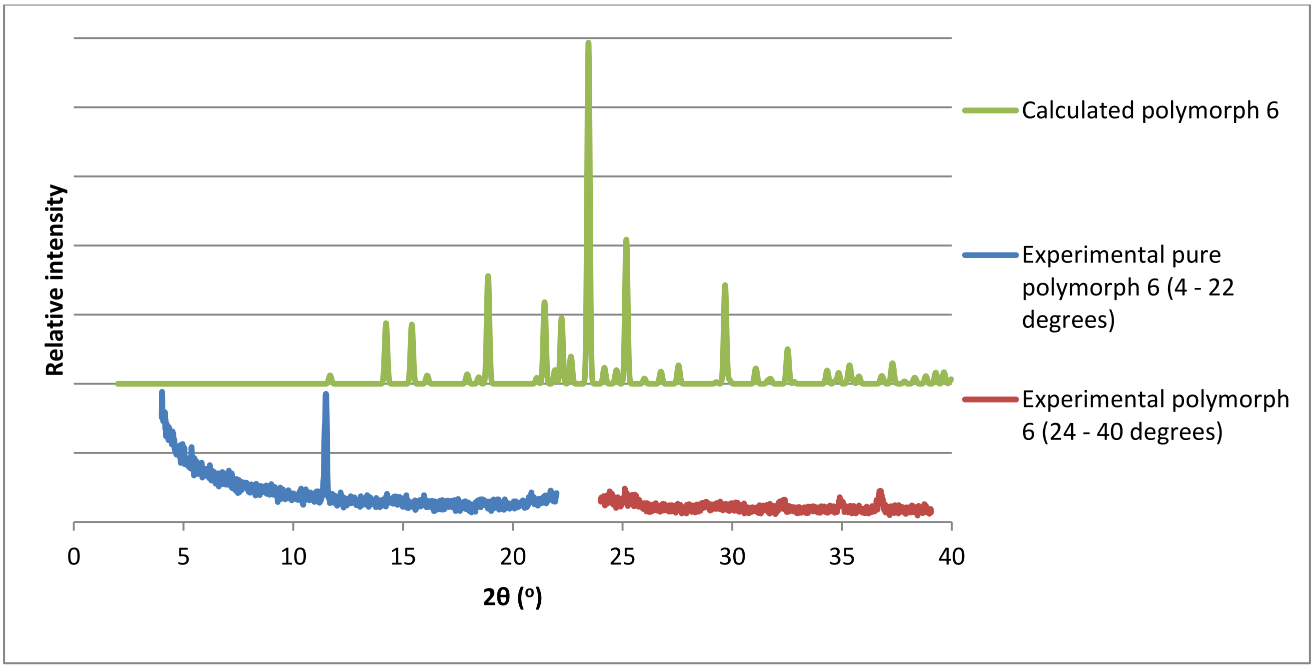

Figure 3.21: The calculated PXRD pattern of polymorph 6 and the two separate experimental PXRD patterns of pure polymorph 6 ranging from 4° – 22° 2θ and from 24° – 40° 2θ.

Consequently, a seeding experiment was attempted where two seed crystals of polymorph 6 were added to a chloroform solution containing 5 mg of isonicotinamide and then left to recrystallize. The PXRD pattern of the bulk crystallized material was recorded. However, it did not display a significant improvement (Figure 3.22a and 3.22b) despite the increased mass used for the analysis. Furthermore, there were both additional (extraneous) peaks and absent peaks in comparison to the calculated PXRD pattern of polymorph 6. As mentioned previously, this comparison was not a reliable indicator for any form of correlation, as the signal-to-noise ratio of the 'low intensity' peaks was very low. This comparison was further complicated by the different temperatures that were used to record the experimental and calculated PXRD patterns. Nevertheless, as before, an attempt to correlate some of the peaks was performed. It appeared that there was the possibility to correlate the 'low intensity peaks' of the experimental PXRD pattern of polymorph 6 (produced *via* seeding) at the 2θ-positions 11.5°, 19.0°, 22.5° and 23.0° with the calculated PXRD pattern of polymorph 6. However, peaks at the 2θ-positions 15.0°, 18.5°, 21.0°, 22.0°, 26.0°, 29.0° and 30.2° of the experimental PXRD pattern of polymorph 6, were not reflected in the calculated PXRD pattern of polymorph 6. Therefore, this indicated that these 'low intensity peaks' were either from another polymorph, and thus the material produced *via* seeding was not polymorphically pure, or they were just variations of noise and should be disregarded. As a result, acquisition of a reliable experimental PXRD pattern of polymorph 6 *via* a seeding experiment was not achieved.

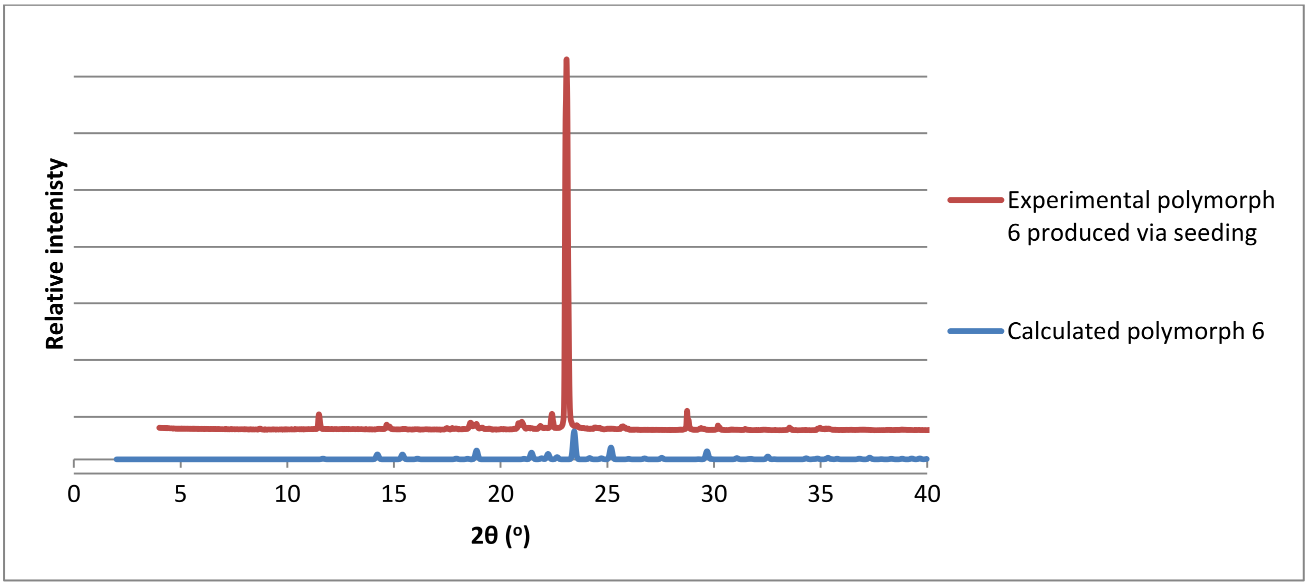

Figure 3.22a: The calculated PXRD pattern of polymorph 6 and the experimental PXRD pattern of polymorph 6, which was produced *via* a seeding experiment.

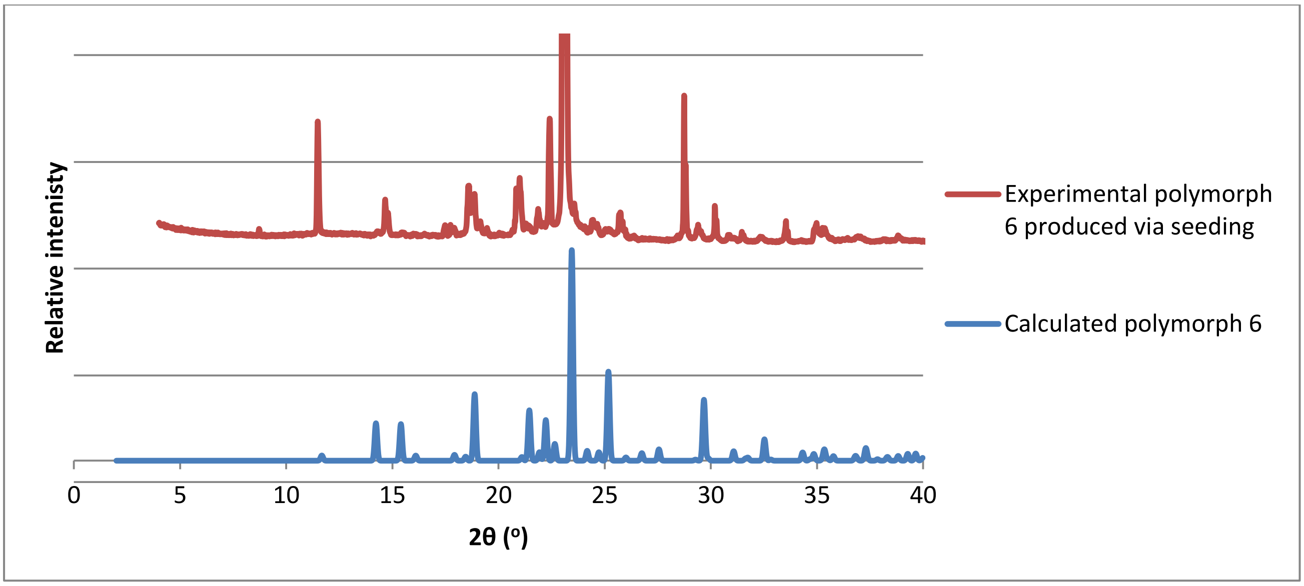

Figure 3.22b: Intensity-enhanced representations of the PXRD patterns shown in Figure 3.22a.

Lastly, two liquid-assisted grinding (LAG) experiments were also employed in order to attempt to produce polymorph 6. The first LAG experiment involved adding 5 mg of isonicotinamide into the mortar and grinding it with a few drops of chloroform for 30 minutes. The second LAG experiment involved the same process, except that a large quantity of chloroform was added until the isonicotinamide had the consistency of a slurry. Unfortunately, neither of these experiments yielded the anticipated results (Figure 3.23) and the experiment produced polymorph 1, as indicated by the direct correlation between the two products of the LAG experiments and the PXRD pattern for polymorph 1.[9,16]

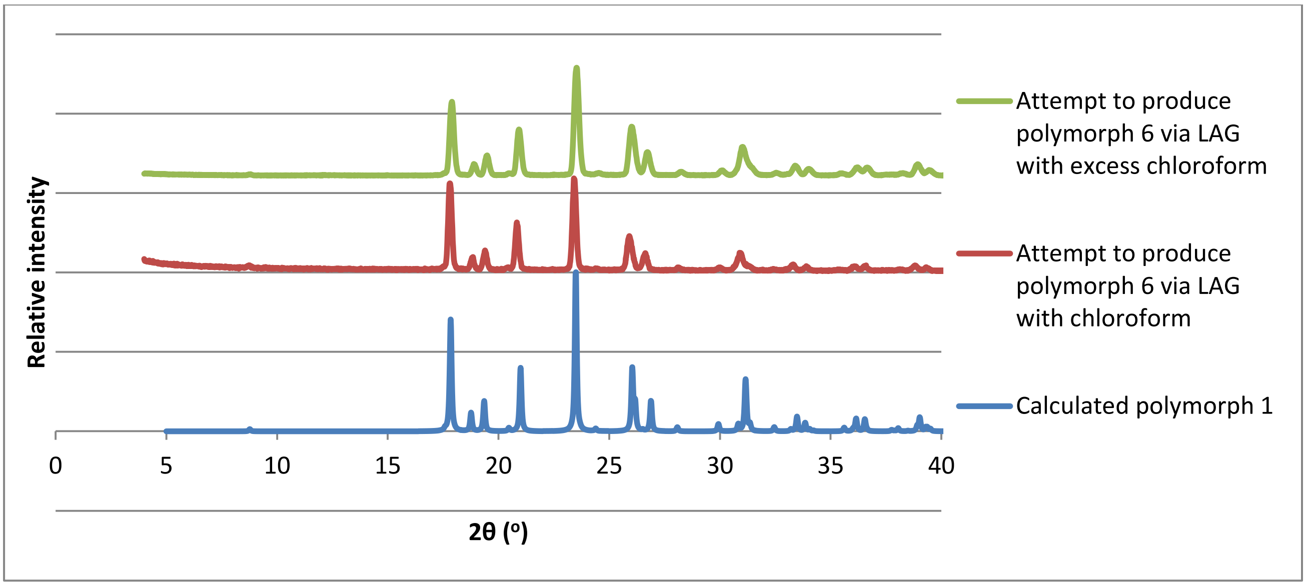

Figure 3.23: The calculated PXRD pattern of polymorph 1, an experimental PXRD pattern resulting from an attempt to produce polymorph 6 *via* LAG with chloroform, and an experimental PXRD pattern resulting from an attempt to produce polymorph 6 *via* LAG with excess chloroform.[9,16]

In conclusion, all efforts to record a representative experimental PXRD pattern of polymorph 6 consistent with the pattern calculated from the single crystal X-ray analysis failed, despite exhaustive attempts.

Hot Stage Microscopy (HSM) analysis

A hot stage microscopy (HSM) analysis was performed in order to compare the simultaneous thermal progression of five out of six of the polymorphs of isonicotinamide, namely polymorphs 1, 2, 3, 4 and 6 at a heating rate of 1 K.min^{-1} The reason that polymorph 5 was omitted, was due to difficulties in reproducing an adequate single crystal of this form. The sequential micrographs displayed below (Figure 3.24) represent the thermal behaviour of the different polymorphs from 27.5 ^{o}C to 161.0 ^{o}C, which included polymorphic transitions and the onset of the various melts. Image 1 displays the crystals at 27.5 ^{o}C where the various polymorphs were arranged clockwise in ascending serial order. No observable changes occurred with any of the polymorphs until 122.8 ^{o}C (Image 2) where the onset of opacity occurred sharply (within the range of 0.5 ^{o}C) in polymorph 3, while the other polymorphs remained unchanged. The onset of opacity in polymorph 3 represented a polymorphic phase transition taking place and this event correlated with a previous report by Li.[24] In the latter reported experiment, the onset of opacity occurred at 131 ^{o}C for polymorph 3 at a heating rate of 10 K.min^{-1}. However, when Li repeated the experiment at a heating rate of 1 K.min^{-1} the onset of opacity occurred over a broad temperature range of 121 – 135 ^{o}C,[24] instead of appearing as a sharp transition within half a degree, as observed in the current experiment. Li also reported that at 133 ^{o}C an onset of opacity occurred in polymorph 2,[24] whereas this thermal event was not observed during the current experiment. At 128.9 ^{o}C (Image 3), polymorph 6 developed the onset of an extremely slow melt. It was deduced that prior to this extremely slow melt commencing, a polymorphic phase transition had taken place, as in an earlier HSM experiment (described in greater detail below) it was evident that nucleation sites began to occur within polymorph 6 at 119.0 ^{o}C. Unfortunately, this particular polymorphic phase transition was not observed in the second HSM analysis where the five polymorphic forms were compared simultaneously. It appeared, after considerable scrutiny, that the onset of a very slow melt began to occur for all the remaining polymorphs at 132.1 ^{o}C (Image 4). The decrease in size from the onset of melting with all the polymorphs was hardly discernible; however, this was carefully analysed by means of overlaying each individual crystal in consecutive HSM micrographs. Furthermore, the onset of opacity occurred in polymorph 4 at 141.9 ^{o}C, associated with a polymorphic phase transition (Image 5). The pace of melting increased significantly at 151.3 ^{o}C (Image 6) where polymorph 6 had completely melted (most likely owing to its more slender and comparatively smaller size). In addition, the fast-paced melt continued and polymorphs 1, 2 and 3 were completely molten at 155.1 ^{o}C (Image 7). In contrast, at this temperature, polymorph 4 hardly exhibited any comparative decrease in size. This possibly suggested that polymorph 4 had not yet transformed into the same phase as polymorphs 1, 2, and 3. Polymorph 4 completely melted at 161.0 ^{o}C, as displayed in Image 8.

Figure 3.24: A series of HSM micrographs which display the thermal progression of polymorphs 1, 2, 3, 4 and 6 of isonicotinamide from 27.5 °C – 161.0 °C.

Image 1: The initial appearance of the polymorphs at 27.5 °C.

Image 2: At 122.8 °C the onset of opacity occurred within polymorph 3.

Image 3: At 128.9 °C the onset of the melt occurred for polymorph 6.

Image 4: At 132.1 °C the remaining polymorphs began to melt.

Image 5: At 141.9 °C the onset of opacity occurred within polymorph 4.

Image 6: At 151.3 °C the melting rate increased and polymorph 6 completely melted.

Image 7: At 155.1 °C polymorphs 1, 2 and 3 had melted, while the melting rate of polymorph 4 decreased significantly.

Image 8: At 161.0 °C all the crystals had fully melted.

An earlier HSM experiment had been conducted, which compared polymorph 3 and polymorph 6 simultaneously at the same heating rate of 1 K.min^{-1}. Unfortunately, the resolution of the successive images was of inadequate quality; nonetheless, during this particular experiment a polymorphic phase transition in polymorph 6 was evident by the appearance of nucleation sites.

The sequential micrographs displayed below (Figure 3.25) represent the thermal progression of the two crystals from 22.8 ^{o}C to 148.3 ^{o}C, which included polymorphic transitions and the onset of melting. Image 1 displays the crystals at room temperature (22.8 ^{o}C) with polymorph 6 on the right-hand side and polymorph 3 on the left-hand side. No changes occurred to either crystal until 119.0 ^{o}C, as displayed in Image 2, where polymorph 6 began to develop spots in the lower region of the crystal. It is this particular event that was not observed in the second HSM analysis. These spots are attributed to nucleation sites of another polymorph forming. It could be speculated that these spots were a result of the light reflecting off the surface of the crystal (as there were some reflective spots initially on the crystal at room temperature in image 1). However, there was no visual evidence of the crystal changing its morphological topography at this temperature (or even for the following 20 ^{o}C) which could have caused additional reflective light spots to appear. Furthermore, the original reflective light spots on the crystal had not changed, which further confirmed that the internal spots were a consequence of a polymorphic transition and not due to the reflective surfaces shifting from, for example, melting. Image 3 indicates the onset of opacity in polymorph 3 at 123.5 ^{o}C, while polymorph 6 remained unchanged. This onset of opacity represented a polymorphic transition taking place. Image 4 displays the development of nucleation sites occurring at 128.3 ^{o}C in polymorph 3. In addition, at this temperature, polymorph 6 developed a significant increase in nucleation sites all over the crystal as well as the onset of a very slow melt. The latter event was noticed by the slight shortening of the triangular, bullet-head shaped point at the bottom tip of the crystal of polymorph 6. Image 5 at 132.5 ^{o}C indicates a significant increase of nucleation sites for polymorph 3, while polymorph 6 continued to melt very slowly. Image 6, at 142.0 ^{o}C indicates polymorph 3 fracturing internally, possibly as a result of the formation of internal bubbles, which were also observed. Simultaneously, the onset of the melt for polymorph 3 began, as the entire crystal began to shrink in size at an extremely slow rate. At the same temperature, polymorph 6 continued to melt; however, at an accelerated pace. Even though more spots were appearing on polymorph 6 during the melt, it was impossible to verify which were due to reflective light, and which were genuine nucleation sites forming. Image 7, at 143.1 ^{o}C displays a very slow melt for polymorph 3 with vigorous internal bubbles, while polymorph 6 was experiencing a relatively faster melt. Image 8 at 148.0 °C indicates both crystals melting rapidly, to the point where they were completely molten at 148.3 °C as represented in Image 9.

Figure 3.25: A series of HSM micrographs which display the thermal progression of polymorphs 3 and 6 of isonicotinamide from 22.8 °C – 148.3 °C.

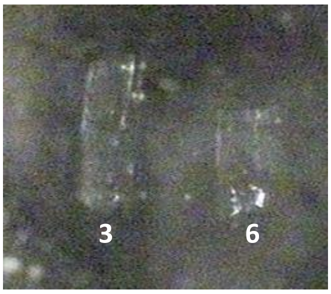

Image 1: The Initial appearance of polymorph 3 (left) and polymorph 6 (right) at 22.8 °C.

Image 2: Polymorph 6 (right) began to develop nucleation sites (in the form of spots) towards the bottom of the crystal at 119.0 °C.

Image 3: The onset of opacity in polymorph 3 (left) at 123.5 °C.

Image 4: At 128.3 °C, polymorph 3 (left) developed nucleation sites (in the form of spots). In addition, polymorph 6 (right) developed a significant increase in nucleation sites all over the crystal as well as the onset of a very slow melt.

Image 5: At 132.5 °C there was a significant increase in nucleation sites for polymorph 3 (left), while polymorph 6 continued to melt very slowly (right).

Image 6: At 142.0 °C polymorph 3 (left) began to fracture internally with internal bubbles forming. In addition, the onset of the melt for polymorph 3 began. Polymorph 6 (right) continued to melt.

Image 7: At 143.1 °C, polymorph 3 (left) experienced a very slow melt with vigorous internal bubbles. Polymorph 6 (right) experienced an accelerated melt.

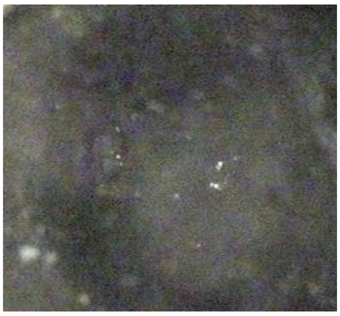

Image 8: Both crystals were melting rapidly at 148.0 °C.

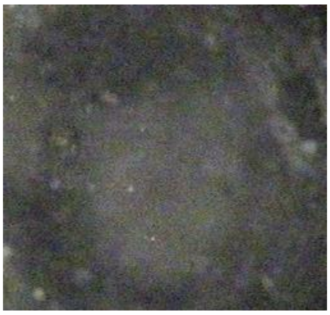

Image 9: Both crystals were completely melted at 148.3 °C.

The results from both of these analyses were inconclusive, as it was not possible to determine to which polymorphic phase the different crystals were transforming. Furthermore, although the same polymorphs were compared and assessed in various experiments, different thermal events were occasionally observed. It is important to note that this does not mean that the data reported by the previous authors, or that the data from the experiments described here, were inconsistent. It rather emphasizes the point that a visual comparison in isolation is not always accurate or justified.

Differential Scanning Calorimetry (DSC) analysis of form 6

The DSC trace indicated two thermal events, which occurred over the temperature range 20.2 – 218.0 °C, as depicted in Figure 3.26 (n = 2). This DSC trace is the average of two experiments, where the heating rate was 10 $K.min^{-1}$ for both of them. In addition, the sample used for both experiments consisted of single crystals that were individually evaluated for polymorphic purity by SCXRD analysis. These thermal events included a hardly observable, broad exothermic peak at 130.7 °C and a sharp endothermic peak at 156.3 °C. (There is a very small, sharp peak at 65 °C. This is attributed to an artefact, since firstly, no thermal event was observed at such a low temperature in the HSM analysis and secondly, the peak is too sharp to represent a thermal event. This artefact was also only present in one of the two DSC traces).

The first thermal event was within the range 120.8 – 138.8 °C and corresponded to a phase transformation of polymorph 6, as this temperature correlated with the development of nucleation sites on the crystal in the HSM analysis. In addition, the onset of the endothermic peak, at 155.5 ± 0.1 °C (peak temperature 156.3 ± 0.1 °C) corresponded to the melt, and the enthalpy of fusion was 163 ± 5 $J.g^{-1}$. However, these temperatures did not correlate with the HSM analysis, which displayed a complete melt at 148.3 °C and 151.3 °C for the two separate experiments. A possible explanation is that the merits of comparing the temperatures of crystals melting on different sets of equipment are not always justified. Thus, it was not possible to easily differentiate or compare the different polymorphs of isonicotinamide, since the melting range of all the polymorphs indicated by the DSC method is between 154 and 158 °C.[16-18]

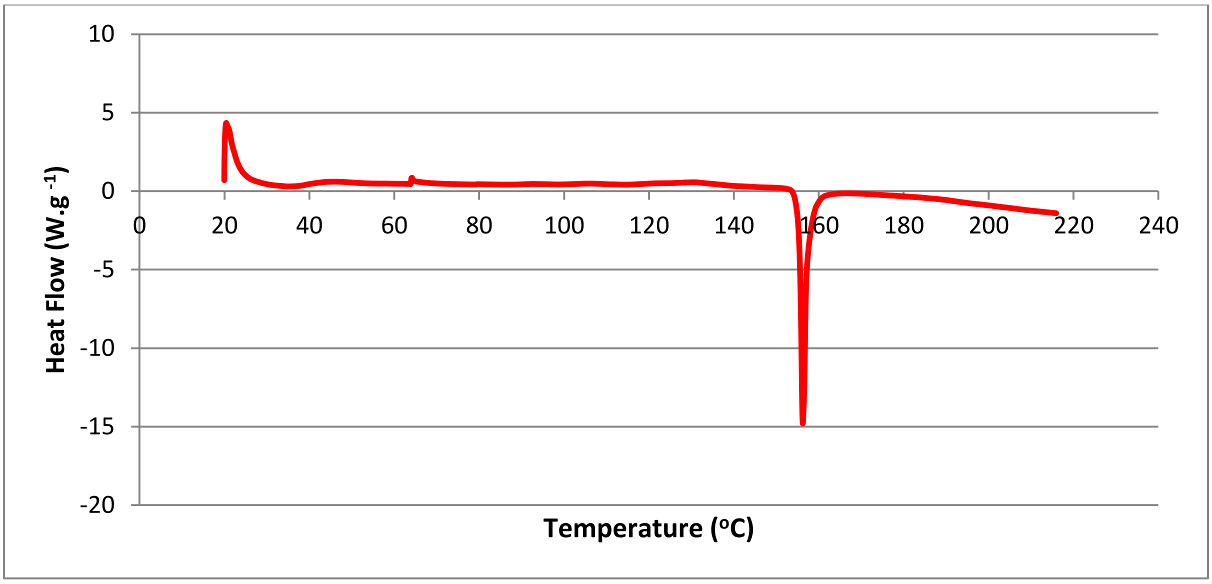

Figure 3.26: The average DSC trace of polymorph 6 from two experiments.

Solution-mediated transformation experiment

A solution-mediated transformation experiment was conducted in order to assess whether polymorph 6 was a metastable phase relative to the most stable polymorph of isonicotinamide, which is polymorph 1. The preparation involved placing a single crystal of polymorph 1 and a single crystal of polymorph 6 in the centre of a Petri dish. A solution of EtOH that was saturated with isonicotinamide[d] was added extremely slowly and carefully to the Petri dish by means of a syringe with a needle. As a result, the two crystals of isonicotinamide were submerged in a bath of EtOH saturated with isonicotinamide, with the surface level of the solution being about three times the height of the top of the crystals, in order to allow for crystal growth. The Petri dish was subsequently covered with a watch glass, to prevent evaporation of the EtOH, and the entire system was placed under a microscope.

According to the literature, the expected result would be that polymorph 1 would increase in size at the expense of polymorph 6, if the latter were the metastable phase.[25] However, this was not the case with the experiment described here. The successive micrographs (Figure 3.27) display the resultant growth of both polymorphs over the duration of 3 hours and 56 minutes. With reference to the first 30 minutes (Images 1 – 3 under Figure 3.27), noticeable growth had occurred on

---

[d] This solution was created by adding an excess amount of isonicotinamide to EtOH and stirring it for 72 hours at room temperature. The solution was successively filtered.

polymorph 1 almost immediately, while, in contrast, polymorph 6 had undergone minimal growth. Furthermore, the initial type of growth that occurred on polymorph 1 was a repair of a fracture that had occurred on the crystal prior to the start of the experiment. The subsequent micrographs (Images 3 – 5) indicate the rapid expansion in all morphological directions that both crystals experienced over the duration of 30 minutes to 3 hours and 56 minutes. In addition, it was still possible to visually track the original crystals of both polymorphs within the expanded growth. Lastly, various satellite crystals began to grow in the Petri dish from 43 minutes onwards (Image 4) and also approximately at the same rate as the two polymorphs under inspection. However, it was possible to observe miniscule crystallization nuclei that eventually grew into these additional crystals from 20 minutes (Image 2). These additional crystals were formed as a consequence of the EtOH slowly evaporating and thus isonicotinamide was precipitating from the supersaturated solution. Despite the fact that a watch glass was used to cover the Petri dish to help prevent the evaporation of the EtOH, it had to be temporarily removed for photographic purposes. The slight evaporation of the EtOH was also further accentuated by the fairly warm light of the microscope. These conditions were unavoidable.

Figure: 3.27: Solution-mediated growth of isonicotinamide polymorphs in EtOH.

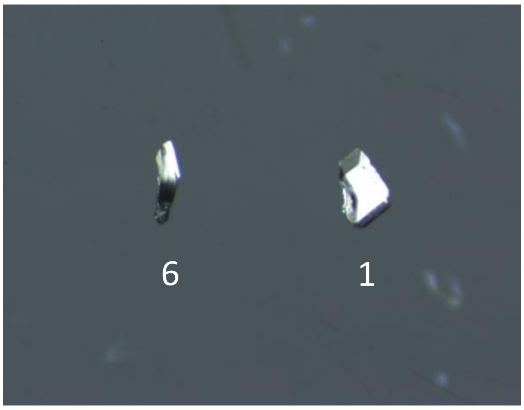

Image 1: Initial appearance of polymorph 6 (left) and polymorph 1 (right) of isonicotinamide submerged in EtOH saturated with isonicotinamide.

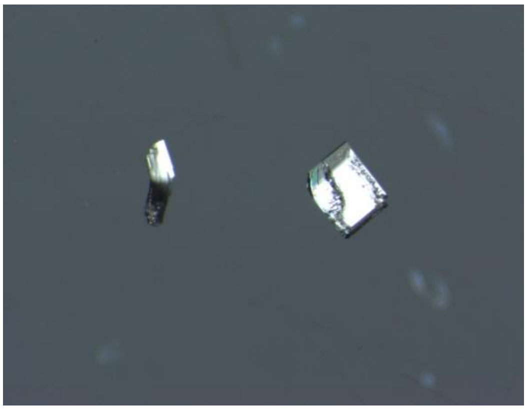

Image 2: 20 minutes.

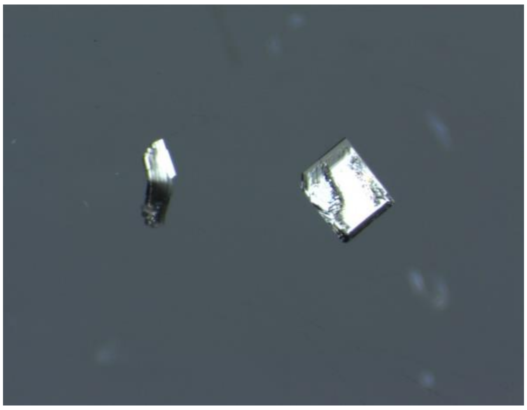

Image 3: 30 minutes.

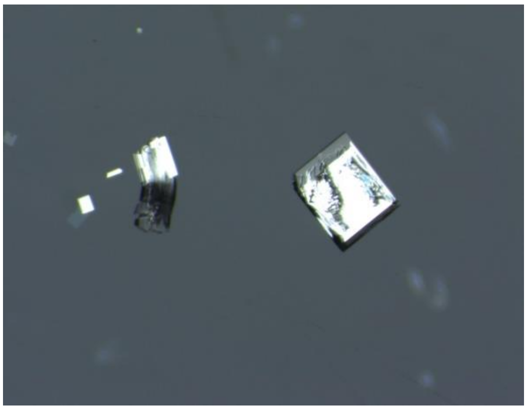

Image 4: 43 minutes.

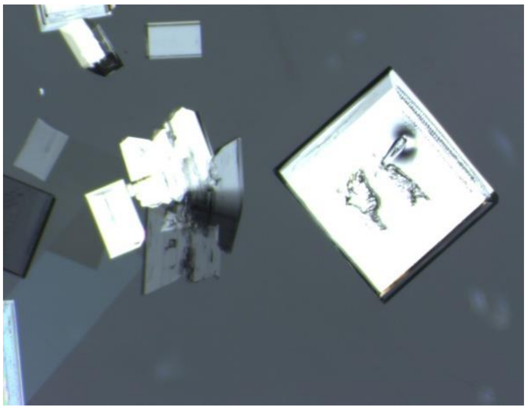

Image 5: 3 hours and 56 minutes.

Once the experiment was completed, the two main crystal forms under inspection, along with three satellite crystals that were adjacent to each polymorph, were removed from the Petri dish and placed in Paratone oil[26] for further examination. With reference to polymorph 1, the crystal had a cubic shape that measured 904 µm along the horizontal and 1024 µm along the vertical. This indicated that the area of the crystal grew approximately 1818 %, as the original dimensions along the same two lengths were 238 µm and 214 µm respectively. The crystal was subsequently cut very carefully to recover the original fragment that was used to initiate the experiment. A unit cell determination was performed which revealed that the original fragment remained as polymorph 1. In addition, three fragments from the new growth on the crystal were selected and analysed for their unit cell parameters. These fragments were from the top left, top right and bottom right corners of the expanded crystal. The results confirmed that all three fragments belonged to polymorph 1, and thus the crystal grew isomorphically.

The same procedure was followed for polymorph 6, where the crystal was cut to reveal its original fragment, and three other fragments from the growth were also selected and cut. However, obtaining the original crystal fragment of polymorph 6 proved to be more difficult than expected, especially as the morphology was in a crooked L-shape. The dimensions of the crystal at face-view measured 595 µm along the horizontal and 952 µm along the vertical. This indicates that the area of the crystal grew approximately 876 %, as the original dimensions along the same two lengths were 143 µm and 452 µm respectively. Nonetheless, the crystal fragment obtained did appear to come from the original crystal and the unit cell dimensions remained those of polymorph 6. However, the various fragments of the new crystal growth that coated the original polymorph 6 single crystal, revealed unit cell dimensions that corresponded to polymorph 2.

Furthermore, additional crystals that grew directly around the local vicinity of polymorph 1 and polymorph 6 were also selected and analysed. Three individual crystals that grew around polymorph 1 and another three crystals that grew around polymorph 6 also had unit cell parameters corresponding to those of polymorph 2. This suggested that the metastable polymorph 2 readily precipitated under these conditions and the experiment was terminated before there was sufficient time for the crystals of polymorph 2 to transform into the most stable form (polymorph 1). Furthermore, the original crystal fragment of polymorph 6 had polymorph 2 preferentially coating it instead of polymorph 6, and thus this suggested that polymorph 6 is a less metastable form than polymorph 2. In contrast, the original crystal fragment of polymorph 1 grew isomorphically, possibly since polymorph 1 is the most stable polymorph of isonicotinamide. Presumably, all the other crystals that were in the system would have eventually changed to the most stable form after a sufficient time.[e]

Lastly, an interesting observation occurred within the first 30 minutes. Prior to the start of the experiment, a small piece of polymorph 1 cracked off, damaging its cubic shape. However, during this half hour, it fully repaired that missing piece before expanding uniformly in a cubic morphology. Furthermore, polymorph 6 had minimal growth during this time period. However, it was possible to observe miniscule crystal growth at various areas on the crystal (Images 1 – 3). Presumably, what is thought to have occurred, is that polymorph 6 was slowly being coated with nucleation sites of polymorph 2, and only once the original crystal was fully coated in these nucleation sites, could it begin to expand as rapidly as polymorph 2.

---

[e] This was performed in a different experiment where a saturated EtOH solution of isonicotinamide was left to recrystallize for one month, and only polymorph 1 was present.

Attempts to crystallize polymorph 6 from a variety of solvents

As a final attempt to reproduce polymorph 6, an alternative method was employed where three different organic solvents were used to dissolve and recrystallize approximately 20 mg of isonicotinamide in separate vials. These three organic solvents were acetone, acetonitrile and isopropanol, and the crystals were removed for analysis within a period of less than 24 hours after precipitating in the mother liquor. The general method of slow evaporation was used to execute the experiment, where the temperature for heating the solution was tailored accordingly for each organic solvent. The results are exhibited in Table 3.8.

Table 3.8: The results from selected crystals of the recrystallization of isonicotinamide from acetone, acetonitrile and isopropanol.

Solvent	Product characteristics	Method of analysis	Results
Acetone	Large, rectangular, transparent crystals.	SCXRD	Polymorphs 6, 4 and 2 were found in approximately equal ratios by mass
Acetonitrile	Medium to large, rectangular, transparent crystals.	SCXRD	Polymorphs 6, 4, 2 were found in approximately equal ratios by mass
Isopropanol	Medium-sized, transparent crystals in the shape of parallelograms.	SCXRD and PXRD	A fair amount of single crystals of polymorph 6 was obtained (majority). However, a few of the other polymorphs (except for polymorph 5) were occasionally found (minority). The PXRD pattern closely resembled that of the low signal-to-noise ratio PXRD pattern of the experimentally harvested, 'pure' polymorph 6.

In the communication reported by Eccles *et al.*,[18] it was discovered that polymorphs 2 and 4 crystallized in pure acetone before the solvent completely evaporated. However, in the experiment described here, which imitated the experiment performed by Eccles *et al.*, polymorph 6 also crystallized in pure acetone.[18] Thus, as mentioned before, either polymorph 6 transformed into another polymorph before Eccles *et al.* had the opportunity to report it, or nuclei of polymorph 6 from the present author's laboratory unintentionally seeded the solution. Furthermore, isopropanol and acetonitrile also produced polymorph 6. Thus, a similar explanation would follow, except that no literature studies have reported previous recrystallizations with either of those organic solvents. Consequently, this recrystallization investigation of isonicotinamide that employed the organic solvents acetone, acetonitrile and isopropanol, indicated the first examples where polymorph 6 could be isolated without the presence of allopurinol.

This recrystallization experiment was performed approximately one and a quarter years later, which was right at the end of the investigation of polymorph 6. The most plausible explanation for the appearance of polymorph 6, amongst the other expected polymorphs, especially in acetone,[18] is that the laboratory had a sufficient amount of time to become "seeded", and thus polymorph 6 could be produced by unintentional seeding. As a result, the metastable polymorph 6 was observed in acetone, acetonitrile and isopropanol before it transformed into the more stable forms. However, the most noteworthy point is that polymorph 6 actually crystallized during this recrystallization study and apparently not in any previous experiments that Eccles *et al*. had performed.[18]

Lastly, a PXRD comparison was performed with the crystals obtained from isopropanol, as polymorph 6 appeared to crystallize as the predominant form at that particular time. A noteworthy observation was that when a small mass (of approximately 4 mg) was used, the PXRD pattern (Figures 3.28a and 3.28b) resembled the initial PXRD pattern that displayed preferred orientation as shown in Figure 3.19a and 3.19b. However, when a larger mass of isonicotinamide was recrystallized from isopropanol (approximately 20 mg), it produced a PXRD pattern that did not reflect any particular polymorph (Figure 3.29). This PXRD pattern contained a few peaks from each polymorph, although there were also an equal number of peaks absent from each polymorph. One possible argument for this occurrence is that polymorphic transitions were in the process of taking place, while the larger mass of isonicotinamide was being recrystallized. Thus, these results were inconclusive.

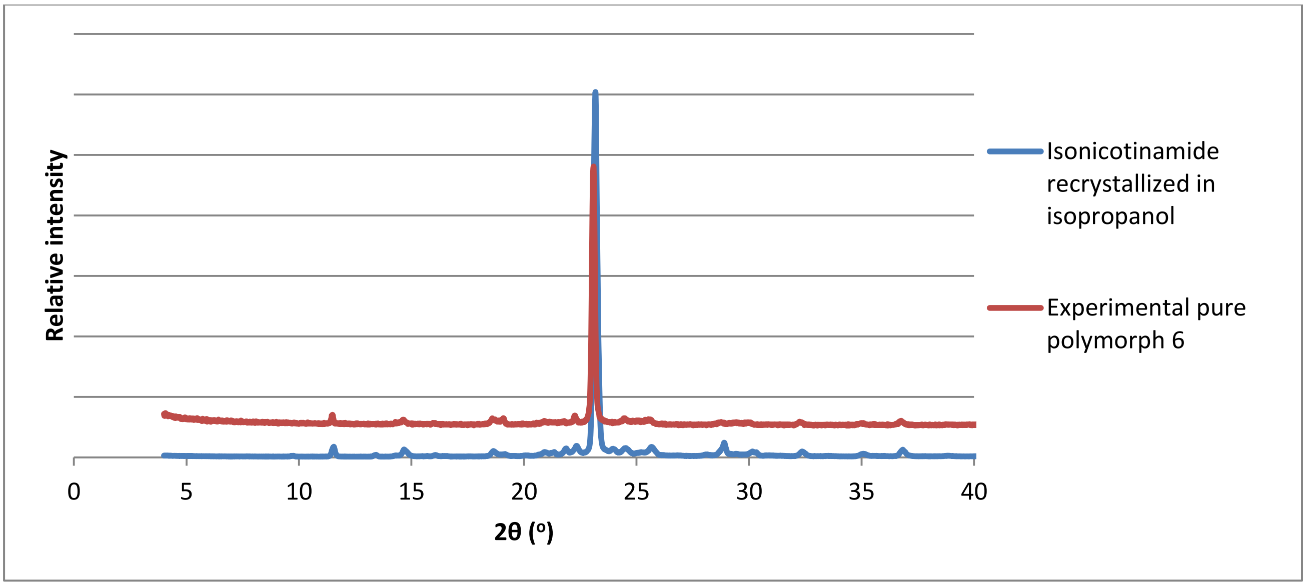

Figure 3.28a: The experimental PXRD pattern of polymorph 6 and the experimental PXRD pattern of isonicotinamide recrystallized in isopropanol.

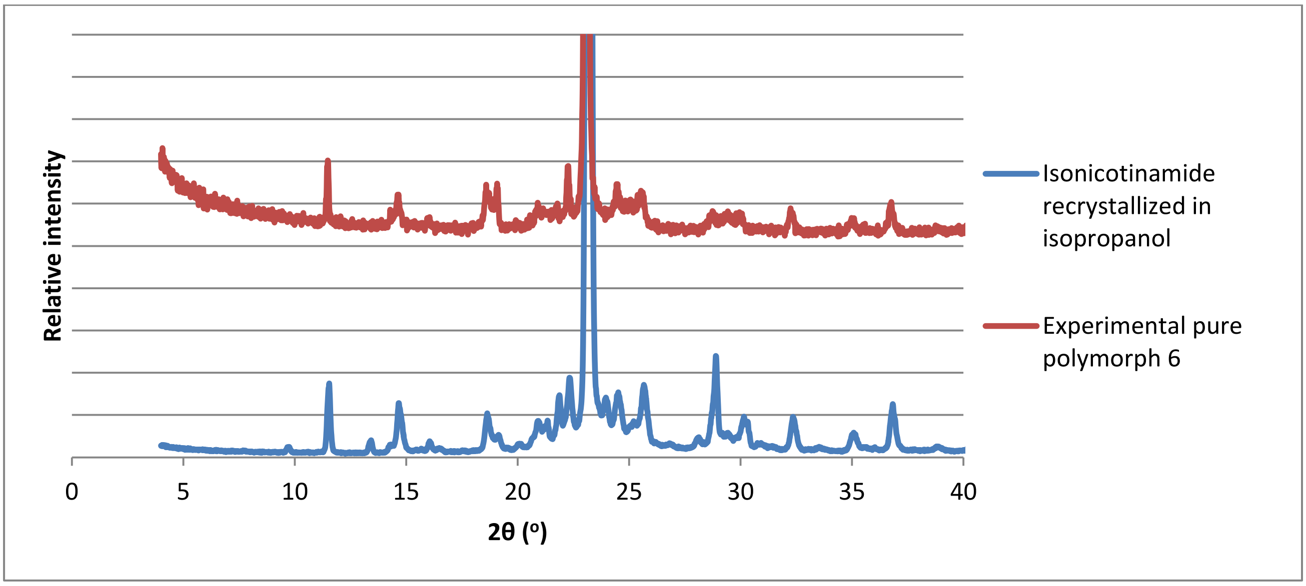

Figure 3.28b: Intensity-enhanced representations of the PXRD patterns shown in Figure 3.28a.

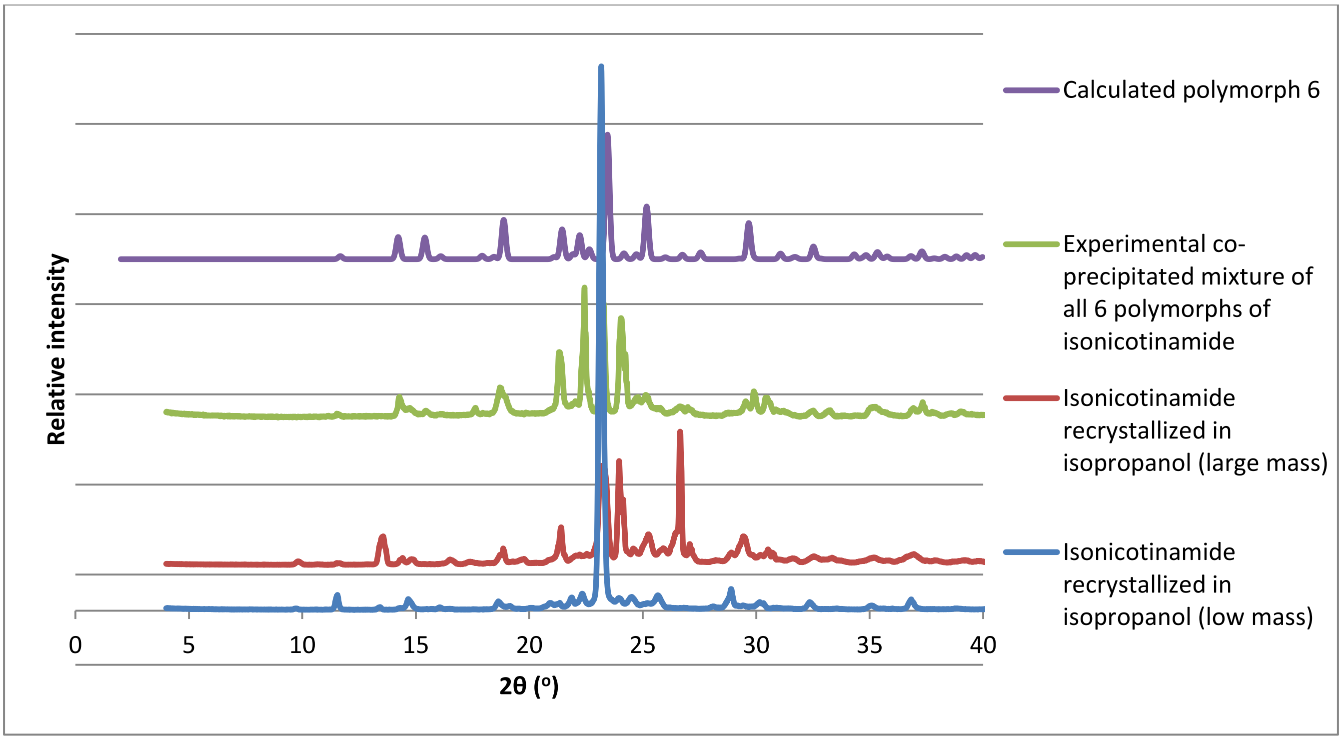

Figure 3.29: The PXRD patterns of the calculated trace for polymorph 6, the experimental co-precipitated mixture containing all 6 polymorphs, isonicotinamide recrystallized in isopropanol (*ca* 4 mg) and in isopropanol (*ca* 20 mg).

In conclusion, the SCXRD analysis reported at the beginning of section 3.2.3 successfully confirmed the presence of the new polymorph of isonicotinamide, which is polymorph 6. The space group assignment and crystal structure solution required considerable manual intervention, which reiterated the point that the routine application of crystallographic computer programs to solve crystal structures cannot always be relied on. The polymorphic comparison between polymorphs 2 and 6 indicated that there was much similarity between them; however, there were distinctive differences, particularly with regard to their molecular packing arrangements and hence their computed PXRD patterns, which confirmed their uniqueness.

3.3) Cyclodextrin inclusion with allopurinol

The experiments that entailed the synthesis of solid CD inclusion complexes with allopurinol were all unsuccessful and the results, with their methodologies and analyses, have been placed in the Appendix under section 3, pp. 15 – 19. The CDs that were analysed with allopurinol included α-CD, β-CD, γ-CD, DMB, TMB and TMA. Kneading experiments, along with a variety of co-precipitation experiments in which three solvent media were involved, were performed. These included pure water, water that contained a small measured volume of EtOH, and water that contained one drop of Tween® 80. In addition, experiments with aqueous solutions of potassium hydroxide (KOH) were attempted with β-CD and allopurinol, in order to produce a β-CD·allopurinol inclusion complex. However, this was unsuccessful as well.

3.4) Solubility experiments

Phase solubility studies were conducted as a final attempt to assess whether the solubility of allopurinol could be improved in a variety of aqueous CD solutions of varying concentration. Three CDs, namely γ-CD, HPBCD and RAMEB, were selected in order to conduct the phase solubility experiments in duplicate. The solubility value of allopurinol, that is quoted in the literature, is 0.48 mg.cm^{-3} at 25 °C,[27] and 0.569 mg.cm^{-3} at 25 °C.[28] As a result, it was of interest to obtain an experimental aqueous solubility value of allopurinol and use it as a control, which could then be compared to the values obtained from the phase solubility experiments. The experimental value of allopurinol was determined through the extrapolation from an experimental calibration curve.

The absorbance-concentration calibration curve is represented in Figure 3.30 and recorded at a λ_{max} of 250 nm.[23] The phase solubility studies were performed with UV-vis spectroscopic techniques, since allopurinol is UV-active, while the CDs are not. Therefore, the UV-vis absorbance of the solution of these components would be caused by allopurinol alone. Five absorbance readings were recorded for each solution and averaged. Consequently, a calibration curve of allopurinol was plotted, which was achieved by dissolving 0.729 mg (0.00536 mmol) of allopurinol in 25 cm^3 of

Milli-Q® water at 25 °C. Thereafter, sixteen aqueous, standard solutions of differing concentrations were prepared, where the overall volume of each was 5 cm^3.

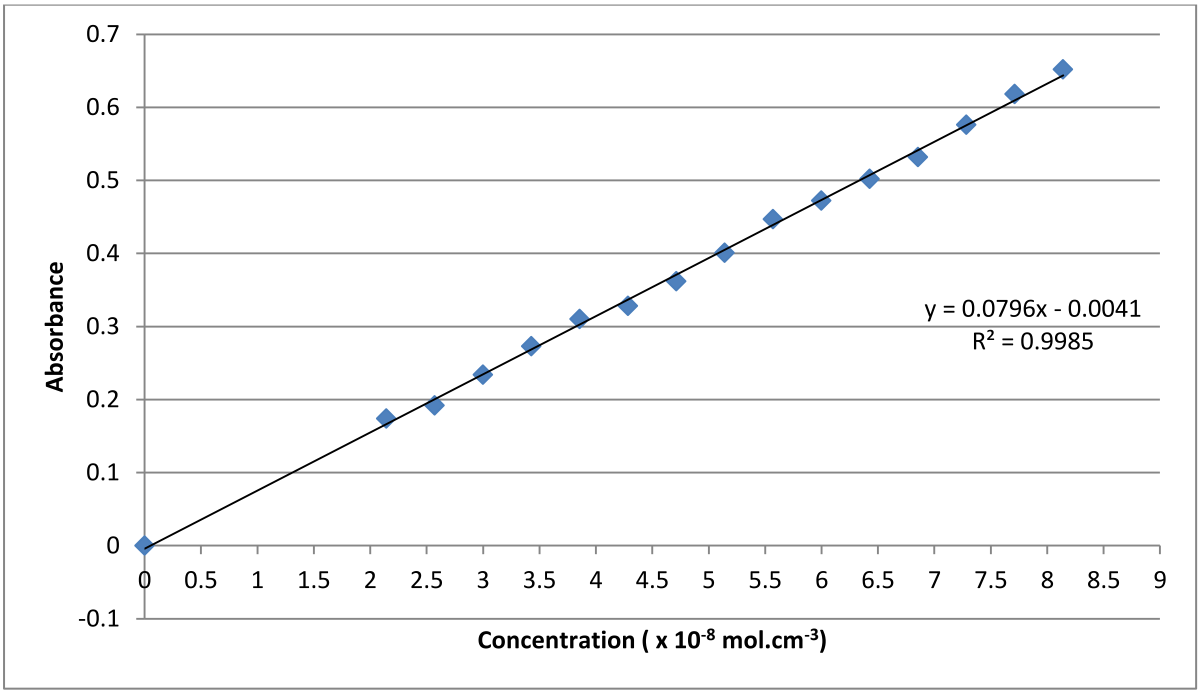

Figure 3.30: Calibration curve for allopurinol in an aqueous solution.

It was important to note that the lowest reliable absorbance at a λ_{max} of 250 nm was 0.174 at a 10 % concentration of the stock solution. Concentrations lower than this value, resulted in a λ_{max} of 245 nm (instead of 250 nm) and consequently were not included in the calibration curve. Furthermore, the y-intercept of the straight line offset the mass determinations by a negligible amount. This offset amount in the mass value was caused by an accumulation of errors that were in the un-recordable range of the equipment used to produce the calibration curve. This value amounted to a mass error of 3.5054 x 10^{-4} mg. The calculation that furnished this value is supplied in the Appendix under section 4.1, p. 20.

The aqueous solubility of allopurinol was determined by dissolving an excess amount of allopurinol in 5 cm^3 of water, the resulting suspension being stirred vigorously for 72 hours at 25 °C. The solution was filtered into a clean vial. Thereafter, 0.1 cm^3 was removed and further diluted to a ratio of 1:50 in preparation for the UV-vis analysis. The UV-vis spectrum was recorded at the λ_{max} of 250 nm and the results are reported in Table 3.9.

Table 3.9: The determination of the aqueous solubility of allopurinol.

Number	Absorbance (nm)	Corresponding diluted concentration ($\times 10^{-8}$ mol.cm^{-3})	Corresponding concentration ($\times 10^{-8}$ mol.cm^{-3})	Solubility of allopurinol (mg.cm^{-3})
1	0.627	7.928	396.420	0.540
2	0.580	7.338	366.897	0.499
3	0.589	7.451	372.550	0.507
Average	**0.624**	**7.891**	**394.535**	**0.515**

As a result, the experimental aqueous solubility of allopurinol was determined to be 0.515 ± 0.017 mg.cm^{-3} at 25 ^{o}C in comparison to the literature values, which were 0.48 mg.cm^{-3} at 25 ^{o}C,[27] and 0.569 mg.cm^{-3} at 25 ^{o}C.[28]

As mentioned previously, the phase solubility experiments were performed with γ-CD, HPBCD and RAMEB in anticipation of forming a complex in solution. Unfortunately, all the results indicated that the solubility of allopurinol was not improved, regardless of the different CDs employed and their respective varying concentrations – the solubility of allopurinol remained unaffected. A full analysis of the unsuccessful results is supplied in the Appendix under section 4.2, pp. 21 – 22.

3.5) References

1) Samy, E. M.; Hassan, M. A.; Tous, S. S.; Rhodes, C. T. *Eur. J. Pharm. Biopharm.,* **2000**, *49*, 119.
2) Jiménez, V.; Alderete, J. B.; Delgado, E. J.; Belmar, J.; Gavín, J. *Struct. Chem.,* **2006**, *17*, 217.
3) Alatas, F.; Ratih, H.; Hartyana, T.; Farhan, S. (2014, April). Pengaruh Pembentukan Ko-Kristal Alopurinol dengan Asam Benzoat atau D-Asam Tartrat terhadap Kelarutan dan Laju Disolusinya. Paper presented at the Seminar National: Ilmu Pengetahuan dan Teknologi Jenderal Achmad Yani, Cimahi. Terusan Jenderal Sudirman, Cimahi: Lembaga Penelitian dan Pengabdian Kepada Masyarakat (LPPM).
4) Kumar, A.; Rajan, S. *Cocrystal of Allopurinol: Synthesis and Preliminary Characterization using PXRD;* Lambert Academic Publishing, 2012.
5) Engel, E. R. Supramolecular Modification of Selected Antiretroviral Drugs. MSc Thesis, University of Cape Town, South Africa, 2011.
6) Sekhon, B. S. *Ars Pharmaceutica,* **2009**, *50*, 99.
7) O'Neil, M. J. (ed.). *The Merck Index - An Encyclopedia of Chemicals, Drugs, and Biologicals;* Whitehouse Station, NJ: Merck and Co., Inc.: 2006.
8) Drugbank. *Allopurinol*. <https://www.drugbank.ca/drugs/DB00437> (Accessed 8 March 2016).
9) Bruno, J.; Cole, J. C.; Edgington, P. R.; Kessler, M.; Macrae, C. F.; McCabe, P. Pearson and R. Taylor, *Acta Cryst*., **2002**, *B58*, 389.
10) Barbour, L. J. X-SEED, *A graphical interface to SHELX,* University of Missouri, Columbia, U.S.A, **1999.**
11) Etter, M. C.; MacDonald, J. C.; Bernstein, J. *Acta Cryst.,* **1990**, *46*, 256.
12) Macrae, C. F.; Bruno, I. J.; Chisholm, J. A.; Edgington, P. R.; McCabe, P.; Pidcock, E., Rodriguez-Monge, L.; Taylor, R.; van de Streek, J.; Wood, P. A. *Appl. Cryst.*, **2008**, *41*, 466.
13) Connolly, L. R. Sample Preparation and Systematic Diffractometer Errors. <http://epswww.unm.edu/media/pdf/07-Errors-Sample-Prep.pdf> (Accessed 4 March 2016).
14) XPREP, *Data Preparation and Reciprocal Space Exploration*. Version 2.0, Bruker Analytical X-ray Systems, **1999.**

15) Hahn, T. (ed.). *International Tables for Crystallography – Volume A Space-Group Symmetry;* D. Reidel Publishing Company: Dordrecht (Holland), Boston (USA), 1983.

16) Aakeröy, C. B.; Beatty, A. M.; Helfrich, B. A.; Nieuwenhuyzen, M. *Cryst. Growth Des.,* **2003**, *3,* 159.

17) Li, J.; Bourne, S. A.; Caira, M. R. *Chem. Comm.,* **2011**, *47*, 1530.

18) Eccles, K. S.; Deasy, R. E.; Fabian, L.; Braun, D. E.; Maguire, A. R.; Lawrence, S. E. *CrystEngComm,* **2011**, *13*, 6923.

19) Sheldrick, G. M. *Acta Cryst*., **2008**, *A64*, 112.

20) Spek, A. L. *Acta Cryst*., **2009**, *D65*, 148.

21) Rautaray, D.; Kumar, A.; Reddy, S.; Sainkar, S. R.; Sastry, M. *Cryst. Growth Des*., **2002**, *2,* 197.

22) Bauer, J.; Spanton, S.; Henry, R.; Quick, J.; Dziki, W.; Porter, W.; Morris, J. *Pharm. Res.,* **2001**, *18*, 859.

23) Pubchem. *Allopurinol*. <https://pubchem.ncbi.nlm.nih.gov/compound/allopurinol> (Accessed 8 March 2016).

24) Li, J. Supramolecular Modification of Selected Antitubercular Drugs. PhD Thesis, University of Cape Town, South Africa, 2010.

25) Li, N.; Shanks, R. A.; Murphy, D. M. *J. Cryst. Growth,* **2001**, *224*, 128.

26) Paratone N oil, Exxon Chemical Co., Texas, USA.

27) O'Neil, M. J. (ed.). *The Merck Index - An Encyclopedia of Chemicals, Drugs, and Biologicals;* Whitehouse Station, NJ: Merck and Co., Inc.: 2006, p. 50.

28) Yalkowsky, S. H.; He, Y.; Jain, P. *Handbook of Aqueous Solubility Data*; CRC Press: Boca Raton, London, New York, 2003, p. 137.

Chapter 4

Supramolecular Derivatisation of 6-Thioguanine

4.1) Introduction

Literature investigations, that included examining the CSD and various journal search engines, such as Scifinder, Science Direct and Google Scholar, indicated that only one article relating to the supramolecular derivatisation of 6-thioguanine, had recently been published in 2017.[1] This article was discovered after the investigation of 6-thioguanine described in this Master's dissertation had been completed. This article gave an account of the synthesis of a ternary system of 6-thioguanine with β-CD and gold nanoparticles, which improved the aqueous solubility and stability of the native drug.[1] The authors initially synthesized a 1:1 β-CD·6-thioguanine inclusion complex by dissolving the drug in water with 100 μl of ammonia. Subsequently, gold atoms were deposited onto the crystal faces of the inclusion complex in order to create the ternary system. Furthermore, molecular modelling was performed in order to study the structure of the derivatised species.[1]

Even though β-CD·6-thioguanine complex crystals had been successfully synthesized and published in the literature, the particle size was too small for a SCXRD analysis.[1] Furthermore, the author of this Master's dissertation wished to assess the possibility of synthesizing a CD complex in a pure aqueous medium. This present study intended to emulate the same investigation that was executed for allopurinol, since the chemical structure of 6-thioguanine is quite similar. This would thus allow one to assess the possibility of synthesizing new supramolecular derivatised products; however, it would also allow for a comparison to be drawn between the potential for both allopurinol and 6-thioguanine to be derivatised *via* supramolecular methods. Therefore, the various CDs that were selected included the native host compounds, namely α-CD, β-CD and γ-CD, as well as methylated CDs, which included DMB, TMB and TMA. Furthermore, it was intended that solubility investigations should be performed with three selected CDs with the expectation of enhancing the aqueous solubility of 6-thioguanine in solution. These CDs included γ-CD, HPBCD and RAMEB. In addition, co-crystallization experiments were to be performed with the same co-formers that were employed for allopurinol.

4.2) Co-crystal screening

4.2.1) Virtual co-crystal screening

The identical virtual co-crystal screening investigation that was performed for allopurinol (as described in Chapter 3.2.1, p. 28) was performed for 6-thioguanine, which resulted in the same choice of co-formers, but for different reasons. As mentioned before, the virtual co-crystal screening investigation entailed the use of the Cambridge Structural Database (CSD)[2] in order to identify the supramolecular synthons that could potentially occur with 6-thioguanine. Initially, the supramolecular synthons from the crystal packing of 6-thioguanine were assessed once the molecular structure was obtained from the CSD and viewed in X-SEED.[3] The drug molecule formed a dual eight-membered ring dimer of type $R_2^2(8)$ (as designated with graph set notation),[4] as well as a discrete synthon (Figure 4.1). This differed from the situation in crystalline allopurinol, which formed two ring synthons, where one of them was dimeric and the other trimeric. The hydrogen bond lengths, along with their corresponding bond angles are displayed in Figure 4.1.

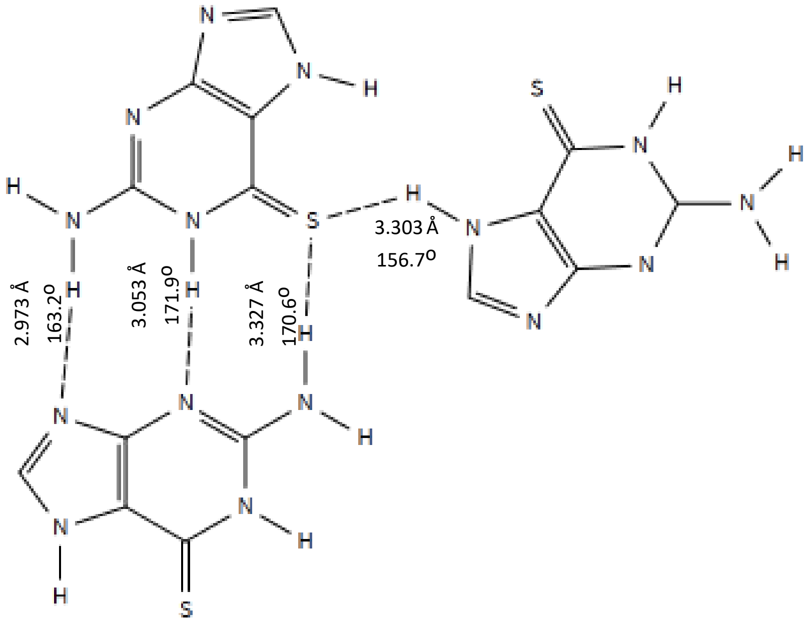

Figure 4.1: The hydrogen bonded motif in the crystal of 6-thioguanine, which displays the formation of the two dual eight-membered ring synthons and a discrete synthon.

A virtual co-crystal screening, very similar to that designed for allopurinol, was conducted for 6-thioguanine. This study likewise involved only analysing the potential to form stable hydrogen bonded ring synthons between the API and other molecules. There are several tautomeric forms of 6-thioguanine to take into account (Figure 4.2), and the potential sites that could form hydrogen bonded ring synthons with the molecule have been circled in red (Figure 4.3).

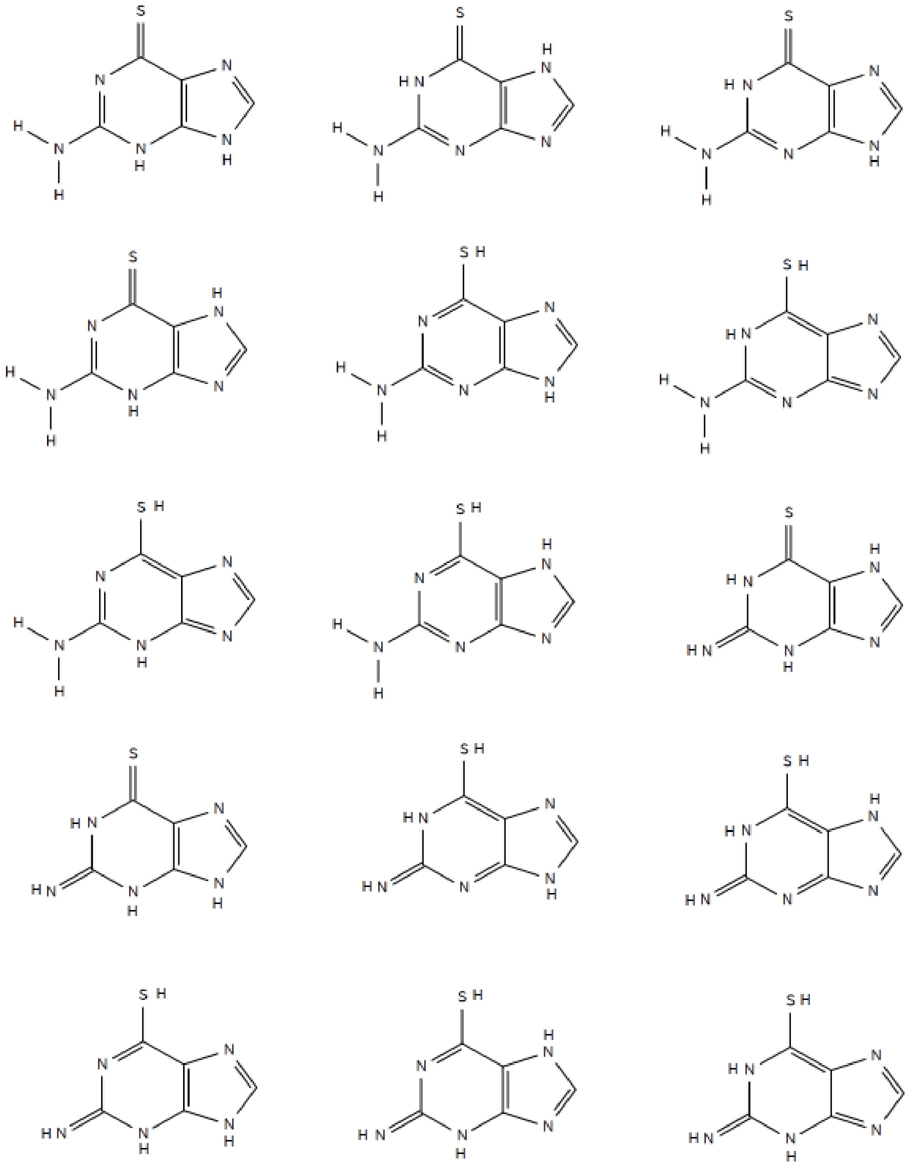

Figure 4.2: The tautomers of 6-thioguanine.

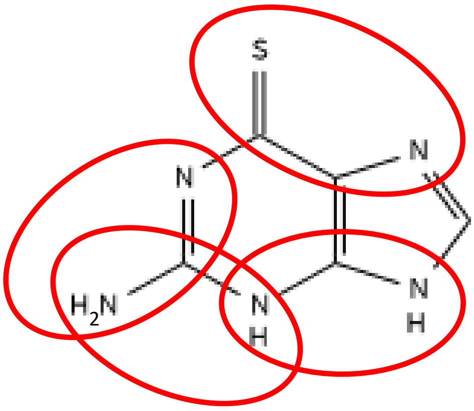

Figure 4.3: The potential hydrogen bonding sites (circled in red).

Similarly to the study with allopurinol, Figure 4.4 displays the selected molecular fragments of 6-thioguanine, which accounted for all the possible tautomers of the molecule. The atoms that are denoted as X in these molecular fragments, accounted for any atom, and the bond orders in C-X (2a-2d) and C-N (3a-3c) were unrestricted in order to account for the multiple tautomers of the molecule (Figure 4.4).

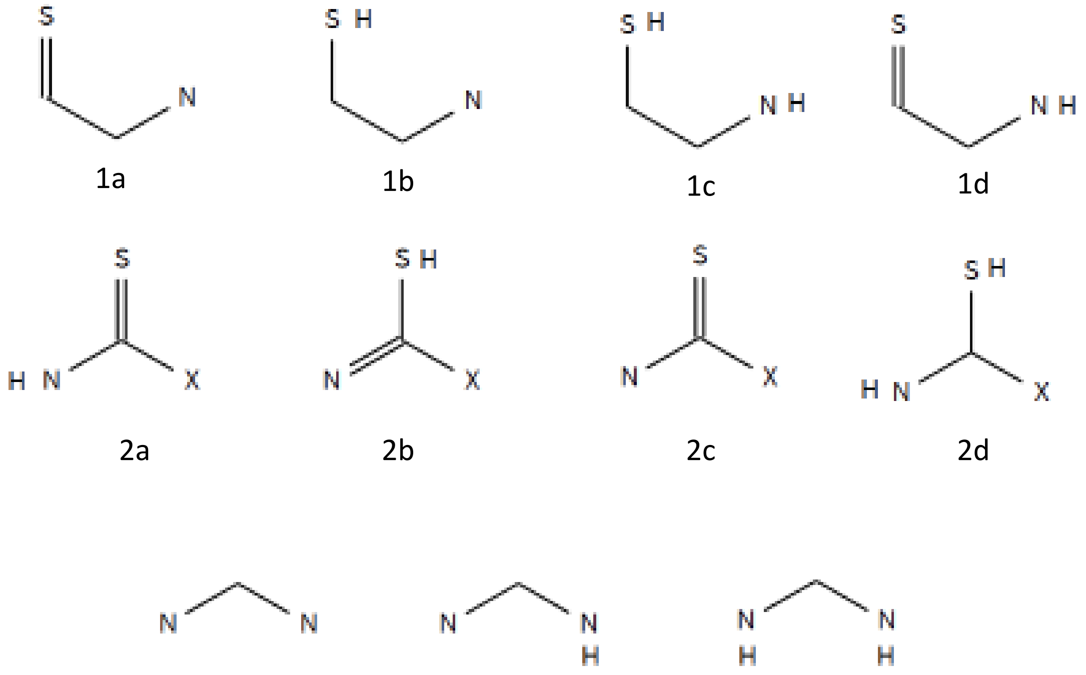
1a 1b 1c 1d

2a 2b 2c 2d

3a 3b 3c

Figure 4.4: The various molecular fragments which accounted for the possible tautomers of 6-thioguanine. Atom X represents any atom, while the bond orders in C-X (2a-2d) and C-N (3a-3c) were unrestricted.

As with allopurinol , the carboxylic acid and amide co-former functional groups were separately assessed for their potential to form stable ring synthons with each of the molecular fragments of 6-thioguanine. (This procedure is fully outlined in the same study that was performed with allopurinol in Chapter 3, under section 3.2.1, p. 31). These results indicated a more equal frequency of both the amide and carboxylic acid functional groups forming such hydrogen bonded ring synthons. However, the only fragments that yielded results were 2a, 3b and 3c. Figure 4.5 displays an example of the formation of a hydrogen bonded ring synthon between the molecular fragment 3b of 6-thioguanine and the carboxylic acid functional group.

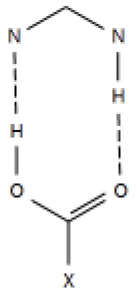

Figure 4.5: The most frequently occurring hydrogen bonded ring synthon, which involved the molecular fragment 3b and a carboxylic acid. The atom X represents any atom and the bonds in the N-C-N fragment were also denoted as 'any'.

As a result, it was justified to employ the same co-formers that were chosen for the co-crystallization with allopurinol. Even though allopurinol and 6-thioguanine are different molecules, there is a level of similarity between the two and it was of interest to compare the results of both attempted co-crystallization experiments. The list of selected co-formers is supplied in Table 4.1.

Table 4.1: The co-formers selected for co-crystallization screening experiments with 6-thioguanine.

Number	**Selected co-former**
1	Benzamide
2	Benzoic acid
3	Fumaric acid
4	Glutaric acid
5	Isonicotinamide
6	Maleic acid
7	Nicotinamide
8	Piperazine
9	Propionamide
10	D-Tartaric acid
11	Urea

4.2.2) Experimental co-crystal screening

An assortment of co-grinding and co-precipitation experiments was performed with 6-thioguanine and the eleven selected co-formers, with the intention of producing new multi-component products. The co-grinding experiments included dry co-grinding of the API and a respective co-former and LAG with EtOH as the solvent. In addition, a set of co-precipitation experiments was performed with the solvent DMSO, as 6-thioguanine appeared to be soluble only in DMSO. However, all the results indicated that no new material was formed. Therefore, the detailed methodology and discussion of these results have been placed in the Appendix under section 5, pp. 23 – 26. An example of a PXRD pattern that displayed a physical mixture of 6-thioguanine and D-tartaric acid following their attempted co-crystallization is illustrated in Figure 4.6.

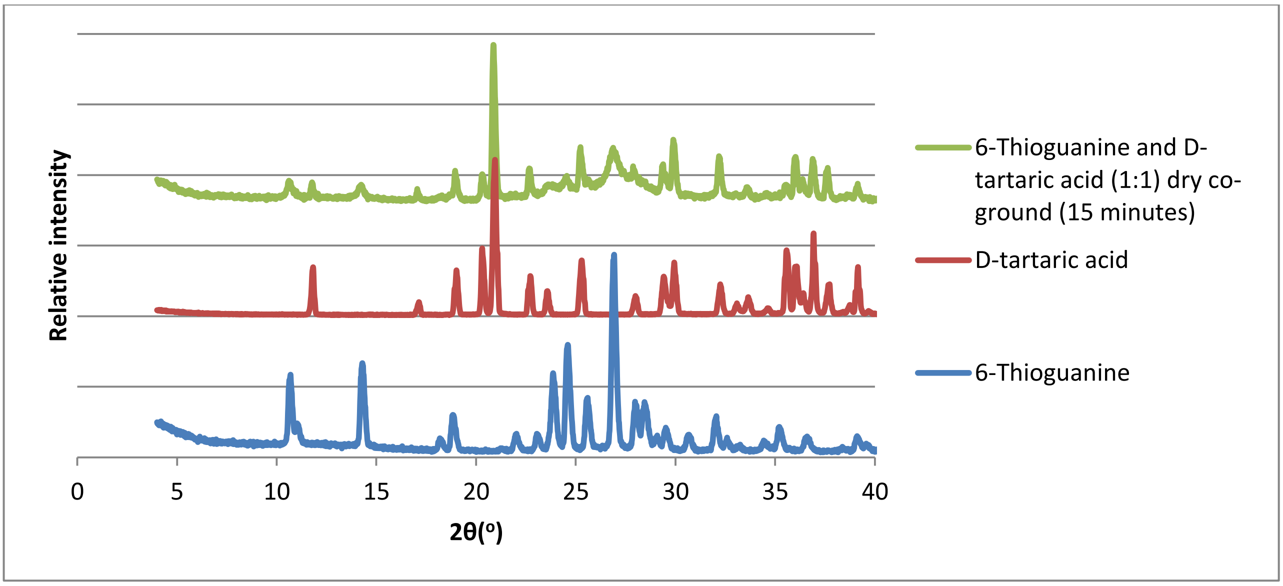

Figure 4.6: PXRD patterns of 6-thioguanine, D-tartaric acid, and the product obtained by dry co-grinding the two components in an equimolar ratio for 15 minutes.

4.3) Cyclodextrin inclusion

The CD inclusion experiments that were performed with 6-thioguanine replicated the methodologies of the CD inclusion experiments with allopurinol. The native and methylated CDs selected for interaction with 6-thioguanine included α-CD, β-CD, γ-CD, DMB, TMB and TMA. Kneading experiments, along with a variety of co-precipitation experiments, were also performed. Three different solvent media were also selected during the co-precipitation experiments. These included pure water, water containing a small measured volume of EtOH, and water that contained one drop of Tween® 80. Unfortunately, the results were also unsuccessful as no new material was synthesized. In addition, further experiments with β-CD as the host and 6-thioguanine as the potential guest were performed where the pH of the aqueous medium was varied with the addition of KOH; however, these experiments also yielded unsuccessful results. Consequently, all of these results, with their respective methodologies and detailed discussions, have been supplied in the Appendix under section 6 (pp. 27 – 30). The lack of affinity of 6-thioguanine for CDs is possibly attributed to its extreme hydrophobicity and its high melting point (> 360 °C).[5-6]

4.4) Solubility experiments

Phase solubility studies were conducted in an attempt to assess whether the aqueous solubility of 6-thioguanine could be improved in a variety of CD solutions of differing concentrations. These sets of experiments mirrored those that were performed with allopurinol, with the same three CDs (viz. γ-CD, HPBCD and RAMEB) being used. Furthermore, the aqueous solubility of 6-thioguanine quoted in the literature is vague, being described as *"less than 1 mg.cm^{-3}"* at 22.5 °C.[7] It was therefore desirable to obtain a more definitive solubility value from a spectrophotometric calibration curve during the course of the phase solubility study.

The absorbance-concentration calibration curve, recorded at a λ_{max} value of 340 nm,[7] is represented in Figure 4.7. Phase solubility studies performed with UV-vis spectroscopic techniques were possible, as 6-thioguanine is UV-vis active, while the selected CDs are not. Therefore, the UV-vis absorbance of CD/6-thioguanine complex solutions would be due to the 6-thioguanine alone. Five absorbance readings were recorded for each solution and averaged, and a calibration curve of 6-thioguanine was plotted. This was achieved by dissolving 1.166 mg (0.00697 mmol) of 6-thioguanine in 20 cm^3 of Milli-Q® water at 25 °C and preparing fourteen aqueous standard solutions of differing concentrations, where the final volume of each, after dilution, was 5 cm^3.

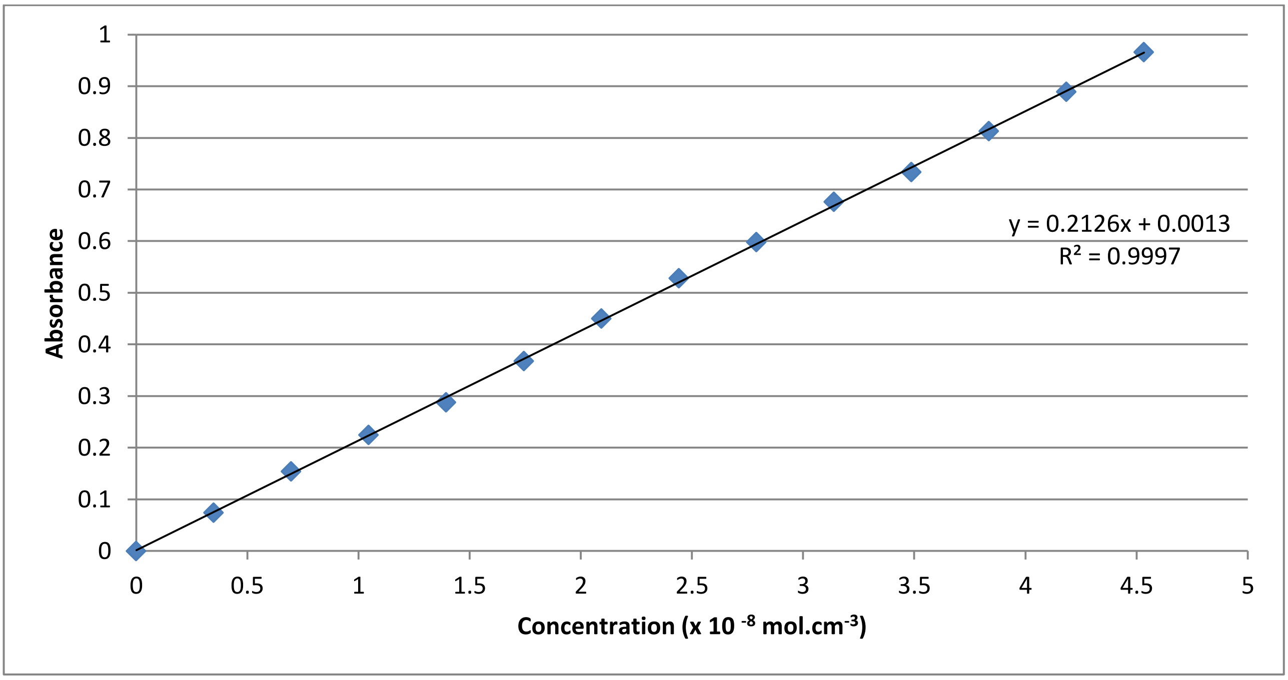

Figure 4.7: Calibration curve for 6-thioguanine in an aqueous solution.

This calibration curve had a miniscule y-intercept, which indicated that the mass determinations were also offset by a negligible amount. As described for allopurinol, this mass offset value was caused by an accumulation of errors that were in the un-recordable range of the equipment used to formulate the calibration curve. This value amounted to a negligible mass error of 5.1117×10^{-5} mg. The full calculation can be viewed in the Appendix under section 7.1, p. 31.

The aqueous solubility of 6-thioguanine was assessed by dissolving an excess amount of 6-thioguanine in 5 cm^3 of water and stirring the suspension vigorously for 72 hours at 25 ^oC. The solution was filtered into a clean vial and 0.1 cm^3 was removed and further diluted to a ratio of 1:50 in preparation for the UV-vis analysis. The UV-vis spectrum was recorded at the λ_{max} value of 340 nm and the results of the experiment repeated in triplicate are reported in Table 4.2.

Table 4.2: The determination of the aqueous solubility of 6-thioguanine

Number	Absorbance (nm)	Corresponding diluted concentration ($\times 10^{-8}$ $mol.cm^{-3}$)	Corresponding concentration ($\times 10^{-8}$ $mol.cm^{-3}$)	Solubility of 6-thioguanine ($mg.cm^{-3}$)
1	0.209	0.977	48.848	0.082
2	0.194	0.906	45.320	0.076
3	0.191	0.892	44.614	0.075
Average	**0.198**	**0.925**	**46.261**	**0.078**

As a result, the experimental aqueous solubility of 6-thioguanine was determined to be 0.078 ± 0.003 $mg.cm^{-3}$ at 25 ^oC in comparison to the literature value of “less than 1 $mg.cm^{-3}$” at 22.5 ^oC.[6-7]

As mentioned above, the phase solubility experiments were performed with γ-CD, HPBCD and RAMEB with the expectation of forming the respective CD complexes in solution. Unfortunately, all the results indicated that the aqueous solubility of 6-thioguanine had not been improved, regardless of the different CDs used and their respective varying concentrations. A full analysis and discussion of these results is supplied in the Appendix under section 7.2, pp. 32 – 33.

In conclusion, it was not possible to form any supramolecular products with 6-thioguanine in spite of the multiple potential H-bonding sites on the molecule. The virtual co-crystal screening analysis had indicated that it was possible in principle to form amide and carboxylic acid ring synthons, but the chemical and physical properties, such as the high melting point and very low aqueous solubility of the drug, evidently hindered this formation.

4.5) References

1) Sierpe, R.; Noyong, M.; Simon, U.; Aguayo, D.; Huerta, J.; Kogan, M. J.; Yutronic, N. *Carbohyd. Polym.,* **2017**, *177*, 22.
2) Bruno, J.; Cole, J. C.; Edgington, P. R.; Kessler, M.; Macrae, C. F.; McCabe, P. Pearson and R. Taylor, *Acta Cryst*., **2002**, *B58*, 389.
3) Barbour, L. J. X-SEED, *A graphical interface to SHELX,* University of Missouri, Columbia, U.S.A, **1999.**
4) Etter, M. C.; MacDonald, J. C.; Bernstein, J. *Acta Cryst.,* **1990**, *46*, 256.
5) Drugbank. *Tioguanine.* <https://www.drugbank.ca/drugs/DB00352> (Accessed 12 March 2016).
6) O'Neil, M. J. (ed.). *The Merck Index - An Encyclopedia of Chemicals, Drugs, and Biologicals;* Whitehouse Station, NJ: Merck and Co., Inc.: 2006, p. 9342.
7) Pub Chem. *6-Thioguanine*. <https://pubchem.ncbi.nlm.nih.gov/compound/6-Thioguanine> (Accessed 12 March 2017).

Chapter 5

Supramolecular Derivatisation of Valproic Acid

5.1) Introduction

The literature investigation for valproic acid indicated that no attempts to synthesise co-crystals of this API have been conducted to date. However, two cyclodextrin (CD) inclusion complexes of valproic acid were synthesised *via* a freeze-drying method and characterised in 2004.[1] The two complexes were hydroxypropyl-β-CD·valproic acid and sulfobutylether-β-CD·valproic acid, both with a 1:1 host-guest stoichiometry. The hydroxypropyl-β-CD·valproic acid inclusion complex displayed a 27-fold increase in the solubility of valproic acid, whereas the sulfobutylether-β-CD·valproic acid inclusion complex yielded less satisfactory results and did not produce a significant solubility increase.[1]

As a result, the author of this dissertation intended to synthesize co-crystals of valproic acid, as well as further investigate potential CD complexation with a variety of crystalline CD compounds and with a methodology that could potentially provide single crystals of the desired multi-component products for X-ray analysis.

5.2) Co-crystal screening

5.2.1) Virtual co-crystal screening

The CSD[2] contained no reported results for co-crystal or salt structures involving the title compound. As a result, it was not possible to investigate any hydrogen-bonded ring supramolecular synthons with the drug. However, since the structure of valproic acid is simple (there are no tautomers and the only functional group is a carboxylic acid), the drug can only form stable ring synthons with either another carboxylic acid functional group or an amide functional group. Consequently, a very general virtual co-crystal screening investigation was conducted using data from the CSD. This involved noting the frequency for the formation of ring synthons between two carboxylic acid functional groups as well as between a carboxylic acid and an amide functional group (Figure 5.1). The hydrogen bond distances between the two oxygen atoms and between the oxygen and nitrogen atoms were pre-set to have a distance range of 2.5 – 3.2 Å. The results indicated that there was a higher frequency for the formation of a hydrogen bonded ring synthon between two carboxylic acid functional groups than between a carboxylic acid and amide functional group. Nevertheless, the selected 12 co-formers comprised mainly carboxylic acids, along with amides, whose names are presented in Table 5.1.

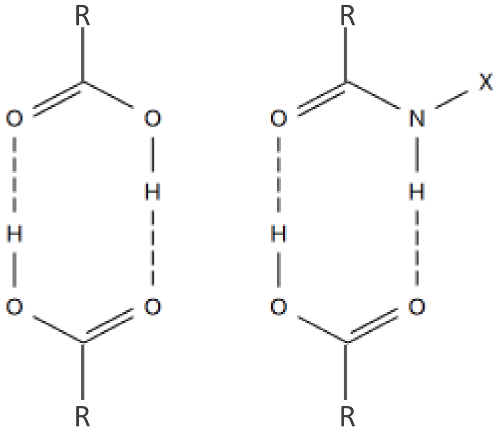

Figure 5.1: Hydrogen bonded ring synthons between two carboxylic acid functional groups (left) and between a carboxylic acid and an amide functional group (right). The symbol X represents any atom.

Table 5.1: The selected co-formers for co-crystallization screening experiments with valproic acid.

Number	**Co-former**
1	Adipic acid
2	Citric acid
3	Glutaric acid
4	Isonicotinamide
5	Maleic acid
6	Malic acid
7	Nicotinamide
8	Pimelic acid
9	Piperazine
10	Propionamide
11	Pyroglutamic acid
12	D-tartaric acid

5.2.2) Co-precipitation

The focus of the valproic acid investigation in this Master's dissertation was primarily around the successful cyclodextrin (CD) inclusion complexation results. Therefore, the co-crystal screening experiments were few and incomplete since there was a limited supply of valproic acid. As a result, only one set of co-precipitation experiments was conducted with valproic acid (a liquid at ambient temperature), and no co-grinding experiments were performed. The co-precipitation experiments followed the method for slow evaporation as outlined in the Experimental Methods (Chapter 2) under section 2.2.4, pp. 18 – 19. These experiments were performed in an ethanol medium with the API and co-former present in an equimolar ratio. Five mg (0.03647 mmol; 5.434 μl) of valproic acid was used for each experiment. After approximately two weeks, these solutions concentrated into an oil, after which it took a further two months for either single crystals or a powdery residue to precipitate. The results were all the same for the individual experiments, namely that only the co-former had crystallized; however, more detail is supplied in the Appendix under section 8 (pp. 34 – 35).

5.3) Cyclodextrin inclusion

5.3.1) Native cyclodextrin inclusion complexes

The native CDs, which include α-CD, β-CD and γ-CD, formed authentic inclusion complexes with valproic acid. These complexes will be referred to as α-CD·VAL, β-CD·VAL and γ-CD·VAL. Furthermore, the β-CD·VAL and γ-CD·VAL complexes produced adequate single crystals for SCXRD analyses and structural characterisation. Each inclusion complex is described in detail below.

5.3.1.1) The α-CD·VAL inclusion complex

Method of preparation

Preliminary preparation of the complex was based on a 1:1 stoichiometric ratio of α-CD and valproic acid. However, when crystals of the inclusion complex were subsequently analysed by ^{1}H NMR spectroscopy (details below), they were found to have a 2:1 host-guest composition. Thus, the final method of reproducible preparation of the complex involved the latter ratio, as follows. A mass of 67.46 mg (0.06934 mmol) of α-CD was dissolved in 0.5 cm^3 of water and the suspension was heated to 70 ^{o}C while being stirred vigorously. Once the α-CD was fully dissolved, 5 mg (0.03467 mmol; 5.434 μl) of valproic acid was added dropwise to the vial containing the aqueous α-CD solution. The valproic acid was added in minimal excess in order to ensure that all the α-CD had reacted. The resultant solution was stirred at 70 ^{o}C for 2 hours. Initially, when the valproic acid was added to the α-CD aqueous solution, it formed an oily immiscible layer on top of the aqueous surface. Within approximately twenty seconds, this oily layer had dissolved and the complex precipitated in the aqueous solution. Subsequently, the addition of a further 0.2 cm^3 of water to the solution was necessary in order to allow the complex to fully dissolve at 70 ^{o}C. The solution was finally filtered and prepared for slow cooling. The crystals appeared after three days.

Crystal morphology

The resultant α-CD·VAL inclusion complex formed white, very fine, fibrous, whisker clusters, which readily trapped the mother liquor (Figure 5.2). Owing to the nature of the crystal size and morphology, a SCXRD analysis could not be performed; however, recrystallization from different solvents was executed in order to attempt to produce larger single crystals. Furthermore, the remaining characterisation could still be accomplished in spite of the adverse morphology and small crystallite size.

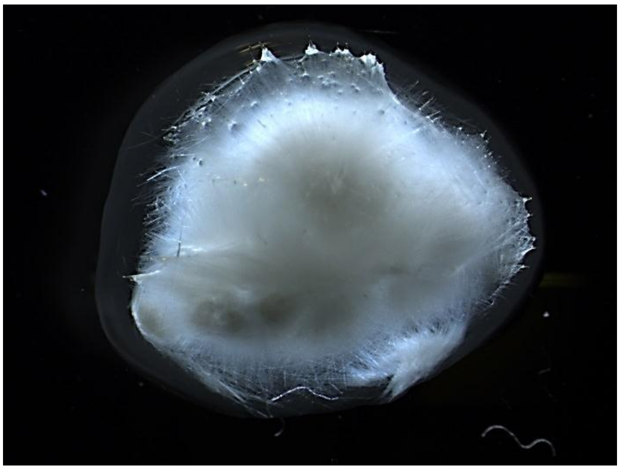

Figure 5.2: The morphology of the α-CD·VAL inclusion complex.

Attempts to obtain single crystal crystals of the α-CD·VAL complex *via* recrystallization

Valproic acid appeared to have a strong affinity for the hydrophobic cavity of the α-CD molecule and thus readily displaced the water molecules from the cavity. This process was apparently very energy-favoured as the complex formed within 20 seconds. This rapid crystallization is what most likely gave rise to the poor crystalline quality. Consequently, a number of recrystallization attempts were performed, which included the use of water and a variety of organic solvents. Normally, it is not possible to use organic solvents in recrystallization experiments with CD inclusion complexes, as not only are most of them insoluble in organic solvents,[3] but organic solvents also have a strong affinity for the hydrophobic cavity of the CD molecule, and thus the guest molecule may be displaced.[4] However, with regard to the particular case of α-CD·VAL, there is a chance that the energy state of this inclusion complex could be lower than the resultant energy states of α-CD with various included organic solvents. Thus, the organic solvents that dissolve α-CD, listed in increasing order of solubility, are propylene glycol, dimethyl sulfoxide (DMSO), pyridine, ethylene glycol and dimethylformamide (DMF).[3] Propylene glycol was not used owing to its unavailability in the laboratory, and DMF was also not used due to the fact that α-CD is extremely soluble in it and thus it would take too long for single crystals to potentially form. In addition, DMF is also often used specifically to displace guest molecules from the CD cavity. The results from these recrystallization experiments in the four solvents (namely water, DMSO, ethylene glycol, pyridine), all had identical outcomes which were the same fine, fibrous, whisker clusters of crystals that were originally obtained. Unfortunately, achieving an improved crystalline morphology and larger crystallite size using these solvents was unsuccessful.

^{1}H NMR analysis of α-CD·VAL

The ^{1}H NMR solution-state spectral analysis of the α-CD·VAL inclusion complex, produced by co-precipitation, indicated a 2:1 stoichiometry of α-CD to valproic acid. This experiment was performed at 298 K and with the complex crystals dissolved in DMSO-d_6. The results are listed in Table 5.2 below, while the original ^{1}H NMR spectrum can be viewed in the Appendix under section 9.1.1, p. 36.

Table 5.2: The ^{1}H NMR spectral analysis of α-CD·VAL.

Assignment	δ (ppm)	Integration	Proton representation (per molecule)	Stoichiometric ratio	Stoichiometric ratio (integer)
2 x C$\underline{H}_3$ (valproic acid)	0.85-0.88	1.00*	6H	1.00	1
4 x C$\underline{H}_2$ (valproic acid)	1.19-1.52	1.29	8H	1.03	1
O$\underline{H}$-6 (α-CD)	4.46-4.49	2.23	6H	2.23	2
C$\underline{H}$-1 (α-CD)	4.80-4.81	2.20	6H	2.20	2

*reference integral

Fourier Transform Infrared (FT-IR) spectroscopic analysis of α-CD·VAL

The α-CD·VAL inclusion complex was also confirmed by a FT-IR analysis. A common portion of the FT-IR spectra of three species is shown in Figure 5.3, which highlights the region of importance for the confirmation of the identity of this inclusion complex. The full FT-IR spectra of the α-CD·VAL inclusion complex, α-CD and valproic acid can be viewed in the Appendix under section 9.1.2, p. 37. The comparison of the FT-IR spectra indicated the effect that complexation had on the carbonyl stretching frequency of the guest molecule, namely valproic acid. The FT-IR spectrum of the α-CD·VAL inclusion complex followed a very similar trace in comparison to the FT-IR spectrum of α-CD. This was partly as a result of a low mass ratio of the guest molecule in comparison to the host molecule.[5] The C=O stretching frequency of valproic acid occurred at 1702 cm^{-1}. However, for the α-CD·VAL inclusion complex, the C=O stretching frequency of valproic acid was displaced to a higher value, measured at 1741 cm^{-1}. This indicated that the extent of hydrogen bonding between the host molecule and the C=O group of valproic acid was less in the complex than the extent of the intermolecular hydrogen bonding within pure valproic acid.[6]

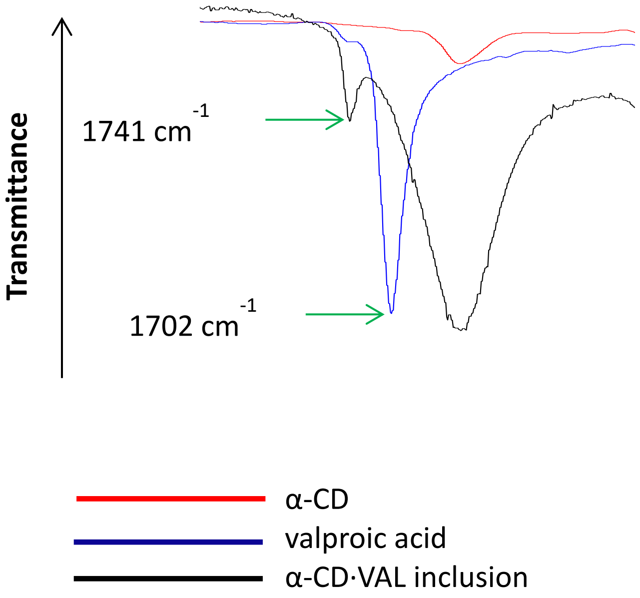

Figure 5.3: A portion of the FT-IR spectra of α-CD (red), valproic acid (blue) and α-CD·VAL (black).

Powder X-ray Diffraction (PXRD) analysis of α-CD·VAL

It is evident that the α-CD·VAL inclusion complex synthesized *via* co-precipitation corresponded to the α-CD·VAL inclusion complex produced by kneading, as depicted in Figure 5.4. The complex could be successfully formed by kneading α-CD and valproic acid in a 2:1 stoichiometry, with a small amount of water, for 30 minutes (Figure 5.4). In addition, the PXRD patterns for the α-CD·VAL inclusion complexes (prepared by kneading and co-precipitation) appeared to correlate with an isostructural PXRD pattern for another α-CD inclusion complex that crystallized in the space group P1 (Figure 5.4).[2,7] The isostructural complex is α-cyclodextrin hemikis(2,2'-azodipyridine) hydrate clathrate (refcode QACCII) and it was the only α-CD inclusion complex that crystallized in P1 with the unit cell parameters of a = 13.699(1), b = 13.970(1), c = 15.772(1) Å, α = 93.18(<1)^{o}, β = 91.94(<1)^{o}, γ = 118.72(<1)^{o}.[2] The PXRD correlation of QACCII with α-CD·VAL is only approximate, as some of the peaks do coincide (for example at the 2θ-positions 6.0^{o} and 19.5^{o}. Furthermore, the overall profile of these PXRD patterns is very similar. However, since the guest molecule in QACCII is different, this may have resulted in the observed differences. As a result, provided this assumption is correct, α-CD·VAL (produced by kneading and co-precipitation) should have similar unit cell parameters to QACCII.[7]

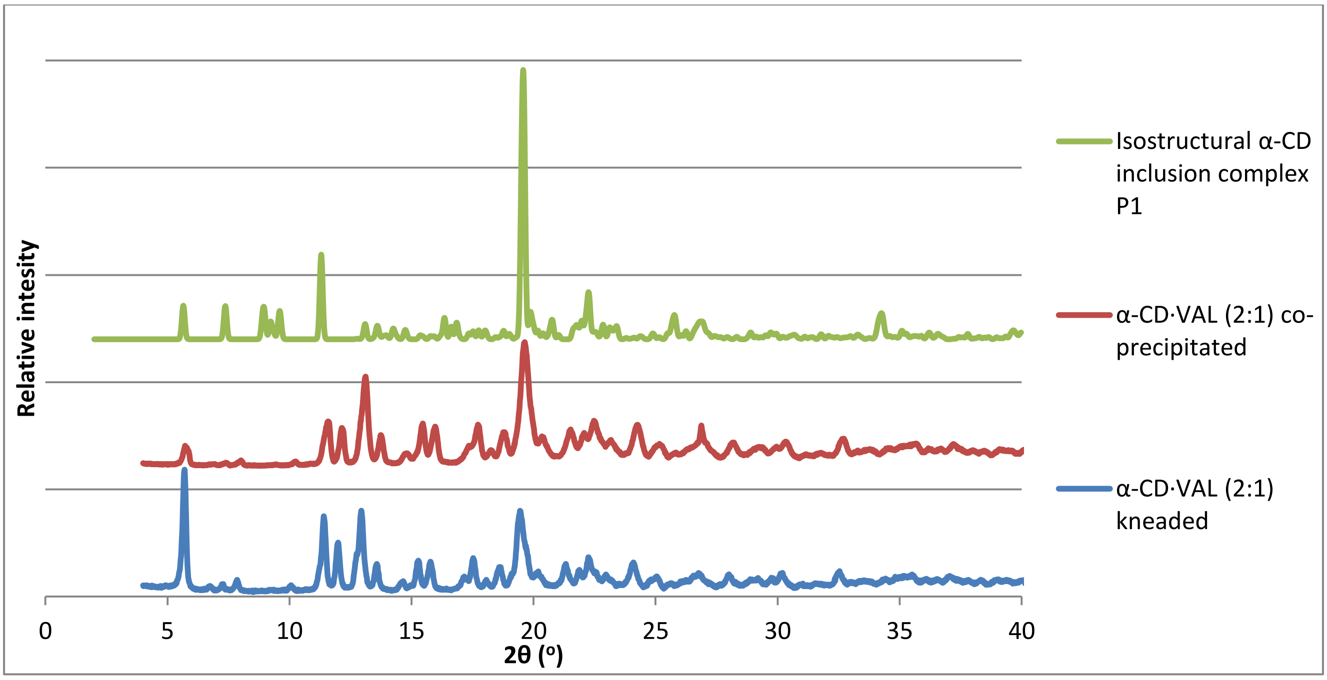

Figure 5.4: The PXRD patterns of an isostructural α-CD inclusion complex that crystallizes in P1, as well as α-CD·VAL produced *via* co-precipitation (2:1) and kneading (2:1).[7]

Hot Stage Microscopy (HSM) analysis of α-CD·VAL

The HSM analysis provided visual evidence for the thermal events that took place when the α-CD·VAL inclusion complex was heated at a constant rate of 10 K.min^{-1} while immersed in silicone oil. The series of micrographs displayed below in Figure 5.5 (representing the thermal progression of the inclusion complex) indicates dehydration, the loss of crystallinity and the decomposition of the crystal. The initial photograph, Image 1, represents the original appearance of the crystal at 28.4 °C. Image 2 indicates the first sign of dehydration at 58.0 °C, which reached a peak at 86.7 °C, as represented in Image 3. However, at 98.4 °C (Image 4) the onset of opacity commenced and the bubbling slowed down until it completely stopped at 180.0 °C, as depicted in Image 5. The bubbling was caused by the dehydration of the crystal; however, owing to the fibrous morphology of the crystal, a significant amount of surface water would have been trapped in between the crystal fibres. Consequently, it is difficult to conclude at which temperature the surface water stopped evolving and when only water from the crystal structure was being lost. However, it can be inferred that the water from the crystal structure was only released at a higher temperature, since it was hydrogen bonded in the crystal structure, and that possibly when the onset of opacity commenced, this water began to evolve. The onset of opacity was caused by the loss of crystallinity, which can result from the loss of water from the crystal structure. Subsequently, the onset of decomposition commenced at 293.8 °C, as depicted in Image 6. The bubble that appears in that image remained from the loss of water. Decomposition bubbles evolved rapidly at 320.1 °C (Image 7) along with the expansion of the bubbles that were already present. Lastly, Image 8 depicts the total decomposition of the crystal with the absence of bubbling at 372.0 °C. Even though it appeared that the bubbling was continuing, these bubbles became frozen by a glassing effect of the silicone oil.

Figure 5.5: A series of micrographs from the HSM analysis of α-CD·VAL.

Image 1: The initial appearance of α-CD·VAL at 28.4 °C.

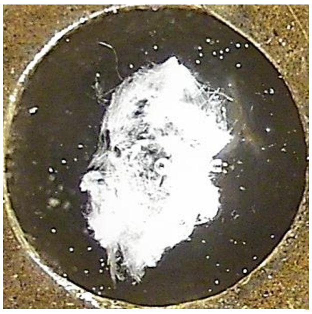

Image 2: The onset of bubbling occurred at 58.0 °C.

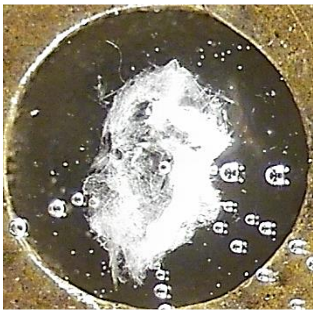

Image 3: The bubbling reached a peak at 86.7 °C.

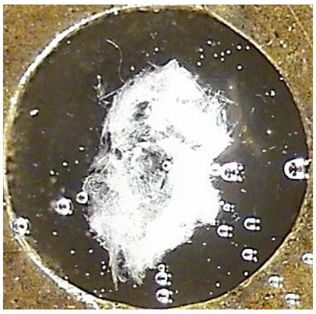

Image 4: The onset of opacity commenced at 98.4 °C. In addition, the bubbling continued.

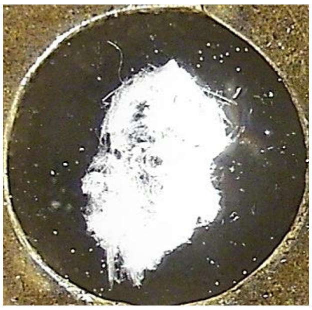

Image 5: The bubbling completely stopped at 180.0 °C. In addition, the crystal became completely opaque.

Image 6: The onset of decomposition occurred at 293.8 °C.

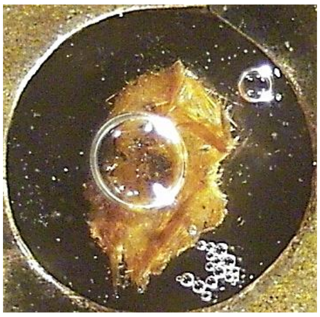

Image 7: Vigorous, small, decomposition bubbles erupted at 320.1 °C.

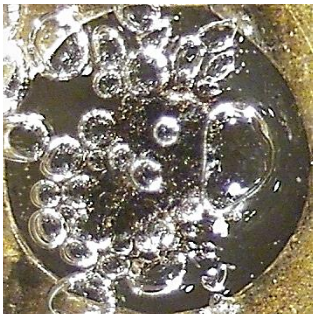

Image 8: The crystal was fully decomposed at 372.0 °C. (The bubbling stopped).

Thermal Gravimetric Analysis (TGA) of α-CD·VAL

The TGA trace signified two distinctive mass losses for the α-CD·VAL inclusion complex which occurred over the temperature range 25.0 – 400.0 °C, as depicted in Figure 5.6. A mass loss of 10.4 ± 0.3 % is associated with the first thermal event which took place between 25.0 and 128.9 °C. This was attributed to the loss of water molecules from the hydrated α-CD·VAL inclusion complex. The loss of water molecules over this temperature range was confirmed by the HSM analysis, where at 86.7 °C the bubbling had reached its peak and then began to slow down.

The second thermal event took place between 271.7 °C and 369.6 °C and it was associated with a mass loss of 77.8 % for the decomposition of the anhydrous α-CD·VAL inclusion complex. In comparison to the HSM results, the loss of water occurred between 58.0 °C and 180.0 °C, while the decomposition process occurred between 293.8 and 372.0 °C. This indicated that the results did not correlate closely. This difference could possibly be due to the different conditions under which the sample is confined in the two sets of apparatus.

Furthermore, the TGA analysis allowed the number of water molecules per CD molecule in the complex to be calculated. A 10.4 ± 0.3 % (n = 2) mass loss of water for this inclusion complex is equivalent to 6.7 ± 0.2 water molecules. This calculation can be viewed in the Appendix under section 9.1.3, p. 37.

The TGA trace also indicated that the mass loss of the inclusion complex started immediately and it was fairly significant. Owing to the fibrous nature of the crystalline morphology, there would be a tendency for surface water to become trapped in between the fibrous needles. As a result, the immediate mass loss could be interpreted as the presence of surface water. However, this was unlikely, as the method that was used to remove the surface water involved spreading the sample over the surface of dry filter paper until the sample became a ‘dry’ powder. Consequently, this was the only method of removing the surface water from the material that gave reproducible and reasonable mass losses. Therefore, this process ensured that all the surface moisture was absorbed and that the immediate mass loss was in fact an inherent property of the α-CD·VAL inclusion complex. If this method of removing the surface water was not followed, a mass loss of approximately 40 % was recorded. Such behaviour is not characteristic of α-CD inclusion complexes and was thus a result of surface water. Consequently, it can be concluded that the water molecules were weakly bound in the crystal structure and thus a mass loss is immediately observed in the TGA trace.

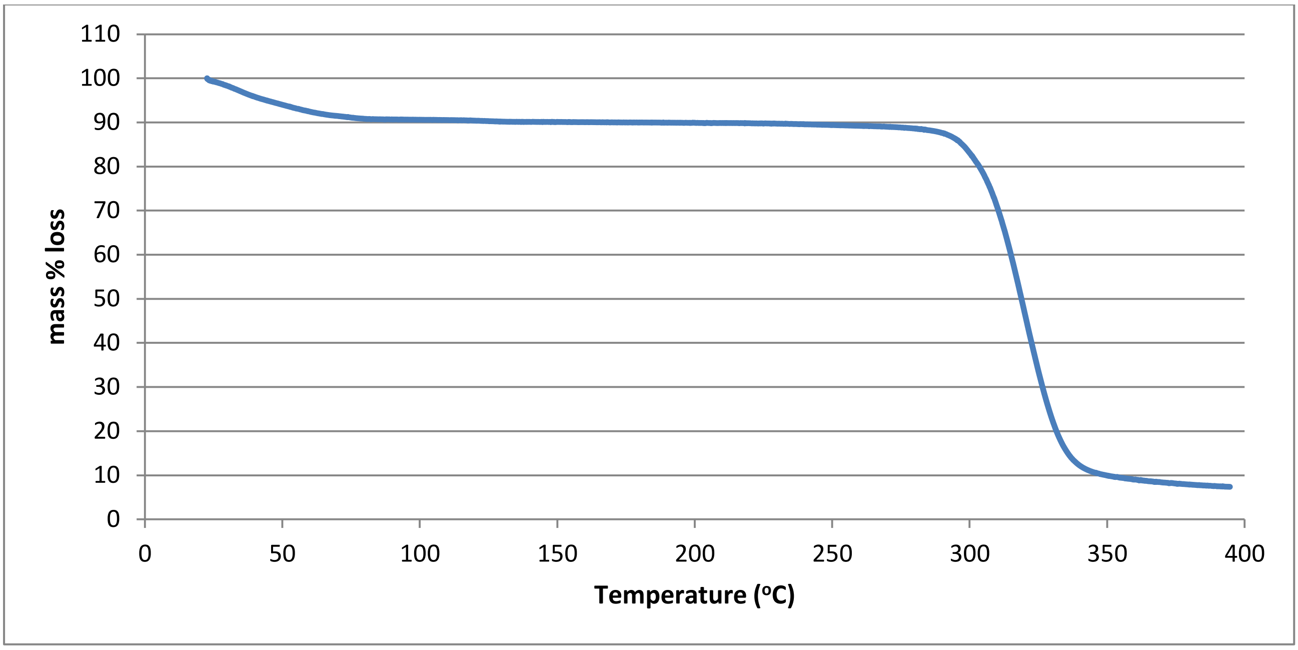

Figure 5.6: The representative TGA trace of α-CD·VAL (n = 2).

Differential Scanning Calorimetry (DSC) analysis of α-CD·VAL

The DSC trace of α-CD·VAL (n = 2) displayed three significant endothermic events (Figure 5.7). The first endotherm is complex and contains a shoulder, while the latter two are single endothermic events. All of these thermal events were measured over the temperature range 20.0 – 240.0 °C and represent the loss of water in a stepwise manner. The onset of the first broad endotherm was at 21.0 °C with the peak occurring at 61.6 ± 1.8 °C. Furthermore, the gradient of this initial complex endotherm significantly changed between the temperature ranges 21.0 – 45.5 °C ± 0.7 °C and 45.5 °C – 61.6 ± 1.8 °C. This possibly indicated that the rate of water loss increased with a steeper decreasing gradient. In addition, the onset of the shoulder endotherm occurred at 81.1 °C ± 0.9 °C and possibly indicated a sudden release of water from another region in the crystals. The two subsequent endothermic peaks in the DSC trace represented smaller losses in water and the onsets were 120.9 ± 0.5 °C (peak endotherm at 133.8 ± 0.1 °C) and 155.9 ± 0.3°C (peak endotherm at 161.5 ± 0.1 °C). These additional endothermic events characterised the stepwise water loss from the crystals, as they occurred at periodic intervals.

These endothermic events were evident in both the HSM and TGA results. With regard to the HSM analysis, the loss of water occurred through bubbling in the temperature range 58.0 °C – 180.0 °C. In addition, with reference to the TGA results the water loss occurred between 25.0 and 128.9 °C. Even though these temperatures did not correlate exactly between the various experiments, the trend is very evident and confirmed the loss of water with the DSC trace, further indicating that the water loss was a stepwise process.

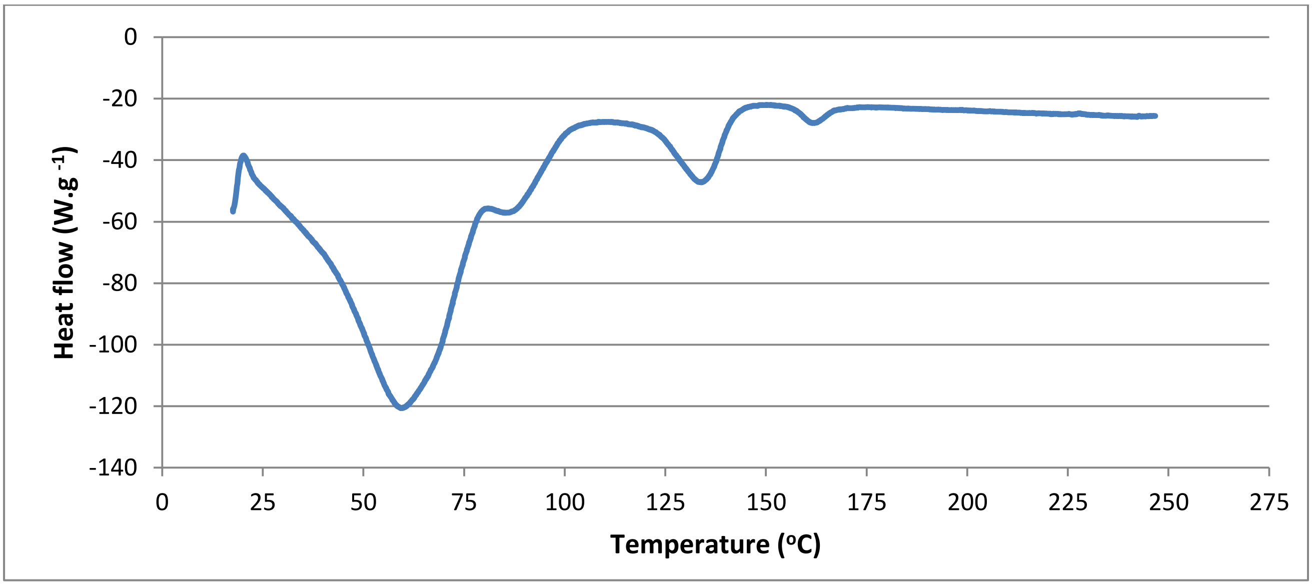

Figure 5.7: A representative DSC trace of α-CD·VAL (n = 2).

In conclusion, it is evident that a hydrated CD complex, with the formula $(\alpha\text{-CD})_2\cdot\text{VAL}\cdot6.7H_2O$, was formed between α-CD and valproic acid. Even though it was not possible to obtain a crystal structure through X-ray analysis, analytical methods were used explicitly to identify its authenticity.

5.3.1.2) The β-CD·VAL inclusion complex

Method of preparation

The β-CD·VAL inclusion complex was synthesized in a 1:1 stoichiometric ratio as confirmed by a ^{1}H NMR analysis (which is described in detail below). The method of preparation was very similar to that outlined for the α-CD·VAL inclusion complex, except that the mass of β-CD, the volume of water and the time taken to produce this inclusion complex were specifically adapted. Thus, a mass of 39.35 mg (0.03467 mmol) of β-CD was dissolved in 2.2 cm^3 of water at 70 ^{o}C and the resultant aqueous solution was thereafter stirred for 6 hours. The oily immiscible layer that valproic acid formed on top of the solution (as described for the α-CD·VAL experiment), took about an hour to dissolve into the aqueous medium. The appearance of crystals was observed after three days.

Crystal morphology of β-CD·VAL

The β-CD·VAL inclusion complex formed transparent crystals with a rhombic-shaped crystalline morphology and the entire sample of crystals analysed contained equally sized specimens, as represented in Figure 5.8. Furthermore, the quality of these crystals was adequate for a SCXRD analysis to be performed, and as a result a full structural characterisation was achieved.

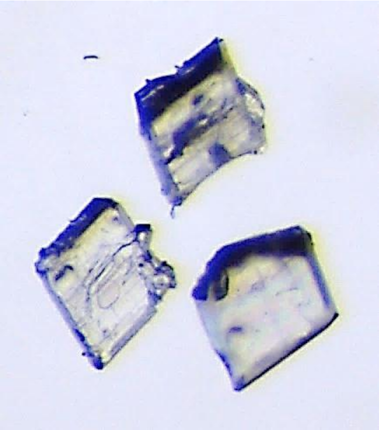

Figure 5.8: The crystal morphology of the β-CD·VAL inclusion complex.

^{1}H NMR analysis of β-CD·VAL

The results from the ^{1}H NMR solution-state spectral analysis of the complex crystals dissolved in DMSO-d_6 at 298 K confirmed an equimolar stoichiometry of β-CD to valproic acid. The results are listed in Table 5.3 below, while the original ^{1}H NMR spectra can be viewed in the Appendix under section 9.2.1, p. 38.

Table 5.3: The ^{1}H NMR analysis of β-CD·VAL.

Assignment	**δ (ppm)**	**Integration**	**Proton representation (per molecule)**	**Stoichiometric ratio**	**Stoichiometric ratio (integer)**
2 x $C\underline{H}_3$ (valproic acid)	0.85-0.88	1.00*	6H	1.00	1
4 x $C\underline{H}_2$ (valproic acid)	1.21-1.53	1.36	8H	1.02	1
$O\underline{H}$-6 (β-CD)	4.42-4.44	1.26	7H	1.08	1
$C\underline{H}$-1 (β-CD)	4.83-4.84	1.25	7H	1.07	1

*reference integral

Fourier Transform Infrared (FT-IR) spectroscopic analysis of β-CD·VAL

The FT-IR analysis also confirmed the formation of the β-CD·VAL inclusion complex and a portion of the FT-IR spectrum is given in Figure 5.9, which emphasises the important region for analysis. As mentioned previously, the C=O stretching frequency of valproic acid occurs at 1702 cm^{-1}. However, for the β-CD·VAL inclusion complex, the C=O stretching vibration of valproic acid was present at 1704 cm^{-1}, representing a negligible shift upon complexation. This suggests that the extent of hydrogen bonding between the host molecule and the C=O group of valproic was nearly the same, if not slightly less, in the complex as compared with the extent of the intermolecular hydrogen bonding within pure valproic acid.[6] The full FT-IR spectrum can be viewed in the Appendix under section 9.2.2, p. 38.

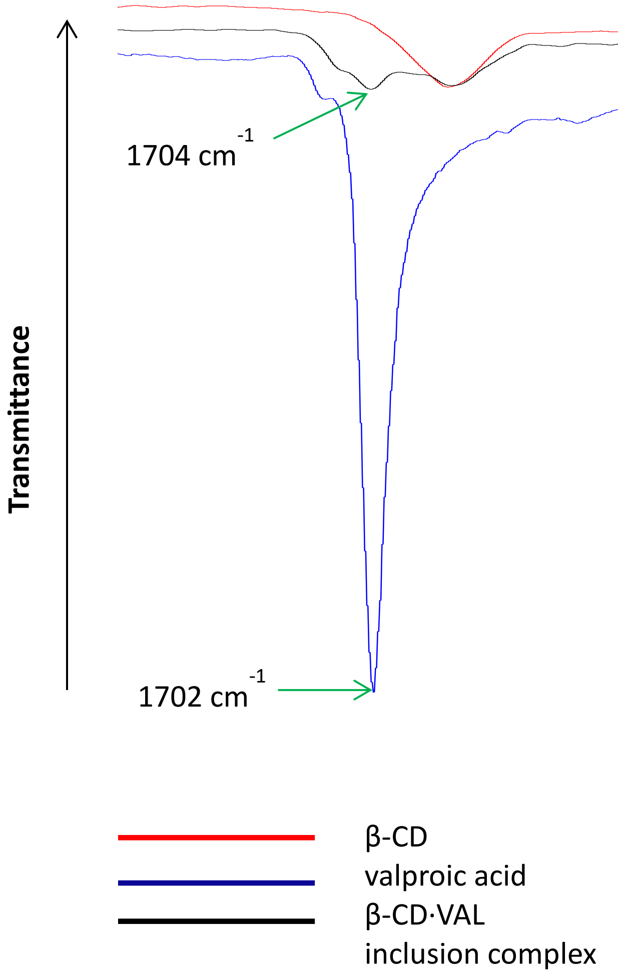

Figure 5.9: A portion of the FT-IR spectra of β-CD (red), valproic acid (blue) and β-CD·VAL (black).

Powder X-ray Diffraction Pattern (PXRD) analysis of β-CD·VAL

In addition, the successful synthesis of the β-CD·VAL inclusion complex (formed *via* co-precipitation) was also confirmed by the correlation of its PXRD pattern with the isostructural PXRD pattern for β-CD inclusion complexes that crystallize in the space group C2 (Figure 5.10).[7] This space group identification from PXRD was vindicated by the subsequent single crystal X-ray analysis, as described below. Furthermore, it was possible to synthesize the same β-CD·VAL inclusion complex *via* kneading the reagents for 30 minutes in an equimolar stoichiometry with a small amount of water (Figure 5.10).

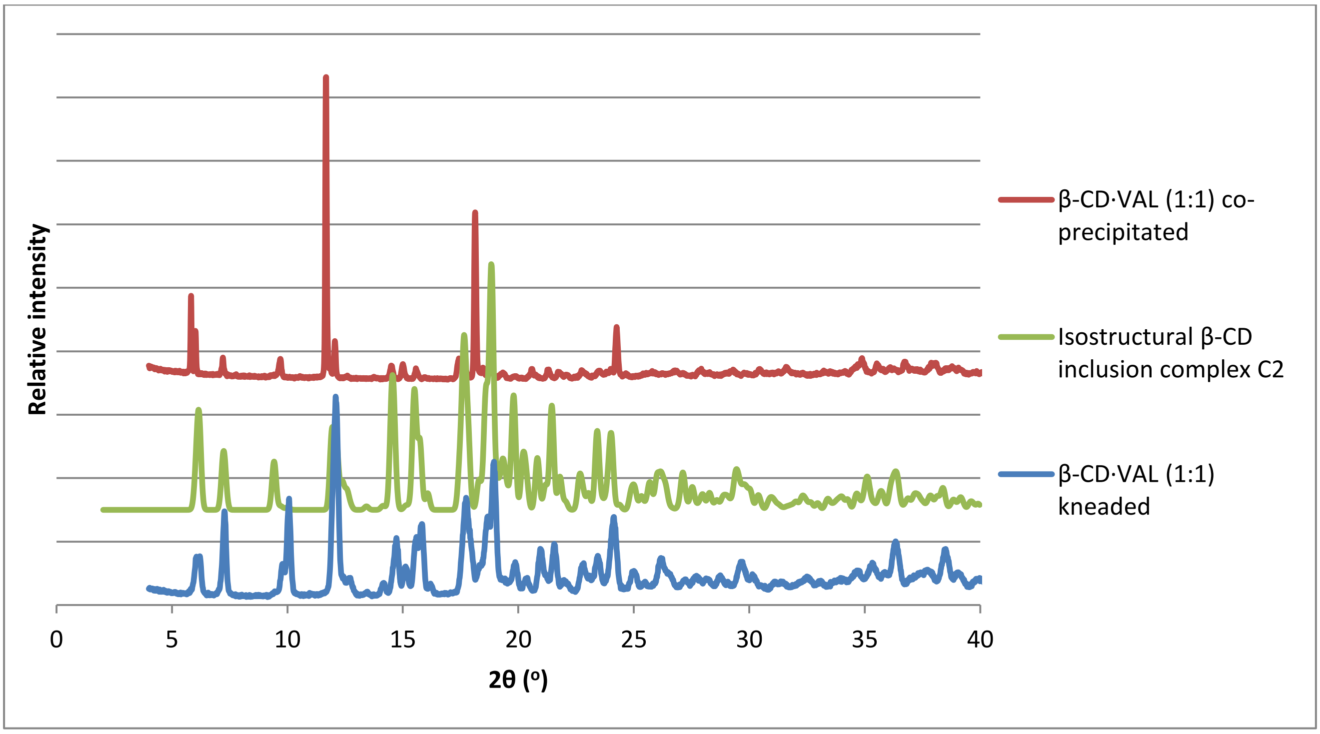

Figure 5.10: The PXRD patterns of β-CD·VAL produced *via* co-precipitation (1:1) and kneading (1:1), and that of an isostructural β-CD inclusion complex that crystallizes in the monoclinic space group C2.[7]

Hot Stage Microscopy (HSM) analysis of β-CD·VAL

The simultaneous HSM analysis of the β-CD·VAL inclusion complex and β-CD conveyed visual evidence for thermal events that took place when the crystals of these two species were immersed in silicone oil and heated at a constant rate of 10 K.min^{-1}. The series of micrographs (Figure 5.11) represents the thermal progression of both crystals. The initial micrograph, Image 1, was recorded at 21.0 °C to depict the features of the β-CD·VAL inclusion complex (left) and the β-CD crystals (right) prior to heating. The first sign of bubbling occurred at the top right-hand corner of β-CD at 96.4 °C (Image 2) while no change was observed for the inclusion complex. The β-CD·VAL inclusion complex only began to bubble at 256.3 °C as displayed in Image 3. This bubbling process was very slow, as only one bubble was released periodically. This process lasted for a further 16 °C until the onset of decomposition commenced at 267.8 °C for the β-CD·VAL inclusion complex, as depicted in

Image 4. However, at 317.2 °C (Image 5) the onset of decomposition of β-CD began, while the β-CD·VAL inclusion complex was vigorously decomposing and producing decomposition bubbles. Finally, both crystals were completely decomposed, with decomposition bubbles, at 351.1 °C, as depicted in Image 6.

Figure 5.11: A series of micrographs from the simultaneous HSM analysis of β-CD·VAL and β-CD.

Image 1: The initial appearance at 21.0 °C of β-CD·VAL (left) and β-CD (right).

Image 2: Very slight bubbling occurred at the top right of β-CD (right) at 96.4 °C. No change was observed for β-CD·VAL (left).

Image 3: β-CD·VAL (left) began to bubble very slowly at 256.3 °C. β-CD (right) remained unchanged.

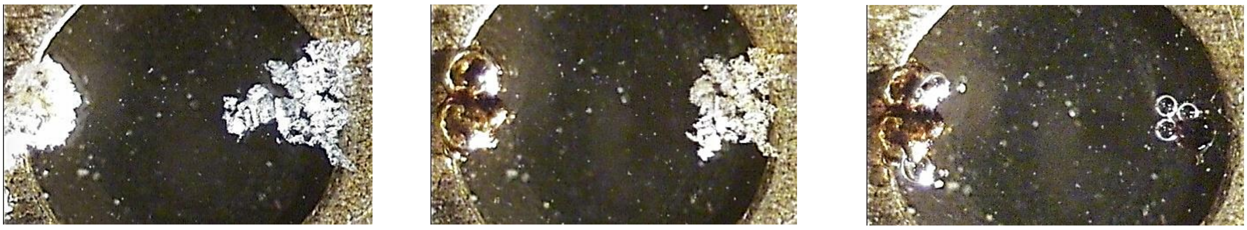

Image 4: The onset of decomposition decomposition at 267.8 °C for β-CD·VAL (left). β-CD (right) remained unchanged.

Image 5: The onset of decomposition for β-CD (right) at 317.2 °C. Vigorous decomposition of β-CD·VAL (left).

Image 6: Both β-CD·VAL (left) and β-CD (right) are fully decomposed at 351.1 °C and have produced decomposition bubbles.

Thermal Gravimetric Analysis (TGA) of β-CD·VAL

The TGA trace of the β-CD·VAL inclusion complex (n = 2) also indicated two distinct mass losses (as described for the α-CD·VAL inclusion complex), which occurred over the temperature range 16.7 – 400.0 ^{o}C, as depicted in Figure 5.12. A mass loss of 11.5 ± 1.0 % was associated with the first thermal event which occurred between 16.7 ^{o}C and 128.6 ^{o}C. This mass loss was also attributed to the loss of water molecules from the β-CD·VAL inclusion complex. In addition, the second thermal event took place between 258.7 and 366.3 ^{o}C and was associated with a mass loss of 73.8 % which represented the decomposition of the anhydrous β-CD·VAL inclusion complex. In comparison with the HSM analysis, which showed no water loss, dehydration was evident from the TGA analysis. However, the onset of decomposition occurred at 267.8 ^{o}C in the HSM analysis, which correlated to some-extent with the onset temperature of decomposition as reported in the TGA trace.

The mass percentage of water loss was 11.5 $\pm$ 1.0 % (n = 2) which is equivalent to 9.2 $\pm$ 0.8 water molecules per complex unit. This calculation can be viewed in the Appendix under section 9.2.3, p. 39.

In the TGA trace there was a small plateau where a miniscule mass loss occurred and then the significant mass loss occurred. The method for drying the β-CD·VAL crystals was simpler than that for the α-CD·VAL crystals (as mentioned above) and it also yielded reproducible results. The rhombus-shaped morphology of the β-CD·VAL crystals allowed the surface water to be removed when they were pressed and gently rubbed between two dry filter papers. Furthermore, another experiment also ensured that no internal water was lost. A cluster of crystals was dried on filter paper and subsequently ground in a mortar. The resultant crystalline powder was used for a TGA experiment and the results indicated the same mass loss as when the material was dried using the first procedure. Even though this is considered an unconventional practice, it supported the assumption that this water loss was not due to surface water.

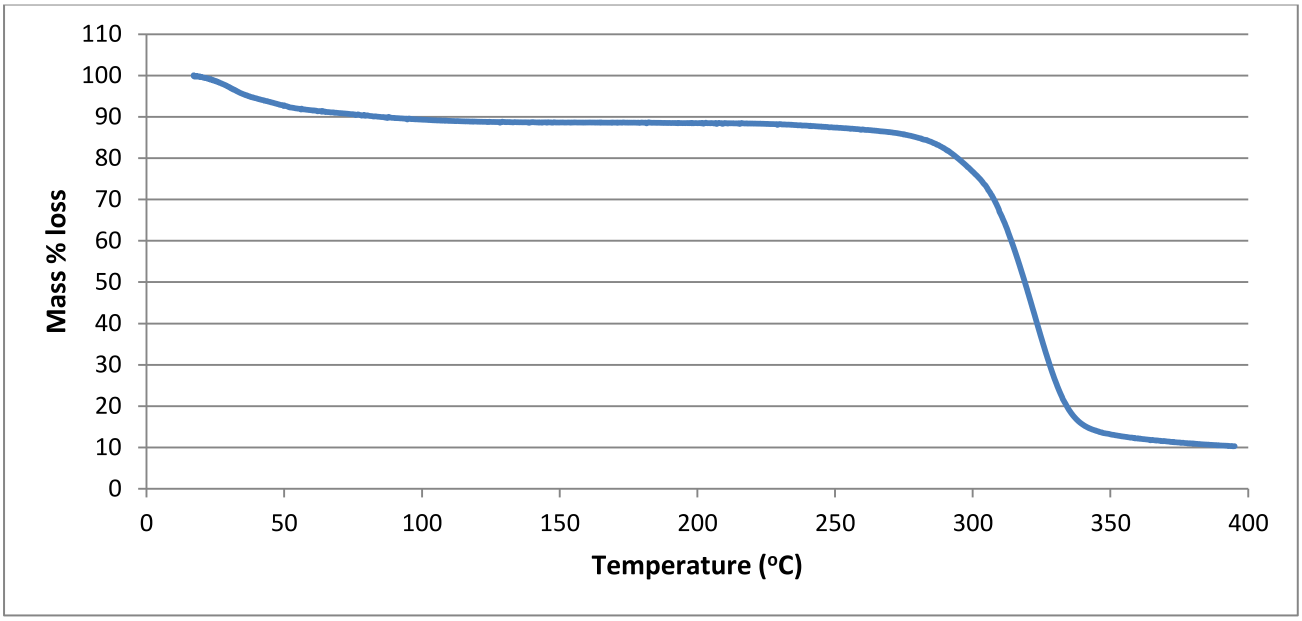

Figure 5.12: Representative TGA trace of the β-CD·VAL inclusion complex (n = 2).

Differential Scanning Calorimetry (DSC) analysis of β-CD·VAL

The DSC trace of the β-CD·VAL inclusion complex also indicated a stepwise loss of water, but to a lesser extent than the α-CD·VAL inclusion complex, as observed in Figure 5.13. The trace is characterised by a very broad endothermic event where the onset occurred at 65.2 °C, with the peak occurring at 67.9 °C. This endotherm is reflected in the TGA trace where the majority of the mass loss, attributed to water, takes place in the temperature range 25.0 – 54.0 °C. The onset of the subsequent, very small endothermic peaks in the DSC trace occurred at 65.5 °C (peaking at 67.9 °C) and 118.0 °C (peaking at 120.0 °C) and represented smaller, stepwise losses of water, which are attributed to different binding strengths of water molecules from different environments in the crystal. These events are relatively too small to be noticed as individual steps in the TGA experiment, and thus once again, in the TGA trace they blurred as a general mass loss over the temperature range 54.0 – 128.6 °C. Thus, the trends between the TGA and DSC traces correlated closely.

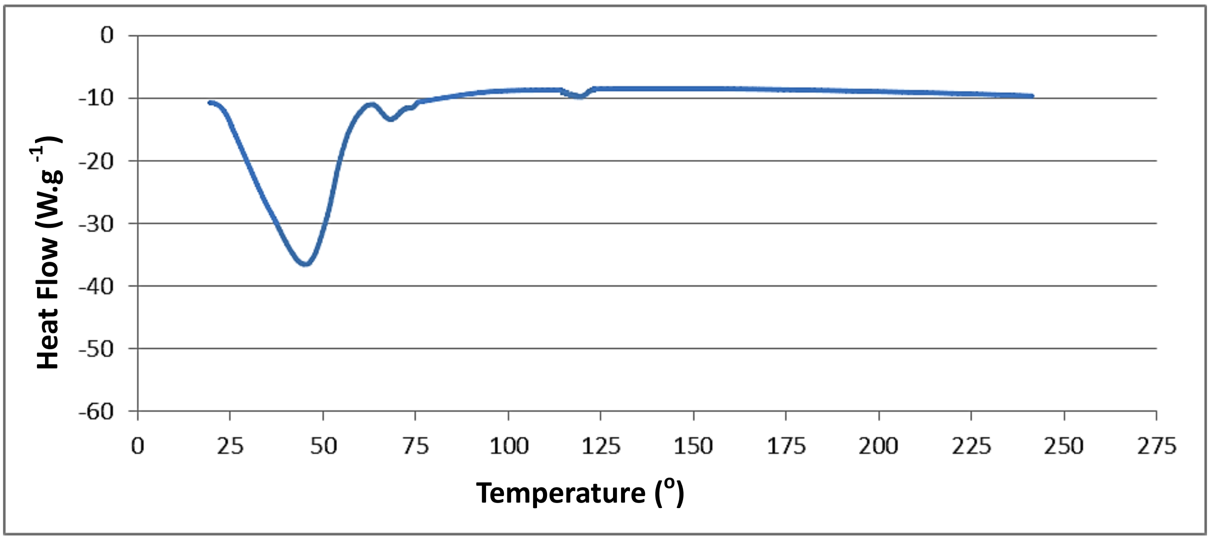

Figure 5.13: DSC trace of β-CD·VAL.

Single Crystal X-ray Diffraction (SCXRD) analysis

Data-collection and space group determination

The intensity data from a single, block-shaped crystal were collected at 173 K. The Laue group of the intensity-weighted reciprocal lattice was 2/*m* which indicated the monoclinic system. The lattice type was determined to be C-centred (condition 1 in Table 5.4) which, together with the remaining conditions indicated the possible space groups C2, C*m* and C2/*m*. However, since CD molecules are chiral, the only possible space group is C2. This assignment, previously predicted above based on the PXRD method, was confirmed by the program XPREP.[8]

Table 5.4: The conditions limiting possible reflections for the crystal of β-CD·VAL.

Number	Conditions limiting possible reflections	Deduction
1	hkl: h+k = 2n	C-centred
2	[h0l: (h = 2n, redundant condition)]	-
3	[0k0: (k = 2n, redundant condition)]	-

Structure solution and refinement

The method of isomorphous replacement was used to solve the structure of the β-CD·VAL inclusion complex. This was achieved by using the co-ordinates of a different β-CD inclusion complex that had matching unit cell parameters. The methodology for isomorphous replacement is described in the Experimental Methods (Chapter 2) under section 2.5, p. 21. However, eventual failure to locate the guest molecule using the data collected at 173 K led to a decision to record the intensity data at 100 K from a fresh crystal as a possible remedy, and the final analysis was based on these data. The host 'skeleton' (which consisted of seven glucose residues minus the conformationally flexible primary hydroxyl oxygen atoms) was imported from the CSD and was used as the trial model. It was refined with SHELXH-97,[9] initially isotropically and subsequently anisotropically. From the subsequent difference electron density (Δρ) map it was evident that five hydroxyl oxygen atoms at the C6 positions were disordered over two positions and were treated accordingly. The treatment involved assigning site-occupancies of *x* and 1-*x* to the major and minor disorder components of each disordered pair, with *x* treated as a free variable, while the bond lengths C6-O6 and C6-O7 were constrained to 1.40 Å with σ = 0.01 Å by means of a DFIX restraint. The major components of the disordered oxygen atoms, which included O6A1, O6A2, O6A4, O6A5 and O6A6, had site-occupancy factors (s.o.f.s) of 0.85(2), 0.79(2), 0.54(3), 0.66(3) and 0.82(2) respectively after refinement. These disordered atoms were only refined isotropically. Furthermore, the hydrogen atoms were placed in idealised positions on the host molecule using the 'maximum electron density' model and an isotropic temperature factor of 1.2 times the value of the U_{iso} of its parent atom was assigned to each hydrogen atom. It was evident from inspection of subsequent Δρ maps that the guest molecule was so severely disordered that it could not be located, the highest value of Δρ within the CD cavity being only 0.88 e.Å^{-3}. The crystallographic data are summarised in Table 5.5.

Table 5.5: The crystal data and refinement parameters for the β-CD·VAL inclusion complex.

Parameter	Value
Complex formula	$C_{42}H_{70}O_{35}·C_8H_{16}O_2·9.2H_2O$
Formula weight (g.mol^{-1})	1681.70
Temperature (K)	100(2)
Wavelength (Å)	0.71073
Crystal system	Monoclinic
Space group	C2
a (Å)	19.133(5)
b(Å)	24.566(7)
c(Å)	15.782(5)
α (°)	90
β (°)	108.873(6)
γ (°)	90
Volume (Å^3)	7019(3)
Z	4
Calculated density (g.cm^{-3})	1.3671
μ (mm^{-1})	0.138
F (000)	3632
Crystal size (mm)	0.120 x 0.150 x 0.270
θ-Range scanned (°)	2.25 - 21.65
Index range	h: -24, 24; k: -31, 31; l: -20, 20
No. of reflections collected	29021
No. of unique reflections	15385
Data completeness (%)	98.6
Data/restraints/parameters	15385/19/808
S (Goodness-of-fit on F^2)	1.118
Final R indices R_1, wR_2, [$I > 2\sigma(I)$]	0.0995, 0.2735
R Indices, all data (R_1, wR_2)	0.1317, 0.3040
Largest diff. peak and hole (e. Å^{-3})	1.27, -0.44

The oxygen atoms of the water molecules were identified through the method that is described in the Experimental Methods (Chapter 2) under section 2.5, p. 21. Initially, the water molecules O1W, O3W and O4W were identified as having full site-occupancy, based on the large sizes of their difference electron density peaks, while O2W had a site-occupancy of 0.5, being located on the twofold axis. In addition, these four water oxygen atoms were all refined anisotropically. The remaining disordered water molecules were placed systematically in a decreasing order of their difference electron density peaks. Initially, the thermal parameter (U_{iso}) of the disordered water molecules was fixed at 0.061 Å^2 (which was the average U_{iso} value for water molecules O1W - O4W) and their s.o.f.s were allowed to vary. When their values converged, the U_{iso} values of the water molecules were allowed to vary; however, a few water molecules still displayed high U_{iso} values and thus the latter were constrained. After consecutive refinements, O3W was subsequently discovered to be disordered over two sites and the two components were assigned partial site-occupancies and were refined isotropically. The refined values for the U_{iso} parameters, as well as the s.o.f.s for the water oxygen atoms, are displayed in Table 5.6. The number of water molecules per β-CD molecule in the crystal structure model was 9.8, which was in close agreement with the TGA results which yielded a calculated value of 9.2 ± 0.8 water molecules per β-CD complex unit.

Table 5.6: The total number of water oxygen sites that were identified, with their respective s.o.f. and U_{iso} values.

Atom	**s.o.f.**	**U_{iso} (Å^2)**	**Atom**	**s.o.f.**	**U_{iso} (Å^2)**	**Atom**	**s.o.f.**	**U_{iso} (Å^2)**
O1W	1.00	0.043(1)	O9W	0.49(5)	0.11(1)	O17W	0.36(4)	0.12(2)
O2W	0.50	0.052(2)	O10W	0.22(4)	0.05(1)	O18W	0.36(5)	0.09(1)
O3W	0.68(5)	0.044(4)	O11W	0.40(3)	0.083(9)	O19W	0.53(6)	0.14(1)
O4W	1.00	0.069(2)	O12W	0.18(3)	0.10(2)	O20W	0.51(6)	0.13(1)
O5W	0.36(4)	0.045(7)	O13W	0.28(3)	0.08(1)	O21W	0.39(5)	0.07(9)
O6W	0.40(3)	0.045(6)	O14W	0.22(2)	10.061*	O22W	0.12(2)	10.061*
O7W	0.32(4)	0.12(1)	O15W	0.59(5)	0.13(1)	O23W	0.53(5)	0.11(1)
O8W	0.20(3)	10.061*	O16W	0.13(2)	10.061*			

*10.061 indicates a *constant* assigned value of 0.061 Å^2

Molecular Structure

The asymmetric unit (ASU) of the β-CD·VAL complex, displayed in Figure 5.14, consists of one β-CD molecule, one valproic acid molecule (not located in the difference electron density map) and 9.8 water molecules distributed over 23 sites. All the water molecules were within a permitted hydrogen bonding distance range of either the host molecule or neighbouring water oxygen atoms, and no hydrogen atoms were placed on them.

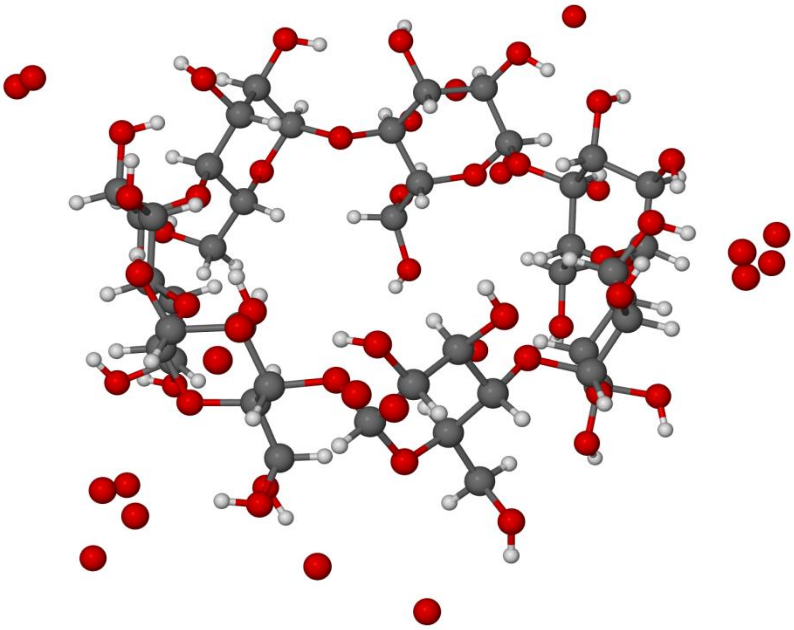

Figure 5.14: The β-CD molecule and water molecule sites of β-CD·VAL.

Unfortunately, the guest molecule could not be observed even though the data were collected at the lower temperature of 100(2) K, and as a result there appears to be a large discrepancy between the calculated and reported molecular mass of the complex in the checkCIF report (in the Electronic Supplementary Information) based on the final refinement. Figure 5.15 displays a stereo diagram of the β-CD molecule and the water molecule sites. It is evident that the residual electron density did not resemble any relative positions that could correspond to the guest molecule, and as a result it was impossible to model the guest molecule, since it appeared to be in several different orientations.

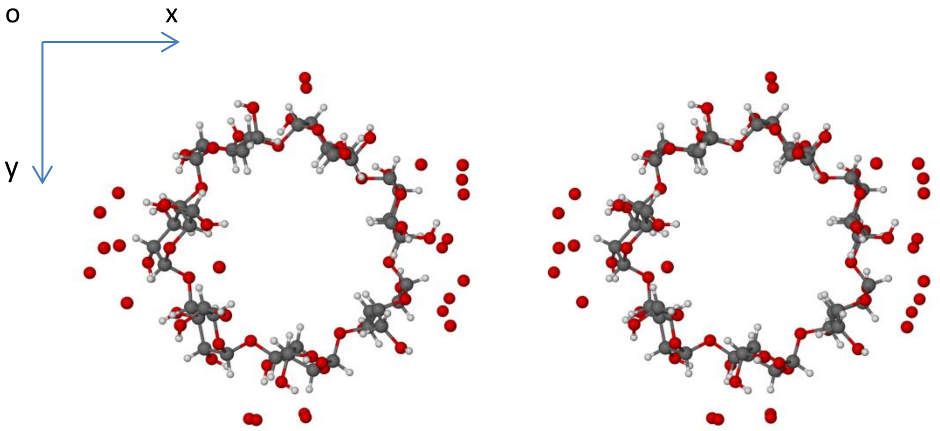

Figure 5.15: A stereoview of the host molecule highlighting the 'empty' cavity (viewed down the c-axis).

Crystal Packing

The dimer of the β-CD·VAL inclusion complex has C_2-symmetry and the dimeric structure is maintained by intermolecular O-H···O hydrogen bonds that link the secondary rims of the β-CD molecules. This inclusion complex adopts a channel-type packing where the β-CD molecules stack themselves as dimeric units along the z-direction (Figure 5.16). This arrangement occurs in all other isostructural β-CD inclusion complexes that belong to the space group C2.[7,10] In addition, the dimeric stacking arrangement of the β-CD molecules contains a small degree of lateral shifting between the tail-to-tail β-CD molecules of adjacent dimers. Lastly, the columns created by the stacked dimeric units are held together by intermolecular hydrogen bonding mediated by water molecules. The host cavities within each column form an infinitely long channel, in which the guest molecules are accommodated in a disordered fashion. As a result, the electron density of the guest molecule is diluted and it is thus not possible to locate it. This is a very common feature of many β-CD complexes that crystallize in the space group C2.

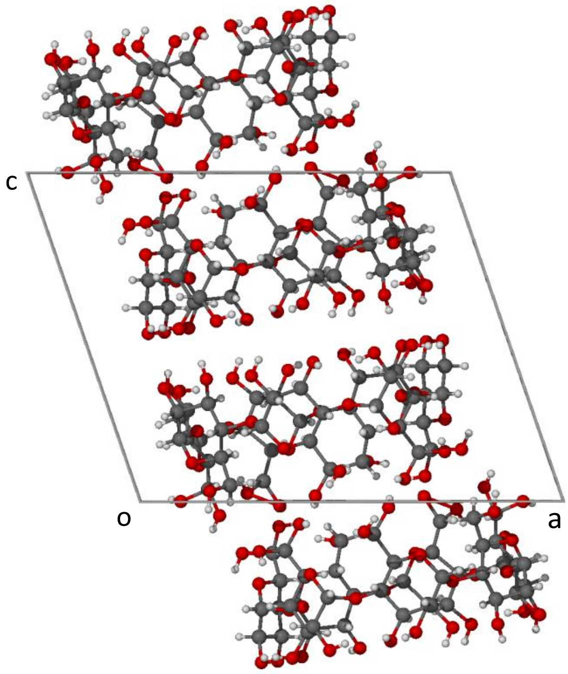

Figure 5.16: The channel-packing arrangement along the z-direction. The β-CD molecules stack themselves in dimeric units, as displayed in the example of the two β-CD molecules in the unit cell.

A stereoview of the channels down the c-axis is displayed in Figure 5.17 which indicates that there are a total of four β-CD molecules in the unit cell.

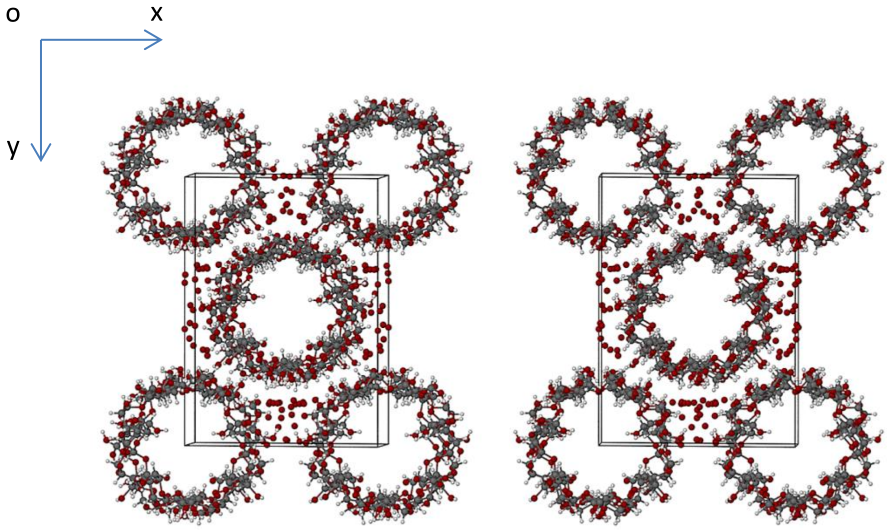

Figure 5.17: A stereoview down the c-axis displaying the packing arrangement of the β-CD molecules.

Host-host hydrogen bonding

The hydroxyl groups on the secondary rim of β-CD molecules generally form hydrogen bonds of a 'flip-flop' nature.[11] These intramolecular hydrogen bonds can alternate between O2-H···O3′ and O3-H···O2′. The β-CD·VAL crystal structure displays a belt of O2-H···O3′ intramolecular hydrogen bonds, which reinforces the heptagonal geometry and generally 'round' shape of the host molecule (Figure 5.18). Intermolecular hydrogen bonding was also observed at the interface of the secondary rims between the O3-H hydroxyl groups of the one molecule and the O3-H or O2-H groups of the molecule related by the twofold axis.

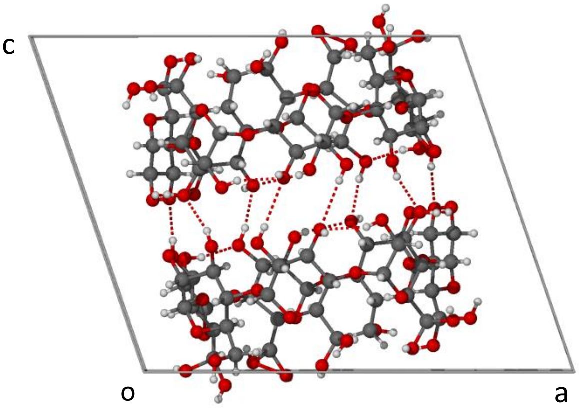

Figure 5.18: The intermolecular and intramolecular hydrogen bonding associated with the β-CD dimers.

Table 5.7 displays the intramolecular and intermolecular hydrogen bonding parameters for the host molecules. It is evident that the intermolecular hydrogen bonds are strong and as a result this implies that the crystal structure is stable. The C-H···O hydrogen bonds that involved C···O distances larger than 3.00 Å were omitted owing to their relatively weak contribution in comparison to the remaining hydrogen bonds.

Table 5.7: The parameters for the hydrogen bond interactions in β-CD·VAL.

Interaction type	Hydrogen bond	D-H (Å)	H···A (Å)	D···A (Å)	D-H···A (°)	Symmetry Code
O2-H···O3 Hydrogen bonds						
Intramolecular	O2A1-H2A2···O3A7	0.84	2.12	2.767(8)	134	x, y, z
Intramolecular	O2A2-H2A3···O3A1	0.84	2.00	2.826(8)	168	x, y, z
Intramolecular	O2A3-H2A4···O3A2	0.84	2.03	2.856(7)	168	x, y, z
Intramolecular	O2A4-H2A5···O3A4	0.84	2.53	2.877(9)	106	x, y, z
Intermolecular	O2A4-H2A5···O3A4	0.84	2.39	3.141(8)	149	1-x, y, 1-z
Intramolecular	O2A5-H2A6···O3A4	0.84	2.07	2.81(1)	147	x, y, z
Intramolecular	O2A6-H2A8···O3A5	0.84	2.11	2.857(8)	148	x, y, z
Intramolecular	O2A7-H2A7···O3A6	0.84	1.96	2.783(7)	166	x, y, z
O2-H···O4 Hydrogen bonds						
Intramolecular	O2A7-H2A7···O4A6	0.84	2.40	2.821(6)	112	x, y, z
Intramolecular	O2A1-H2A2···O4A7	0.84	2.46	2.762(7)	103	x, y, z
Intramolecular	O2A2-H2A3···O4A1	0.84	2.38	2.799(9)	112	x, y, z
Intramolecular	O2A3-H2A4···O4A2	0.84	2.35	2.775(8)	112	x, y, z
Intramolecular	O2A5-H2A6···O4A4	0.84	2.48	2.789(9)	103	x, y, z
Intramolecular	O2A6-H2A8···O4A5	0.84	2.46	2.80(1)	105	x, y, z
O3-H···O2 and O3-H···O3 Hydrogen bonds						
Intramolecular	O3A1-H3A2···O2A1	0.84	2.57	2.879(8)	103	x, y, z
Intermolecular	O3A1-H3A2···O3A7	0.84	1.95	2.787(7)	170	1-x, y, 1-z
Intermolecular	O3A2-H3A3···O3A6	0.84	2.02	2.845(8)	168	1-x, y, 1-z
Intermolecular	O3A3-H3A9···O3A5	0.84	1.93	2.734(8)	160	1-x, y, 1-z
Intramolecular	O3A2-H3A3···O2A2	0.84	2.59	2.899(7)	103	x, y, z
O6-H···O5 and O6-H···O6 Hydrogen bonds						
Intermolecular	O6A3-H1···O5A1	0.84	2.57	3.327(7)	151	½-x, -½+y, -z
Intermolecular	O6A7-H2···O6A3	0.84	2.09	2.861(8)	152	½+x, ½+y, z
Intramolecular	O6A2-H4···O5A2	0.84	2.43	2.83(1)	109	x, y, z
Intramolecular	O6A5-H6···O5A5	0.84	2.26	2.69(2)	112	x, y, z
Intramolecular	O6A6-H6AY···O5A6	0.84	2.15	2.57(3)	111	x, y, z
C-H···O Hydrogen bonds						
Intramolecular	C4A7-H4A7···O6A7	1.00	2.54	2.921(9)	102	x, y, z
Intramolecular	C5A1-H5A1···O4A7	1.00	2.48	2.84(1)	100	x, y, z
Intramolecular	C5A2-H5A2···O4A1	1.00	2.46	2.82(1)	100	x, y, z
Intramolecular	C4A4-H4A4···O6A4	1.00	2.57	2.96(2)	103	x, y, z
Intramolecular	C4A5-H4A5···O6A5	1.00	2.58	2.96(2)	102	x, y, z

Hydrogen bonds involving water molecules

The hydrogen bonding involving the water molecules includes water-water and water-host interactions. Table 5.8 summarises the interactions where the water molecules are hydrogen bond acceptors of either an O3 or an O6 hydroxyl group from the host molecule.

Table 5.8: The parameters for the intermolecular interactions in β-CD·VAL where the water molecules are the hydrogen bond acceptors.

Hydrogen bond interaction	**D-H (Å)**	**H···A (Å)**	**D···A (Å)**	**D-H···A (°)**	**Symmetry code**
O6A3-H1···O1W	0.84	2.34	2.743(7)	110	x, y, z
O3A7-H3A7···O20W	0.84	2.10	2.72(4)	130	1-x, y, 1-z
O3A5-H12···O3W	0.84	2.07	2.85(1)	156	½+x, -½+y, z
O3A5-H12···O20W	0.84	1.96	2.78(3)	163	½+x, -½+y, z
O3A4-H3A5···O23W	0.84	2.03	2.86(2)	173	x, y, z
O3A6-H3A8···O10W	0.84	2.26	2.96(3)	140	½+x, ½+y, z

Host molecular geometry

The geometrical parameters that define the conformation of the O4-heptagon for the host molecule are described in Table 5.9. These parameters have been described in detail in Chapter 1 under section 1.4.3, pp. 6 – 8.

In a regular heptagon all the lengths and angles should be equal; however, the values of *l*, D and Φ are not equal and instead vary very slightly. This indicates that the O4-heptagon is distorted, which is expected for CD molecules in a crystalline state. Furthermore, the results indicate that the degree of planarity of the O4-heptagon is high, since the variation in the torsion angles (d) and the deviations (α) are very small. The D_3 values range between 2.767(8) Å and 2.857(8) Å which is expected for O···O distances for O-H···O hydrogen bonds. The values of the tilt angles for the glucose residues are similar, with the exception of A3 and A7, which are tilted to a lesser extent towards the centre of the cavity of the β-CD molecule. The average tilt angle for the uncomplexed β-CD molecule is 14(10)° and as a result it is noticeable that the tilt angles for β-CD·VAL are within this range.[12] Consequently, it is not apparent that any additional distortion occurred on host-guest complexation.

Table 5.9: The geometrical parameters of the host molecule in the complex β-CD·VAL.

Residue	l (Å)	D(Å)	Φ (°)	d(°)	α[a](Å)	D_3(Å)	τ_2 (°)[b]
A1	5.003	4.375	129.4	2.2	-0.030	2.767(8)	11.1
A2	5.167	4.300	125.8	-0.5	0.043	2.826(8)	13.0
A3	5.015	4.460	129.6	-0.3	-0.012	2.856(7)	8.5
A4	4.956	4.338	130.1	-0.4	-0.017	2.805(9)	11.8
A5	5.086	4.391	127.8	0.5	0.005	2.81(1)	12.0
A6	5.118	4.311	127.0	1.2	0.020	2.857(8)	11.0
A7	4.963	4.467	130.4	-2.7	-0.009	2.783(7)	5.1

[a] mean esd: 0.004 Å; [b] mean esd: 0.2°

PXRD analysis

The PXRD pattern of β-CD·VAL produced *via* co-precipitation is in reasonable correspondence with the calculated PXRD pattern from the single crystal X-ray structure (Figure 5.19). This indicates that the latter model is a reasonable representation of the bulk material. Discrepancies in the relative intensities of corresponding peaks are attributed to preferred orientation in the experimental sample.

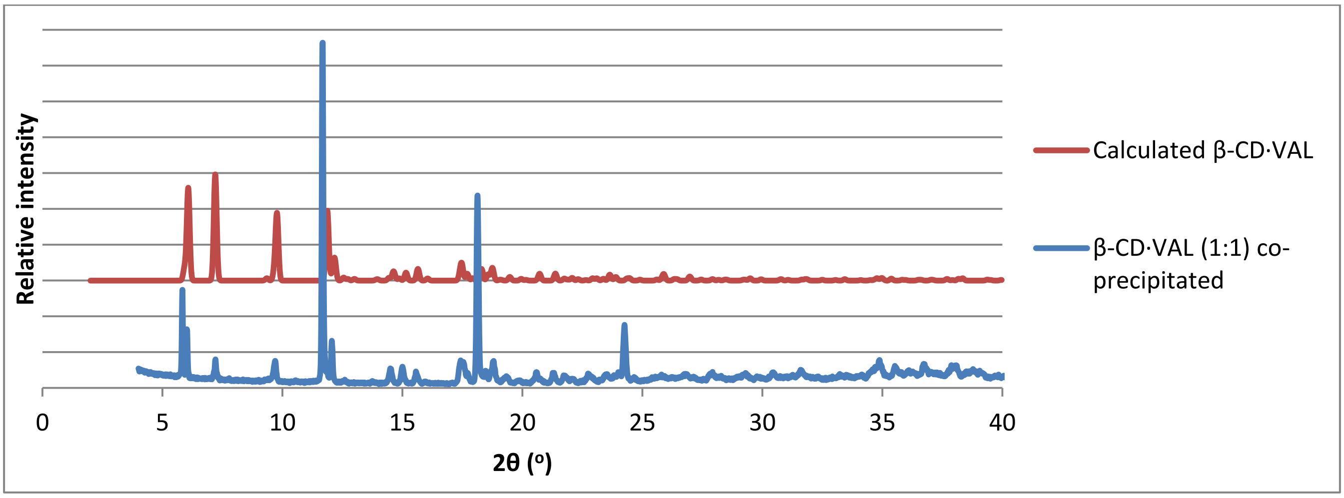

Figure 5.19: The PXRD pattern calculated from a single crystal X-ray structure of β-CD·VAL and the PXRD pattern of β-CD·VAL prepared *via* co-precipitation.

5.3.1.3) The γ-CD·VAL inclusion complex

Method of preparation

The initial preparation of the γ-CD·VAL inclusion complex involved an equimolar ratio of valproic acid and γ-CD. However, a ^{1}H NMR analysis confirmed that the stoichiometric ratio was 4:3 (γ-CD : valproic acid) and as a result, this stoichiometric ratio was used to reproduce the γ-CD·VAL inclusion complex in all the subsequent experiments. Once again, the method of preparation followed the same procedure as described for the α-CD·VAL inclusion complex, where the mass of γ-CD, the volume of water and time taken to perform the synthesis were specifically tailored. Consequently, a mass of 59.96 mg (0.04623 mmol) of γ-CD was initially dissolved in 2 cm^3 of water at 70 °C and the resultant aqueous solution was stirred for 6 hours. The requisite amount of valproic acid added to this solution formed an oily immiscible layer on the surface and also coated the sides of the vial (as described in detail for the α-CD·VAL inclusion complex) eventually dissolving after a few hours. The crystals appeared after three days.

Crystal morphology

The γ-CD·VAL inclusion complex consisted of transparent rectangular-shaped crystals (Figure 5.20). These crystals were elongated, unlike the equant crystals of the β-CD·VAL inclusion complex.

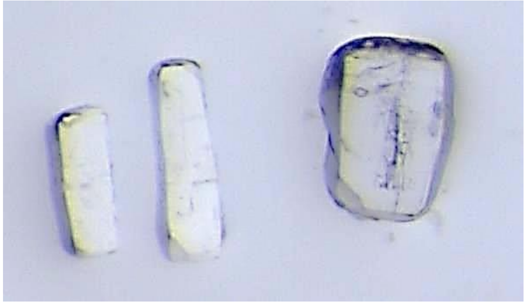

Figure 5.20: The crystal morphology of the γ-CD·VAL inclusion complex.

^{1}H NMR analysis of γ-CD·VAL

The ^{1}H NMR solution-state spectral analysis for the γ-CD·VAL inclusion complex indicated a 4:3 stoichiometry of γ-CD to valproic acid. This particular stoichiometric ratio is not uncommon for CD inclusion complexes.[13] The results are listed in Table 5.10 below and the original ^{1}H NMR spectra can be viewed in the Appendix under section 9.3.1, p. 40. This experiment was performed at 298 K using the solvent DMSO-d_6.

Table 5.10: The ^{1}H NMR analysis of γ-CD·VAL.

Assignment	δ (ppm)	Integration	Proton representation (per molecule)	Stoichiometric ratio	Stoichiometric ratio (integer)
2 x C$\underline{H}_3$ (valproic acid)	0.84-0.88	1.00*	6H	1.00	3
4 x C$\underline{H}_2$ (valproic acid)	1.21-1.52	1.40	8H	1.05	3
O$\underline{H}$-6 (γ-CD)	4.49-4.52	1.02	8H	1.31	4
C$\underline{H}$-1 (γ-CD)	4.89-4.90	1.01	8H	1.32	4

*reference integral

Fourier Transform Infrared (FT-IR) spectroscopic analysis of γ-CD·VAL

Similarly, as with the previous CD inclusion complex analyses, the FT-IR analysis also confirmed the formation of the γ-CD·VAL inclusion complex. The C=O stretching frequency of uncomplexed valproic acid occurs at 1702 cm^{-1} and in the case of the γ-CD·VAL inclusion complex, the same frequency was observed (Figure 5.21). This implies that the degree of hydrogen bonding between the host molecule and the C=O functional group of valproic acid remained the same in the complex, as compared with the extent of the intermolecular hydrogen bonding within pure valproic acid.[6] It could be argued that the product is a physical mixture; however, the product material was confirmed to be a complex with PXRD analysis prior to the FT-IR analysis. The full FT-IR spectrum is supplied in the Appendix under section 9.3.2, p. 40.

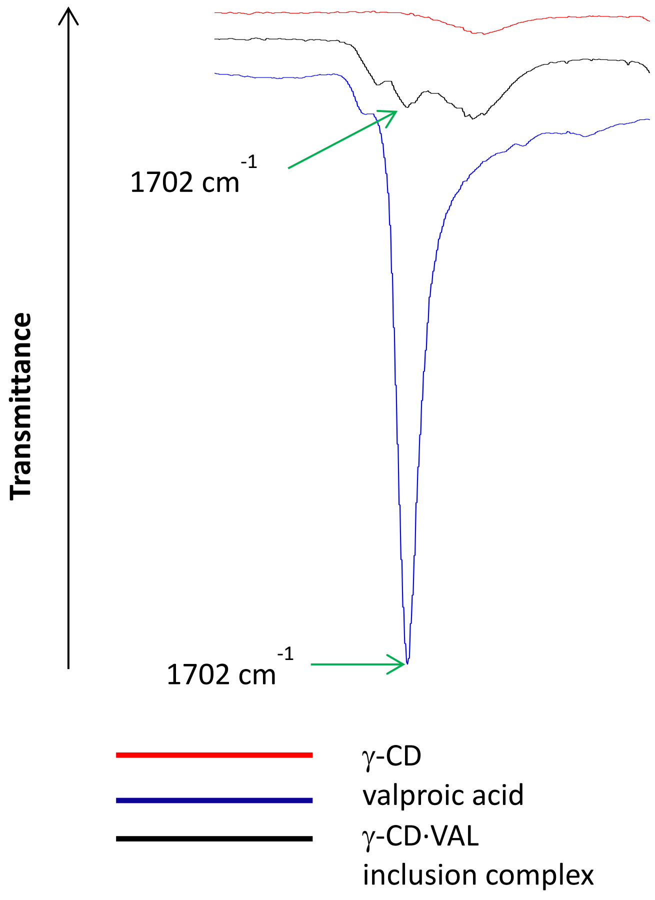

Figure 5.21: A portion of the FT-IR spectra of γ-CD (red), valproic acid (blue) and γ-CD·VAL (black).

Powder X-ray Diffraction (PXRD) analysis of γ-CD·VAL

The PXRD pattern for the γ-CD·VAL inclusion complex formed *via* co-precipitation correlated with the PXRD pattern for γ-CD inclusion complexes that crystallize in the tetragonal space group $P42_12$.[7] This can be observed in Figure 5.22 below. The same γ-CD·VAL inclusion complex could also be successfully synthesised *via* kneading the host and guest components in a 4:3 stoichiometry with a small amount of water for 30 minutes, as there was also a direct correlation with this PXRD pattern and the former PXRD patterns (Figure 5.22).

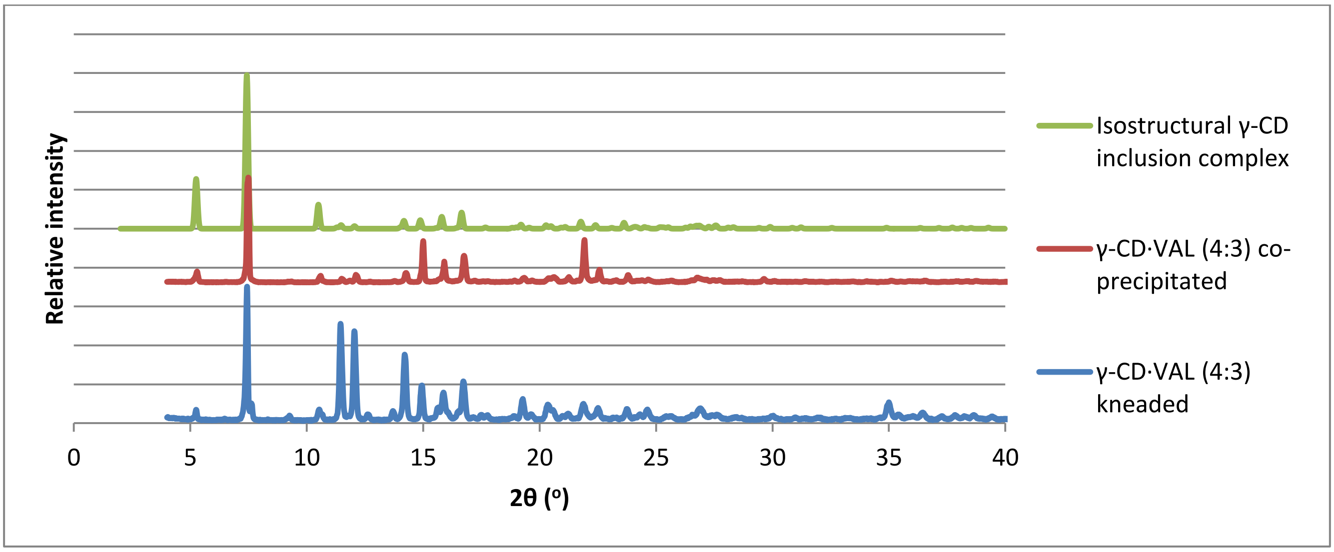

Figure 5.22: The PXRD patterns of an isostructural γ-CD inclusion complex that crystallizes in $P42_12$, and the γ-CD·VAL inclusion complex produced *via* co-precipitation (4:3) and kneading (4:3).[7]

Hot Stage Microscopy (HSM) analysis for γ-CD·VAL

Figure 5.23 displays a series of micrographs for the analysis of the complex crystals immersed in silicone oil and heated at 10 K.min^{-1}. The first micrograph, Image 1, was recorded at 26.9 °C and depicts the features of the γ-CD·VAL inclusion complex crystal before heating. At 103.2 °C, (Image 2) the bubbling commenced slowly along with the onset of opacity. This indicates that the water lost through bubbling was water from the crystal structure, as the crystallinity simultaneously decreased as shown by the onset of opacity in the crystal. This image also suggests that there was no surface water on the crystal, since it became opaque with the first sign of bubbling, and thus is indicative of water loss only from the crystal structure. The bubbling reached a peak at 123.6 °C (Image 3) until it completely stopped at 153.7 °C (Image 4). Throughout both of these processes the opacity increased; however, full opacity was achieved at 199.6 °C as displayed in Image 5. In addition, the onset of decomposition occurred at 293.7 °C (Image 6) and decomposition bubbles were sighted at 305.7 °C (Image 7). The bubbling became vigorous at 333.9 °C (Image 8) until the crystal was fully decomposed at 375.7 °C, as depicted in Image 9.

Figure 5.23: A series of micrographs from the HSM analysis of γ-CD·VAL.

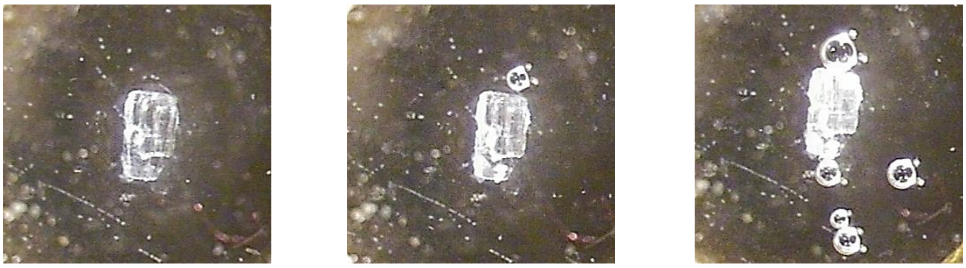

Image 1: The initial appearance of γ-CD·VAL at 26.9 °C.

Image 2: At 103.2 °C the first appearance of bubbling, as well as the onset of opacity, occurred.

Image 3: The most vigorous bubbling occurred at 123.6 °C.

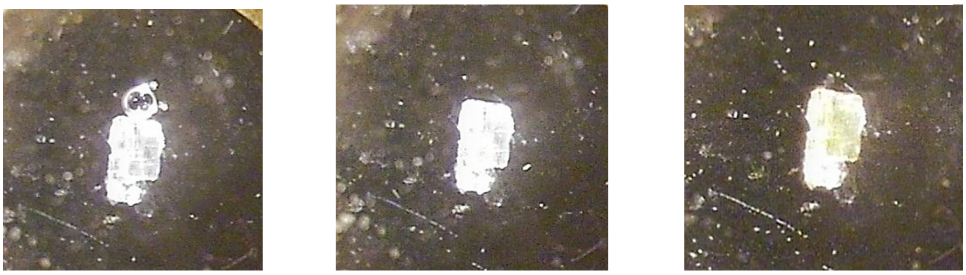

Image 4: The bubbling completely stopped at 153.7 °C.

Image 5: Full opacity occurred at 199.6 °C.

Image 6: The onset of decomposition occurred at 293.7 °C.

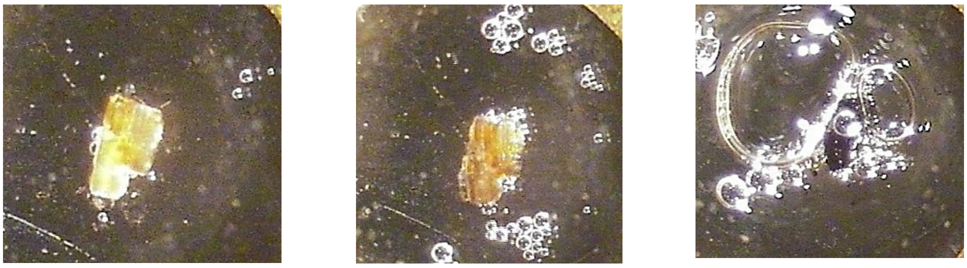

Image 7: Decomposition bubbles appeared at 305.7 °C.

Image 8: At 333.9 °C the decomposition bubbling became vigorous.

Image 9: At 375.7 °C the crystal was fully decomposed.

Thermal Gravimetric Analysis (TGA) of γ-CD·VAL

The TGA trace signified two distinct mass losses for the γ-CD·VAL inclusion complex which occurred over the temperature range 21.7 – 400.0 °C, as depicted in Figure 5.24. A mass loss of 16.4 ± 0.6 % (n = 3) was associated with the first thermal event, which took place between 21.7 and 112.3 °C. This initial mass loss was attributed to the loss of water molecules from the γ-CD·VAL inclusion complex. The second thermal event took place between 265.3 and 375.8 °C and was associated with a mass loss of 71.4 %, which represented the decomposition of the anhydrous γ-CD·VAL inclusion complex.

In comparison, the loss of water only occurred between 103.2 and 153.7 °C in the HSM analysis, and thus it is evident that these results did not correlate. Furthermore, the onset of decomposition in the HSM analysis (which was at 293.7 °C) also did not correlate with the onset of decomposition in the TGA trace at 265.3 °C.

The number of water molecules calculated to be present in the γ-CD·VAL inclusion complex was 15.3 ± 0.6 as this corresponded to a water mass loss of 16.4 ± 0.6 % (n = 3). The calculation can be viewed in the Appendix under section 9.3.3, p. 41.

In addition, the loss of water also occurred instantaneously after the experiment commenced, as with the α-CD·VAL inclusion complex. The method for drying the γ-CD·VAL inclusion complex crystals followed the same procedure as for the β-CD·VAL inclusion complex, since the overall morphology was similar. Once again this method revealed expected reproducible results and the immediate loss of water is thus a characteristic of the γ-CD·VAL inclusion complex.

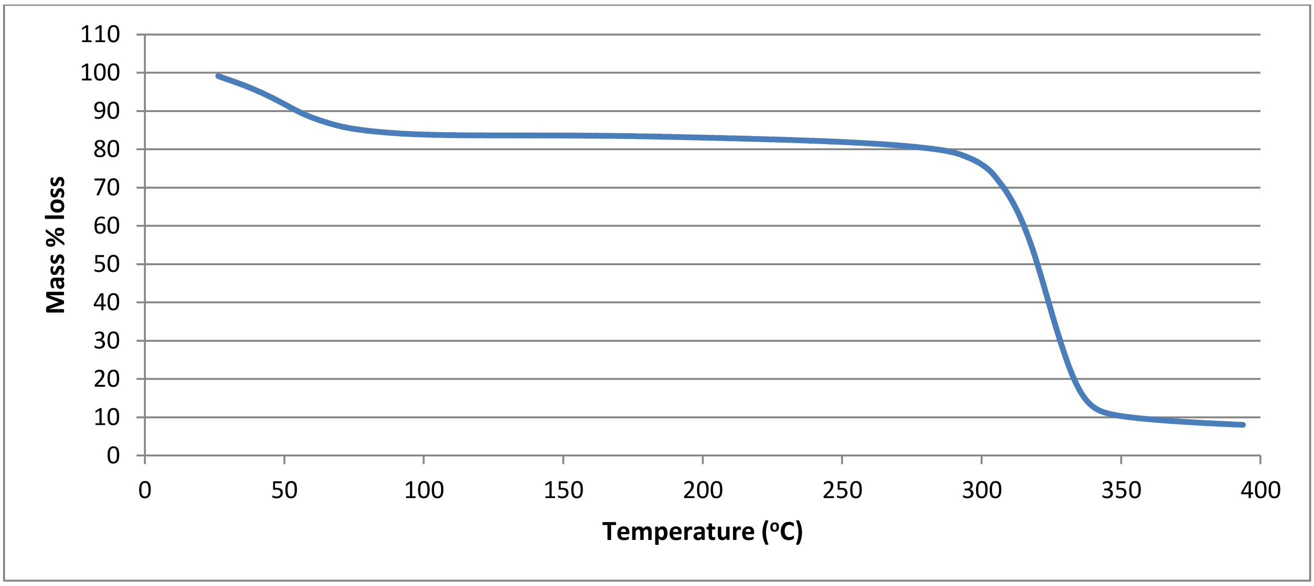

Figure 5.24: Representative TGA trace of the γ-CD·VAL inclusion complex (n = 3).

Differential Scanning Calorimetry (DSC) analysis of γ-CD·VAL

The DSC trace of γ-CD·VAL (n = 2) displayed a single endothermic peak with onset at 21.0 °C, while the peak occurred at 82.8 ± 0.1 °C (Figure 5.25). Unlike the DSC traces of α-CD·VAL and β-CD·VAL, that of γ-CD·VAL indicated the loss of water to be a single event. This is further confirmed by the TGA and HSM analyses. Firstly, in the TGA analysis, there was a single mass loss for dehydration between 21.7 and 112.3 °C, and this correlated well with that of the DSC analysis. Secondly, with reference to the HSM analysis, a single event of bubbling was observed. This was attributed to the loss of water which occurred between 103.2 and 153.7 °C. The temperature correlations between the HSM and DSC experiments were not precise; however, this tendency is often expected.

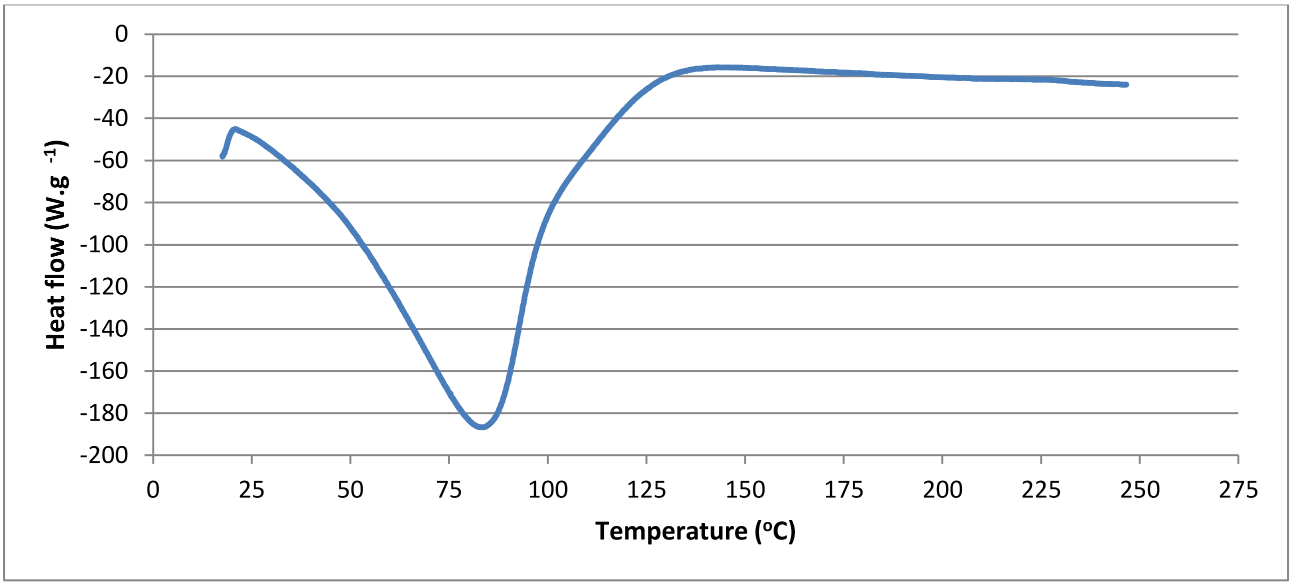

Figure 5.25: Representative DSC trace of γ-CD·VAL (n = 2).

Single Crystal X-ray Diffraction (SCXRD) analysis

Data-collection and space group determination

The PXRD analysis of the complex had indicated the tetragonal space group $P42_12$, and γ-CD complex crystals crystallizing in this space group generally have unit cell dimensions a ~ 23.8 Å, c ~ 23.1 Å. However, careful determination of the unit cell of the γ-CD·VAL complex at the chosen data-collection temperature of 173(2) K yielded a = 23.702(1) Å, c = 45.934(6) Å, i.e. a unit cell with a c-axis length that is approximately double that usually observed. This phenomenon is known to occur occasionally when a crystal is cooled to low temperatures. However, low-temperature data-collection was pursued, since this has potential for revealing the guest molecule in γ-CD complex structures. The intensity-weighted reciprocal lattice indicated that the Laue group was 4/*mmm*, confirming the tetragonal system previously deduced from the PXRD analysis described above. Likewise, the space group $P42_12$, also deduced from the PXRD analysis, was confirmed from the conditions limiting possible reflections, as listed in Table 5.11. Even though this space group is extremely rare, it is the one which characterises the most common crystal packing arrangement of γ-CD inclusion complexes.[14]

Table 5.11: The conditions limiting possible reflections for the crystal of γ-CD·VAL.

Number	Conditions limiting possible reflections	Deduction
1	hkl: none	Primitive lattice
2	h00: h = 2n, (0k0: k = 2n)	Twofold screw axis parallel to the a-axis (and to the b-axis, which is identical to the a-axis by symmetry)
3	00l: none	-

Structure solution and refinement

The intensity-weighted reciprocal lattice was inspected and it was found that there was an alternation of high and low intensity reflections with increasing l-index (Figure 5.26). This indicated the presence of a pseudo-translation of c*/2 implying that the contents of the unit cell from z = 0 to ½ was not identical to that in the interval z = ½ to 1, the differences between them resulting in the very weak intensities in the layers with l = 2n+1. However, this also indicated that a trial model for the structure could be constructed by repeating the structural model contained within the interval z = 0 to ½ within the interval z = ½ to 1, as described in detail below.

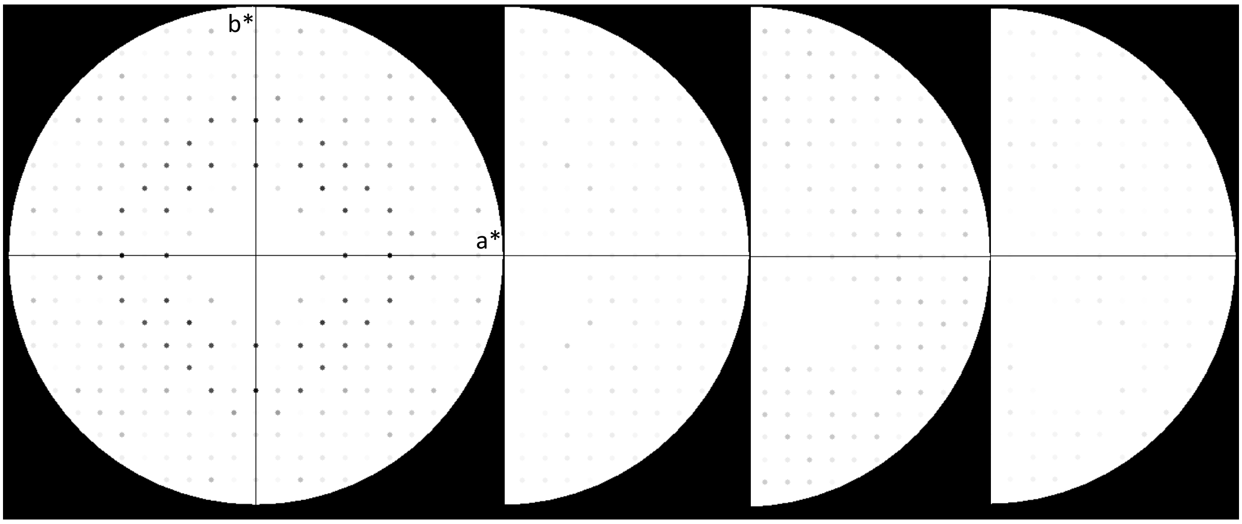

Figure 5.26: The intensity-weighted reciprocal lattice images indicating the alternating high and low intensity reflections in consecutive levels from hk0 to hk3.

The method of isomorphous replacement was employed to obtain the trial model for the γ-CD·VAL inclusion complex. However, owing to the fact that the c-axis had doubled in length relative to the typical value, additional manipulation of the host atomic co-ordinates of a known γ-CD complex with a conventional unit cell was necessary to generate a trial model for the new complex. Thus, a γ-CD inclusion complex that crystallized in the same space group and had very similar unit cell parameters was selected as a template from the CSD. The co-ordinates of the asymmetric unit (ASU) of the template inclusion complex were placed in the .ins file of γ-CD·VAL. However, in order to account for the approximately doubled c-axis length of the γ-CD·VAL complex, (a) the full unit cell content was generated by adding a duplicate set of co-ordinates with a translation of 0.5 added to each of their z-co-ordinates, and (b) the z-co-ordinates of all atoms were finally scaled by the factor c/c′, where c is the length of the unique axis of the γ-CD·VAL complex and c′ that of the template structure. The trial (ASU) thus generated is displayed in Figure 5.27 below. It consisted of six pairs of glucose rings. Operation of the fourfold rotational symmetry parallel to the c-axis generates six complete γ-CD molecules from the ASU.

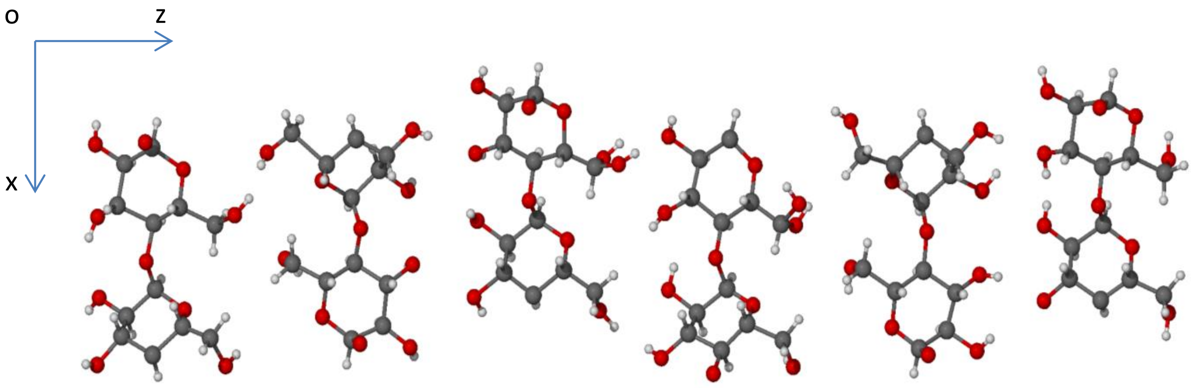

Figure 5.27: ASU of γ-CD·VAL. The water molecules were removed for clarity.

The trial structure was refined isotropically with SHELXL-97,[9] resulting in reasonable thermal parameters for the majority of the atoms. However, attempts to refine the host atoms anisotropically in a stepwise manner failed, as indicated by 'non-positive definite' warnings and reversion to isotropic modelling followed in such cases. The hydrogen atoms were placed in idealised positions with U_{iso} values 1.2 times those of their parent atoms. Owing to the fourfold rotational symmetry axis running through the centre of the cavity of each CD molecule, it was not possible to locate the guest molecule (a typical situation with γ-CD complexes). There were only six difference electron density peaks ($\Delta\rho_{max}$ = 1.0 e.Å^{-3}) that could be attributed to the guest molecule within the continuous channel formed by the six γ-CD molecules. In addition, 45 sites of water oxygen atoms were observed in the ASU, of which the majority were partially occupied (Figure 5.28). The number of water molecules present per γ-CD molecule was 16.3 which correlated with the TGA results indicating 15.3 ± 0.6 water molecules per γ-CD molecule. Figure 5.28 also displays the presence of the water molecules in the ASU, which were all external to the cavity.

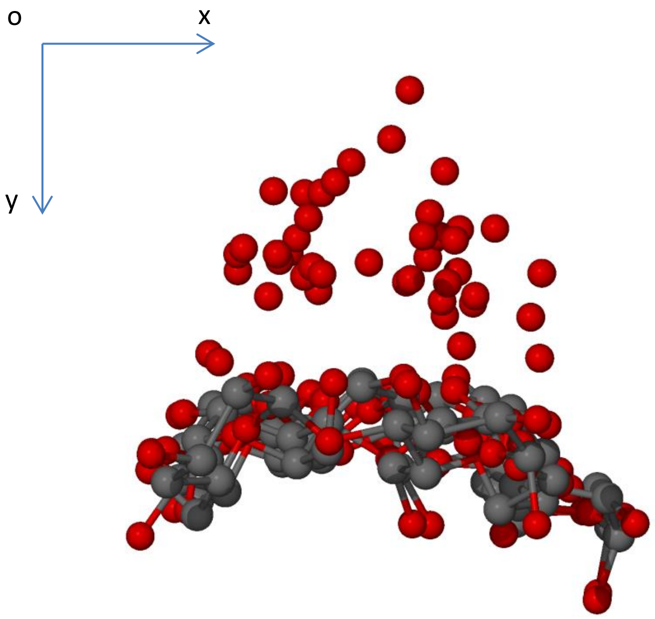

Figure 5.28: The presence of the water molecules which are all external to the channel of γ-CD·VAL. For simplicity, only the ASU is shown. Hydrogen atoms were omitted for clarity.

As expected, the R_1-factor for the γ-CD·VAL inclusion complex model was abnormally high at a value of 24.0 %. This was expected since the model was incomplete and could not be improved any further. The crystal data for this inclusion complex are displayed in Table 5.12.

Table 5.12: The crystal data and refinement parameters for the γ-CD·VAL inclusion complex.

Parameter	**Value**
Complex formula	$C_{48}H_{80}O_{40}\cdot(C_8H_{16}O_2)_{0.75}\cdot15.3H_2O$
Formula weight (g.mol^{-1})	1680.91
Temperature (K)	173(2)
Wavelength (Å)	0.71073
Crystal system	Tetragonal
Space group	$P42_12$
a (Å)	23.7023(14)
c (Å)	45.934(6)
α (°)	90
β (°)	90
γ (°)	90
Volume (Å^3)	25806(5)
Z	12
Calculated density (g.cm^{-3})	1.298
μ (mm^{-1})	0.118
F (000)	10812
Crystal size (mm)	0.200 x 0.210 x 0.360
θ-Range scanned (°)	2.47 – 24.16
Index range	h: -28, 23; k: -23, 27; l: -54, 54
No. of reflections collected	106046
No. of unique reflections	22964
Data completeness (%)	99.9
Data/restraints/parameters	22964/16/772
S (Goodness-of-fit on F^2)	2.866
Final R indices R_1, wR_2, [I > 2σ(I)]	0.2403, 0.6031
R Indices, all data (R_1, wR_2)	0.2631, 0.6214
Largest diff. peak and hole (e. Å^{-3})	1.31, -1.53

Crystal Packing

The γ-CD·VAL inclusion complex structure contains six independent γ-CD molecules, namely A, B, C and A′, B′, C′ (Figure 5.29). This unusual crystallographic repeat unit consists of two sets of three molecules in the ASU, which arrange themselves as shown.[14] In other words, a head-to-tail motif occurs between C and A′, a tail-to-tail motif occurs between the molecular pair B and C, and lastly, a head-to-head motif occurs between the molecular pair A and B.[14] This type of structural arrangement, involving, however, just three molecules (A, B, C) in the ASU, has been observed in all the isostructural γ-CD inclusion complexes.[7]

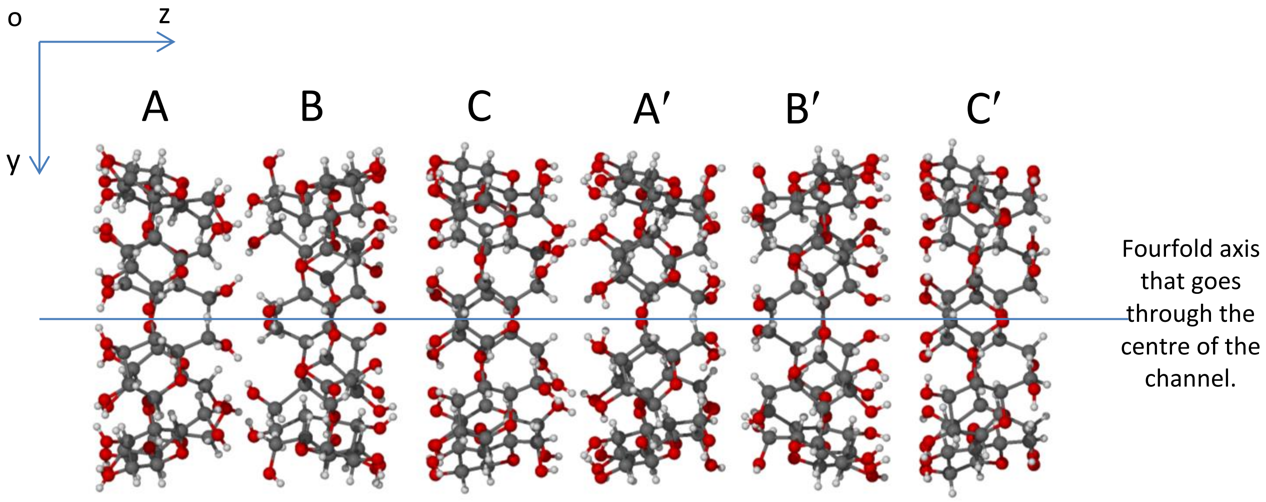

Fourfold axis that goes through the centre of the channel.

Figure 5.29: The packing arrangement of the host molecules in the complex γ-CD·VAL which displays the unique crystallographic repeat unit, as well as the fourfold axis parallel to the c-axis.

Figure 5.30 displays a view down the c-axis of the channels in the unit cell in which the guest molecules are included, but not observed. The water molecules occupy the spaces between the columns and they are responsible for the adhesion of the columns *via* water-water and water-host O-H···O hydrogen bonding.

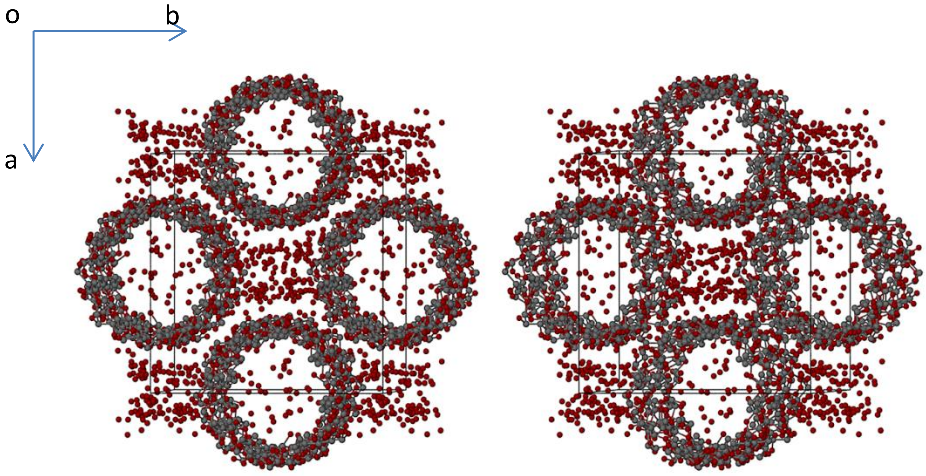

Figure 5.30: A stereoview of γ-CD·VAL viewed down the c-axis which displays the packing arrangement of each CD molecule. Water molecules and hydrogen atoms are removed for clarity.

PXRD analysis

The PXRD pattern of γ-CD·VAL produced by co-precipitation correlated very well with the calculated PXRD pattern of γ-CD·VAL with regard to the 2θ values. However, the intensities are significantly different, an effect attributed to preferred orientation. This is further promoted by the columnar morphology of the tetragonal complex which would even be evident in finely ground samples. Nevertheless, it can be concluded that the single crystal selected for the analysis was representative of the bulk material (Figure 5.31).

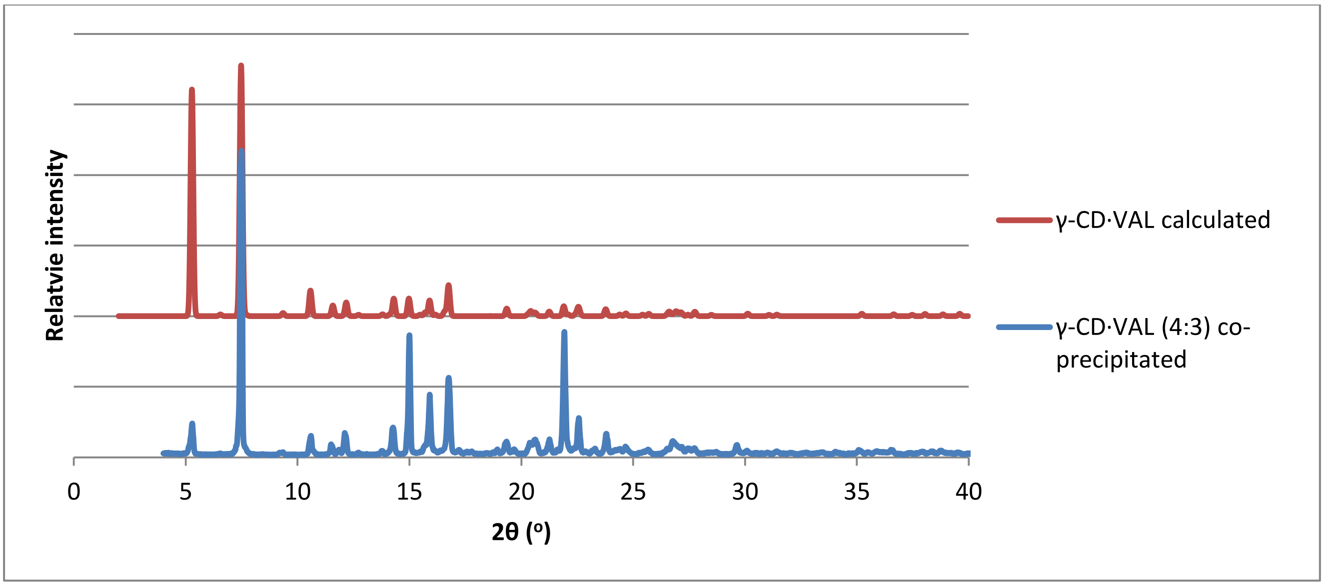

Figure 5.31: The PXRD pattern calculated from a single crystal X-ray structure of γ-CD·VAL and the PXRD pattern of γ-CD·VAL prepared *via* co-precipitation.

In conclusion, it is evident that the molecular formula for the γ-CD·VAL inclusion complex is (γ-CD)·(VAL)$_{0.75}$·15.3H_2O. Even though the results from the X-ray analysis were very limited and the model was incomplete, the present study, based on sound analytical techniques, has amply demonstrated the successful synthesis of the γ-CD·VAL inclusion complex.

5.3.1.4) Solubility analysis of the native CD inclusion complexes with valproic acid

An aqueous solubility investigation was performed for the α-CD·VAL, β-CD·VAL and γ-CD·VAL inclusion complexes that were produced *via* co-precipitation as well as those produced *via* kneading. The method that was followed is described in the Experimental Methods (Chapter 2) under section 2.9.2, p. 24. Unfortunately, a more accurate solubility determination method, for example UV-vis spectrophotometry, could not be performed due to the λ_{max} value of the guest, valproic acid, occurring below 200 nm. As a result, the 'actual' solubility value lies between the estimated values based on the penultimate and the final successive masses of complex material added to the solvent (water) of known volume (3.0 cm^3) at 23 °C. The solubility results obtained were compared to the solubility value of valproic acid quoted as 1.3 $mg.cm^{-3}$,[15] even though the temperature was unspecified. This literature value was presumably recorded at 'room temperature', since an experiment conducted by the author of this dissertation appeared to reflect this. Table 5.13 displays the solubility results, where $S_{complex}$ is the aqueous solubility of the CD complex with valproic acid, and S_{VA} is the aqueous solubility of valproic acid. A sample calculation can be viewed in the Appendix under section 9.4.1, p. 42.

Table 5.13: Aqueous solubility investigation for the α-CD·VAL, β-CD·VAL and γ-CD·VAL inclusion complexes at 23 °C.

Number	**CD complex**	**Range of mass dissolved (mg)**	**Solubility range of valproic acid ($mg.cm^{-3}$)**	**Approximate solubility enhancement ratio ($S_{complex}/S_{VA}$)**
1	α-CD·VAL (produced *via* co-precipitation)	24.14 – 24.54	0.497 – 0.505	0.39
2	α-CD·VAL (produced *via* kneading)	23.89 – 24.74	0.492 – 0.510	0.39
3	β-CD·VAL (produced *via* co-precipitation)	16.74 – 17.28	0.558 – 0.576	0.44
4	β-CD·VAL (produced *via* kneading)	15.56 – 16.27	0.519 – 0.543	0.41
5	γ-CD·VAL (produced *via* co-precipitation)	16.61 – 17.23	0.356 – 0.369	0.28
6	γ-CD·VAL (produced *via* kneading)	24.37 – 25.26	0.522 – 0.541	0.41

The approximate solubility enhancement ratio ($S_{complex}/S_{VA}$) was calculated by averaging the two values from each solubility range of valproic acid. The solubility values for both the kneaded and co-precipitated material of the same complex were very similar for α-CD·VAL and β-CD·VAL. However, the solubility values differed significantly between the γ-CD·VAL inclusion complexes that were prepared *via* kneading and co-precipitation. A possible explanation for this is that different textures were obtained for the two materials owing to the different methods employed; however, further experimentation would be needed to verify this.

The solubility enhancement ratio indicated that there was an approximate 3 fold decrease in the aqueous solubility of valproic acid in all three inclusion complexes (produced *via* both co-precipitation and kneading) in comparison to the native drug, namely valproic acid (1.3 mg.cm^{-3} at an unspecified temperature).[15] Possible applications for a slow release form of valproic acid could be investigated owing to the fact that a lower aqueous solubility was obtained. General comments on the potential benefits of CD inclusion of valproic acid for drug delivery are provided in the final chapter of this dissertation.

5.3.2) Inclusion of valproic acid in methylated cyclodextrins

The three methylated cyclodextrins (CDs), which include heptakis(2,6-di-*O*-methyl)-β-cyclodextrin (DMB), heptakis(2,3,6-tri-*O*-methyl)-β-cyclodextrin (TMB) and hexakis(2,3,6-tri-*O*-methyl*)*-α-cyclodextrin (TMA)*,* formed authentic inclusion complexes with valproic acid. These new products will be referred to as DMB·VAL, TMB·VAL and TMA·VAL. Furthermore, the DMB·VAL and TMA·VAL inclusion complexes produced adequate single crystals for analysis and structural characterisation.

5.3.2.1) The DMB·VAL inclusion complex

Method of preparation

A DMB·VAL inclusion complex was successfully synthesized in an equimolar ratio, which was later confirmed by a ^{1}H NMR analysis. This inclusion complex could be prepared by adding 46.16 mg (0.03467 mmol) of DMB to 0.6 cm^3 of water which was stirred vigorously at 298 K until the DMB was fully dissolved. Subsequently, 5 mg (0.03467 mmol; 5.434 µl) of valproic acid was added to the vial containing the DMB solution. (The valproic acid was added in minimal excess in order to ensure that all the DMB had reacted). The resultant solution was stirred overnight at 298 K. Initially, when the valproic acid was added to the solution of DMB, it formed an oily immiscible layer, which subsequently coated the sides of the vial. This same incidence was observed for the native CD experiments as described previously and this immiscible oily layer dissolved after the overnight stirring. Even though the valproic acid was dissolved in the minimum volume of the aqueous solution, temperature cycling was still employed as a precaution, in case complexation had not taken place.[a] The solution was heated to 70 ^{o}C while stirring for 10 minutes and then rapidly cooled to 4 ^{o}C while stirring. This process was repeated four times and the solution in the vial was subsequently filtered into a clean vial, which was sealed and placed in the oven at 60 ^{o}C. After three days, single crystals of the complex had precipitated.

---

[a] A subsequent experiment was performed where temperature cycling was not employed. The result was that an inclusion complex was not formed. One experiment cannot validate this, as multiple experiments would have to be performed to confirm it. However, owing to the expense of the material, this was considered inappropriate and thus temperature cycling was instead employed as a precaution.

Crystal morphology

Two distinct types of crystal morphologies were observed in the vial containing the DMB·VAL inclusion complex (Figures 5.32A and 5.32B). The crystals that grew on the bottom of the vial formed conglomerates of rhombic-shaped crystals where a few of them were slightly opaque instead of transparent (Figure 5.32A). However, the crystals that grew on the sides of the vial were plate-like and slightly powdery, and also ranged from transparent to slightly opaque (Figure 5.32B). Solutions prepared by dissolving crystals of each morphology in DMSO-d_6 at 298 K were analysed separately by ^{1}H NMR solution-state spectroscopy in order to establish their composition.

Figure 5.32A: Crystal morphology of the DMB·VAL inclusion complex isolated from the bottom of the vial.

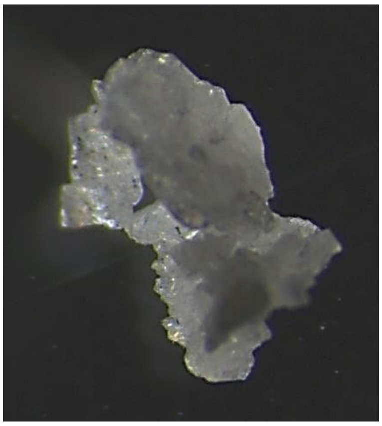

Figure 5.32B: Crystal morphology of the DMB·VAL inclusion complex isolated from the sides of the vial.

^{1}H NMR analysis of DMB·VAL

The results of the ^{1}H NMR solution-state spectral analysis revealed that crystals of both morphologies had host-guest stoichiometric composition 1:1 and thus appeared to represent complexes, generically named DMB·VAL. Representative spectral results are listed in Table 5.14 below and the original ^{1}H NMR spectra can be viewed in the Appendix under section 9.5.1, p. 43.

Table 5.14: The ^{1}H NMR analysis of DMB·VAL.

Assignment	**δ (ppm)**	**Integration**	**Proton representation (per molecule)**	**Stoichiometric ratio**	**Stoichiometric ratio (integer)**
2 x C$\underline{H}_3$ (valproic acid)	0.84-0.88	1.00*	6H	1.00	1
4 x C$\underline{H}_2$ (valproic acid)	1.21-1.52	1.51	8H	1.13	1
OME (DMB)	3.26	3.69	21H	1.05	1
OME (DMB)	3.49-3.52	3.35	21H	1.04	1

*reference integral

Fourier Transform Infrared (FT-IR) spectroscopic analysis of DMB·VAL

The identity of the material as a DMB·VAL inclusion complex was also confirmed with FT-IR spectroscopy (Figure 5.33). The full FT-IR spectrum can be viewed in the Appendix under section 9.5.2, p. 43. The C=O stretching frequency of pure valproic acid occurred at 1702 cm^{-1}, while in the putative complex it was observed at a significantly higher frequency of 1731 cm^{-1}, indicating a reduction in the extent of hydrogen bonding of the C=O group in the complex relative to that in the pure acid.

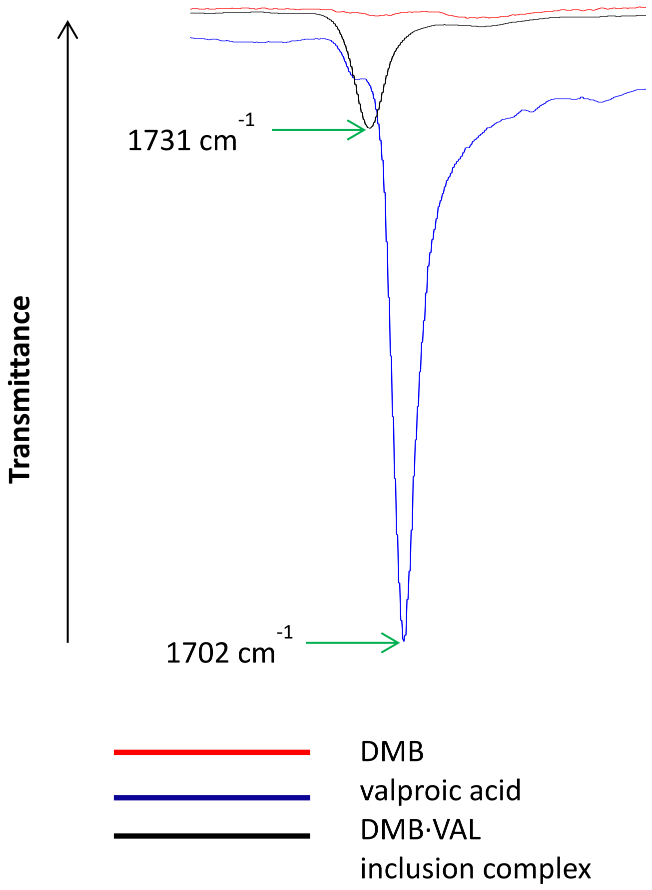

Figure 5.33: FT-IR spectra of DMB (red), valproic acid (blue) and DMB·VAL (black).

Powder X-ray Diffraction (PXRD) analysis of DMB·VAL

Both morphological forms of DMB·VAL produced *via* co-precipitation were confirmed to be the same phase by PXRD analysis. The PXRD pattern of DMB·VAL, produced *via* co-precipitation indicated that it was not isostructural with any other β-CD derivative inclusion complexes. Furthermore, the DMB·VAL inclusion complex that was synthesized *via* co-precipitation was not replicated with the kneading experiment. An unknown species was produced *via* kneading, since its PXRD trace did not match the PXRD traces of either a known polymorph of DMB, DMB·VAL (produced by co-precipitation) or any inclusion complexes of β-CD derivatives. Consequently, this product may either be a new polymorph of DMB or a DMB complex with no isostructural counterparts. Furthermore, traces of DMB may also be present in the PXRD trace of the product obtained *via* kneading, as some peaks coincide with the peaks from the PXRD pattern of a known polymorph of DMB (Figure 5.34). The kneading method for this product followed the general procedure, where the starting reagents (DMB and valproic acid) were kneaded for 30 minutes in an equimolar ratio with a small amount of water (Figure 5.34). However, producing a PXRD trace displaying high product crystallinity presented certain difficulties, as the kneading process had to be very specific and involved a strict time limit of only 30 minutes (no more and no less). In addition, the sample could not dry out while kneading and it had to be applied as a slurry to the zero background holder in the diffractometer. Any deviations from this method led to the material acquiring a rather amorphous character.

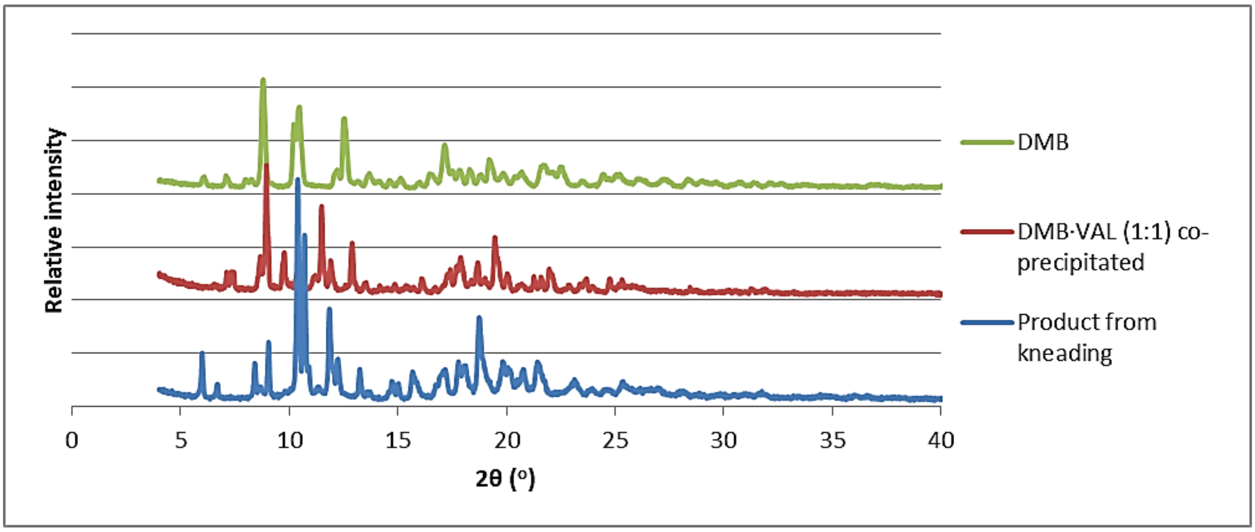

Figure 5.34: The PXRD patterns of the crystal form of DMB employed in this study (polymorph 1, CSD refcode QIYKEO), DMB·VAL produced *via* co-precipitation (1:1), and a product from kneading DMB and valproic acid.

Hot Stage Microscopy (HSM) analysis of DMB·VAL

The DMB·VAL inclusion complex was subjected to a heating rate of 10 K.min^{-1} while placed in silicone oil. The loss of crystallinity and the onset of decomposition are observed in the progression of micrographs (Figure 5.35). The initial photograph, Image 1, was taken at 29.7 °C to depict the features of the DMB·VAL complex crystal before heating. The onset of opacity commenced at 59.2 °C (Image 2) until it became fully opaque at 199.8 °C (Image 3) and this process is associated with the loss of crystallinity. Furthermore, the decomposition process is displayed by the following three images (Image 4, 5 and 6) where the onset of decomposition occurred at 294.4 °C, until it was fully decomposed at 342.8 °C.

Figure 5.35: A series of micrographs from the HSM analysis of DMB·VAL.

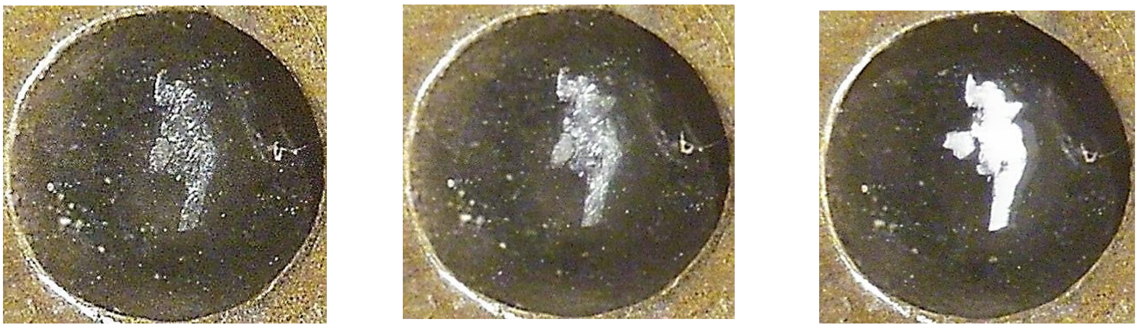

Image 1: The initial appearance of DMB·VAL at 29.7 °C.

Image 2: The onset of opacity at 59.2 °C.

Image 3: The crystal became fully opaque at 199.8 °C.

Image 4: The onset of decomposition occurred at 294.4 °C.

Image 5: The continuation of decomposition at 333.8 °C.

Image 6: The decomposition melt occurred at 342.8 °C.

Thermal Gravimetric Analysis (TGA) of DMB·VAL

The TGA trace (n = 2) of the co-precipitated DMB·VAL inclusion complex indicated two prominent mass losses which occurred over the temperature range 23.1 – 400.0 °C, as depicted in Figure 5.36. A mass loss of 2.1 ± 0.3 % was associated with the first thermal event, which took place between 23.1 and 41.9 °C. This was accredited to the loss of water molecules from the DMB·VAL inclusion complex. Furthermore, the second thermal event, which took place between 300.5 °C and 390.7 °C, was associated with a mass loss of 84.3 % and represented the decomposition of DMB·VAL. In comparison to the HSM analysis, the loss of water was not observed, possibly because there was a miniscule amount of sample present; however, with regard to the onset of decomposition, the HSM and TGA results correlated closely, within 6.1 °C.

A water mass loss of 2.1 ± 0.3 % for this inclusion complex is equivalent to 1.8 ± 0.3 water molecules per complex unit. This calculation can be viewed in the Appendix under section 9.5.3, p. 44.

The method for drying the DMB·VAL crystals followed the same procedure as that for the β-CD·VAL complex as the morphology was very similar.

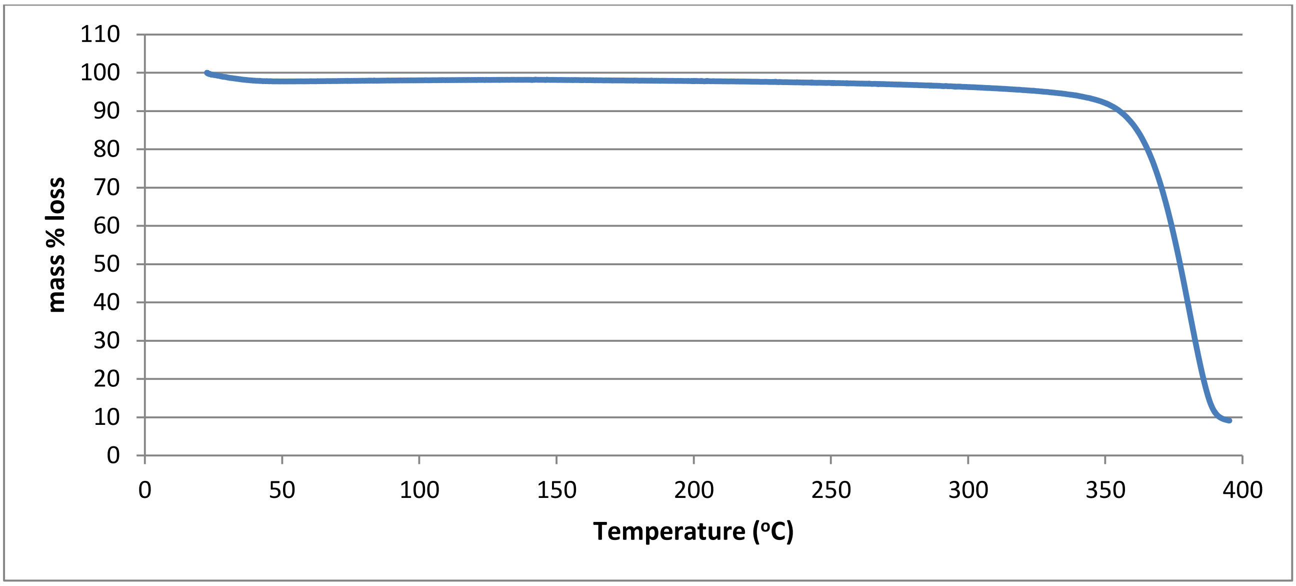

Figure 5.36: Representative TGA trace of the DMB·VAL inclusion complex (n = 2).

Differential Scanning Calorimetry (DSC) of DMB·VAL

The DSC trace (n = 2) of DMB·VAL prepared by co-precipitation indicated only a single shoulder which occurred over the temperature range 25.5 – 49.0 °C (Figure 5.37). This endothermic event was characteristic of the loss of water, as it correlated with the temperature of the mass loss of water in the TGA trace. The DSC trace did not reflect any correlation with the HSM experiment over this temperature range, as no bubbling was observed during the HSM experiment.

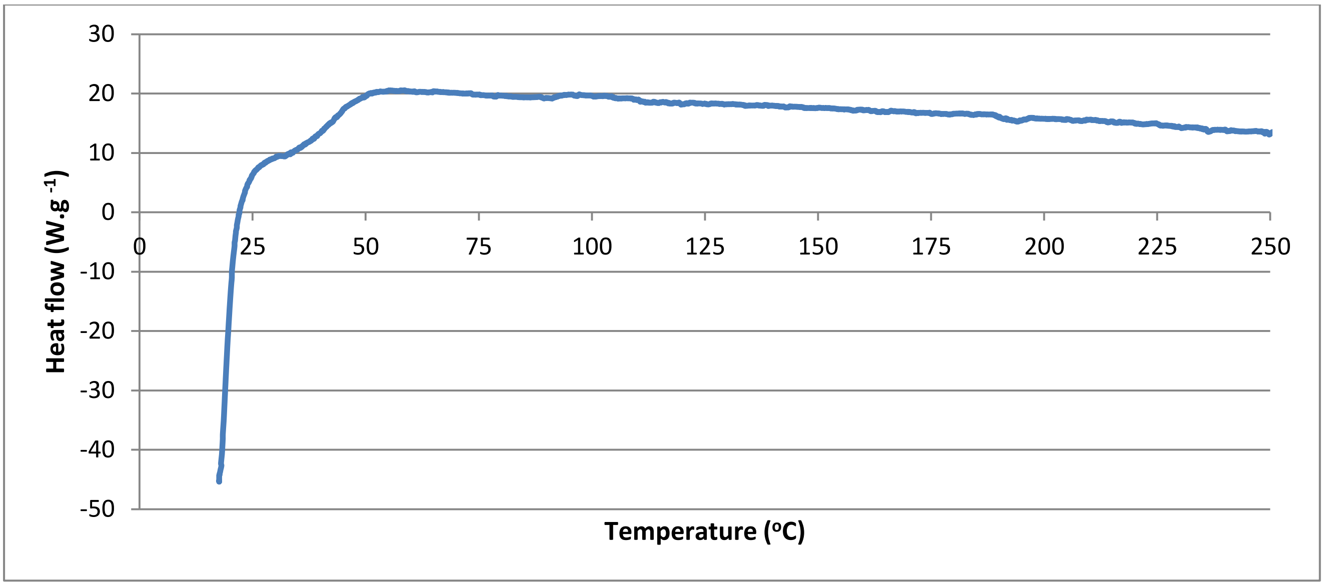

Figure 5.37: Representative DSC trace of DMB·VAL (n = 2).

Single Crystal X-ray Diffraction (SCXRD) analysis

Data-collection and space group determination

The intensity data for DMB·VAL were collected from a single, approximately cubic-shaped crystal at 173(2) K. The symmetry of the intensity-weighted reciprocal lattice was $\bar{1}$, indicating the triclinic crystal system. Since CD molecules are chiral, the only possible space group option was P1, an assignment that was confirmed by the value of $|E^2-1|$, namely 0.774, obtained using the program XPREP. Furthermore, from density and unit cell volume considerations a value of Z = 2 was predicted, indicating that the asymmetric unit (ASU) contained two independent DMB molecules.

Structure solution and refinement

The structure was solved using SHELXD-97,[9] since SHELXS-97 failed, even though the number of phase sets in the TREF command was set to very large numbers. With regard to SHELXD-97, the instruction "FIND 151" was inserted with the PLOP command ranging from 60 to 240 at intervals of 20. This gave a solution with a CC value of 79.6 and most of the atoms of the two independent host molecules appeared in the E-map. The model was refined with SHELXL-97. The atoms of the host molecules were initially refined isotropically and subsequently anisotropically; however, there were several atoms whose thermal ellipsoids were physically unreasonable and for these, reversion to the isotropic model followed. In addition, two primary hydroxyl oxygen atoms were disordered over two positions. The general treatment for this, as mentioned previously, involved assigning s.o.f.s of x and 1-x (x = a free variable) to the respective major and minor components of a disordered hydroxyl group. In addition, the bond lengths C6-O6 and C6-O7 were fixed at 1.40 Å with σ = 0.01 Å *via* a DFIX restraint. The s.o.f.s of the major components of the disordered oxygen atoms O6A4 and O7B4 refined to 0.55(2) and 0.58(2) respectively.

Once the host molecules had been refined to an adequate level, the electron density peaks in the difference Fourier map that belonged to the respective guest molecules were assigned. The atoms were identified by studying the geometrical features of the $\Delta\rho$ peaks, which had lower than normal intensities, indicating relatively high guest thermal motion. The C-C bonds were all constrained at a distance of 1.50 Å and the C-CO_2 unit was constrained to be planar with an O-C-O angle of 120^o. The guest molecules were refined isotropically as they displayed very large U_{iso} values that ranged from 0.2 to 0.4 $Å^2$. Despite these high U_{iso} values, a full site-occupancy was assumed for all the guest atoms based on the ^{1}H NMR results which had indicated 1:1 host-guest stoichiometry. Refinement of individual isotropic thermal parameters assigned to atoms of the guest molecules produced physically unreasonable and inconsistent values. Hence, global U_{iso} values were assigned to each guest molecule and these refined to 0.225(4) $Å^2$ and 0.221(4) $Å^2$ for guest molecules A and B respectively. These results implied a genuinely high overall thermal vibration of the valproic acid molecules relative to the host molecules. Finally, hydrogen atoms were placed in idealised positions in a riding model on the host and guest molecules and an isotropic temperature factor, which ranged between 1.2 and 1.5 times the value of the U_{iso} value of its parent atom, was assigned to each hydrogen atom. In addition, one of the glucose units in molecule B was fully methylated at the C3 position. This can occur since the DMB employed was only ≥ 98 % pure. The crystallographic data for DMB·VAL are summarised in Table 5.15, the formula in the table taking into account the C3-methylation anomaly.

Table 5.15: The crystal data and refinement parameters for the DMB·VAL inclusion complex.

Parameter	**Value**
Complex formula	$[(C_{56}H_{98}O_{35})_{0.5}(C_{57}H_{100}O_{35})_{0.5}]\cdot C_8H_{16}O_2\cdot 1.8H_2O$
Formula weight (g.mol^{-1})	1514.99
Temperature (K)	173(2)
Wavelength (Å)	0.71073
Crystal system	Triclinic
Space group	P1
a (Å)	10.396(2)
b (Å)	15.111(3)
c (Å)	25.494(5)
α (°)	83.247(4)
β (°)	81.556(4)
γ (°)	89.475(4)
Volume (Å^3)	3934(1)
Z	2
Calculated density (g.cm^{-3})	1.279
μ (mm^{-1})	0.106
F (000)	1632
Crystal size (mm)	0.100 x 0.220 x 0.510
θ-Range scanned (°)	2.25 – 21.62
Index range	h:-12, 12; k:-17, 17; l:-30, 30
No. of reflections collected	44688
No. of unique reflections	26358
Data completeness (%)	99.4
Data/restraints/parameters	26358/29/1651
S (Goodness-of-fit on F^2)	1.205
Final R indices R_1, wR_2, [I > 2σ(I)]	0.1075, 0.2953
R Indices, all data (R_1, wR_2)	0.1518, 0.3342
Largest diff. peak and hole (e. Å^{-3})	0.84, -0.47

The water molecules were also identified as described in the Experimental Methods (Chapter 2) under section 2.5, p. 21. A total of four sites were identified to be water oxygen atoms, which equated to 1.9 water molecules per DMB molecule. Table 5.16 lists the refined values for the s.o.f.s and the U_{iso} values for the water molecules. The positions of two of these were identified as having full site-occupancy, and the remaining two water molecules were assigned partial site-occupancies in descending order of their electron density peaks. Initially, the U_{iso} values of the disordered water molecules were constrained to 0.090 Å^2 (the average of the U_{iso} values of O1W and O2W) and their s.o.f.s were allowed to vary. Subsequently, the U_{iso} value was unconstrained and its value converged satisfactorily. The TGA analysis had indicated that 1.8 ± 0.3 water molecules were present per DMB molecule, which correlated very closely with the model which accounted for 1.9.

Table 5.16: The total number of water oxygen sites that were identified, with their respective s.o.f.s and U_{iso} values.

Atom	**s.o.f.**	**U_{iso} (Å^2)**	**Atom**	**s.o.f.**	**U_{iso} (Å^2)**
O1W	1.00	0.090(3)	O3W	0.94(4)	0.101(5)
O2W	1.00	0.102(3)	O4W	0.85(4)	0.101(6)

Molecular structure

The ASU of DMB·VAL is displayed in Figure 5.38. It contains two crystallographically independent DMB molecules, each accommodating a guest molecule in the cavity. In addition, there are four sites that were identified for water molecules, of which two were disordered. The water molecules were located within hydrogen bonding distance of the host molecule and no hydrogen atoms were placed on them, since they were not evident from difference electron density maps.

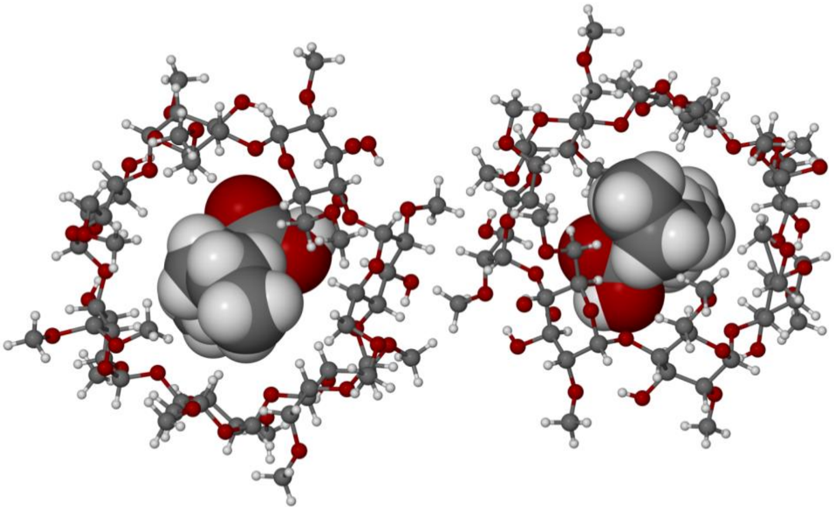

Figure 5.38: The ASU of DMB·VAL.

Host-guest hydrogen bond interactions

Figure 5.39 is a stereoview showing the common mode of inclusion of each of the guest molecules in their respective host cavities. This involves hydrogen bonding of the guest –COOH group to a water molecule, which in turn is hydrogen bonded to an oxygen atom O2 of a glucose residue. Table 5.17 contains the hydrogen bonding data for these interactions as well as those for water-host interactions involving O3W and O4W.

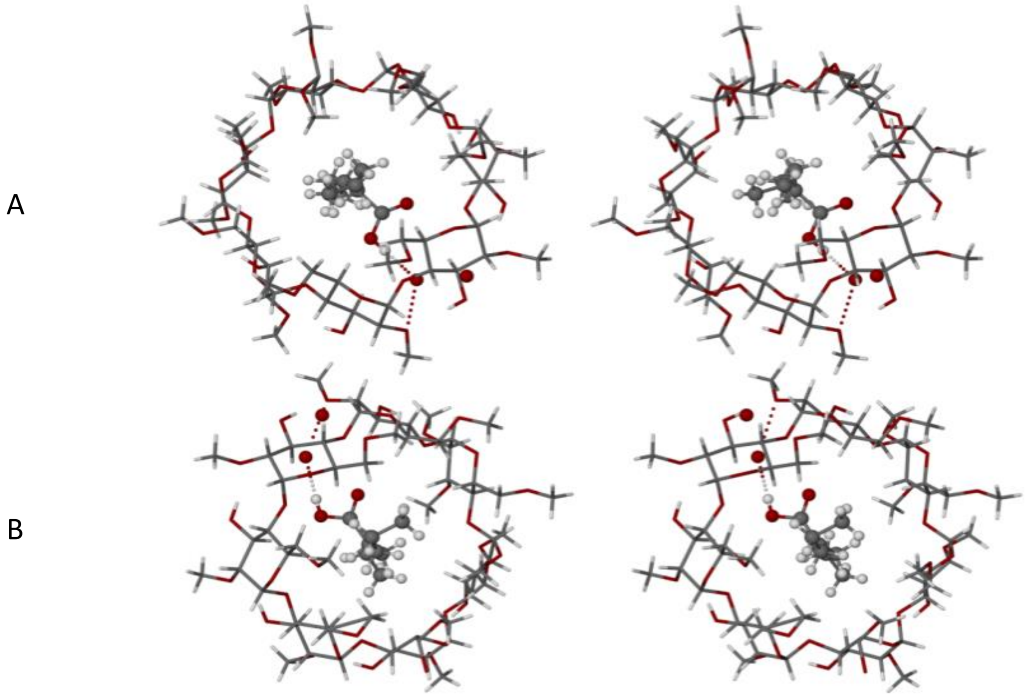

Figure 5.39: A stereoview of the ASU of DMB·VAL.

Table 5.17: The parameters for the intermolecular interactions with the water molecules in DMB·VAL.

Hydrogen bond	D-H (Å)	H···A (Å)	D···A (Å)	D-H···A (°)	Symmetry Code
O1A-H1A···O4W	0.84	1.94	2.78(3)	174	x, y, z
O4W-H*···O2A1	N/A	N/A	2.99(2)	N/A	x, y, z
O1B-H1B···O1W	0.84	2.05	2.88(3)	169	x, y, z
O1W-H*···O2B1	N/A	N/A	2.95(1)	N/A	x, y, z
O3W-H*··· O6A7	N/A	N/A	2.73(2)	N/A	x, y, z
O2W-H*···O6B7	N/A	N/A	2.76(2)	N/A	x, y, z

*Hydrogen atom presence inferred (not located in $\Delta\rho$ synthesis or included in the model)

The absence of hydrogen bonding of the carbonyl oxygen atoms is consistent with the results that were obtained in the FT-IR analysis. Figure 5.39 indicates that there are no hydrogen bonds involving the carbonyl oxygen atoms and thus the C=O stretching frequency in the complex is significantly higher than ν_{CO} in pure valproic acid.

A more detailed view of the host-guest interactions is displayed in the space-filling cutaway representation (Figure 5.40). The guest-water-host hydrogen bonding interactions (e.g. O1A-H···O4W-H···O2A1) are evident and labelled.

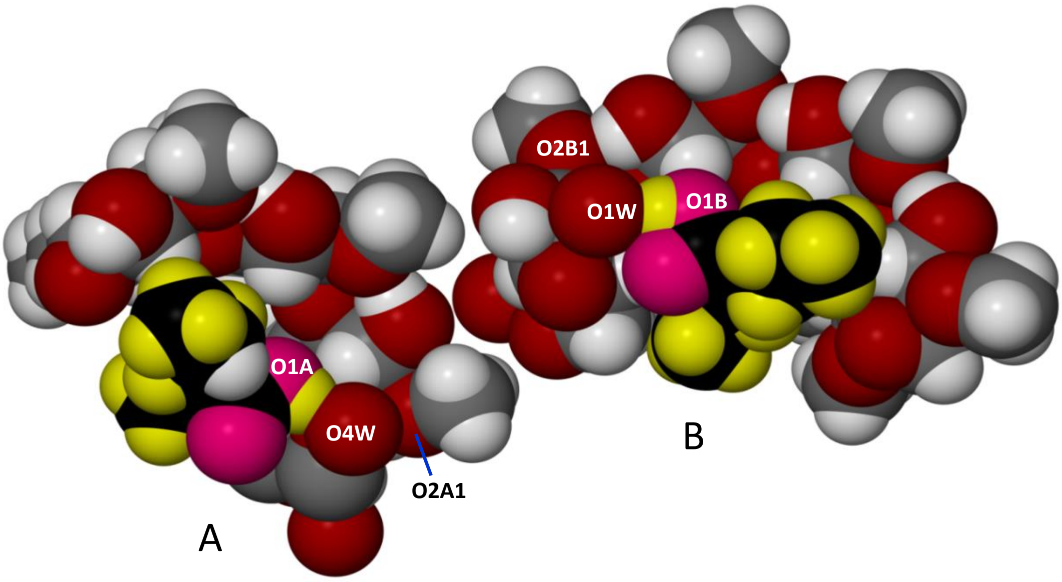

Figure 5.40: A space-filling representation of the cross-section of complex units A and B in the ASU of DMB·VAL that displays the bridging hydrogen bonds. Atoms in the common hydrogen bonding scheme (guest)-COOH···OW···O2(host) are labelled.

Guest molecule conformations

The guest conformations in molecules A and B are slightly different, as displayed in the molecular overlay diagram in Figure 5.41. The diagram displays small differences in the guest conformations, which are confirmed by the RMSD value of 0.644 Å.

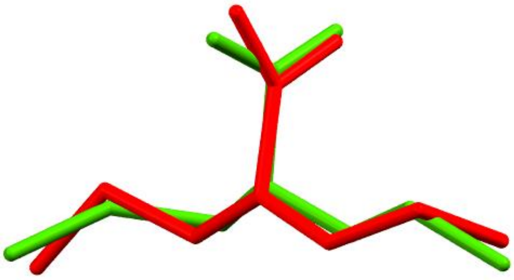

Figure 5.41: The molecular overlap of the included valproic acid molecules A (green) and B (red).

Host intramolecular and intermolecular hydrogen bonding

A belt of O2-H···O3′ intramolecular hydrogen bonds linking contiguous glucose residues was observed on the secondary rings of both DMB molecules (Figure 5.42). These hydrogen bonds reinforced the heptagonal geometry of the host molecule.

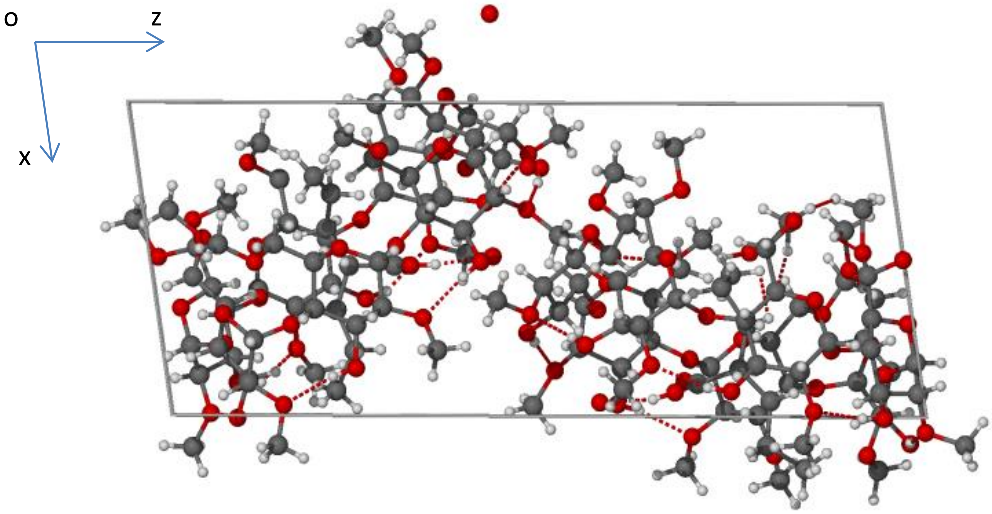

Figure 5.42: The host intramolecular hydrogen bonding.

The hydrogen bonds that involve the DMB molecules were mostly observed to be intramolecular and are mainly of the type O-H···O. There are no hydrogen bond interactions between molecules A and B in the ASU. However, there are a few weak intermolecular interactions, (but these were only of the type C-H···O) which were observed between symmetry generated molecules. These weak interactions occurred between molecules A-A′, B-B′, A-B′ and B-A′ and their respective C···O distances ranged from 3.26(1) Å to 3.49(2) Å. The sum of the van der Waals radii of carbon and oxygen is 3.22 Å, which indicates that these interactions are weak. Nevertheless, collectively they play an important role in holding the DMB molecules of the crystal structure together. Their individual hydrogen bond parameters are summarised in Table 5.18A for molecule A and in Table 5.18B for molecule B.

Table 5.18A: The parameters for the hydrogen bond interactions in DMB·VAL for molecule A.

Interaction type	Hydrogen bond	D-H (Å)	H···A (Å)	D···A (Å)	D-H···A (°)	Symmetry Code
O3-H···O2 Hydrogen bonds						
Intramolecular	O3A4 -H1···O2A5	0.84	2.11	2.79(1)	138	x, y, z
Intramolecular	O3A2-H3A2···O2A3	0.84	2.11	2.83(1)	143	x, y, z
Intramolecular	O3A1-H3A1···O2A2	0.84	1.97	2.81(1)	173	x, y, z
Intramolecular	O3A5-H3A5···O2A6	0.84	2.16	2.81(1)	134	x, y, z
Intramolecular	O3A6-H3A6···O2A7	0.84	2.07	2.84(1)	151	x, y, z
Intramolecular	O3A3-H3A4···O2A4	0.84	2.16	2.95(2)	157	x, y, z
Intramolecular	O3A7-H3AY···O2A1	0.84	2.14	2.97(1)	169	x, y, z
O3-H···O4 Hydrogen bonds						
Intramolecular	O3A2-H3A2···O4A2	0.84	2.47	2.79(1)	103	x, y, z
Intramolecular	O3A1-H3A1···O4A1	0.84	2.52	2.91(1)	109	x, y, z
Intramolecular	O3A6-H3A6···O4A6	0.84	2.46	2.84(1)	109	x, y, z
Intramolecular	O3A3-H3A4···O4A3	0.84	2.48	2.82(1)	105	x, y, z
Intramolecular	O3A7-H3AY···O4A7	0.84	2.59	2.91(1)	104	x, y, z
C-H···O Hydrogen bonds						
Intramolecular	C4A7-H4A7···O6A7	1.00	2.51	2.87(2)	101	x, y, z
Intramolecular	C5A1-H5A1···O4A7	1.00	2.47	2.83(2)	101	x, y, z
Intramolecular	C5A6-H5A6···O4A5	1.00	2.47	2.84(1)	101	x, y, z
Intermolecular	C2A2-H2A2···O3A5	1.00	2.42	3.26(1)	142	x, -1+y, z
Intramolecular	C6A2-H6A4···O5A3	0.99	2.58	3.27(1)	126	x, y, z
Intramolecular	C6A3-H6A7···O5A4	0.99	2.47	3.35(2)	148	x, y, z
Intramolecular	C7A1-H7A9···O3A1	0.98	2.54	3.02(2)	111	x, y, z
Intermolecular	C2A7-H2A7···O3B6	1.00	2.59	3.49(2)	149	1+x, 1+y, z
Intramolecular	C7A5-H7AX···O3A5	0.98	2.40	3.04(2)	122	x, y, z
Intramolecular	C7A3-H7AE···O3A3	0.98	2.60	3.23(3)	122	x, y, z
Intermolecular	C7A4-H7AG···O6A4	0.98	2.35	3.32(2)	168	-1+x, y, z
Intermolecular	C8A1-H8A3···O3A2	0.98	2.51	3.49(1)	174	1+x, y, z

Table 5.18B: The parameters for the hydrogen bond interactions in DMB·VAL for molecule B.

Interaction type	Hydrogen bond	D-H (Å)	H···A (Å)	D···A (Å)	D-H···A (°)	Symmetry Code
O3-H···O2 Hydrogen bonds						
Intramolecular	O3B1-H3B1···O2B2	0.84	2.04	2.86(1)	166	x, y, z
Intramolecular	O3B5-H3B5···O2B6	0.84	2.05	2.81(1)	150	x, y, z
Intramolecular	O3B4-H3B4···O2B5	0.84	2.03	2.87(1)	172	x, y, z
Intramolecular	O3B6-H3B6···O2B7	0.84	2.00	2.83(1)	165	x, y, z
Intramolecular	O3B7-H3B2···O2B1	0.84	2.06	2.89(1)	173	x, y, z
Intramolecular	O3B3-H3BX···O2B4	0.84	2.17	2.98(2)	164	x, y, z
O3-H···O4 Hydrogen bonds						
Intramolecular	O3B1-H3B1···O4B1	0.84	2.43	2.85(1)	112	x, y, z
Intramolecular	O3B5-H3B5···O4B5	0.84	2.48	2.81(1)	105	x, y, z
Intramolecular	O3B4-H3B4···O4B4	0.84	2.54	2.87(1)	105	x, y, z
Intramolecular	O3B6-H3B6···O4B6	0.84	2.44	2.85(1)	111	x, y, z
Intramolecular	O3B7-H3B2···O4B7	0.84	2.45	2.84(1)	109	x, y, z
Intramolecular	O3B3-H3BX···O4B3	0.84	2.49	2.84(1)	106	x, y, z
C-H···O Hydrogen bonds						
Intramolecular	C5B1-H5B1···.O4B7	1.00	2.47	2.82(2)	101	x, y, z
Intramolecular	C5B3-H5B3···O4B2	1.00	2.49	2.84(2)	100	x, y, z
Intramolecular	C5B2-H5B2···O4B1	1.00	2.42	2.79(2)	101	x, y, z
Intermolecular	C2B7-H2B7···O3A6	1.00	2.51	3.38(2)	146	x, -1+y, z
Intermolecular	C2B2-H2B2···O3B5	1.00	2.52	3.34(1)	137	x, 1+y, z
Intramolecular	C6B2-H6B2···O5B3	0.99	2.37	3.14(2)	134	x, y, z
Intramolecular	C6B2-H6B2···O6B3	0.99	2.55	3.49(2)	157	x, y, z
Intermolecular	C7B6-H7B4···O3A7	0.98	2.60	3.36(2)	134	-1+x, -1+y, z
Intramolecular	C6B3-H6B9···O5B4	0.99	2.53	3.34(2)	138	x, y, z
Intramolecular	C6B5-H6BY···O5B6	0.99	2.54	3.35(2)	139	x, y, z
Intermolecular	C9B2-H9B2···O5A4	0.98	2.58	3.35(2)	135	x, y, -1+z
Intramolecular	C7B5-H7BF···O3B5	0.98	2.38	3.01(3)	121	x, y, z

Host molecular geometry

The geometrical parameters that define the conformation of the O4-heptagon for the host molecule are described in Table 5.19A for molecule A and Table 5.19B for molecule B. These parameters have been described in detail in Chapter 1 under section 1.4.3 (pp. 6 – 8).

The small variations in the individual values of *l*, D and Φ of the O4-heptagon indicate that deviations have occurred from a regular heptagonal shape on complexation. In addition, the degree of planarity of the O4-heptagon is modified and the variations in the torsion angles and the deviations of the O4 atoms from the O4-heptagon (α) are more significant in comparison to the O4-heptagon of β-CD·VAL. Furthermore, the D_3 values which range between 2.79(1) Å and 2.97(1) Å for molecule A and 2.81(1) Å and 3.26(2) Å for molecule B, indicate that the steric hindrance from the methyl groups was not large enough to prevent hydrogen bonds from occurring. This is a well-known feature of DMB.

Table 5.19A: The geometrical parameters for the host molecule A in the complex DMB·VAL.

Residue	***l* (Å)**	**D(Å)**	**Φ (°)**	**d(°)**	**α[a](Å)**	**D_3(Å)**	**τ_2 (°)[b]**
A1	4.992	4.446	129.7	8.2	-0.083	2.97(1)	11.9
A2	4.992	4.401	130.5	-3.1	-0.094	2.81(1)	6.9
A3	5.207	4.340	124.8	-10.3	0.176	2.83(1)	19.0
A4	5.046	4.427	129.5	16.0	0.019	2.95(2)	22.2
A5	4.949	4.452	130.0	-8.2	-0.243	2.79(1)	3.9
A6	5.112	4.316	127.2	0.3	0.189	2.81(1)	6.9
A7	5.157	4.419	126.9	-2.8	0.036	2.84(1)	22.7

[a] mean esd: 0.005 Å; [b] mean esd: 0.5°

Table 5.19B: The geometrical parameters for the host molecule B in the complex DMB·VAL.

Residue	l (Å)	D(Å)	Φ (°)	d(°)	α^a(Å)	D_3(Å)	τ_2 (°)^b
B1	5.001	4.425	129.1	12.4	-0.187	2.89(1)	11.8
B2	5.074	4.441	129.0	-10.3	-0.096	2.86(1)	6.2
B3	5.206	4.302	123.9	-8.0	0.307	3.26(2)	27.8
B4	4.925	4.486	132.4	18.8	-0.072	2.98(2)	24.3
B5	5.008	4.353	128.0	-9.3	-0.305	2.87(1)	4.0
B6	5.154	4.341	126.0	-3.6	0.277	2.81(1)	8.6
B7	5.061	4.467	128.9	-0.4	0.076	2.83(1)	25.3

[a] mean esd: 0.006 Å; [b] mean esd: 0.4°

The tilt angles of the individual glucose units for both molecules vary significantly and are generally large. However, the average tilt angles of the uncomplexed DMB molecule is 14(8)° which also falls within this range of the DMB·VAL tilt angles.[12] In addition, as mentioned previously the average tilt angles for β-CD are 14(10)°, which suggests that the addition of the single methyl group on the secondary ring of each glucose unit did not affect the tilt angle. The tilt angle becomes more pronounced with a molecule such as (fully-methylated) TMB, which has an average tilt angle of 25(20)°. Therefore, β-CD and DMB inclusion complexes should have similar tilt angles, unless the guest molecule induces distortion. As a result, it can be concluded that valproic acid induced distortion in the DMB molecules of DMB·VAL, as the tilt angles are overall larger than the tilt angles that were observed for the β-CD·VAL inclusion complex.

With regard to DMB·VAL, it is evident that the glucose units A3, A4, and A7 and similarly B3, B4 and B7 are tilted the most towards the centre of the cavity of the DMB molecules, in comparison to the remaining glucose units in the macrocycles. Furthermore, the level of distortion and sizes of the tilt angles on molecule B are overall larger than molecule A, which could be due to slightly different modes of inclusion of the guest molecule.

Crystal packing

Figure 5.43a indicates that a column arrangement of inclined monomeric units is adopted instead of ‘straight’ channel packing. Each CD molecule is displaced to a certain extent in the packing arrangement, which prevents the formation of an infinitely long channel, and a herringbone stacking pattern comprising A and B columns is observed. In addition, there is an equal distribution of methylated O6 residues that are directed towards and away from the cavity of each CD molecule

(A and B). Furthermore, a small amount of interpenetration occurs with the guest molecule and the cavity of the adjacent CD molecule within the column. Figure 5.43b displays a space-filling cutaway representation of this effect in molecules of A, the same effect occurring for molecules of B.

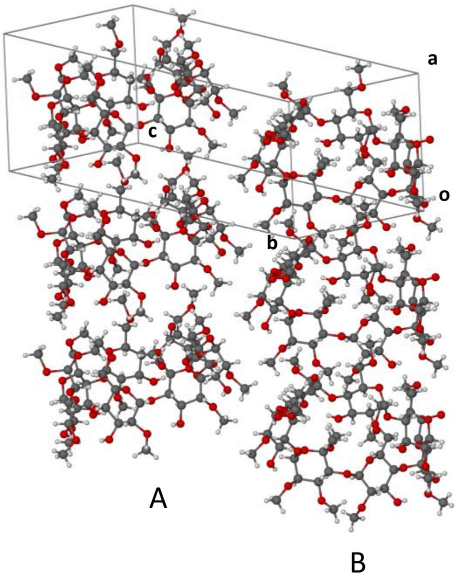

Figure 5.43a: The packing arrangement of molecules A and B in DMB·VAL. The guest and water molecules are omitted for clarity.

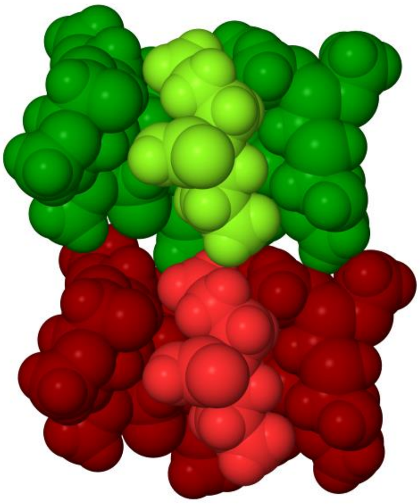

Figure 5.43b: A cutaway space-filling representation of the guest molecule interpenetrating the adjacent CD molecule to a small extent. The two monomeric units of column A are displayed in green and red respectively.

PXRD analysis

Finally, the PXRD pattern of the DMB·VAL inclusion complex, prepared by co-precipitation, corresponded with the calculated PXRD pattern of the DMB·VAL inclusion complex (Figure 5.44). There is generally a 1:1 correspondence with the 2θ angular precision of the peaks from both PXRD patterns. However, the intensities of a few corresponding peaks differ significantly, an effect which is most likely caused by preferred orientation in the experimental sample. Furthermore, there is a slight shift in the 2θ-positions of corresponding peaks, which is due to the different temperatures that were used to record the two PXRD patterns. Despite this, the single crystal that was selected for analysis is nevertheless reasonably representative of the bulk material.

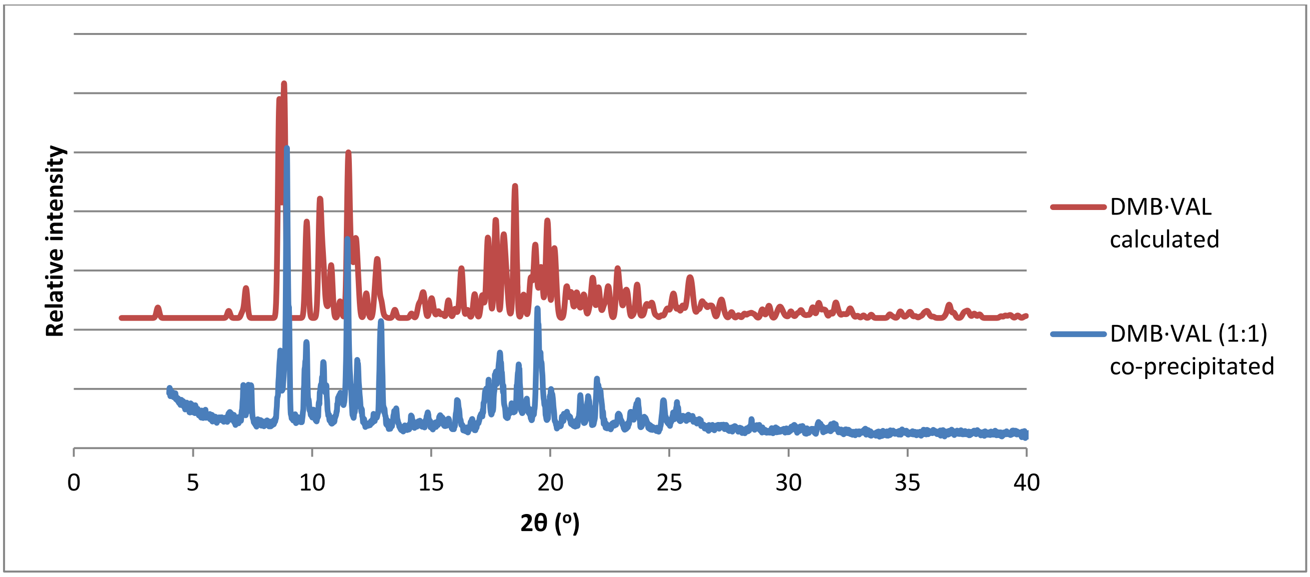

Figure 5.44: The PXRD pattern calculated from a single crystal X-ray structure of DMB·VAL and the PXRD pattern of DMB·VAL prepared *via* co-precipitation.

5.3.2.2) The TMB·VAL inclusion complex

Method of preparation

An inclusion complex between the host TMB and guest valproic acid was successfully synthesized in an equimolar ratio, as confirmed by a ^1H NMR analysis. The method of preparation was identical to that followed for the DMB·VAL inclusion complex, except that the mass of TMB and volume of water were specifically adapted. A mass of 49.56 mg (0.03467 mmol) of TMB was dissolved in 0.8 cm^3 of water at 25 C°. When the valproic acid was added to the CD solution, it formed an oily immiscible layer on the solution surface and the sides of the vial. However, after the overnight stirring, the immiscible valproic acid layer dissolved and thus, since valproic acid is poorly soluble in water, it was inferred that it had formed an inclusion complex with TMB. Despite this, temperature cycling was still employed as a precaution and the solution was heated to 70 ^{o}C while stirring the suspension for 10 minutes and then rapidly cooled to 7 ^{o}C while stirring. This process was repeated four times and the solution was subsequently filtered into a clean vial, sealed and placed in the oven at 60 ^{o}C, after which it took approximately 3 days for crystals to appear.

Crystal morphology

The crystal morphology of the TMB·VAL inclusion complex was that of fragmented, arbitrarily shaped lamellae (Figure 5.45). Unfortunately, as a result of the nature of the morphology it was not possible to perform a SCXRD analysis.

Figure 5.45: The crystal morphology of the TMB·VAL inclusion complex.

^{1}H NMR analysis of TMB·VAL

A sample of the pure TMB·VAL inclusion complex was dissolved in DMSO-d_6 at 298 K and the solution was subjected to ^{1}H NMR spectral analysis, which indicated an equimolar ratio of TMB to valproic acid. The results are displayed in Table 5.20, while the original ^{1}H NMR spectra can be viewed in the Appendix under section 9.6.1, p. 45.

Table 5.20: The ^{1}H NMR analysis of TMB·VAL.

Assignment	**δ (ppm)**	**Integration**	**Proton representation (per molecule)**	**Stoichiometric ratio**	**Stoichiometric ratio (integer)**
2 x C$\underline{H}_3$ (valproic acid)	0.85-0.88	1.00*	6H	1.00	1
4 x C$\underline{H}_2$ (valproic acid)	1.21-1.53	1.46	8H	1.09	1
OME (TMB)	3.25	3.45	21	1.01	1
OME (TMB)	3.40	3.42	21	1.02	1
OME (TMB)	3.51	3.63	21	1.03	1

*reference integral

Fourier Transform Infrared (FT-IR) spectroscopic analysis of TMB·VAL

FT-IR spectroscopic results were consistent with complexation between TMB and valproic acid (Figure 5.46). Interaction between these molecules resulted in a significant shift of the C=O frequency from 1702 cm^{-1} (uncomplexed valproic acid) to 1726 cm^{-1}, indicating a stronger C=O bond in the complexed guest and hence the relative lack of engagement of the carbonyl oxygen atom in hydrogen bonding.[6] This conclusion is supported by analogy with the findings reported for the DMB·VAL inclusion complex, where an increase in the C=O frequency of very similar magnitude was observed and the crystal structure revealed that the carbonyl bond was not involved in hydrogen bonding in the complexed state. (The full FT-IR spectrum can be viewed in the Appendix under section 9.6.2, p. 45).

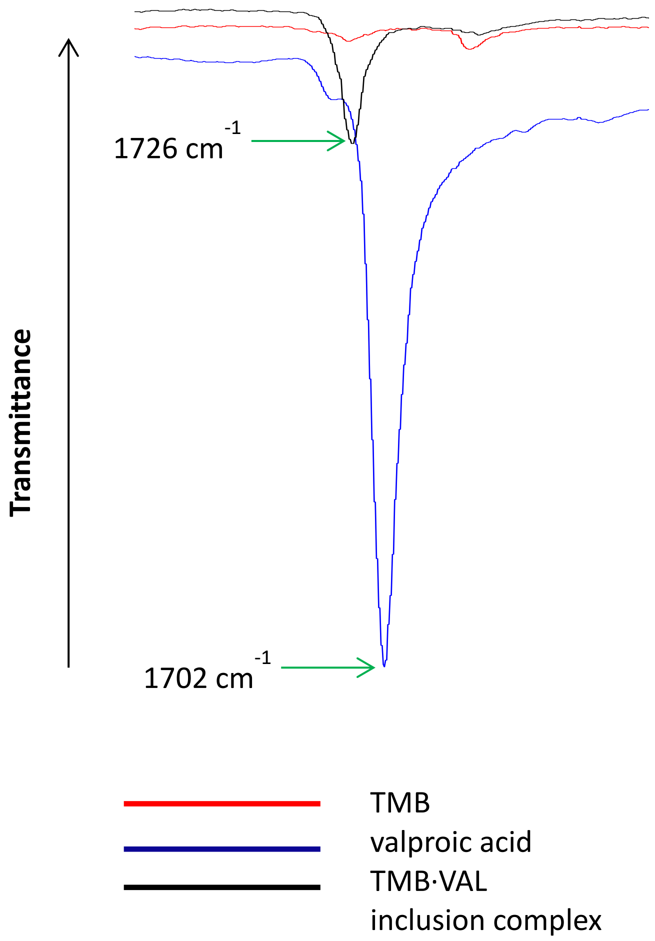

Figure 5.46: A portion of the FT-IR spectra of TMB (red), valproic acid (blue) and TMB·VAL (black).

Powder X-ray Diffraction (PXRD) analysis

The PXRD pattern of the TMB·VAL inclusion complex produced *via* co-precipitation showed some resemblance to the PXRD pattern for a particular TMB inclusion complex (Figure 5.47), namely heptakis(2,3,6-tri-*O*-methyl)-β-cyclodextrin methylcyclohexane clathrate (refcode XAQJII), which crystallizes in the space group $P2_12_12_1$ with the unit cell parameters a = 11.149, b = 25.664, c = 29.427 Å.[2,7] This correlation is only approximate, as some peaks correlate while there are a few that do not.

A putative TMB inclusion complex containing valproic acid, distinct from TMB·VAL, could be synthesized *via* kneading the components for 30 minutes in an equimolar ratio with a small amount of water (Figure 5.47). Its PXRD trace did not match that of TMB·VAL, but it correlated fairly well with the PXRD pattern exclusive for one isostructural series of TMB inclusion complexes that crystallize in the space group $P2_12_12_1$ with approximate unit cell parameters a ≈ 15 Å, b ≈ 21 Å, c ≈ 28 Å [2,7] (Figure 5.47).

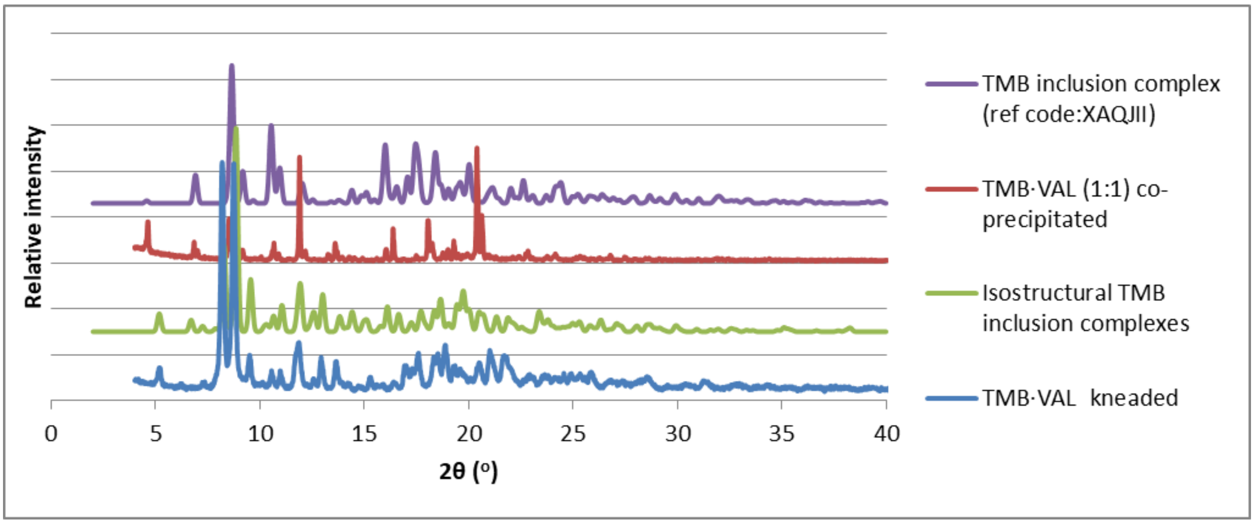

Figure 5.47: The PXRD patterns of a TMB complex that crystallizes in $P2_12_12_1$ (refcode XAQJII), a TMB·VAL complex (1:1) produced *via* co-precipitation, a representative isostructural TMB inclusion complex that crystallized in $P2_12_12_1$ (refcode PAFSOE, with different unit cell data from XAQJII) and a different TMB·VAL complex produced *via* kneading.[7]

Hot Stage Microscopy (HSM) analysis of TMB·VAL

Figure 5.48 represents the thermal progression of TMB·VAL submerged in silicone oil and subjected to a heating rate of 10 $K.min^{-1}$. The individual micrographs display the loss of the guest molecule (valproic acid), the melt of TMB and lastly, the onset of decomposition of the crystals. The initial micrograph, Image 1, was recorded at 29.6 °C, prior to heating. The onset of bubbling commenced at 80.3 °C as depicted in Image 2. The bubbling reached a peak at 104.3 °C (Image 3) and continued until it stopped at 122.1 °C (Image 5). However, simultaneously the onset of transparency occurred. This is represented in Image 3 at 104.3 °C where this event commenced until the crystals were completely transparent at 111.4 °C, as displayed in Image 4. The bubbling and the subsequent onset of transparency appeared to be due to the loss of the guest molecules only. The onset of the melt commenced at 137.1 °C (Image 6) until the crystals had completely melted at 141.1 °C (Image 7). Lastly, the onset of decomposition occurred at 257.4 °C as displayed in Image 8.

Figure 5.48: A series of micorgraphs from the HSM analysis of TMB·VAL.

Image 1: The initial appearance of TMB·VAL at 29.6 °C.

Image 2: The onset of bubbling began at 80.3 °C.

Image 3: The bubbling reached a peak at 104.3 °C. In addition, the onset of transparency commenced.

Image 4: The crystal became completely transparent, while bubbling, at 111.4 °C.

Image 5: The bubbling stopped at 122.1 °C.

Image 6: The onset of the melt commenced at 137.1 °C.

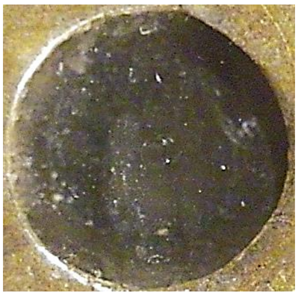

Image 7: The crystal had completely melted at 141.1 °C.

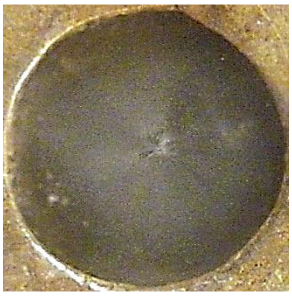

Image 8: The onset of decomposition began at 257.4 °C.

Thermal Gravimetric Analysis (TGA) of TMB·VAL

The surface water of the TMB·VAL complex was removed by pressing the material between two sheets of dry filter paper and then spreading it over the dry surface of the filter paper in order to ensure that all the surface moisture was absorbed. This method also yielded reproducible results.

The TGA traces (n = 2) for the TMB·VAL inclusion complex prepared *via* co-precipitation displayed two prominent mass losses, which occurred over the temperature range between 22.8 and 400.0 °C, as depicted in Figure 5.49. A mass loss of 8.3 ± 0.9 % was associated with the first (apparently three-step) thermal event that took place between 110.5 and 239.0 °C. Unlike the interpretation given for the previously described valproic CD complexes, this mass loss was attributed to the loss of the guest molecule from the TMB·VAL inclusion complex. It is thus evident that this inclusion complex did not contain any water within the crystal structure. These results also correlated with the ^{1}H NMR results that yielded an equimolar ratio of TMB to valproic acid. As stated above, the 8.3 ± 0.9 % mass loss of valproic acid correlated with the percentage ratio of valproic acid to an equimolar anhydrous complex, which is 9.2 %. This calculation can be viewed in the Appendix under section 9.6.3, p. 46. The second thermal event took place between 298.2 °C and 385.8 °C and was associated with a mass loss of 86.7 %, representing the decomposition of TMB.

In the HSM analysis, the loss of the guest molecules was observed by the onset of bubbling and the subsequent onset of transparency, which took place between 80.3 and 122.1 °C. A portion of this thermal event overlapped with the corresponding thermal event in the TGA analysis; however, they did not directly correlate. In addition, the onset of decomposition in the HSM analysis (257.4 °C) did not correlate with the onset of decomposition in the TGA trace at 298.2 °C.

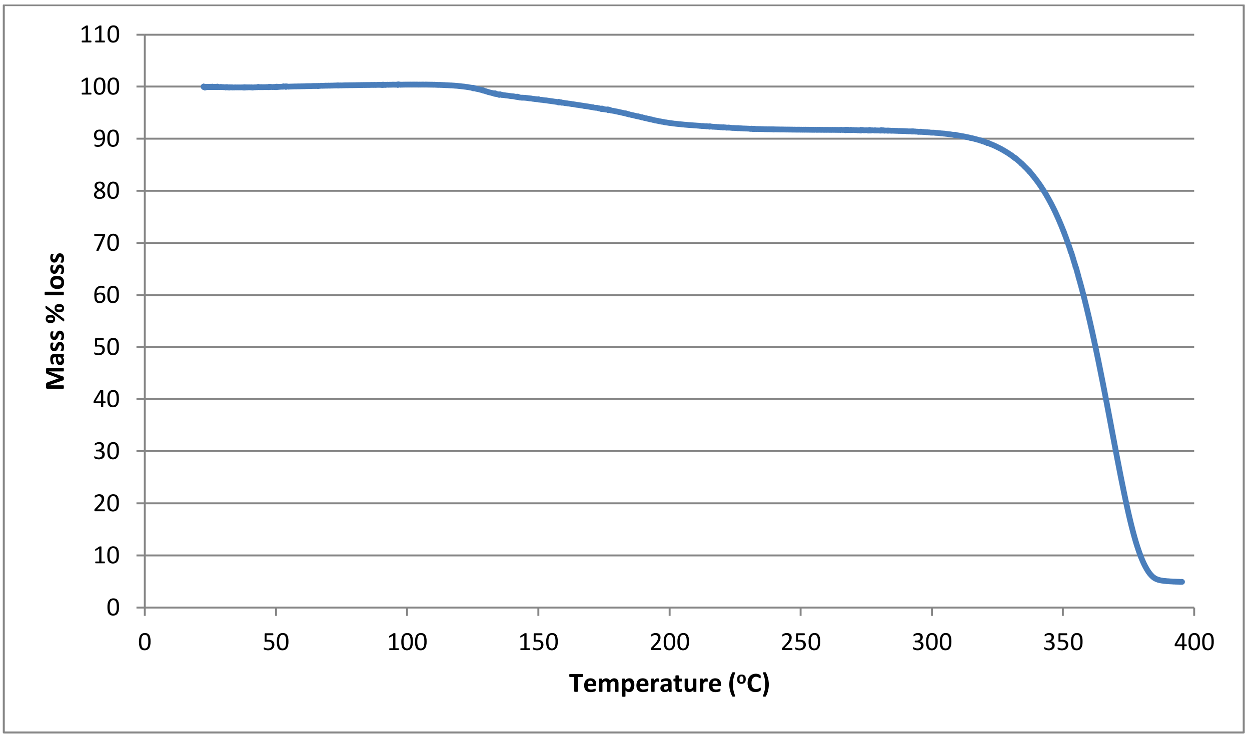

Figure 5.49: Representative TGA trace for TMB·VAL (n = 2).

Differential Scanning Calorimetry (DSC) analysis of TMB·VAL

The DSC trace of the TMB·VAL complex (n = 3) prepared *via* co-precipitation, was significantly different from those of all the other CD/valproic acid inclusion complexes described previously (Figure 5.50). This trace displays only a sharp endotherm with the onset at 126.7 ± 0.8 ^{o}C (peak temperature 130.3 ± 0.1 ^{o}C) and this is characteristic of a melt. No water loss from the crystal structure was observed in the DSC trace which was also previously confirmed by the HSM and TGA results. In the HSM experiment, the onset of the melt occurred at 137.1 ^{o}C and neither melting points from the HSM or DSC results correspond with the literature melting point for the different forms of TMB (which are in the range 148 – 157 ^{o}C).[16] A reason that these results did not correlate could have been due to the fact that the loss of the guest molecules was a composite process and as a result it could have caused the melt of TMB to occur earlier.

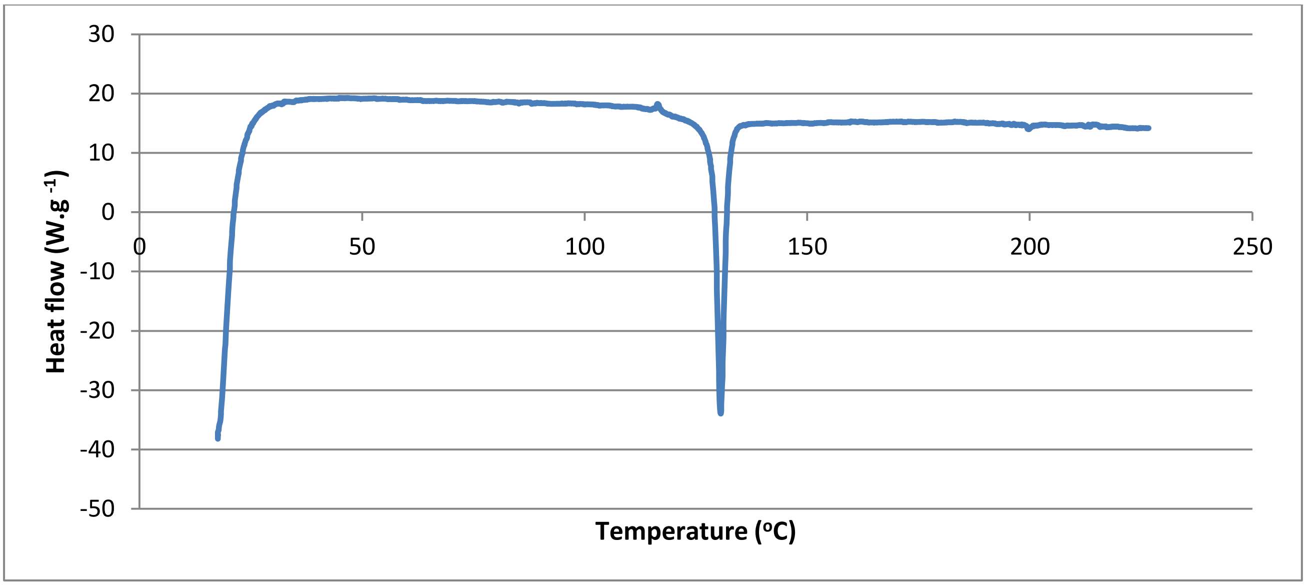

Figure 5.50: Representative DSC trace of TMB·VAL (n = 3).

In conclusion, a new anhydrous CD complex, with the formula TMB·VAL, was synthesized. However, analysis of its structure using X-ray analysis was not possible due to the intractable nature of the crystals.

5.3.2.3) The TMA·VAL inclusion complex

Method of preparation

An inclusion complex containing TMA (host molecule) and valproic acid (guest molecule) was successfully synthesized in an equimolar ratio, as confirmed by a ^{1}H NMR analysis. The equivalent method of preparation, as outlined for DMB·VAL, was followed for this experiment, except that the mass of TMA and the volume of water were specifically tailored. Thus, 42.48 mg (0.03467 mmol) of TMA was initially dissolved in 0.8 cm^3 of water and the remainder of the method was followed as previously described. Crystals were formed within two days.

Crystal morphology

The crystal morphology of the TMA·VAL inclusion complex was generally of a very poor quality, as the crystals were frequently plate-like with irregular shapes (Figure 5.51A). Very few crystals grew significantly in the third dimension, and thus obtaining a crystal for a SCXRD analysis was exceedingly challenging. These few crystals, which contained a more three-dimensional character, still had an irregular shape (Figure 5.51B); however, it was possible to collect the data for a SCXRD analysis.

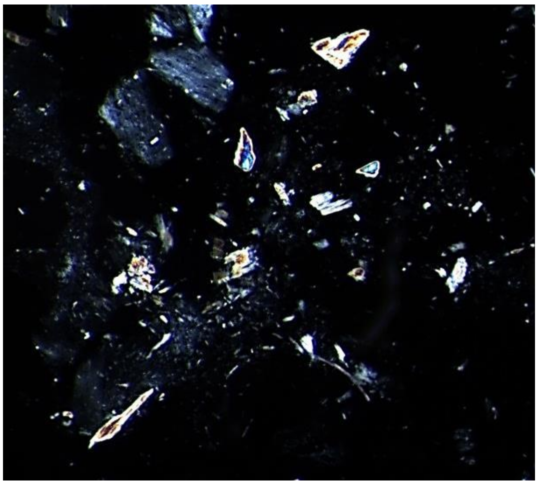

Figure 5.51A: The generally poor quality plate-like crystals obtained for the TMA·VAL inclusion complex.

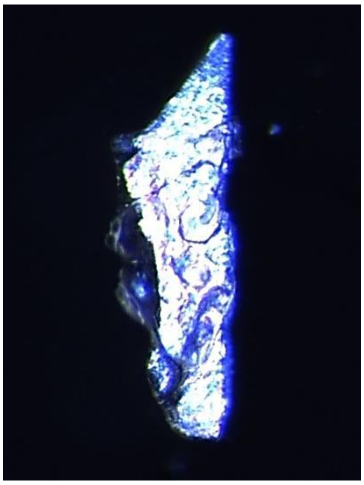

Figure 5.51B: The crystal morphology of the TMA·VAL inclusion complex which had a more three-dimensional character.

^{1}H NMR analysis of TMA·VAL

The ^{1}H NMR solution-state spectral analysis of single crystals of the inclusion complex dissolved in DMSO-d_6 at 298 K indicated an equimolar ratio of TMA to valproic acid. The results are listed in Table 5.21 below, while the original ^{1}H NMR spectra can be viewed in the Appendix under section 9.7.1, p. 47.

Table 5.21: The ^{1}H NMR analysis of TMA·VAL.

Assignment	**δ (ppm)**	**Integration**	**Proton representation (per molecule)**	**Stoichiometric ratio**	**Stoichiometric ratio (integer)**
2x$C\underline{H}_3$ (valproic acid)	0.83-0.87	1.00*	6H	1.00	1
4x$C\underline{H}_2$ (valproic acid)	1.21-1.52	1.36	8H	1.02	1
OME (TMA)	3.24	2.93	18H	1.02	1
OME (TMA)	3.38	3.07	18H	1.02	1
OME (TMA)	3.50	2.83	18H	1.06	1

*reference integral

Fourier Transform Infrared (FT-IR) spectroscopic analysis of TMA·VAL

The FT-IR analysis of the TMA·VAL inclusion complex also confirmed the identity of this inclusion complex. The C=O stretching frequency of valproic acid in the complex was shifted to a significantly higher frequency (1734 cm^{-1}) in comparison to its stretching frequency in uncomplexed valproic acid (1702 cm^{-1}). This indicates that the extent of the C=O hydrogen bonding in the complex was reduced in comparison to that of pure valproic acid.[6] Figure 5.52 displays a section of the FT-IR spectrum, while the full FT-IR spectrum is available in the Appendix under section 9.7.2, p. 47.

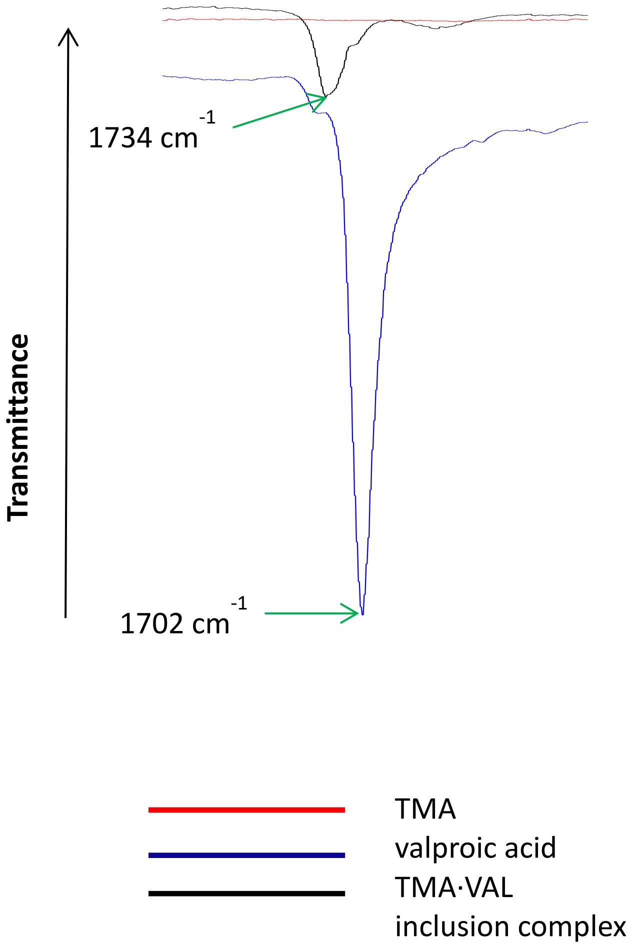

Figure 5.52: A portion of the FT-IR spectra of TMA (red), valproic acid (blue) and TMA·VAL (black).

Powder X-ray Diffraction (PXRD) analysis of TMA·VAL

The TMA·VAL inclusion complex could also be formed *via* kneading the host and guest components for 40 minutes in an equimolar stoichiometry with a small amount of water (Figure 5.53). This was evident since the 2θ-positions in the PXRD patterns of the TMA·VAL inclusion complex, produced *via* co-precipitation and kneading, directly correlated. The major difference is the peak intensity discrepancy at 2θ = 8.0°, which is attributed to preferred orientation in the co-precipitated sample. Proof for the latter conclusion is provided at the end of this chapter. It is important to note that the sample produced *via* kneading had to be applied as a dry powder to the zero background holder in the diffractometer.

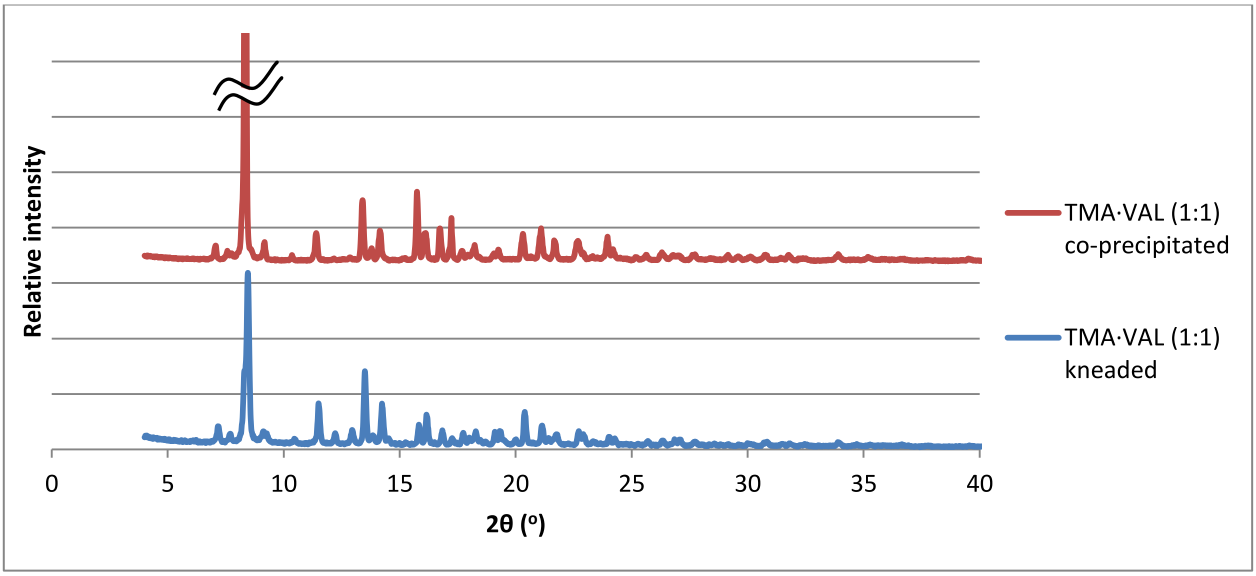

Figure 5.53: The PXRD patterns of the TMA·VAL inclusion complex produced *via* co-precipitation (1:1) and kneading (1:1).

Hot Stage Microscopy (HSM) analysis of TMA·VAL

The thermal progression of a TMA·VAL inclusion complex crystal and TMA crystals are displayed in the series of micrographs in Figure 5.54. These crystals were subjected to a constant heating rate of 10 K.min^{-1}, while immersed in silicone oil. This analysis displayed loss in the crystallinity of TMA·VAL, the melt of TMA and the onset of decomposition. The initial micrograph, Image 1, was recorded at 25.0 ^{o}C to depict the features of the TMA·VAL inclusion complex crystal (left) and TMA crystals (right) prior to heating. Image 2 depicts the onset of opacity at 98.8 ^{o}C for the TMA·VAL inclusion complex, the maximum opacity being achieved at 154.3 ^{o}C (Image 3). TMA remained unchanged during these thermal events. TMA·VAL began to melt very slowly at 173.4 ^{o}C (Image 4), while TMA remained unchanged. However, at 210.3 ^{o}C (Image 5) the melt for TMA commenced, and they were both completely melted at 271.5 ^{o}C (Image 6). This behaviour suggested that the heating process involved the removal of valproic acid from the TMA·VAL inclusion complex crystal and thus pure solid TMA remained. The boiling point of valproic acid is 219.5 ^{o}C,[15] and thus valproic acid would have left the inclusion complex in liquid form and become dispersed within the silicone oil. As a result, it was expected that no bubbling would be observed. Consequently, the loss in crystallinity, which is represented by the onset of opacity for the TMA·VAL inclusion complex crystal, is most likely due to the guest molecules (valproic acid) leaving the crystal.

Furthermore, the onset of decomposition occurred at 287.5 °C (Image 7) and full decomposition was achieved at 356.4 °C (Image 8). It is clearly understood that both samples would have the same decomposition thermal events, as they had become the same substance.

Figure 5.54: A series of micrographs from the HSM analysis of TMA·VAL.

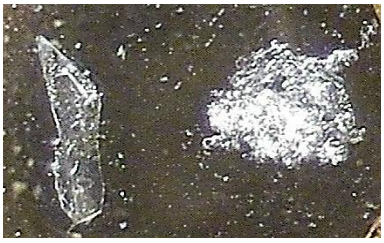

Image 1: Initial appearance of TMA·VAL (left) and TMA (right) at 25.0 °C.

Image 2: The onset of opacity for TMA·VAL (left) at 98.8 °C. TMA (right) remained unchanged.

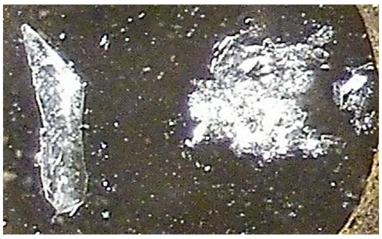

Image 3: The peak opacity occurred at 154.3 °C for TMA·VAL. TMA (right) remained unchanged.

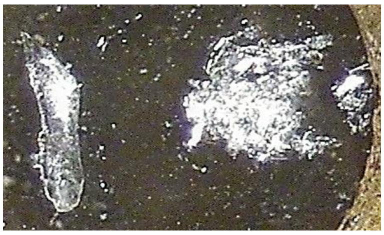

Image 4: At 173.4 °C the onset of the melt began very slowly for TMA·VAL (left). TMA (right) remained unchanged.

Image 5: The continuation of the melt for TMA·VAL (left) at 210.3 °C. The melt for TMA (right) commenced.

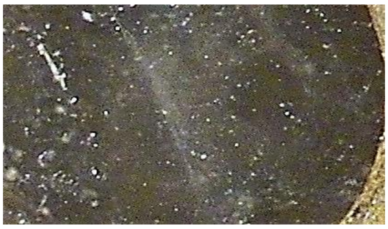

Image 6: Both compounds were completely melted at 271.5 °C.

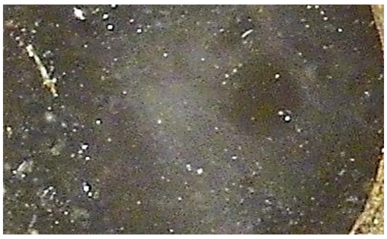

Image 7: The onset of decomposition commenced at 287.5 °C for both residues.

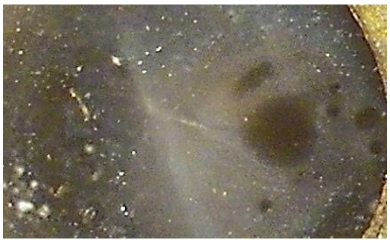

Image 8: The decomposition was completed at 356.4 °C for both residues.

Thermal Gravimetric Analysis (TGA) of TMA·VAL

The general morphology of the TMA·VAL crystals was plate-like; however, there were occasionally a few more three-dimensional crystals in the batch. Removal of surface mother liquor for the purpose of estimating the crystal water content by TGA posed a challenge. In the first trial experiment, where the crystals were only pressed between the two sheets of filter paper, a 10 % mass loss due to water was recorded. A possible explanation for this is that surface water could have been trapped in between the plates of the crystals. In the latter experiments, where the crystals were pressed and spread across a sheet of filter paper, the results indicated a 1.5 % mass loss due to water, and these results were reproducible.

The TGA traces (n = 2) signified three distinctive mass losses for the TMA·VAL inclusion complex which took place over the temperature range 20.8 – 400.0 ^{o}C as depicted in Figure 5.55. A mass loss of 1.5 ± 0.1 % was associated with the first thermal event which occurred between 20.8 ^{o}C and 38.2 ^{o}C. This mass loss was attributed to the loss of water molecules from the TMA·VAL inclusion complex. (The absence of bubbling in the HSM analysis, in the dehydration temperature range, is assumed to have been due to the very small percentage of water present in the crystal).

The second thermal event can be split into two processes – a sharp, large mass loss and then a very small gradual mass loss. Both of these events are attributed to the loss of guest molecules and it is evident that this is a consecutive two-stage process. The first stage took place between 99.4 ^{o}C and 125.1 ^{o}C and was associated with a mass loss of 6.7 ± 0.9 %. The second stage occurred over the temperature range between 125.1 and 214.8 ^{o}C and represented a mass loss of 3.2 ± 0.4 %. The combined mass loss percentages of valproic acid (9.9 ± 0.7 %) correlated with the percentage ratio of valproic acid to an equimolar anhydrous complex (10.5 %). Thus, this further confirms the equimolar stoichiometry of TMA to valproic acid in the inclusion complex, as determined by the ^{1}H NMR spectroscopy. This calculation can be viewed in the Appendix under section 9.7.3, p. 48.

The last thermal event took place over the temperature range between 287.0 ^{o}C and 388.3 ^{o}C with an associated mass loss of 84.6 % and represents the decomposition of TMA. In addition, the loss of the guest molecules in the HSM analysis was observed by the onset of opacity at 98.8 ^{o}C. This event correlated very closely with the onset of the loss of the guest molecules in the TGA analysis, which was observed at 99.4 ^{o}C. The onset of decomposition in the HSM analysis directly correlated with the onset of decomposition in the TGA trace within a temperature range of 0.5 ^{o}C.

This analysis also allowed the number of water molecules to be calculated in the inclusion complex. Thus, a 1.5 ± 0.1 % mass loss of water amounted to 1.2 ± 0.1 water molecules. This calculation can be viewed in the Appendix under section 9.7.4, p. 48.

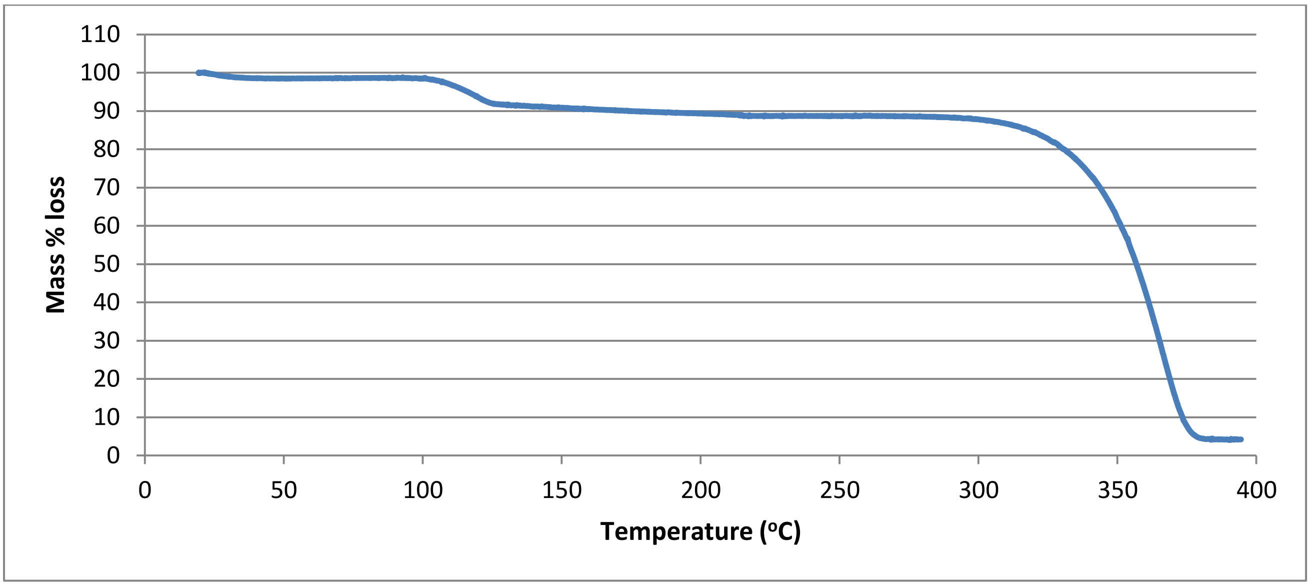

Figure 5.55: Representative TGA trace of the TMA·VAL inclusion complex (n = 2).

Differential Scanning Calorimetry (DSC) analysis of TMA·VAL

The DSC traces of TMA·VAL (n = 2) indicated two complex endothermic events taking place (Figure 5.56). Furthermore, the water loss was not observed due to the fact that the DSC instrument only equilibrated at 50 ^{o}C. The first complex endothermic event occurred over the temperature range between 95.1 ± 0.6 ^{o}C and 152.3 ± 0.1 ^{o}C and represented the loss of guest molecules from the inclusion complex. This complex endothermic event was a two-step process which is accompanied by a broad shoulder at the end. The onset temperatures of these consecutive events took place at 95.1 ± 0.6 ^{o}C (where the peak occurred at 101.5 ± 0.5 ^{o}C), 108.3 ± 0.7 ^{o}C (where the peak occurred at 114.6 ± 0.1 ^{o}C), and the broad shoulder which spanned the range from 119.5 ± 0.1 ^{o}C to 152.3 ± 0.1 ^{o}C. Overall, these temperature ranges represented the initial loss of the guest molecules periodically over two stages, and subsequently more of the guest molecules were lost over an extended period of time, as displayed by the broad shoulder endothermic event. This event correlated with both the HSM analysis and the TGA analysis: with reference to the HSM analysis the onset of opacity occurred at 98.8 °C, which was attributed to the loss of the guest molecules. In addition, with reference to the TGA analysis, this initial complex DSC endotherm correlated with the onset of the first stage of the loss of the guest molecules in the TGA experiment, which took place between 99.4 and 125.1 °C.

The onset temperature of the second endothermic event occurred at 214.8 ± 2.2 °C (with the peak occurring at 220.0 ± 0.1 °C) and represented the melt of TMA. The peak of this endothermic event (the melt) correlated reasonably well with the literature value for the melting temperature of TMA, which has been reported as 217.6 ± 0.1 °C.[17-18] The asymmetry of this endothermic peak could be attributed to the simultaneous loss of remaining guest molecules and melting of TMA, which would account for the gradual depression towards the peak at 220.0 ± 0.1 °C. This explanation arose from the results observed in the TGA analysis, where the second stage guest loss is occurring over a similar temperature range 125.1 – 214.8 °C. Furthermore, the HSM analysis had indicated the start of a slow melt at 173.4 °C, which corresponds to the negative deviation of the baseline towards 220 ± 0.1 °C in the DSC trace. Owing to the sensitivity of the DSC instrument to possible spillage of material from the pan, it was decided not to take the sample to decomposition.

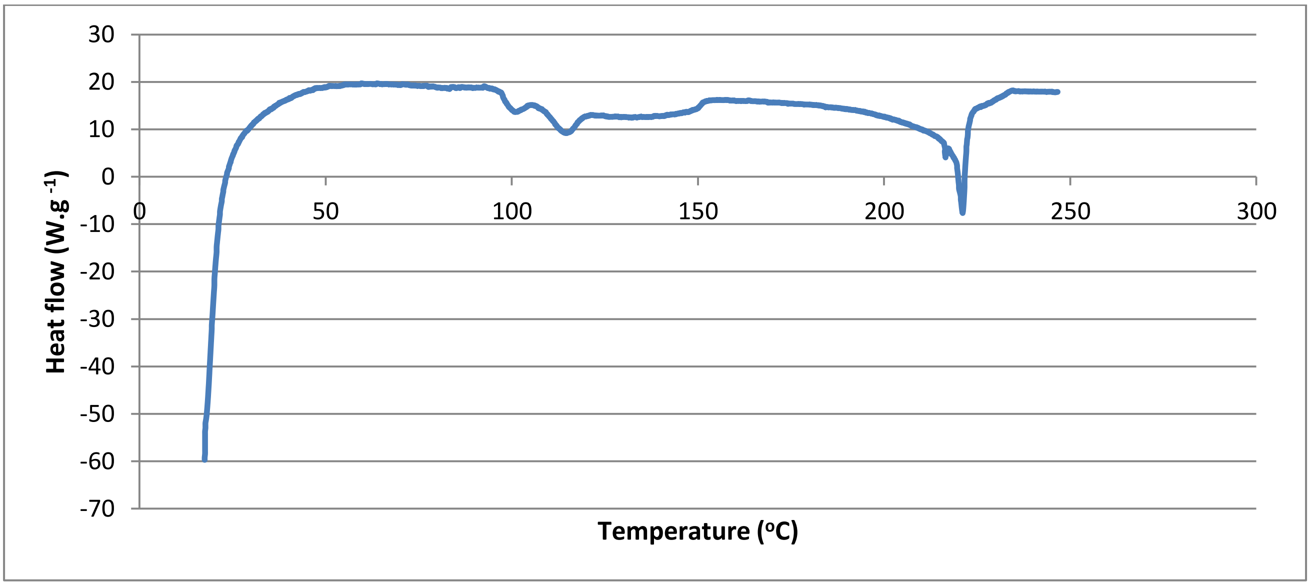

Figure 5.56: Representative DSC trace of TMA·VAL (n = 2).

Single Crystal X-ray Diffraction (SCXRD) analysis

Data-collection and space group determination

Three attempts were made to collect the intensity data of TMA·VAL in order to ensure that a successful crystal structure solution was achieved. The first crystal was cooled to 100 K; however, it was concluded that the crystal had been cooled too rapidly, since the b-axis tripled in length relative to the value measured at 294 K (room temperature). The structure refinement for the host molecule based on these data could not be completed as the geometries of the glucose rings were unstable, and as a result these intensity data were abandoned. A second crystal was selected and prepared for two consecutive data-collections; for the first collection the crystal was cooled to 220 K and for the second, to 100 K. The data-collection at 220 K was performed as a precaution in the event that the b-axis might increase in multiplicity at a lower temperature, even though the temperature of the crystal was lowered extremely slowly during this attempt. The intensity data at 220 K enabled the host to refine accurately; however, the electron density in the host cavity did not resemble the relevant atomic connectivities expected for the molecule of valproic acid, and thus the atoms of the guest molecule could not be assigned. Therefore, the crystal was cooled further very slowly to 100 K and it did not display any multiplication of the b-axis (which had previously occurred at 100 K). Intensity data-collection on this specimen proceeded and the structural model deduced from electron density maps based on these data revealed the host, guest and water molecules and was successfully refined. Details of the structure solution and refinement follow.

The Laue group of the intensity-weighted reciprocal lattice was *mmm* which indicated that the crystal system was orthorhombic. The lattice type was determined to be primitive and the space group $P2_12_12_1$ was determined from the conditions limiting possible reflections, as listed in Table 5.22. These results were also confirmed using the program XPREP.

Table 5.22: The conditions limiting possible reflections for the crystal TMA·VAL

Number	**Conditions limiting possible reflections**	**Deduction**
1	hkl: none	Primitive lattice
2	0kl: none	No glide plane ⊥ a
3	h0l: none	No glide plane ⊥ b
4	hk0: none	No glide plane ⊥ c
5	h00: h = 2n	2_1-axis parallel to the a-axis
6	0k0: k = 2n	2_{1-}axis parallel to the b-axis
7	00l: l = 2n	2_{1-}axis parallel to the c-axis

Structure solution and refinement

The structure was solved with SHELXS-97[9] and refined with SHELXL-97. The host molecule was fully ordered and the guest molecule was observed in the host cavity. Only the carboxylic acid group was disordered over two positions, the larger component accounting for 72 % of the site-occupancy. All the host and guest atoms were refined isotropically initially and subsequently anisotropically, except for the disordered –COOH group on the guest molecule, which was refined isotropically. The majority of the hydrogen atoms were placed in idealised positions on the host and guest molecules. However, the placement of the hydrogen atoms on the disordered –COOH group was non-routine, since sufficiently strong $\Delta\rho$ peaks were absent. However, from the distribution of oxygen atoms in the vicinity of the disordered components of the –COOH acid group, it could be inferred that in each of these components, only one of the oxygen atoms could act as a donor in forming a hydrogen bond, while the other could not act as a donor or an acceptor. Placement of the acidic H atoms was thus based on the above considerations. An isotropic temperature factor between 1.2 and 1.5 times the U_{iso} value of its parent atom was assigned to each hydrogen atom in the model. The crystallographic data are summarised in Table 5.23.

Table 5.23: The crystal data and refinement parameters for the TMA·VAL inclusion complex.

Parameter	**Value**
Complex formula	$C_{54}H_{96}O_{30}\cdot C_8H_{16}O_2\cdot 1.2H_2O$
Formula weight (g.mol^{-1})	1391.17
Temperature (K)	100(2)
Wavelength (Å)	0.71073
Crystal system	Orthorhombic
Space group	$P2_12_12_1$
a (Å)	15.335(3)
b(Å)	20.727(4)
c(Å)	23.102(5)
α (°)	90
β (°)	90
γ (°)	90
Volume (Å^3)	7343(3)
Z	4
Calculated density (g.cm^{-3})	1.2582
μ (mm^{-1})	0.102
F (000)	3008
Crystal size (mm)	0.162 x 0.192 x 0.426
Θ Range scanned (°)	2.71 – 20.29
Index range	h: -19, 19; k: -26, 25; l: -29, 29
No. of reflections collected	67797
No. of unique reflections	16293
Data completeness (%)	99.2
Data/restraints/parameters	16293/0/865
S (Goodness-of-fit on F^2)	1.014
Final R indices R_1, wR_2, [$I > 2\sigma(I)$]	0.0675, 0.1461
R Indices, all data (R_1, wR_2)	0.1342, 0.1737
Largest diff. peak and hole (e. Å^{-3})	0.42, -0.37

Two sites were identified as locations of disordered water molecules. Initially, the thermal parameters (U_{iso}) of the water oxygen atoms were constrained and their site-occupancy factors (s.o.f.s) were allowed to vary. Subsequently, their U_{iso} values were unconstrained and both sets of parameters converged. The combined site-occupancy of the water molecules was 0.5 per TMA molecule, which did not correlate with TGA results that indicated the presence of 1.2 ± 0.1 water molecules per TMA molecule. A possible explanation is that there could have still been residual surface water in the samples used for the TGA analysis, despite the thorough drying process employed as explained above. The distance between these two water molecule sites was 1.07 Å and therefore this suggested that this could represent one site with large anisotropic motion. An attempt was made to treat it as one site, but the U_{iso} value of a single water oxygen site was not stable. Consequently, the former model with two partially occupied water molecule sites treated isotropically, was reinstated. In addition, no attempts were made to place hydrogen atoms on these partial water molecules owing to their disorder. Table 5.24 summarises the refined values for the U_{iso} parameters, as well as the s.o.f.s for the water oxygen atoms.

Table 5.24: The total number of water oxygen sites that were identified, along with their respective s.o.f.s and U_{iso} values.

Atom	s.o.f.	U_{iso} (Å^2)
O1W	0.19(2)	0.031(8)
O2W	0.32(2)	0.10(1)

Molecular Structure

The asymmetric unit (ASU) of TMA·VAL contains one TMA molecule, one valproic acid molecule and two water oxygen atoms located at sites that have a combined site-occupancy of 0.5 water molecules, as shown in Figure 5.57 below. It should be noted that guest inclusion involves insertion of only one of the propyl groups within the host cavity, while the rest of the molecule protrudes from the secondary side of the TMA molecule. This is most evident from the Figure 5.57 (right). Also noteworthy is that this X-ray analysis presents the only accurate model for the valproic acid molecule determined to date, those contained in the two DMB·VAL complex units displaying very high thermal motion and considerably lower precision in their geometrical parameters.

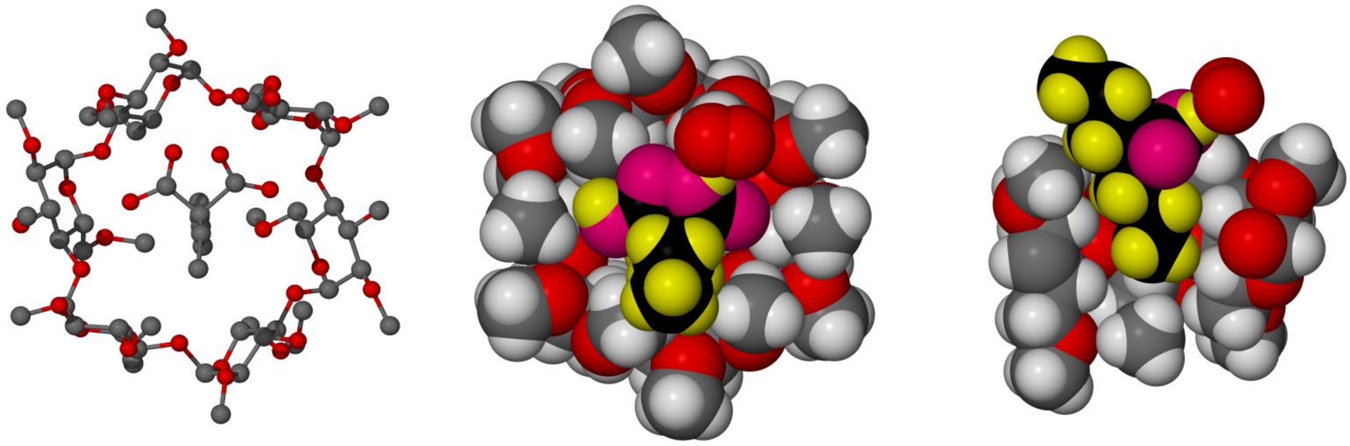

Figure 5.57: The ASU of TMA·VAL: A ball-and-stick model of the guest and host molecules is displayed on the left (hydrogen atoms and water molecules are omitted for clarity), while a space-filling model of the ASU is displayed in the centre, and a cross-section of TMA·VAL is displayed on the right.

Hydrogen bonding

The hydrogen bonding of the host molecule in the TMA·VAL inclusion complex involved both intermolecular and intramolecular interactions of the type C-H···O. This was to be expected as the TMA molecule is fully methylated and thus does not contain any hydroxyl donor or acceptor groups. The majority of these C-H···O bonds are rather weak; however, collectively they have an important role. These interactions are listed in Table 5.25.

Further details of the unusual guest inclusion mode observed here, as well as the host-guest interactions follow. The aliphatic chain of the valproic acid molecule is in a fully extended conformation (Figure 5.58) and only one of the propyl groups is included within the cavity of the TMA molecule, while the two disordered components of the carboxylic acid group and the second propyl group protrude from the secondary side of the host molecule. Thus, neither of the disordered –COOH components engages with the TMA molecule of the asymmetric unit; instead, for one of them, the –OH group is directly hydrogen bonded to atom O6F of a symmetry-related TMA molecule, while for the other, the –OH group is hydrogen bonded to water oxygen atom O1W, which in turn donates a H-bond to atom O6B of a second symmetry-related TMA molecule (parameters in Table 5.25).

Table 5.25: The parameters for the hydrogen bond interactions in TMA·VAL.

Interaction type	Hydrogen bond	D-H	H…A	D…A	D-H…A (°)	Symmetry Code
C-H···O Hydrogen bonds						
Intermolecular	C2A-H2A···O6B	1.00	2.44	3.416(7)	165	½+x, ½-y, -z
Intermolecular	C2B-H2B···O5A	1.00	2.34	3.318(6)	165	x-½, ½-y, -z
Intermolecular	C2D-H2D···O6E	1.00	2.45	3.418(6)	164	x-½, ½-y, 1-z
Intermolecular	C2E-H2E···O5D	1.00	2.57	3.542(6)	165	½+x, ½-y, 1-z
Intramolecular	C4E-H4E···O6E	1.00	2.49	2.852(7)	101	x, y, z
Intramolecular	C5B-H5B···O4A	1.00	2.38	2.780(5)	103	x, y, z
Intramolecular	C6A-H6A1···O5B	0.99	2.29	3.193(7)	151	x, y, z
Intramolecular	C6E-H6E2···O5F	0.99	2.53	3.286(7)	134	x, y, z
Intramolecular	C6B-H6B2···O5C	0.99	2.46	3.180(7)	129	x, y, z
Intramolecular	C6F-H6F1···O5A	0.99	2.52	3.351(8)	141	x, y, z
Intramolecular	C6F-H6F1···O6A	0.99	2.60	3.475(8)	147	x, y, z
Intramolecular	C6D-H6D1···O5E	0.99	2.31	3.206(7)	150	x, y, z
Intermolecular	C7F-H7F3···O3C	0.98	2.45	3.260(7)	140	1+x, y, z
Intramolecular	C7E-H7E3···O3E	0.98	2.51	3.121(8)	120	x, y, z
Intramolecular	C8C-H8C3···O2C	0.98	2.42	3.044(8)	121	x, y, z
Intramolecular	C8F-H8F3···O2F	0.98	2.45	3.070(8)	121	x, y, z
Intramolecular	C9C-H9C1···O6D	0.98	2.58	3.488(8)	154	x, y, z
Intramolecular	C9F-H9F3···O6A	0.98	2.55	3.451(8)	153	x, y, z
Hydrogen bonds involving the guest molecule						
Intermolecular	O1G-H1G···O6F	0.84	2.05	2.829(8)	154	-x, ½+y, ½-z
Intermolecular	O2H-H2H···O1W	0.84	1.95	2.78(2)	170	x, y, z
Intermolecular	O1W-H*···O6B	-	-	2.54(2)	-	-1-x, ½+y, ½-z

*H atom inferred but not located or included in the model

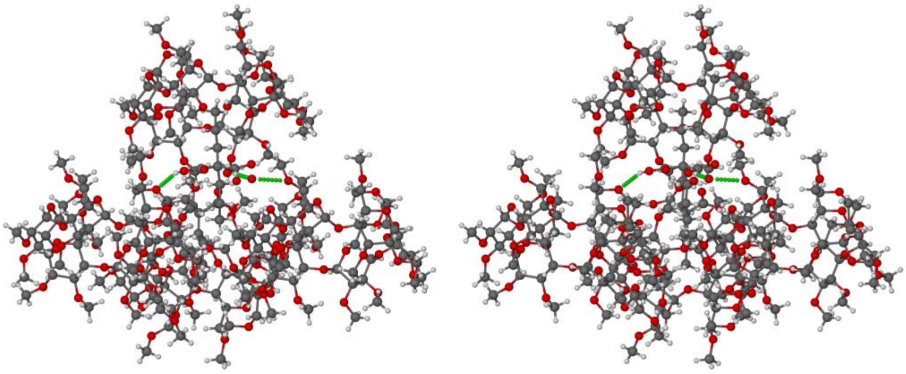

Figure 5.58: A stereoview of the hydrogen bonding (green lines) involving the guest molecule. The TMA molecule of the ASU is shown at the top of the figure. The guest and water molecules in the lower CD level are omitted for clarity.

The observed host-guest interactions, involving exclusively the –OH groups of the disordered –COOH components, are also consistent with the results obtained by FT-IR analysis. These indicated that the extent of hydrogen bonding involving the valproic acid C=O group in the inclusion complex was much less than that in the uncomplexed acid. These results parallel those which were reported earlier in Chapter 5, pp. 140 – 141 for the DMB·VAL complex.

Host molecular geometry

The conformation of the O4-hexagon for the host molecule is described by the parameters in Table 5.26. These parameters have been described in detail in Chapter 1 under section 1.4.3, pp. 6 – 8. The lengths and angles in a regular hexagon are all equal; however, the values of l, D and Φ of the O4-hexagon are not equal and vary somewhat. This is expected since the O4-hexagon becomes distorted in a crystalline state,[12] and this distortion is further enhanced by complexation. Furthermore, the results indicate that the degree of planarity of the O4-hexagon is modified, since the variation in the torsion angles (d) and the atomic deviations from the O4-plane (α) are more significant. The O4-hexagon is less planar than the O4-heptagon of β-CD·VAL and the O4-hexagon is distorted to about the same extent as the O4-heptagon of DMB·VAL. This is owing to the steric interactions of the methyl groups in TMA. This is further confirmed by the D_3 values which range between 3.156 Å and 3.441 Å and indicate that the steric repulsive effects between these methyl groups have caused these distances to increase significantly from the value of around 2.8 Å, observed in native CDs.

The tilt angles of the glucose units vary significantly and are generally large, due to the steric interactions between the secondary methyl groups. These results complement those for previously reported TMA inclusion complexes as the tilt angles follow a very similar trend.[18] It is evident from Table 5.26 that the glucose units C and F are tilted the most towards the centre of the cavity of the TMA molecule. The tilt angles of uncomplexed TMA have an average value of 18(12)° which suggests that there was no significant change in distortion upon complexation in TMA·VAL.[12] This is due to the fact that only one propyl group of the valproic acid molecule is located within the host cavity and that the host-guest interactions are consequently minimal, as shown by the data in Table 5.25. Generally, the distortion of the α-CD family of molecules can be affected by host-guest interactions; however, in this case it is not obviously apparent.[12] This further confirms that the large tilt angles are mainly caused by the steric strain of methyl groups and that the inclusion of the guest molecule had a negligible contribution.

Table 5.26: The geometrical parameters of the host molecule in the complex TMA·VAL.

Residue	**l (Å)**	**D(Å)**	**Φ (°)**	**d(°)**	**α[a](Å)**	**D_3(Å)**	**τ_2 (°)[b]**
A	4.380	4.376	115.6	-6.4	0.282	3.316	9.1
B	4.123	4.240	123.0	-9.7	-0.245	3.427	17.5
C	4.273	4.211	120.2	17.3	-0.041	3.277	33.5
D	4.384	4.334	114.9	-7.9	0.294	3.278	7.2
E	4.084	4.241	124.3	-8.6	-0.260	3.440	17.2
F	4.301	4.225	118.9	16.0	-0.030	3.156	30.0

[a] mean esd: 0.002 Å; [b] mean esd: 0.1°

Crystal Packing

The TMA molecules pack themselves in layers according to a brickwork (monomeric) arrangement, where one of the monomeric units centres itself above the void space created by three monomeric units in the layer below (Figure 5.59a). As noted previously, the aliphatic chain of valproic acid is fully extended through the centre of the CD cavity, half of the aliphatic chain being included in the CD cavity and the remaining half being centrally positioned in the void space between the three monomeric units in the lower layer (Figure 5.59b).

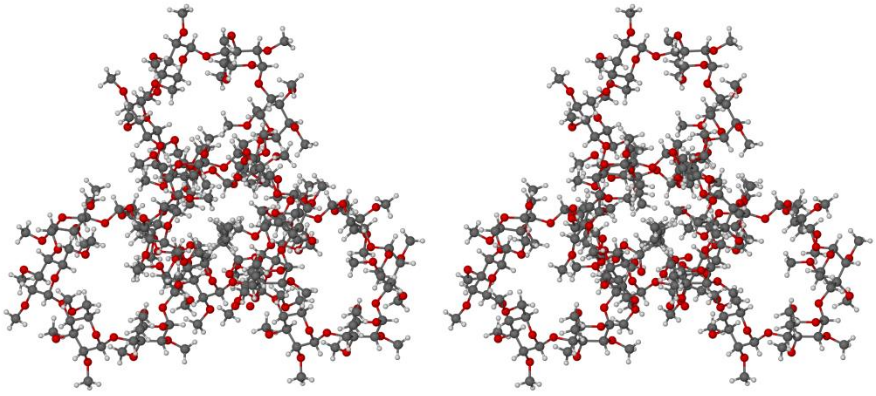

Figure 5.59a: A stereoview showing a packing feature of TMA·VAL. The guest and water molecules in the lower CD layer are omitted for clarity.

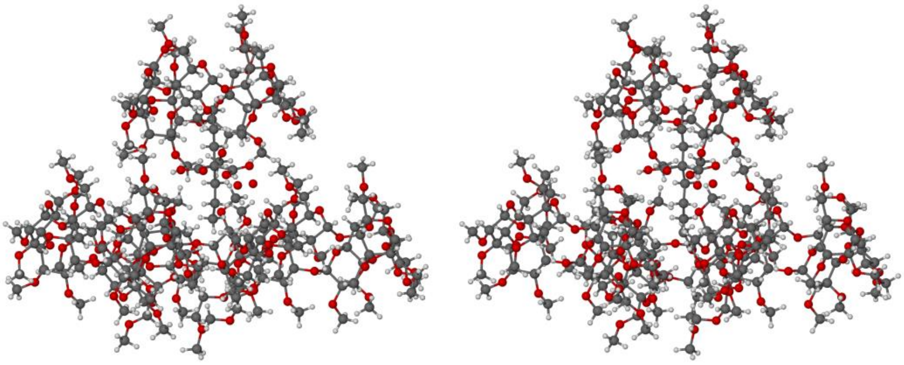

Figure 5.59b: A steroview which displays half of the fully extended aliphatic chain of valproic acid penetrating into the void between the three monomeric units in the lower layer. The guest and water molecules in the lower CD layer are omitted for clarity.

PXRD analysis

Figure 5.60 shows the computed PXRD pattern based on the single-crystal X-ray data and the experimental pattern obtained from the co-precipitated TMA·VAL complex. Since the respective temperatures to which these traces correspond are different (100 K and 294 K), there are small shifts in the angular positions of corresponding peaks (generally in the direction of increasing 2θ in the computed pattern, as expected). In addition, it is evident that the intensities of several peaks in the experimental pattern suffer from preferred orientation effects, the most serious case being that involving the peak at 2θ = 8.0°. (This, incidentally, vindicates the conclusion in the description of

Figure 5.53 above that it was the co-precipitated product, rather than the complex prepared by kneading, whose abnormally high peak intensity at this angular position was due to preferred orientation).

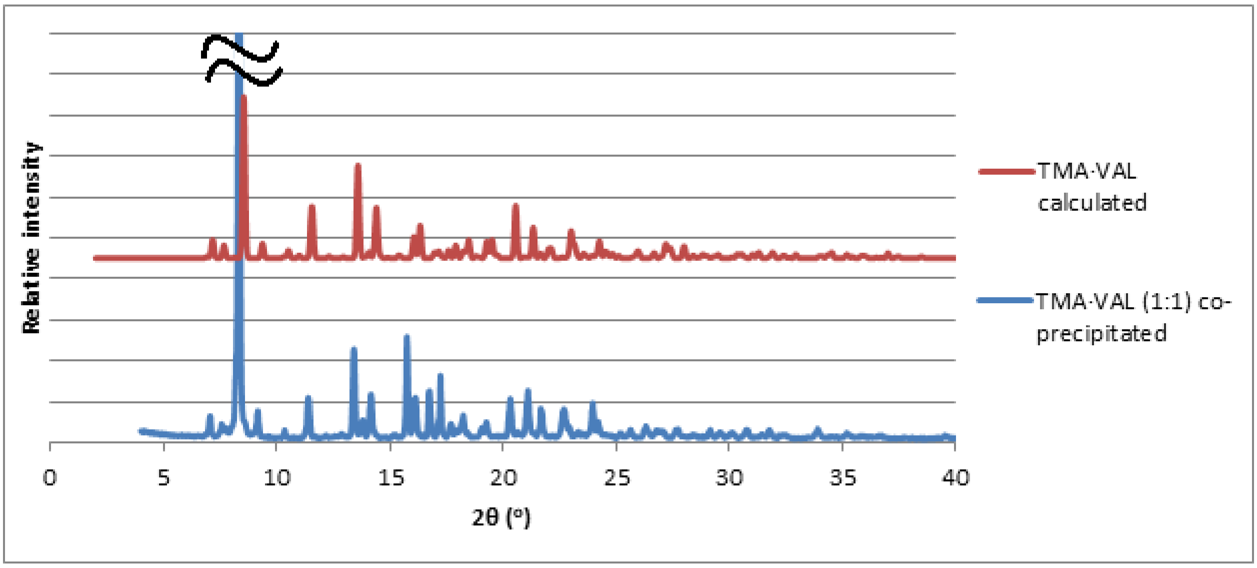

Figure 5.60: The PXRD pattern calculated from a single crystal X-ray structure of TMA·VAL and the PXRD pattern of TMA·VAL prepared *via* co-precipitation.

5.4) References

1) Trapani, G.; Cutrignelli, A.; Latrofa, A.; Franco, M.; Serra, M.; Pisu, M. G.; Biggio, G.; Liso, G. *Drug Dev. Ind. Pharm.*, **2004**, *30*, 53.
2) Bruno, J.; Cole, J. C.; Edgington, P. R.; Kessler, M.; Macrae, C. F.; McCabe, P. Pearson and R. Taylor, *Acta Cryst*., **2002**, *B58*, 389.
3) De Miranda, J. C.; Martins, T. E. A.; Veiga, F.; Ferraz, H. G. *Braz. J. Pharm. Sci.,* **2011**, *47*, 665.
4) Cyclodextrin-containing Supramolecular Structures From pseudo-polyrotaxanes towards molecular tubes, insulated molecular wires and topological networks M. van den Boogaard Ph.D. Thesis University of Groningen, The Netherlands January 2003 MSC Ph.D.-thesis series 2003-01 ISSN 1570-1530.
5) Bongiorno, D.; Ceraulo, L.; Ferrugia, M.; Filizzola, F.; Ruggirello, A.; Liveri, V. T. *Arch. Org. Chem.,* **2005**, *14*, 118.
6) Giordano, F.; Bettini, R. R.; Donini, C.; Gazzaniga, A.; Caira, M. R.; Zhang, G. G. Z.; Grant, D. J. W. *J. Pharm. Sci.*, **1999**, *88*, 1210.
7) Caira, M. R. *Rev. Roum. Chim.*, **2001**, *46*, 371.
8) XPREP, *Data Preparation and Reciprocal Space Exploration*. Version 2.0, Bruker Analytical X-ray Systems, **1999**.
9) Sheldrick, G. M. *Acta Cryst*., **2008**, *A64*, 112.
10) Lubhelwana, S. Crystal Isostructurality and X-ray Diffraction Studies of Cyclodextrin Inclusion Compounds, Msc Thesis, University of Cape Town, South Africa, **2005**.
11) Mentzafos, D.; Mavridis, I. M.; Le Bas, G.; Tsoucaris, G. *Acta Cryst.* 1991, *B47*, 746.
12) Harata, K. *Chem. Rev.*, **1998**, *98,* 1803.
13) Caira, M. R.; Dodds, D. R.; Nassimbeni, L. R. *Supramol. Chem.*, **2001**, *13*, 61.
14) Steiner, T.; Saenger, W. *Acta Cryst.,* **1998**, *B54*, 450.
15) Pubchem. *Valproic acid*. <https://pubchem.ncbi.nlm.nih.gov/compound/valproic_acid> (Accessed 16 January 2017).
16) Caira, M. R.; Bourne, S. A.; Mhlongo, W. T.; Dean, P. M. *Chem. Commun.,* **2004**, *19*, 2216.
17) Trollope, L.; Cruickshank, D. L.; Noonan, T.; Bourne, S. A.; Sorrenti, M.; Catenacci, L.; Caira, M. R. *Beilstein J. Org. Chem.,* **2014**, *10*, 3136.

18) Cruickshank, D. L. Physicochemical Studies of the Inclusion of Selected Agrochemicals in Cyclodextrins. PhD Thesis, University of Cape Town, South Africa, 2011.

Chapter 6
Conclusions

6.1) Conclusions

In summary, the author of this Master's dissertation discovered and fully characterized a new polymorph of isonicotinamide, namely polymorph 6, and also synthesized six new CD inclusion complexes, namely α-CD·VAL (2:1), β-CD·VAL (1:1), γ-CD·VAL (4:3), DMB·VAL (1:1), TMB·VAL (1:1) and TMA·VAL (1:1). In addition, the aqueous solubilities of the α-CD·VAL, β-CD·VAL and γ-CD·VAL inclusion complexes were assessed, the results indicating that they were generally approximately 30 % that of valproic acid. Further details and comments on the above results are provided below.

6.1.1) Allopurinol and 6-thioguanine

The attempts to produce either co-crystals or CD inclusion complexes with allopurinol and 6-thioguanine failed. However, there were a few preliminary results that displayed the formation of new material during the co-crystallization experiments with allopurinol, but unfortunately, none of these products could be further analysed.

A possible explanation for the formation of a few preliminary new phases with allopurinol, but not with 6-thioguanine, could be due to small chemical differences between the two molecules, and the fact that the aqueous solubility of 6-thioguanine is an order of magnitude lower than that of allopurinol.[1-2] The CD inclusion complex experiments all failed despite the different methods employed. The adverse physical properties, such as the high melting points (due to the extensive hydrogen bonding in the crystal structures and the resulting high lattice energies) and consequently low aqueous solubilities of these compounds, could have also contributed to the lack of any new CD complex products. Consequently, a hypothetical co-crystal or CD inclusion complex with either of the APIs would most likely be thermodynamically less stable than the individual crystals of each component.[3-5]

However, the attempted co-crystallization experiments with allopurinol led to the serendipitous discovery of a new polymorph of isonicotinamide (polymorph 6). Isonicotinamide is a widely used co-former in the research field of co-crystallization, and therefore the detailed characterisation of the X-ray crystal structure of polymorph 6 serves to alert researchers working with isonicotinamide to the possible unexpected formation of this polymorph in their research. ‘Serendipitous polymorphs’ of isonicotinamide have occurred previously[6] and it is imperative to provide researchers with the crystallographic data of such new crystal forms, so that a new product will not be mistaken for a co-crystal when it is rather a polymorph of the co-former.

6.1.2) Valproic acid

The results with regard to the ability of valproic acid to form co-crystals with the twelve selected co-formers are inconclusive. This is due to the fact that the focus on valproic acid was shifted towards CD inclusion complexation and thus the co-crystallization experiments were abandoned in favour of this more productive avenue. Only one set of co-precipitation experiments was performed using EtOH as the solvent medium, yet only the respective co-formers precipitated and thus those experiments did not produce the desired results.

In contrast, with regard to CD complexation, it was possible to form six new CD complexes with valproic acid, of which four of them were amenable to X-ray crystal structure elucidation. These are the first X-ray crystal structures of CD complexes with valproic acid and also the first documented crystal structures containing valproic acid.[7]

Valproic acid is known to cause pre-absorption gastrointestinal discomfort owing to the carboxylic acid functionality;[8-9] however, CD inclusion could mask the acidic residue (as observed in the relevant crystal structures reported here), thus reducing these gastrointestinal effects. From a commercial perspective CD inclusion could improve the efficacy of the drug and it could therefore possibly be prescribed to a larger group of patients. The pre-absorption side effects have been cited as a major disadvantage of valproic acid and previous attempts to prevent these side effects have been reported.[8-9] In addition, pure valproic acid is in the liquid state over a wide range of ‘ambient’ temperatures, while its CD complexes are crystalline solids, which are more convenient from the perspective of administration. Furthermore, the fact that a lower aqueous solubility was obtained for the CD complexes of valproic acid, indicates that there is the possible commercial application of a slow release form of valproic acid. However, partly due to paucity of the API, the method of solubility assessment of representative CD complexes undertaken here was rather rudimentary and the results should be viewed as preliminary only and worthy of re-investigation.

6.2) Future Work

6.2.1) Allopurinol and 6-thioguanine

Large numbers of co-crystallization experiments under a wide variety of differing conditions were performed for both allopurinol and 6-thioguanine. It may appear that not much more scope for this kind of research is left for these two drugs; however, different methodologies of preparation, as well as a different selection of co-formers, can be attempted in the future.

A very extensive variety of CD inclusion experiments were also performed under different conditions. However, future studies could extend the variety of non-crystalline CDs to include host compounds such as the sulfobutylether β-CD sodium salt, for possible interaction with allopurinol and 6-thioguanine.

6.2.2) Valproic acid

With regard to co-crystallization, multiple co-crystallization experiments that incorporate a wide range of methods, as well as the use of different co-formers, should be performed. Only one set of twelve individual experiments was performed during this Master's project, and the results obtained were not conclusive with regard to what could potentially be synthesized with different co-formers, methods and experimental conditions.

With reference to CD inclusion, the aqueous solubilities of the DMB·VAL, TMB·VAL and TMA·VAL complexes should be determined accurately, and more pertinent solubility values for α-CD·VAL, β-CD·VAL and γ-CD·VAL should be obtained, preferably using synthetic gastrointestinal fluids and ultimately in mouse models and human subjects. Likewise, for all six CD-valproic acid complexes reported here, assessment of their potential to reduce pre-absorption side effects is warranted and recommended for further studies.

6.3) References

1. Pubchem. *Allopurinol*. <https://pubchem.ncbi.nlm.nih.gov/compound/allopurinol> (Accessed 8 February 2016).
2. Pubchem. *6-Thioguanine*. <https://pubchem.ncbi.nlm.nih.gov/compound/6-Thioguanine> (Accessed 8 February 2016).
3. Sekhon, B. S. *Ars Pharmaceutica,* **2009**, *50*, 99.
4. Mirza, S.; Miroshnyk, I.; Heinämäki, J.; Yliruusi, J. *Dosis*, **2008**, *24*, 90.
5. Del Valle, M. *Process Biochem.*, **2004**, *39*, 1033.
6. Li, J.; Bourne, S. A.; Caira, M. R. *Chem. Comm.,* **2011**, *47*, 1530.
7. Bruno, J.; Cole, J. C.; Edgington, P. R.; Kessler, M.; Macrae, C. F.; McCabe, P. Pearson and R. Taylor, *Acta Cryst*., **2002**, *B58*, 389.
8. Schwartz, T. L.; Massa, J. L.; Gupta, S.; Al-Samarrai, S.; Devitt, P.; Masand, P. S. *J. Clin. Psychiat.,* **2000**, *2*, 45.
9. Sawyer, W. T.; Carson, S. W.; Early, J. J. *Am. J. Health-Syst. Ph.,* **1997**, *54*, 1716.

Appendix

Section 1: General

Table 1.1: List of available co-formers in the supramolecular laboratory at the University of Cape Town.

Number	Co-former	Number	Co-former
1	Adipic acid	19	L-Valine
2	Aspartic acid	20	Maleic acid
3	Benzamide	21	Malonic acid
4	Caffeine	22	Nicotinic acid
5	Cinnamamide	23	Nicotinamide
6	Citric acid	24	Orotic acid
7	D-Tartaric acid	25	Oxalic acid
8	Fumaric acid	26	Piperazine
9	Glutaric acid	27	Propionamide
10	Glycine	28	Pyrazinecarboxamide
11	Isonicotinamide	29	L-Pyroglutamic acid
12	Lactic acid	30	Saccharin
13	L-Arginine	31	Salicylic acid
14	L-Ascorbic acid	32	Sorbic acid
15	L-Glutamic acid	33	Suberic acid
16	L-Malic acid	34	Succinic acid
17	L-Proline	35	Uracil
18	L-Tartaric acid	36	Urea

Section 2: Co-crystallization of allopurinol

Table 2.1: The selected co-formers for co-crystallization screening experiments with allopurinol.

Number	**Selected co-former**
1	Benzamide
2	Benzoic acid
3	Fumaric acid
4	Glutaric acid
5	Isonicotinamide
6	Maleic acid
7	Nicotinamide
8	Piperazine
9	Propionamide
10	D-Tartaric acid
11	Urea

Co-grinding experiments with allopurinol

Extensive co-grinding experiments were performed in order to attempt to produce a new crystalline phase by co-grinding allopurinol with each of the variety of 11 co-formers that were selected. Initially, dry co-grinding experiments were performed, where three of the experiments verified formation of a new crystalline phase (Table 2.2). These included the experimental combinations of allopurinol and isonicotinamide, allopurinol and piperazine, as well as allopurinol and maleic acid.

Table 2.2: Dry co-grinding experiments with allopurinol and the selected co-formers.

Number	**API**	**Selected co-former**	**Result**
1	Allopurinol	Benzamide	Physical mixture
2	Allopurinol	Benzoic acid	Physical mixture
3	Allopurinol	Fumaric acid	Physical mixture
4	Allopurinol	Glutaric acid	Physical mixture
5	Allopurinol	Isonicotinamide	New crystalline phase
6	Allopurinol	Maleic acid	New crystalline phase
7	Allopurinol	Nicotinamide	Physical mixture
8	Allopurinol	Piperazine	New crystalline phase
9	Allopurinol	Propionamide	Physical mixture
10	Allopurinol	D-Tartaric acid	Physical mixture
11	Allopurinol	Urea	Physical mixture

With regard to the PXRD pattern of the product of dry co-grinding allopurinol and isonicotinamide in an equimolar ratio, distinctive new peaks appeared which represented the new crystalline phase (Figure 2.1). However, there were still peaks from the remaining original reagents. This either suggested that a longer grinding time would have been required to complete the reaction to fully produce the new crystalline phase, or that a different stoichiometric ratio of allopurinol and isonicotinamide was required.

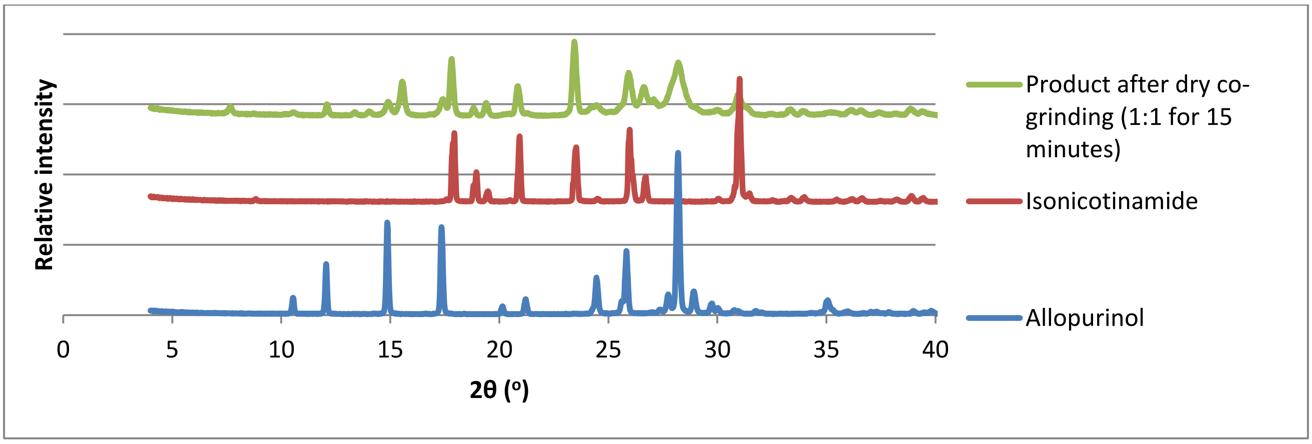

Figure 2.1: PXRD patterns of allopurinol, isonicotinamide, and the product of dry co-grinding these components in a 1:1 molar ratio for 15 minutes.

As a result, different stoichiometric ratios of allopurinol and isonicotinamide, as well as longer grinding times, were attempted. Consequently, the combination that revealed a pure, new crystalline phase was achieved with the components present in an equimolar ratio and dry co-ground for 35 minutes (Figure 2.2). The 2θ-positions of this new crystalline phase are 7.5°, 10.2°, 13.5°, 14.0°, 15.5°, 16.8°, 17.9°, 21.0°, 23.5°, 24,2°, 25.0°, 25.5°, 26.5°, 27.0°, 27.8°, 28.5°, 31.2°, 35.0°, 37.5°.

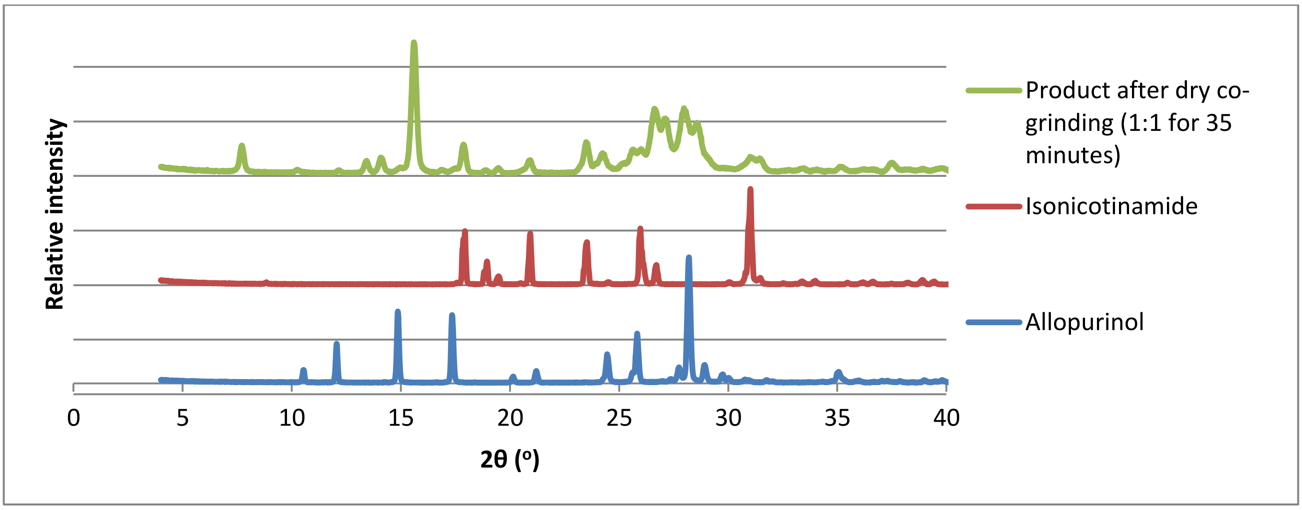

Figure 2.2: PXRD patterns of allopurinol, isonicotinamide, and the product of dry co-grinding these components in a 1:1 molar ratio for 35 minutes.

Furthermore, as mentioned above, the PXRD pattern of the product of dry co-grinding allopurinol and piperazine in an equimolar ratio for 15 minutes also indicated the development of a new crystalline phase (Figure 2.3). However, it is evident that the peaks that represent allopurinol are still present and consequently experiments with different stoichiometric ratios of allopurinol and piperazine were attempted in order to generate the pure, new, crystalline phase.

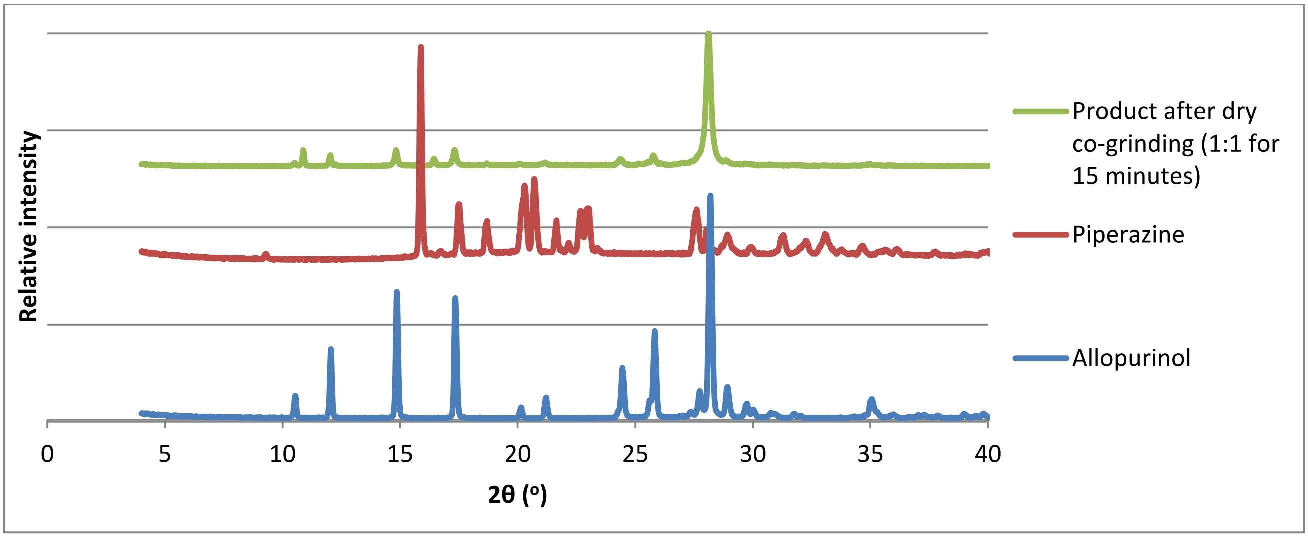

Figure 2.3: PXRD patterns of allopurinol, piperazine, and the product of dry co-grinding these components in a 1:1 molar ratio for 15 minutes.

As a result, the experiment that produced the pure, crystalline product was a 1:3 stoichiometric ratio of allopurinol to piperazine dry co-ground for 15 minutes (Figure 2.4). The 2θ-positions of this new crystalline phase occurred at 10.9°, 12.2°, 16.5°, 18.8°, 21.0°, 24.5°, 25.2°, 26.2°, 27.0°, 29.0°, 32.5°, 33.0° and 39.0°. The peak that could possibly still belong to allopurinol is the peak at 28.0°. This particular peak displayed a significant decrease in intensity from the experiment performed in an equimolar ratio (Figure 2.3) in comparison to the experiment conducted in a 1:3 stoichiometric ratio (Figure 2.4). Therefore, it could be attributed to negligible trace amounts of allopurinol remaining.

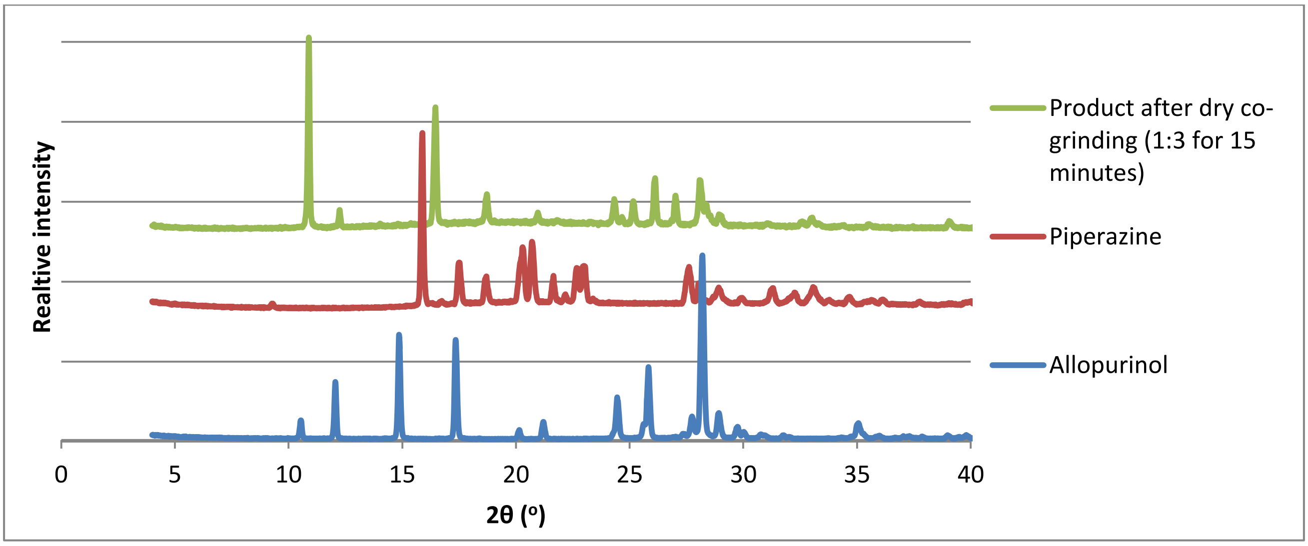

Figure 2.4: PXRD patterns of allopurinol, piperazine, and the product of dry co-grinding these components in a 1:3 molar ratio for 15 minutes.

However, an unexpected phenomenon occurred with this new crystalline phase as time progressed: it disintegrated and separated, only the presence of allopurinol being evident in the final PXRD trace (Figure 2.5). When allopurinol and piperazine were dry co-ground for 15 minutes, a liquid-based paste formed, which was representative of the new, product crystalline phase. However, when this paste dried, the phase separated and only allopurinol was observed. Presumably, piperazine became amorphous during the co-grinding procedure and thus a physical mixture of the original components was produced.

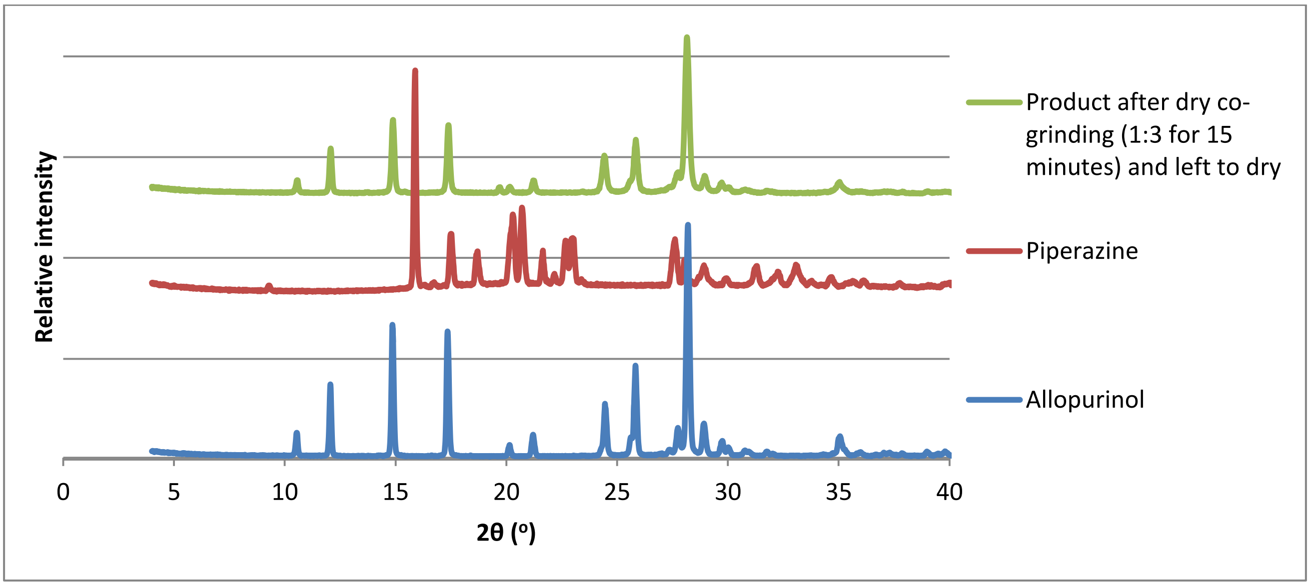

Figure 2.5: PXRD patterns of allopurinol, piperazine, and the product of dry co-grinding these components in a 1:3 molar ratio for 15 minutes and subsequently left to dry.

In addition, the product PXRD pattern resulting from dry co-grinding allopurinol and maleic acid in an equimolar ratio for 15 minutes also indicated the presence of a new and seemingly pure crystalline phase (Figure 2.6). The 2θ-positions of the new peaks are at 6.5°, 11.5°, 13.0°, 14.6°, 18.5°, 18.8°, 19.5°, 20.5°, 22.5°, 23.8°, 24.5°, 25.2°, 26.2°, 26.9°, 27.6°, 29.2°, 31.1°, 32.0°, 33.0° and 34.2°.

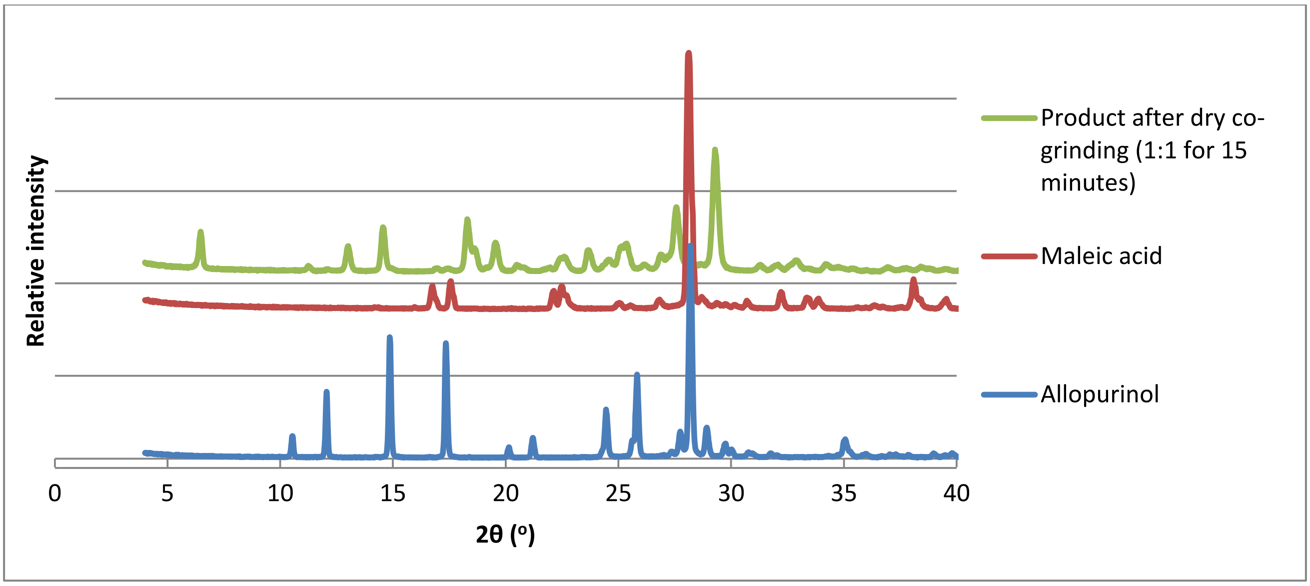

Figure 2.6: PXRD patterns of allopurinol, maleic acid, and the product of dry co-grinding these components in a 1:1 molar ratio for 15 minutes.

The remaining PXRD patterns produced from dry co-grinding indicated that only a physical mixture of allopurinol and the respective co-former resulted. This was confirmed since the peaks from the PXRD patterns of the starting material directly overlapped with the peaks from the PXRD patterns of the co-ground material. Furthermore, liquid-assisted grinding (LAG) experiments were also performed with a variety of different solvents with the expectation of producing new crystalline phases. This was executed with the combinations from the unsuccessful dry co-grinding experiments. The role of the solvent in LAG is not well understood; however, it is thought that the solvent coating the reacting particles allows the reagents to diffuse in order to interact to form the product by acting as an interface which assists in solubility.[1] The different solvents that were selected included EtOH, ethyl acetate, hexane, dimethyl sulfoxide (DMSO) and chloroform. The total volume of solvent added for each LAG experiment ranged between 0.5 – 6.0 μl per mg of API, depending on the volatility of the solvent. All five sets of these LAG experiments only mimicked the results that were obtained from the dry co-grinding experiments, with the exception that allopurinol and propionamide with DMSO became slightly amorphous with LAG. The results are summarised below in Tables 2.3 – 2.7.

Table 2.3: The results from the LAG experiments of allopurinol and eight of the selected co-formers with EtOH.

Number	API	Selected co-former	Result
1	Allopurinol	Benzamide	Physical mixture
2	Allopurinol	Benzoic acid	Physical mixture
3	Allopurinol	Fumaric acid	Physical mixture
4	Allopurinol	Glutaric acid	Physical mixture
5	Allopurinol	Nicotinamide	Physical mixture
6	Allopurinol	Propionamide	Physical mixture
7	Allopurinol	D-Tartaric acid	Physical mixture
8	Allopurinol	Urea	Physical mixture

Table 2.4: The results from the LAG experiments of allopurinol and eight of the selected co-formers with ethyl acetate.

Number	API	Selected co-former	Result
1	Allopurinol	Benzamide	Physical mixture
2	Allopurinol	Benzoic acid	Physical mixture
3	Allopurinol	Fumaric acid	Physical mixture
4	Allopurinol	Glutaric acid	Physical mixture
5	Allopurinol	Nicotinamide	Physical mixture
6	Allopurinol	Propionamide	Physical mixture
7	Allopurinol	D-Tartaric acid	Physical mixture
8	Allopurinol	Urea	Physical mixture

Table 2.5: The results from the LAG experiments of allopurinol and eight of the selected co-formers with hexane.

Number	**API**	**Selected co-former**	**Result**
1	Allopurinol	Benzamide	Physical mixture
2	Allopurinol	Benzoic acid	Physical mixture
3	Allopurinol	Fumaric acid	Physical mixture
4	Allopurinol	Glutaric acid	Physical mixture
5	Allopurinol	Nicotinamide	Physical mixture
6	Allopurinol	Propionamide	Physical mixture
7	Allopurinol	D-Tartaric acid	Physical mixture
8	Allopurinol	Urea	Physical mixture

Table 2.6: The results from the LAG experiments of allopurinol and eight of the selected co-formers with DMSO.

Number	**API**	**Selected co-former**	**Result**
1	Allopurinol	Benzamide	Physical mixture
2	Allopurinol	Benzoic acid	Physical mixture
3	Allopurinol	Fumaric acid	Physical mixture
4	Allopurinol	Glutaric acid	Physical mixture
5	Allopurinol	Nicotinamide	Physical mixture
6	Allopurinol	Propionamide	Physical mixture became slightly amorphous
7	Allopurinol	D-Tartaric acid	Physical mixture
8	Allopurinol	Urea	Physical mixture

Table 2.7: The results from the LAG experiments of allopurinol and eight of the selected co-formers with chloroform.

Number	API	Selected co-former	Result
1	Allopurinol	Benzamide	Physical mixture
2	Allopurinol	Benzoic acid	Physical mixture
3	Allopurinol	Fumaric acid	Physical mixture
4	Allopurinol	Glutaric acid	Physical mixture
5	Allopurinol	Nicotinamide	Physical mixture
6	Allopurinol	Propionamide	Physical mixture
7	Allopurinol	D-Tartaric acid	Physical mixture
8	Allopurinol	Urea	Physical mixture

Co-precipitation experiments with allopurinol

A full co-precipitation analysis was performed with all the selected allopurinol and co-former combinations. This was in spite of the fact that the majority of the PXRD dry co-grinding results and all of the LAG results were unsuccessful in forming new crystalline material.

It is not necessarily conclusive that new crystalline material cannot be created through co-precipitation experiments, even if the dry co-grinding and LAG experiments indicated otherwise.[2] As a result, co-precipitation experiments, were performed according to the method outlined in the Experimental Methods (Chapter 2 in the main dissertation) under section 2.2.4 on pp. 18 – 19, with the solvents chloroform and DMSO. One of the co-precipitation experiments with DMSO incorporated the use of different stoichiometric ratios.

As already discussed in the main dissertation, the majority of the results from both the organic solvent sets did not reveal any new crystalline material (Tables 2.8 – 2.11). However, there was one experiment (in which allopurinol and the respective co-former were dissolved in chloroform) which revealed a new crystalline phase. This involved allopurinol and isonicotinamide, where a new polymorph of isonicotinamide was produced serendipitously. This is discussed in detail in the main dissertation in Chapter 3 under section 3.2.3 on pp. 36 – 74.

Table 2.8: Co-precipitation of allopurinol with various co-formers prepared in a 1:1 molar ratio in chloroform *via* slow evaporation.

Number	API	Selected co-former	Result
1	Allopurinol	Benzamide	Physical mixture
2	Allopurinol	Benzoic acid	Physical mixture
3	Allopurinol	Fumaric acid	Physical mixture
4	Allopurinol	Glutaric acid	Physical mixture
5	Allopurinol	Isonicotinamide	A new polymorph of isonicotinamide formed
6	Allopurinol	Maleic acid	Physical mixture
7	Allopurinol	Nicotinamide	Physical mixture
8	Allopurinol	Piperazine	Physical mixture
9	Allopurinol	Propionamide	Physical mixture
10	Allopurinol	D-Tartaric acid	Physical mixture
11	Allopurinol	Urea	Physical mixture

Table 2.9: Co-precipitation of allopurinol with various co-formers prepared in a 1:1 molar ratio in DMSO *via* slow evaporation.

Number	API	Selected co-former	Result
1	Allopurinol	Benzamide	Physical mixture
2	Allopurinol	Benzoic acid	Physical mixture
3	Allopurinol	Fumaric acid	Physical mixture
4	Allopurinol	Glutaric acid	Physical mixture
5	Allopurinol	Isonicotinamide	Physical mixture
6	Allopurinol	Maleic acid	Physical mixture
7	Allopurinol	Nicotinamide	Physical mixture
8	Allopurinol	Piperazine	Physical mixture
9	Allopurinol	Propionamide	Physical mixture
10	Allopurinol	D-Tartaric acid	Physical mixture
11	Allopurinol	Urea	Physical mixture

Table 2.10: Co-precipitation of allopurinol with various co-formers prepared in a 1:1 molar ratio in DMSO *via* slow cooling followed by slow evaporation.

Number	**API**	**Selected co-former**	**Result**
1	Allopurinol	Benzamide	Physical mixture
2	Allopurinol	Benzoic acid	Physical mixture
3	Allopurinol	Isonicotinamide	Physical mixture
4	Allopurinol	Nicotinamide	Physical mixture
5	Allopurinol	Piperazine	Physical mixture
6	Allopurinol	Propionamide	Physical mixture
7	Allopurinol	D-Tartaric acid	Physical mixture
8	Allopurinol	Urea	Physical mixture

Table 2.11: Co-precipitation of allopurinol with three selected co-formers that were prepared in different stoichiometric ratios (performed in the solvent DMSO *via* slow evaporation).

Number	**API**	**Selected co-former**	**Stoichiometric ratio**	**Result**
1	Allopurinol	Isonicotinamide	1:3	A physical mixture with a variety of known polymorphs of isonicotinamide
2	Allopurinol	Isonicotinamide	1:5	A physical mixture with a variety of known polymorphs of isonicotinamide
3	Allopurinol	Isonicotinamide	3:1	Physical mixture
4	Allopurinol	Isonicotinamide	5:1	Physical mixture
5	Allopurinol	Piperazine	1:3	Physical mixture
6	Allopurinol	Piperazine	1:5	Physical mixture
7	Allopurinol	Piperazine	3:1	Physical mixture
8	Allopurinol	Piperazine	5:1	Physical mixture
9	Allopurinol	Maleic acid	1:3	Physical mixture
10	Allopurinol	Maleic acid	1:5	Physical mixture
11	Allopurinol	Maleic acid	3:1	Physical mixture
12	Allopurinol	Maleic acid	5:1	Physical mixture

Recrystallization of products initially obtained from dry co-grinding experiments

Furthermore, experiments were performed which involved recrystallizing some of the new material that was produced from the various dry co-ground experiments (Table 2.12). The two systems in question were allopurinol and isonicotinamide dry co-ground for 35 minutes in an equimolar ratio, and allopurinol and piperazine dry co-ground for 15 minutes in a 1:3 stoichiometric ratio. In the latter case, the product was dissolved in the respective solvents before it dried. The aim of the recrystallization experiments was to produce single crystals of the new material for further analysis. Furthermore, the new material that was produced *via* dry co-grinding allopurinol and maleic acid could not be reproduced for this experiment. Unfortunately, the reasons for the inconsistency of reproducing this species remained unknown. However, this new phase could have been pressure-dependent when the dry co-grinding experiment was performed. Unfortunately, the results indicated that the new crystalline phase in all the experiments dissolved and the original reagents recrystallized (Table 2.12).

Table 2.12: Results of the recrystallization of the products from the dry co-grinding of allopurinol and isonicotinamide (1:1) for 35 minutes, as well as dry co-grinding of allopurinol and piperazine (1:3) for 15 minutes.

Number	**Material recrystallized**	**Solvent**	**Result**
1	Allopurinol with isonicotinamide (1:1) dry co-ground for 35 minutes	EtOH	The original reagents crystallized
2	Allopurinol with isonicotinamide (1:1) dry co-ground for 35 minutes	Chloroform	The original reagents crystallized
3	Allopurinol with isonicotinamide (1:1) dry co-ground for 35 minutes	Water	The original reagents crystallized
4	Allopurinol with piperazine (1:1) dry co-ground for 15 minutes	EtOH	The original reagents crystallized
5	Allopurinol with piperazine (1:3) dry co-ground for 15 minutes	EtOH	The original reagents crystallized
6	Allopurinol with piperazine (1:3) dry co-ground for 15 minutes	Water	The original reagents crystallized
7	Allopurinol with piperazine (1:3) dry co-ground for 15 minutes	DMSO	The original reagents crystallized

Section 3: Cyclodextrin inclusion with allopurinol

Native cyclodextrin inclusion with allopurinol

Kneading experiments with allopurinol

Kneading experiments were attempted with the aim of including allopurinol in the native CDs, namely α-CD, β-CD and γ-CD (Table 3.1). A mixture containing an equimolar ratio of each CD and allopurinol (5 mg, 0.0367 mmol) was prepared and kneaded using small additions of water as the medium for 30 minutes.

Table 3.1: The results from the kneading experiments of the native CDs with allopurinol.

Number	API	Cyclodextrin	Result
1	Allopurinol	α-cyclodextrin	Physical mixture
2	Allopurinol	β-cyclodextrin	Physical mixture
3	Allopurinol	γ-cyclodextrin	Physical mixture

Unfortunately, the results did not indicate any inclusion taking place, since the resultant PXRD patterns were the sum of the PXRD patterns of the original reagents.

Co-precipitation experiments with allopurinol

CD inclusion co-precipitation experiments of allopurinol were also attempted with the native CDs. An equimolar ratio and a 2:1 molar ratio of CD and allopurinol (5 mg, 0.0367 mmol) was prepared for each native CD. Each CD was dissolved in the respective amount of water depending on the stoichiometric ratio used. For α-CD, 0.8 cm^3 of water was used for both stoichiometric ratios, while for β-CD and γ-CD, 2 cm^3 and 4 cm^3 of water were used for the 1:1 and 2:1 stoichiometric ratios respectively. The reagents were heated to 75 ^oC while stirring.[3] The 5 mg of allopurinol was slowly added to each aqueous solution of pre-dissolved CD while stirring at 75 ^oC. The solutions were further stirred and capped for 3 hours, while maintaining a temperature of 75 °C. The saturated solutions were filtered into clean vials and prepared for slow cooling. This entire experiment was repeated twice, except that a small measured volume of EtOH was added to the resultant solution for the first repetition, and a drop of Tween® 80 was added to the resultant solution for the second repetition. The results are displayed in Tables 3.2 – 3.4.

Table 3.2: The results from the various native CD co-precipitation experiments with allopurinol, co-precipitated in water.

Number	**System**	**Result**
1	α-CD and allopurinol (1:1)	The original reagents precipitated
2	α-CD and allopurinol (2:1)	The original reagents precipitated
3	β-CD and allopurinol (1:1)	The original reagents precipitated
4	β-CD and allopurinol (2:1)	The original reagents precipitated
5	γ-CD and allopurinol (1:1)	The original reagents precipitated
6	γ-CD and allopurinol (2:1)	The original reagents precipitated

Table 3.3: The results from the various native CD co-precipitation experiments with allopurinol, co-precipitated in water with a few drops of EtOH.

Number	**System**	**Result**
1	α-CD and allopurinol (1:1)	The original reagents precipitated
2	α-CD and allopurinol (2:1)	The original reagents precipitated
3	β-CD and allopurinol (1:1)	The original reagents precipitated
4	β-CD and allopurinol (2:1)	The original reagents precipitated
5	γ-CD and allopurinol (1:1)	The original reagents precipitated
6	γ-CD and allopurinol (2:1)	The original reagents precipitated

Table 3.4: The results from the various native CD co-precipitation experiments with allopurinol, co-precipitated in water with a drop of Tween® 80.

Number	System	Result
1	α-CD and allopurinol (1:1)	A Tween® 80 α-CD inclusion complex precipitated
2	α-CD and allopurinol (2:1)	A Tween® 80 α-CD inclusion complex precipitated
3	β-CD and allopurinol (1:1)	A Tween® 80 β-CD inclusion complex precipitated
4	β-CD and allopurinol (2:1)	A Tween® 80 β-CD inclusion complex precipitated
5	γ-CD and allopurinol (1:1)	A Tween® 80 γ-CD inclusion complex precipitated
6	γ-CD and allopurinol (2:1)	A Tween® 80 γ-CD inclusion complex precipitated

Unfortunately, the results did not yield any desired CD inclusion complexes, even though different stoichiometric ratios and solvent-media were employed.

Furthermore, a final attempt to produce a β-CD inclusion complex with allopurinol was performed using a 0.1 M solution of KOH. Allopurinol is very soluble in a basic solution and thus a liquid formulation of allopurinol and KOH was added dropwise into an aqueous β-CD solution.[4] A base will only hydrolyse a CD molecule if the pH of the solution exceeds 12.[5] According to Jiménez *et al.*, a β-CD·allopurinol inclusion complex was synthesized in D_2O with a minimal amount of KOH. The pH of the solution was 10.5.[6]

Thus, 5 mg (0.0367 mmol) of allopurinol was pre-dissolved in 0.2 cm^3 of 0.1 M KOH solution and added dropwise to a 1.8 cm^3 aqueous solution of β-CD. This experiment was performed in duplicate where one vial was allowed to stir at 55 ^oC and the other vial was left to stir at room temperature. The resultant solutions were left to stir for 2 days, and their pH was subsequently measured after filtering and the solutions were then prepared for slow evaporation.[a] The results are summarised in Table 3.5.

---

[a] The pH measurements were performed on the Crison micropH 2000 pH meter, which was equipped with a Ω Metrohm glass electrode.

Table 3.5: Co-precipitation of β-CD and allopurinol, where allopurinol was pre-dissolved in 0.2 cm^3 of aqueous KOH solution.

Number	**System**	**pH**	**Result**
1	Allopurinol and β-CD stirred at 55 °C	9.29	The original reagents precipitated
2	Allopurinol and β-CD stirred at room temperature	9.21	The original reagents precipitated

As indicated, the results were unsatisfactory and thus the experiment was repeated; however, the aim was to raise the pH of the overall solution in order to assess whether a higher pH might influence inclusion complexation. Furthermore, according to the paper by Jiménez *et al.*, the authors obtained a resultant solution with a pH of 10.5.[6] As a result, the same procedure was followed as described above, although 0.4 cm^3 of KOH solution was used to pre-dissolve the allopurinol instead of 0.2 cm^3. The results are displayed in Table 3.6.

Table 3.6: Co-precipitation of β-CD and allopurinol, where allopurinol was pre-dissolved in 0.4 cm^3 of aqueous KOH solution.

Number	**System**	**pH**	**Result**
1	Allopurinol and β-CD stirred at 55 °C	11.30	The original reagents precipitated
2	Allopurinol and β-CD stirred at room temperature	10.21	The original reagents precipitated

Unfortunately, the results replicated those obtained previously. The higher pH, of 11.30, obtained in experiment number 1 (Table 3.6), in comparison to the pH of 10.21 as obtained in experiment number 2 (Table 3.6), was most likely owing to errors in the volume measurements of the respective solutions when preparing the system. Consequently, the overall experimentation that used a base to produce a β-CD·allopurinol inclusion complex, was unsuccessful.

Methylated cyclodextrin inclusion with allopurinol

Kneading experiments with allopurinol

CD inclusion kneading experiments of allopurinol were attempted with the methylated CDs, namely DMB, TMB and TMA. Equimolar amounts of each methylated CD and allopurinol (5 mg, 0.0367 mmol), were prepared and the three combinations were kneaded for 30 minutes. Unfortunately, the results were unsuccessful and they are summarised in Table 3.7.

Table 3.7: The results from the kneading experiments with the methylated cyclodextrins and allopurinol.

Number	API	Cyclodextrin	Result
1	Allopurinol	DMB	Became amorphous
2	Allopurinol	TMB	Physical mixture
3	Allopurinol	TMA	Physical mixture

Co-precipitation experiments with allopurinol

CD inclusion co-precipitation experiments of allopurinol were attempted with the same methylated CDs as in the kneading experiments described above. Equimolar amounts of each methylated CD and allopurinol (5 mg, 0.0367 mmol), were prepared. Masses of 48.91 mg (0.0367 mmols) of DMB, 52.51 mg (0.0367 mmols) of TMB and 45.01 mg (0.0367 mmol) of TMA were dissolved in 1.5 cm^3 of water in separate vials at room temperature while stirring. The allopurinol was added very slowly to each solution which contained the dissolved methylated CD. Owing to the fact that not all of the allopurinol dissolved, temperature cycling was employed. The stirring solutions were heated to 70 ^{o}C for 15 minutes and thereafter rapidly cooled in the cold room to 4 ^{o}C. This process was repeated eight times. The saturated solutions were filtered immediately after being removed from the cold room. The filtered solutions were sealed and placed in the oven at 60 ^{o}C and left undisturbed in order to induce crystallization. The products of these experiments were precipitated crystals of the pure methylated CD, as confirmed by ^1H NMR.

Section 4: Solubility experiments with allopurinol

4.1) Calculation of the error in mass from the calibration curve

- $y = 0.0796\,x - 0.0041$ *equation 1*
- $y = 0.0796$ *equation 2*

A point selected at $y = 0.447$, therefore:

- $0.447 = 0.0796\,x - 0.0041$

  $x = 5.66708542171 \times 10^{-8}$ mol.cm^{-3} *from equation 1*

- $0.447 = 0.0796$

  $x = 5.6155778894 \times 10^{-8}$ mol.cm^{-3} *from equation 2*

The absolute value determined from the subtraction of the two x values:

- $/\ x_{\text{equation 2}} - x_{\text{equation 1}}\ / = 5.15075323 \times 10^{-10}$ mol.cm^{-3}

Obtaining the mass from the concentration:

- $5.15075323 \times 10^{-10}$ mol.cm^{-3} = number of moles / 5 cm^{3}

  number of moles = $2.575376625 \times 10^{-9}$ mols

  Therefore:

  $2.575376625 \times 10^{-9}$ mols = mass / 136.112 g.mol^{-1}

  Error mass = $3.505396597792 \times 10^{-7}$ g

  = 3.5054×10^{-4} mg

4.2) Phase solubility analysis of allopurinol with γ-CD, HPBCD and RAMEB

A predetermined mass of each CD was dissolved in water in a volumetric flask. With regard to γ-CD, a mass of 1.19232 g (9.19206 x 10^{-4} mol) was dissolved in water in a 50 cm^3 volumetric flask. While, with regard to HPBCD and RAMEB, masses of 2.69189g (1.92767 x 10^{-3} mol) and 2.51149 g (1.92747 x 10^{-3} mol) respectively were separately dissolved in 100 cm^3 volumetric flasks. The method was followed according to the Experimental Methods (Chapter 2 in the main dissertation) under section 2.9.1 on pp. 23 – 24. The resultant phase solubility curves are displayed below (Figure 4.1 – 4.3).

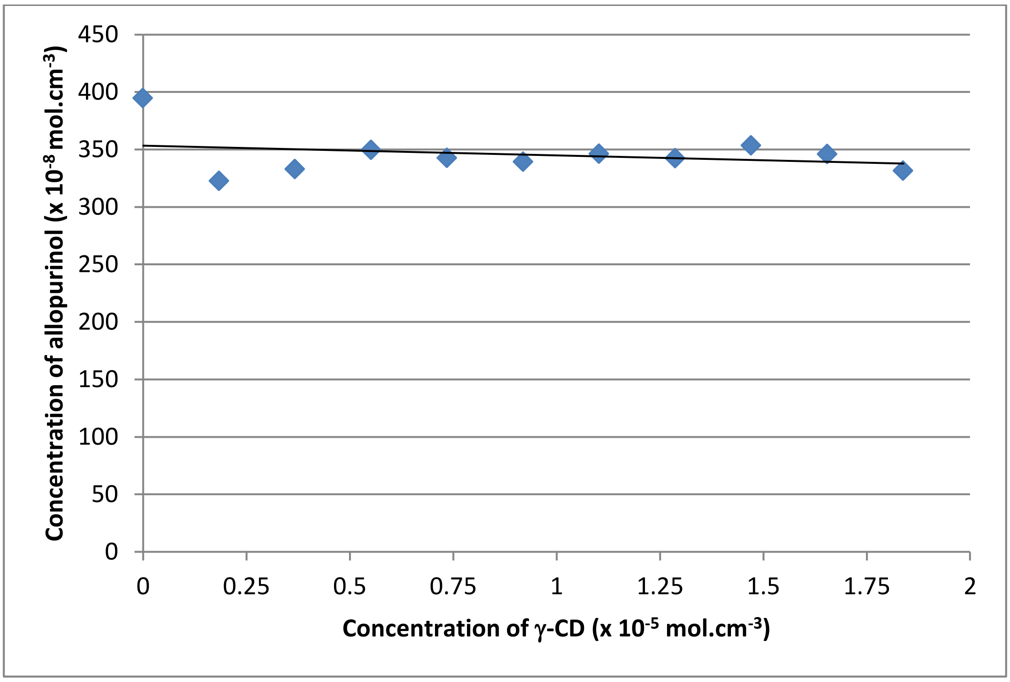

Figure 4.1: Phase solubility curve of the concentration of allopurinol versus the concentration of γ-CD.

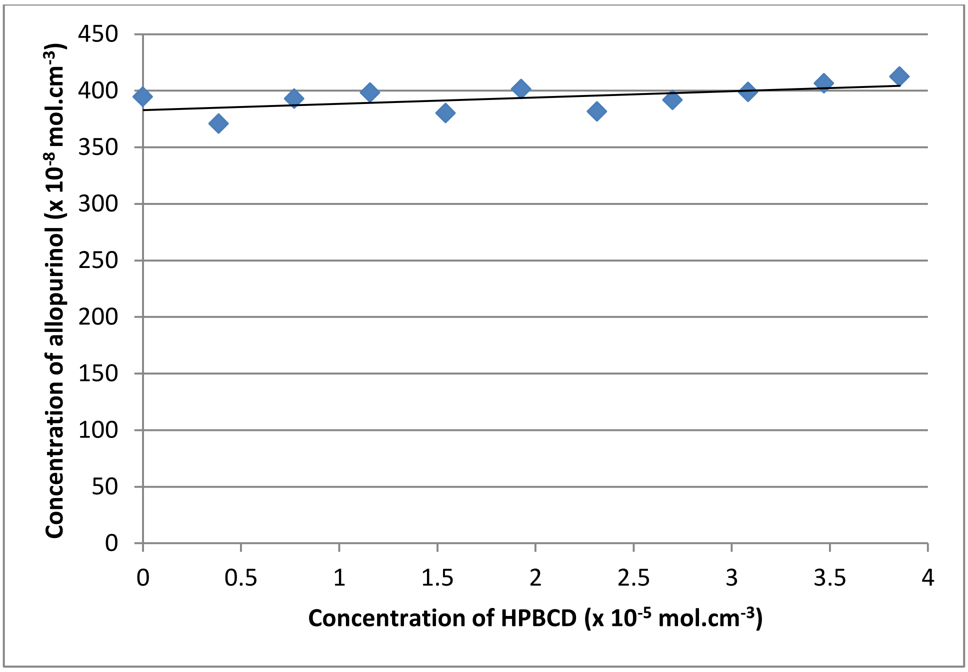

Figure 4.2: Phase solubility curve of the concentration of allopurinol versus the concentration of HPBCD.

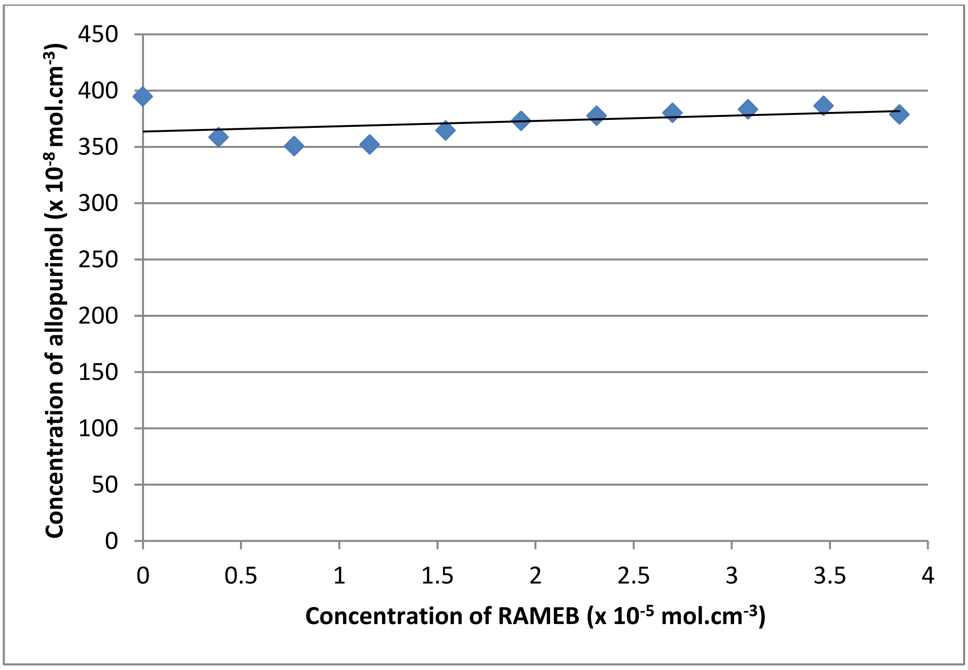

Figure 4.3: Phase solubility curve of the concentration of allopurinol versus the concentration of RAMEB.

As a result, it is evident that the solubility of allopurinol was not improved, despite the varied selection of CDs and the varying solution concentrations employed.

Section 5: Co-crystallization of 6-thioguanine

Table 5.1: The selected co-formers for co-crystallization screening experiments with 6-thioguanine.

Number	Selected co-former
1	Benzamide
2	Benzoic acid
3	Fumaric acid
4	Glutaric acid
5	Isonicotinamide
6	Maleic acid
7	Nicotinamide
8	Piperazine
9	Propionamide
10	D-Tartaric acid
11	Urea

Numerous co-grinding experiments were performed in order to attempt to produce a new crystalline phase with 6-thioguanine and each of the 11 co-formers that were selected. Initially, dry co-grinding experiments were performed; however, none of the results yielded a new crystalline phase, as displayed in Table 5.2. This was confirmed since the peaks from the PXRD patterns of the co-ground material were the sum of the PXRD patterns of the starting materials.

Table 5.2: Dry co-grinding experiments with 6-thioguanine and the eleven selected co-formers.

Number	API	Selected co-former	Result
1	6-Thioguanine	Benzamide	Physical mixture
2	6-Thioguanine	Benzoic acid	Physical mixture
3	6-Thioguanine	Fumaric acid	Physical mixture
4	6-Thioguanine	Glutaric acid	Physical mixture
5	6-Thioguanine	Isonicotinamide	Physical mixture
6	6-Thioguanine	Maleic acid	Physical mixture
7	6-Thioguanine	Nicotinamide	Physical mixture
8	6-Thioguanine	Piperazine	Physical mixture
9	6-Thioguanine	Propionamide	Physical mixture
10	6-Thioguanine	D-Tartaric acid	Physical mixture
11	6-Thioguanine	Urea	Physical mixture

Subsequently, liquid-assisted grinding (LAG) experiments were also performed with EtOH as the medium, added in very small volumes (approximately 3 µl per mg of API). These LAG experiments produced only physical mixtures of the two respective reagents used. The results are summarised in Table 5.3 below.

Table 5.3: The results from the LAG experiments of 6-thioguanine and the eleven selected co-formers with EtOH.

Number	API	Selected co-former	Result
1	6-Thioguanine	Benzamide	Physical mixture
2	6-Thioguanine	Benzoic acid	Physical mixture
3	6-Thioguanine	Fumaric acid	Physical mixture
4	6-Thioguanine	Glutaric acid	Physical mixture
5	6-Thioguanine	Isonicotinamide	Physical mixture
6	6-Thioguanine	Maleic acid	Physical mixture
7	6-Thioguanine	Nicotinamide	Physical mixture
8	6-Thioguanine	Piperazine	Physical mixture
9	6-Thioguanine	Propionamide	Physical mixture
10	6-Thioguanine	D-Tartaric acid	Physical mixture
11	6-Thioguanine	Urea	Physical mixture

Co-Precipitation experiments with 6-thioguanine

A full set of co-precipitation experiments was performed for all selected 6-thioguanine and co-former combinations, despite all of the co-grinding experiments having been unsuccessful. Furthermore, as mentioned previously, it is not necessarily conclusive that new crystalline material cannot be created through co-precipitation experiments, even if the dry co-grinding and LAG experiments indicated otherwise.[2] As a result, equimolar co-precipitation experiments were performed with DMSO as the solvent, according to the method outlined in the Experimental Methods (Chapter 2 in the main dissertation) under section 2.2.4 pp. 18 – 19. DMSO was selected owing to the fact that 6-thioguanine was rather insoluble in every other organic solvent. The majority of the results from all the organic solvent sets did not reveal any new crystalline material. These results are summarised in Table 5.4.

Table 5.4: Co-precipitation of 6-thioguanine with the selected co-formers prepared in a 1:1 molar ratio in DMSO *via* slow evaporation.

Number	**API**	**Selected co-former**	**Result**
1	6-Thioguanine	Benzamide	Physical mixture
2	6-Thioguanine	Benzoic acid	Physical mixture
3	6-Thioguanine	Fumaric acid	Physical mixture
4	6-Thioguanine	Glutaric acid	Physical mixture
5	6-Thioguanine	Isonicotinamide	Physical mixture
6	6-Thioguanine	Maleic acid	Physical mixture
7	6-Thioguanine	Nicotinamide	Physical mixture
8	6-Thioguanine	Piperazine	Physical mixture
9	6-Thioguanine	Propionamide	Physical mixture
10	6-Thioguanine	D-Tartaric acid	Physical mixture
11	6-Thioguanine	Urea	Physical mixture

Section 6: Cyclodextrin inclusion with 6-thioguanine

The native and methylated CD experiments in this section were identical replicates of those that were performed for allopurinol in Section 3, pp. 15 – 19 of this Appendix. In addition, the results that were obtained for these replicated experiments were also very similar. As a result, a summary of the results is tabulated for each experiment, where the full description of the methodology and explanation for the results are provided in the Section 3 (pp. 15 – 19) dedicated to allopurinol in this Appendix. For all the CD experiments involving 6-thioguanine, 5 mg (0.0299 mmol) of the drug was used with the corresponding molar amount (or a multiple thereof) for the native and methylated CDs.

Native cyclodextrin inclusion with 6-thioguanine

Kneading experiments with 6-thioguanine

Table 6.1: The results from the kneading experiments of the native cyclodextrins with 6-thioguanine.

Number	API	Cyclodextrin	Result
1	6-Thioguanine	α-cyclodextrin	Physical mixture
2	6-Thioguanine	β-cyclodextrin	Physical mixture
3	6-Thioguanine	γ-cyclodextrin	Physical mixture

Co-precipitation experiments with 6-thioguanine

Table 6.2: The results from the various native CD co-precipitation experiments with 6-thioguanine, co-precipitated in water.

Number	System	Result
1	α-CD and 6-thioguanine (1:1)	The original reagents precipitated
2	α-CD and 6-thioguanine (2:1)	The original reagents precipitated
3	β-CD and 6-thioguanine (1:1)	The original reagents precipitated
4	β-CD and 6-thioguanine (2:1)	The original reagents precipitated
5	γ-CD and 6-thioguanine (1:1)	The original reagents precipitated
6	γ-CD and 6-thioguanine (2:1)	The original reagents precipitated

Table 6.3: The results from the various native CD co-precipitation experiments with 6-thioguanine, co-precipitated in water with a few drops of EtOH.

Number	System	Result
1	α-CD and 6-thioguanine (1:1)	The original reagents precipitated
2	α-CD and 6-thioguanine (2:1)	The original reagents precipitated
3	β-CD and 6-thioguanine (1:1)	The original reagents precipitated
4	β-CD and 6-thioguanine (2:1)	The original reagents precipitated
5	γ-CD and 6-thioguanine (1:1)	The original reagents precipitated
6	γ-CD and 6-thioguanine (2:1)	The original reagents precipitated

Table 6.4: The results from the various native CD co-precipitation experiments with 6-thioguanine, co-precipitated in water with a drop of Tween® 80.

Number	System	Result
1	α-CD and 6-thioguanine (1:1)	A Tween® 80 α-CD inclusion complex precipitated
2	α-CD and 6-thioguanine (2:1)	A Tween® 80 α-CD inclusion complex precipitated
3	β-CD and 6-thioguanine (1:1)	A Tween® 80 β-CD inclusion complex precipitated
4	β-CD and 6-thioguanine (2:1)	A Tween® 80 β-CD inclusion complex precipitated
5	γ-CD and 6-thioguanine (1:1)	A Tween® 80 γ-CD inclusion complex precipitated
6	γ-CD and 6-thioguanine (2:1)	A Tween® 80 γ-CD inclusion complex precipitated

Table 6.5: Co-precipitation of β-CD and 6-thioguanine, where 6-thioguanine was pre-dissolved in 0.2 cm^3 of aqueous KOH solution.

Number	System	pH	Result
1	6-thioguanine and β-CD stirred at 55 °C	8.80	The original reagents precipitated
2	6-thioguanine and β-CD stirred at room temperature	8.90	The original reagents precipitated

Table 6.6: Co-precipitation of β-CD and 6-thioguanine, where 6-thioguanine was pre-dissolved in 0.4 cm^3 of aqueous KOH solution.

Number	System	pH	Result
1	6-thioguanine and β-CD stirred at 55 °C	9.38	The original reagents precipitated
2	6-thioguanine and β-CD stirred at room temperature	10.23	The original reagents precipitated

Methylated cyclodextrin inclusion with 6-thioguanine

Kneading experiments with 6-thioguanine

Table 6.7: The results from the kneading experiments of the methylated cyclodextrins with 6-thioguanine.

Number	API	Cyclodextrin	Result
1	6-Thioguanine	DMB	Became amorphous
2	6-Thioguanine	TMB	Physical mixture
3	6-Thioguanine	TMA	Physical mixture

Co-precipitation experiments with 6-thioguanine

Table 6.7: The results from the co-precipitation experiments of the methylated cyclodextrins with 6-thioguanine.

Number	API	Cyclodextrin	Result
1	6-Thioguanine	DMB	DMB crystallized
2	6-Thioguanine	TMB	TMB crystallized
3	6-Thioguanine	TMA	TMA crystallized

Section 7: Solubility experiments with 6-thioguanine

7.1) Calculation of the error in mass from the calibration curve

- $y = 0.2126\,x + 0.0013$ *equation 1*
- $y = 0.2126\,x$ *equation 2*

A point selected at $y = 0.225$, therefore:

- $0.225 = 0.2126\,x + 0.0013$

  $x = 1.0522107244 \times 10^{-8}$ mol.cm^{-3} *from equation 1*

- $0.225 = 0.2126\,x$

  $x = 1.0583254939 \times 10^{-8}$ mol.cm^{-3} *from equation 2*

The absolute value determined from the subtraction of the two x values:

- $/\ x_{\text{equation 2}} - x_{\text{equation 1}}\ /\ = 6.1147695 \times 10^{-11}$ mol.cm^{-3}

Obtaining the mass from the concentration:

- $6.1147695 \times 10^{-11}$ mol.cm^{-3} = number of moles / 5 cm^{3}

  number of moles = $3.05738475 \times 10^{-10}$ mols

  Therefore:

  $3.05738475 \times 10^{-10}$ mols = mass / 167.193 g.mol^{-1}

  Error mass = $5.111732850675 \times 10^{-8}$ g

  = 5.1117×10^{-5} mg

7.2) Phase solubility analysis of 6-thioguanine with γ-CD, HPBCD and RAMEB

The method described in the Experimental Methods (Chapter 2 in the main dissertation) under section 2.9.1 on pp. 23 – 24 was followed in order to perform this experiment. A predetermined mass of each CD was dissolved in water in a volumetric flask. For γ-CD, a mass of 1.19848 g (9.23893 x 10^{-4} mol) was dissolved in water in a 50 cm^3 volumetric flask, while for HPBCD and RAMEB, masses of 2.64816 g (1.89635 x 10^{-3} mol) and 2.44570 g (1.87698 x 10^{-3} mol) respectively were separately dissolved in 100 cm^3 volumetric flasks. The resultant phase solubility curves are provided below (Figure 7.1 – 7.3).

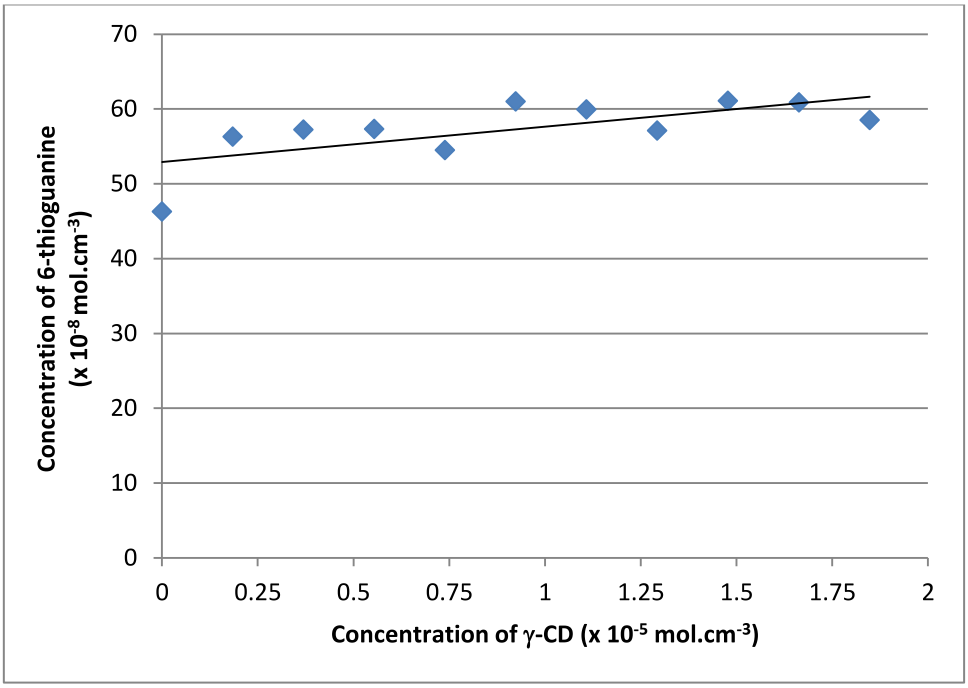

Figure 7.1: Phase solubility curve of the concentration of 6-thioguanine versus the concentration of γ-CD.

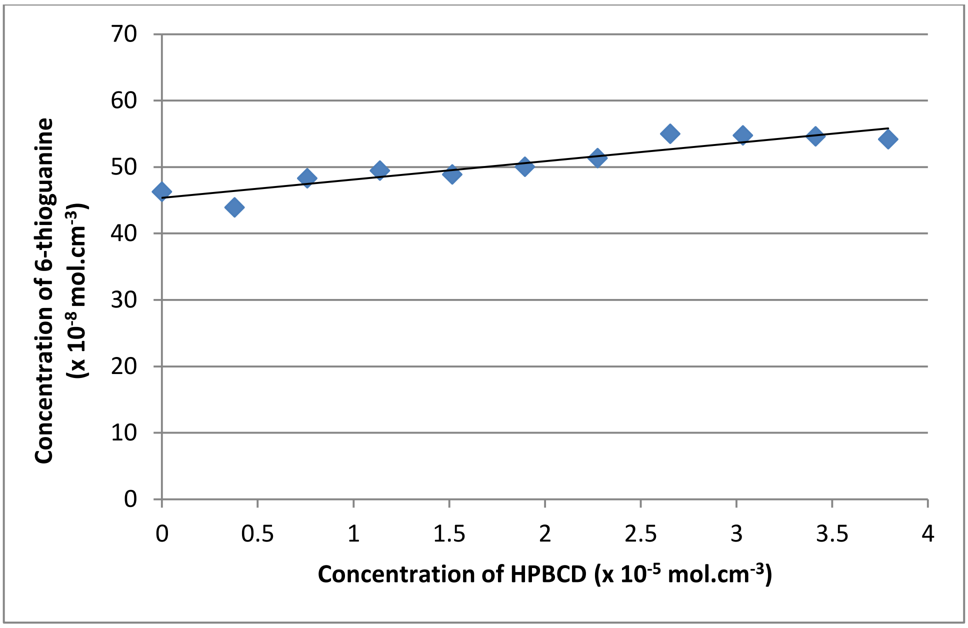

Figure 7.2: Phase solubility curve of the concentration of 6-thioguanine versus the concentration of HPBCD.

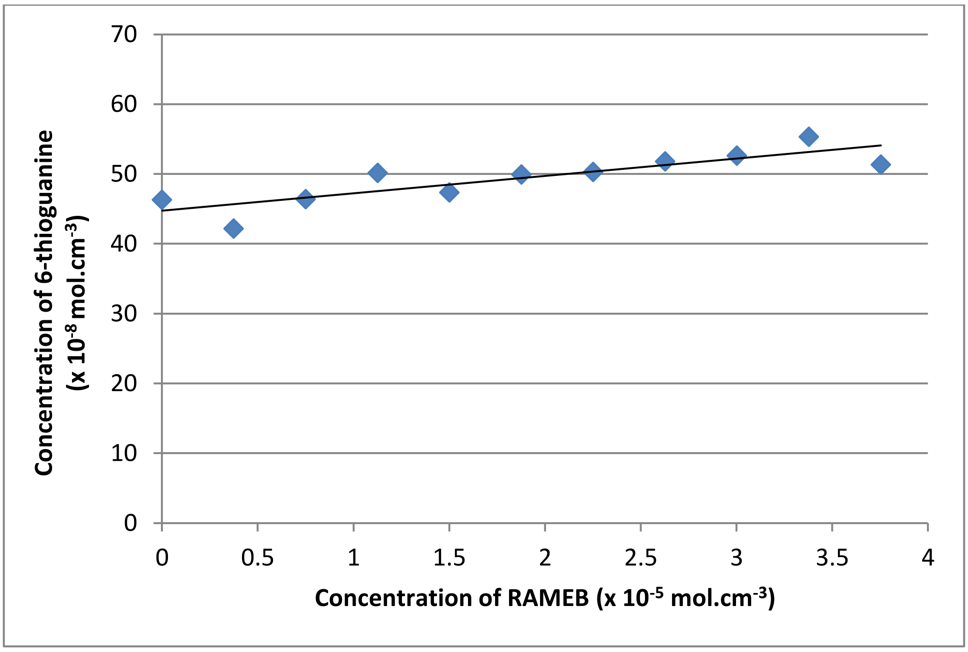

Figure 7.3: Phase solubility curve of the concentration of 6-thioguanine versus the concentration of RAMEB.

As a result, even though a variety of different CDs with varying solution concentrations were employed, it is evident that the solubility of 6-thioguanine was not improved.

Section 8: Co-crystallization of valproic acid

Table 8.1: The selected co-formers for co-crystallization screening experiments with valproic acid.

Number	Co-former
1	Adipic acid
2	Citric acid
3	Glutaric acid
4	Isonicotinamide
5	Maleic acid
6	Malic acid
7	Nicotinamide
8	Pimelic acid
9	Piperazine
10	Propionamide
11	Pyroglutamic acid
12	D-Tartaric acid

Co-precipitation experiments with valproic acid

Co-precipitation experiments were executed with equimolar combinations of valproic acid and the selected co-formers (Table 8.1) in attempts to synthesize co-crystals. Consequently, 5 mg (3.467×10^{-3} mol; 5.434 µl) of valproic acid and an equimolar mass of a co-former were separately dissolved in 1 cm^3 of EtOH at 50 ^{o}C while stirring. The solutions were subsequently filtered into a clean, common vial and prepared for slow evaporation. These results are summarised in Table 8.2 and they were confirmed either by SCXRD or PXRD analysis.

Table 8.2: Co-precipitation of valproic acid with various co-formers prepared in a 1:1 molar ratio in EtOH *via* slow evaporation.

Number	**API**	**Co-former**	**Result**
1	Valproic acid	Adipic acid	The co-former crystallised
2	Valproic acid	Citric acid	The co-former crystallised
3	Valproic acid	Glutaric acid	The co-former crystallised
4	Valproic acid	Isonicotinamide	The co-former crystallised
5	Valproic acid	Maleic acid	The co-former crystallised
6	Valproic acid	Malic acid	The co-former crystallised
7	Valproic acid	Nicotinamide	The co-former crystallised
8	Valproic acid	Pimelic acid	The co-former crystallised
9	Valproic acid	Piperazine	The co-former crystallised
10	Valproic acid	Propionamide	The co-former crystallised
11	Valproic acid	Pyroglutamic acid	The co-former crystallised
12	Valproic acid	D-Tartaric acid	The co-former crystallised

Unfortunately, no new product was obtained and with all the results, only the co-former was evident in the PXRD pattern (since valproic acid is a liquid at room temperature).

Section 9: Cyclodextrin inclusion complexation with valproic acid

9.1) Supplementary data for the α-CD·VAL inclusion complex

9.1.1) The ^{1}H NMR spectrum of α-CD·VAL

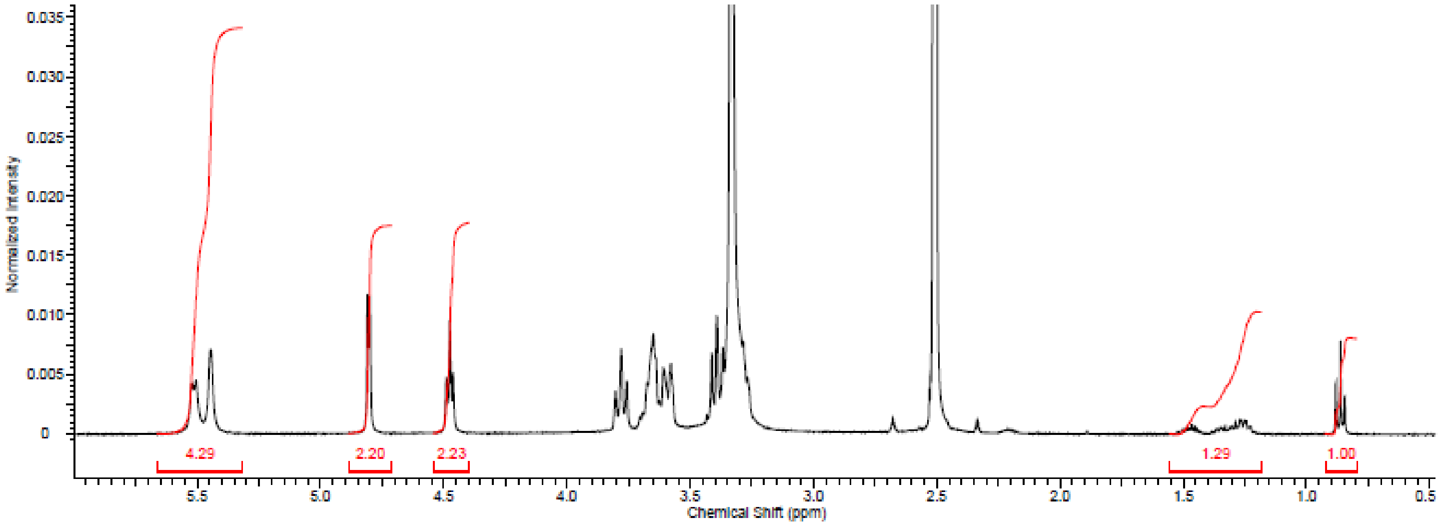

9.1.2) The FT-IR Spectrum of α-CD·VAL

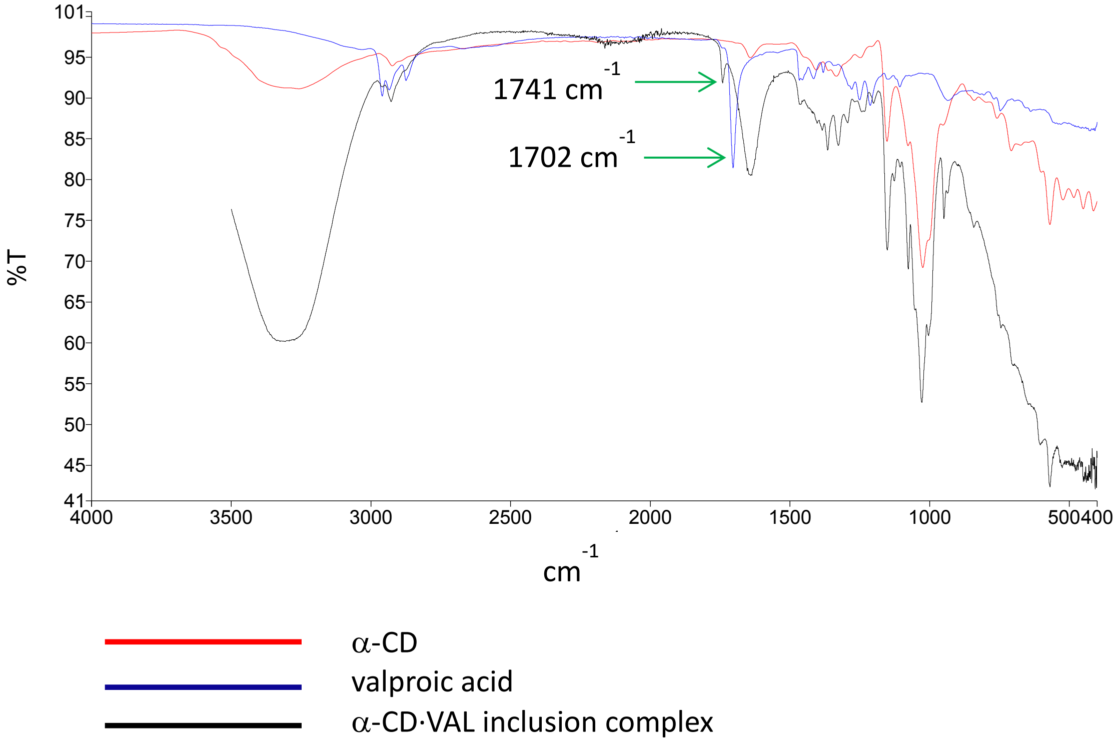

9.1.3) Calculation of the number of water molecules in $(\alpha\text{-CD})_2\cdot\text{VAL}\cdot n\text{H}_2\text{O}$, and the number of water molecules per α-CD molecule (from the TGA analysis).

$$10.4\ \% = \frac{MW(Water)n}{2(MW(\alpha - CD)) + MW(Valproic\ acid) + MW(Water)n}$$

$$0.104 = \frac{18.016n}{2(972.846) + 144.211 + 18.016n}$$

$\underline{\boldsymbol{n = 13.5\ water\ molecules}}$

Therefore there are 6.7 water molecules per α-CD molecule.

9.2) Supplementary data for the β-CD·VAL inclusion complex

9.2.1) The ^{1}H NMR spectrum of β-CD·VAL

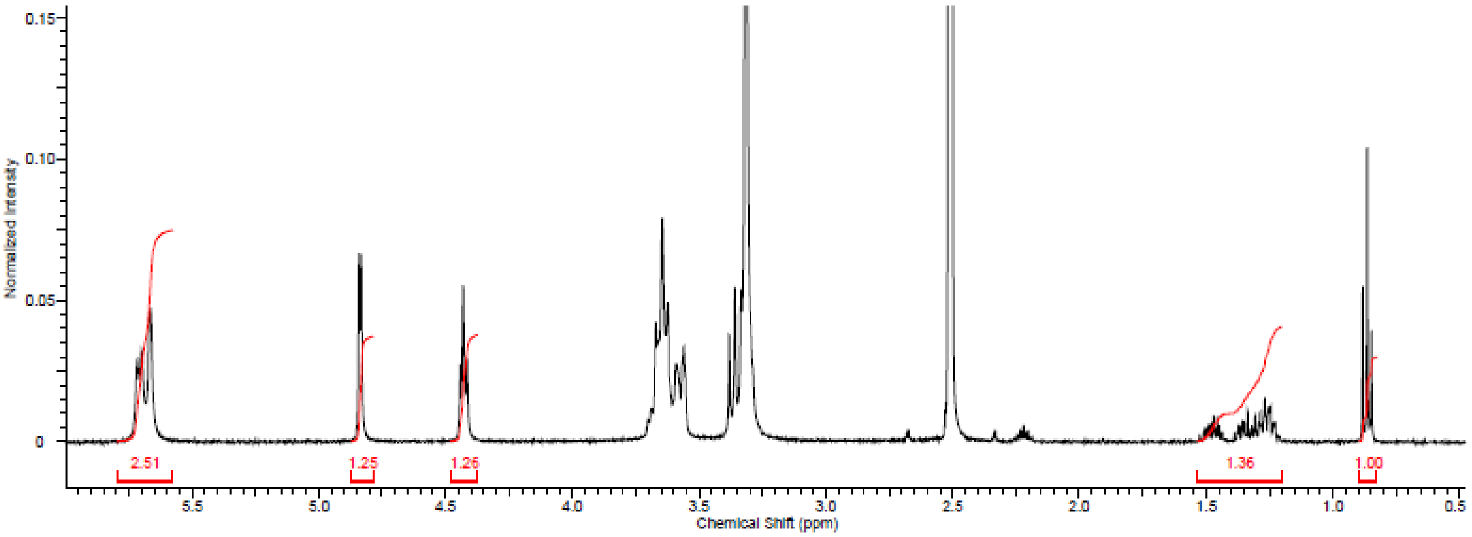

9.2.2) The FT-IR Spectrum of β-CD·VAL

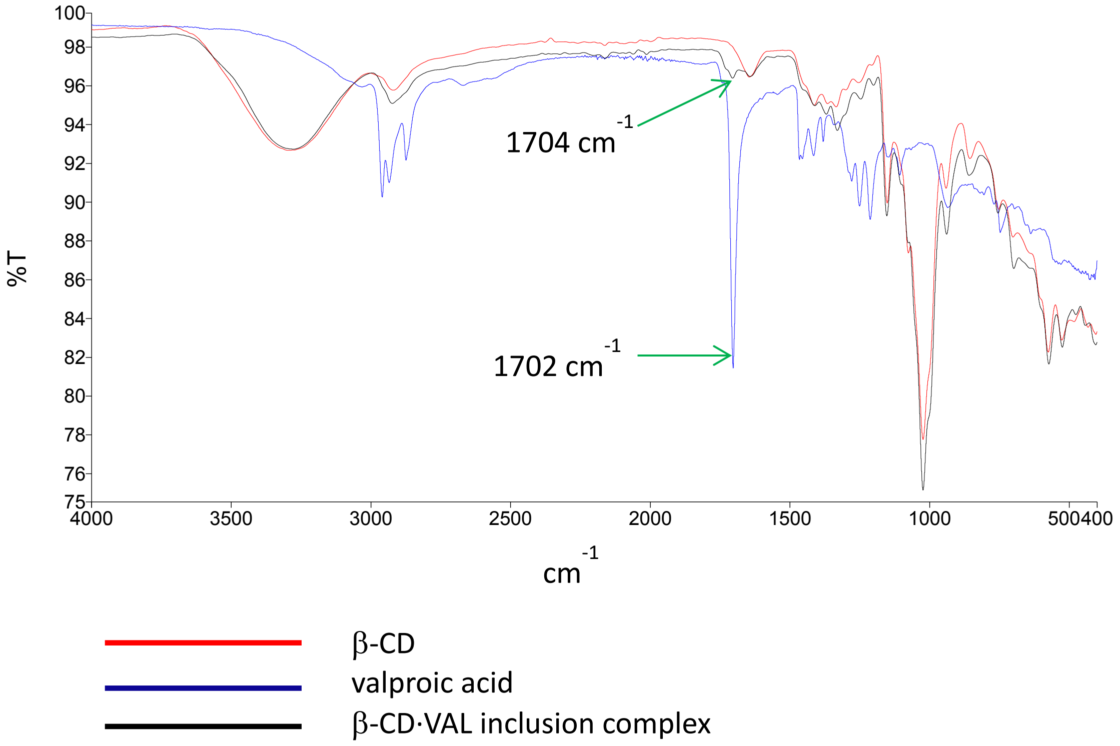

9.2.3) Calculation of the number of water molecules in β-CD·VAL·nH$_2$O, and the number of water molecules per β-CD molecule (from the TGA analysis).

$$11.5\ \% = \frac{MW(Water)n}{(MW(\beta - CD)) + MW(Valproic\ acid) + MW(Water)n}$$

$$0.115 = \frac{18.016n}{1134.987 + 144.211 + 18.016n}$$

$\underline{\boldsymbol{n = 9.2\ water\ molecules}}$

Therefore there are 9.2 water molecules per β-CD molecule.

9.3) Supplementary data for the γ-CD·VAL inclusion complex

9.3.1) The ^{1}H NMR spectrum of γ-CD·VAL

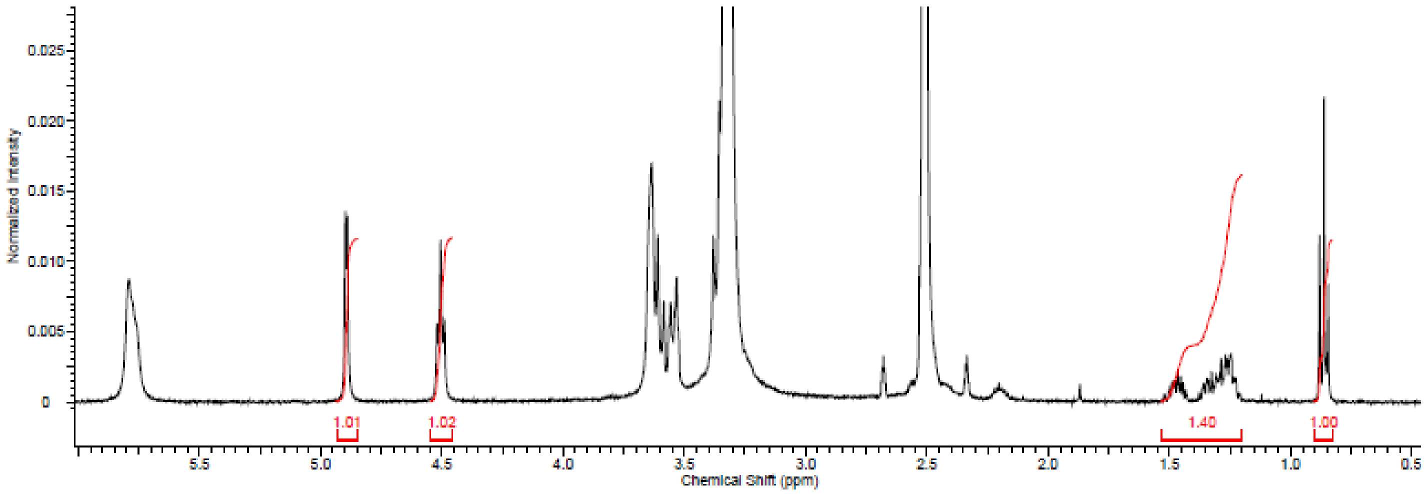

9.3.2) The FT-IR Spectrum of γ-CD·VAL

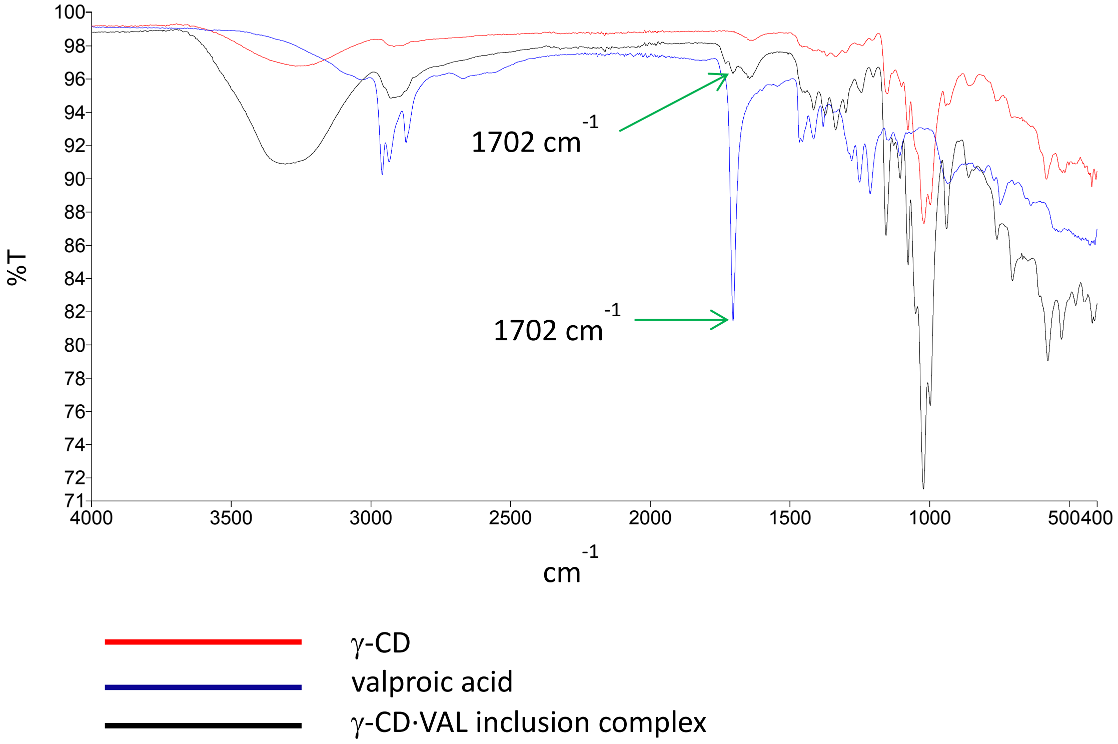

9.3.3) Calculation of the number of water molecules in $(\gamma\text{-CD})_{4/3}\cdot\text{VAL}\cdot n\text{H}_2\text{O}$, and the number of water molecules per γ-CD molecule (from the TGA analysis).

$$16.4\ \% = \frac{MW(Water)n}{\frac{4}{3}(MW(\gamma - CD)) + MW(Valproic\ acid) + MW(Water)n}$$

$$0.164 = \frac{18.016n}{\frac{4}{3}(1297.128) + 144.211 + 18.016n}$$

$\underline{\boldsymbol{n = 20.4\ water\ molecules}}$

Therefore there are 15.3 water molecules per γ-CD molecule.

9.4) Solubility calculations

9.4.1) Sample calculation for the mass of valproic acid dissolved per cm^3 from the co-precipitated hydrated α-CD·VAL.

Molar mass of valproic acid: 144.211 g.mol^{-1}

Molar mass of α-CD: 972.846 g.mol^{-1}

Mass of 6.7 mol of water (from complex formula): 119.548 g

Percentage of valproic acid in a 2:1 α-CD·VAL complex:

$$\frac{144.211}{144.211 + 2(972.846) + 119.548} \times 100 = 6.527\ \%$$

Therefore, 0.06527 x 24.14 mg = 1.576 mg in 3 cm^3 of water (lower limit)

Therefore, 0.06527 x 24.54 mg = 1.602 mg in 3 cm^3 of water (upper limit)

Therefore, the mass of valproic acid dissolved per cm^3: **0.525 – 0.534 mg.cm^{-3}**

9.5) Supplementary data for the DMB·VAL inclusion complex

9.5.1) The ^{1}H NMR spectrum of DMB·VAL

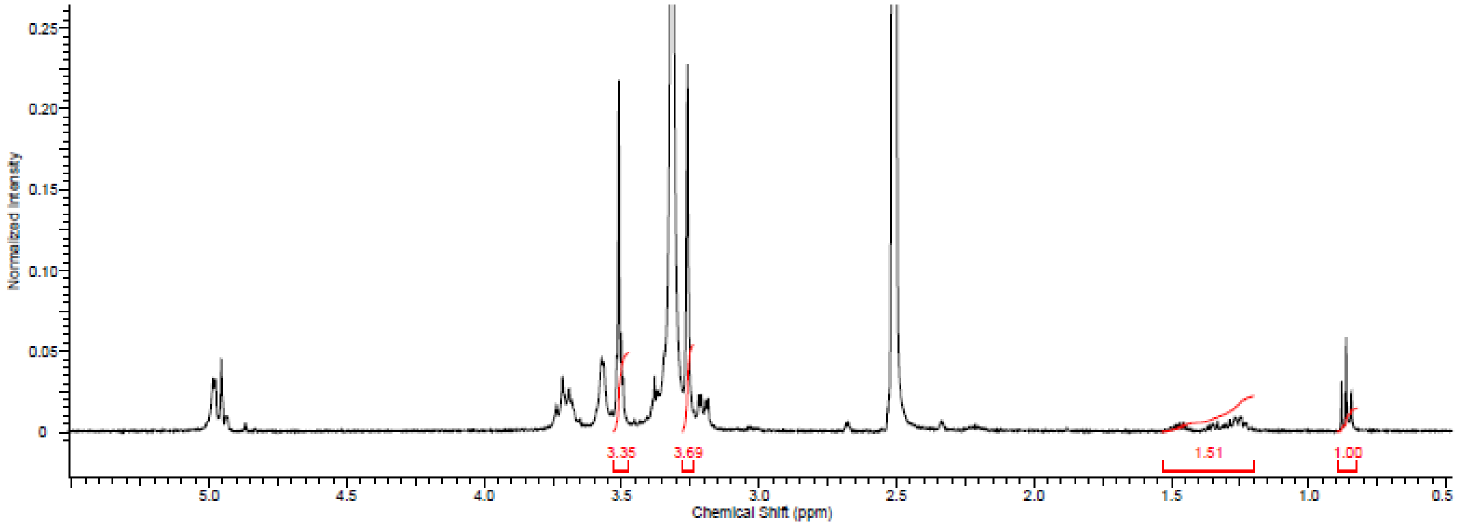

9.5.2) The FT-IR Spectrum of DMB·VAL

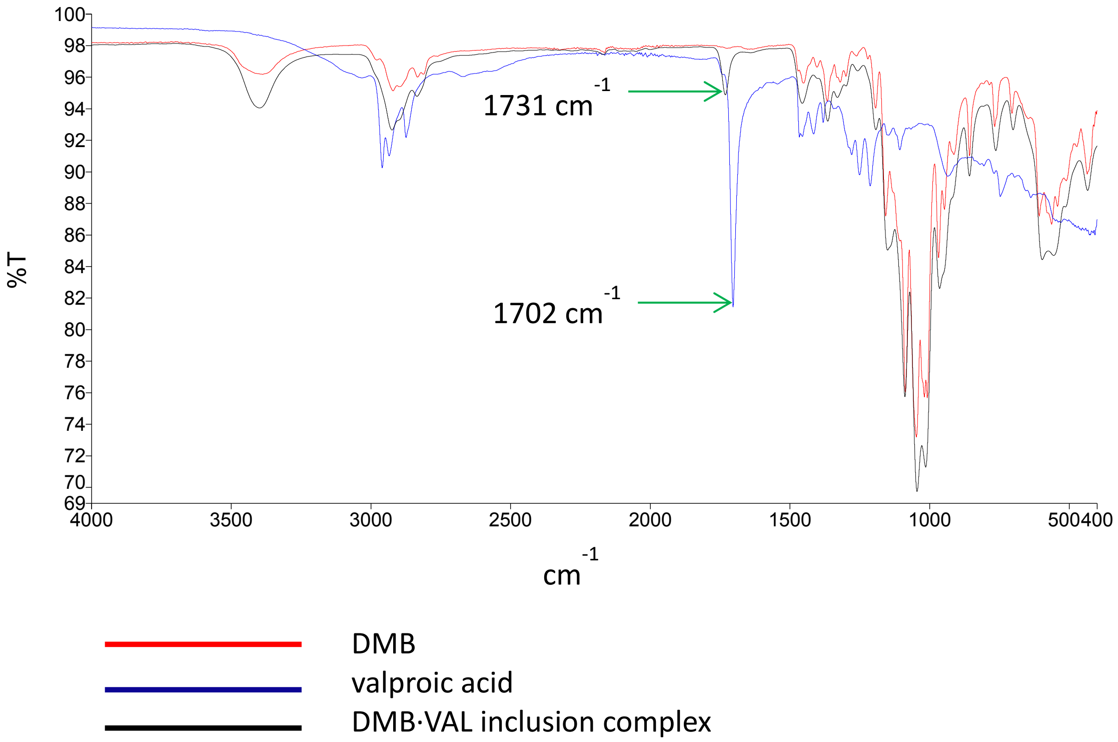

9.5.3) Calculation of the number of water molecules in DMB·VAL·nH$_2$O, and the number of water molecules per DMB molecule (from the TGA analysis).

$$2.1\ \% = \frac{MW(Water)n}{MW(DMB) + MW(Valproic\ acid) + MW(Water)n}$$

$$0.021 = \frac{18.016n}{1331.36 + 144.211 + 18.016n}$$

$\underline{\boldsymbol{n = 1.8\ water\ molecules}}$

Therefore there are 1.8 water molecules per DMB molecule.

9.6) Supplementary data for the TMB·VAL inclusion complex

9.6.1) The ^{1}H NMR spectrum of TMB·VAL

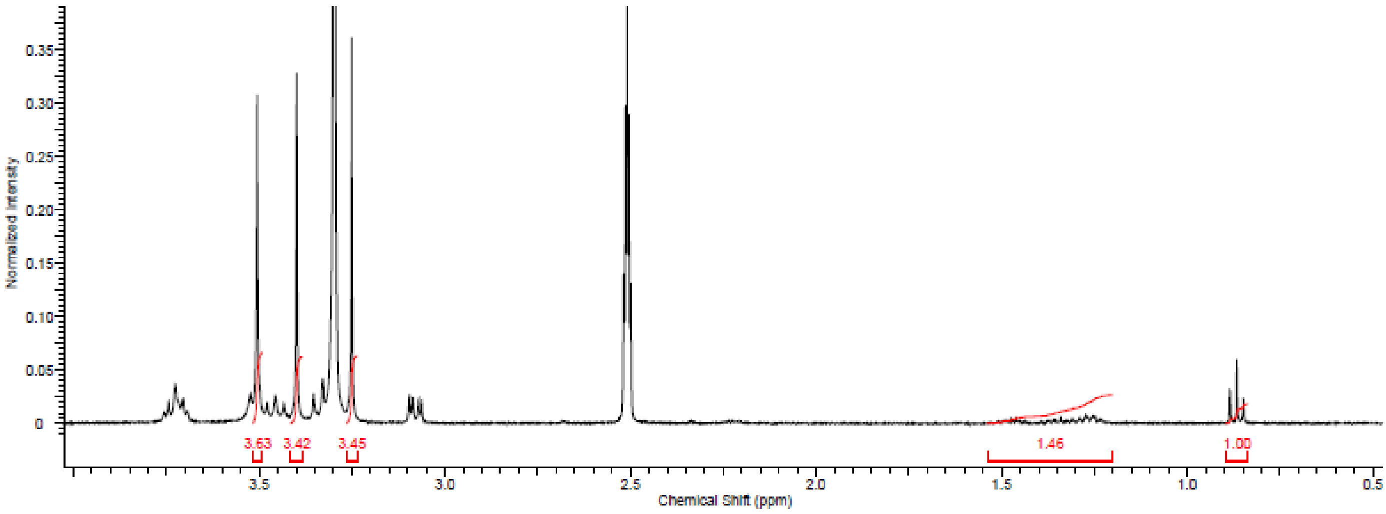

9.6.2) The FT-IR Spectrum of TMB·VAL

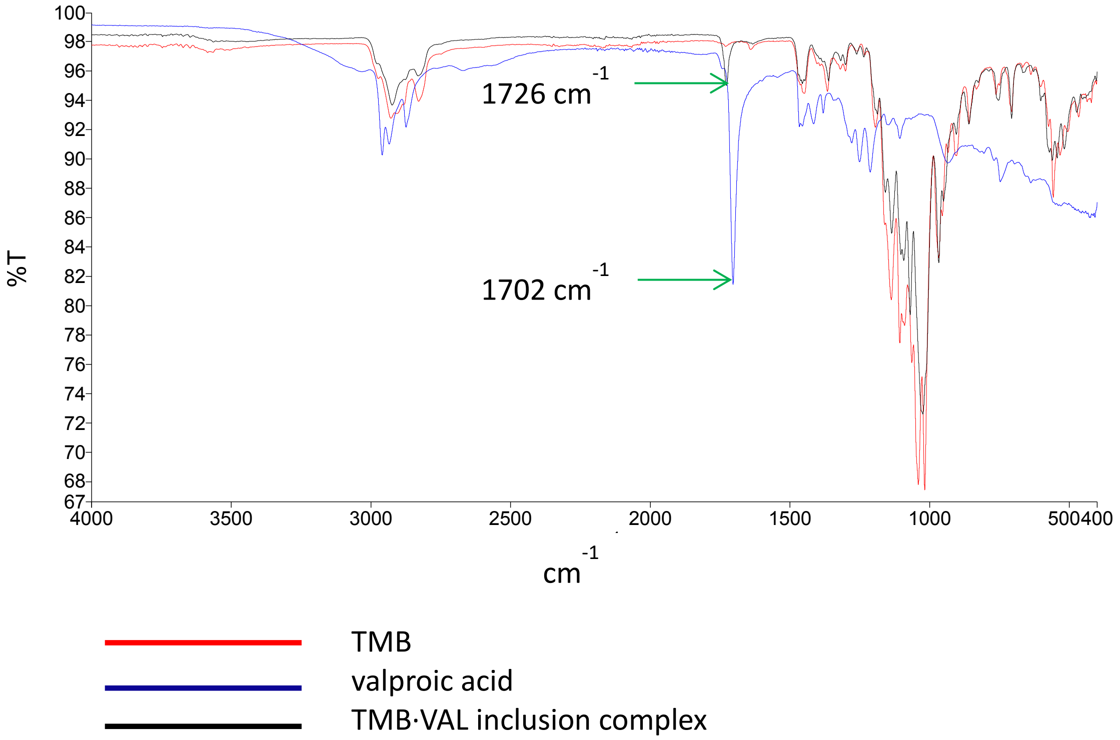

9.6.3) Calculation for determining the stoichiometry of the anhydrous TMB·VAL inclusion complex (from the TGA analysis).

Percentage mass loss of valproic acid: 8.3 ± 0.9 %

Ratio of valproic acid to an equimolar anhydrous inclusion complex:

$$\frac{M(Valproic\ acid)}{M(Valproic\ acid) +\ M(TMB)}$$

$$\frac{144.211}{144.211 + 1429.55} \times 100 = 9.2\ \%$$

9.7) Supplementary data for the TMA·VAL inclusion complex

9.7.1) The ^{1}H NMR spectrum of TMA·VAL

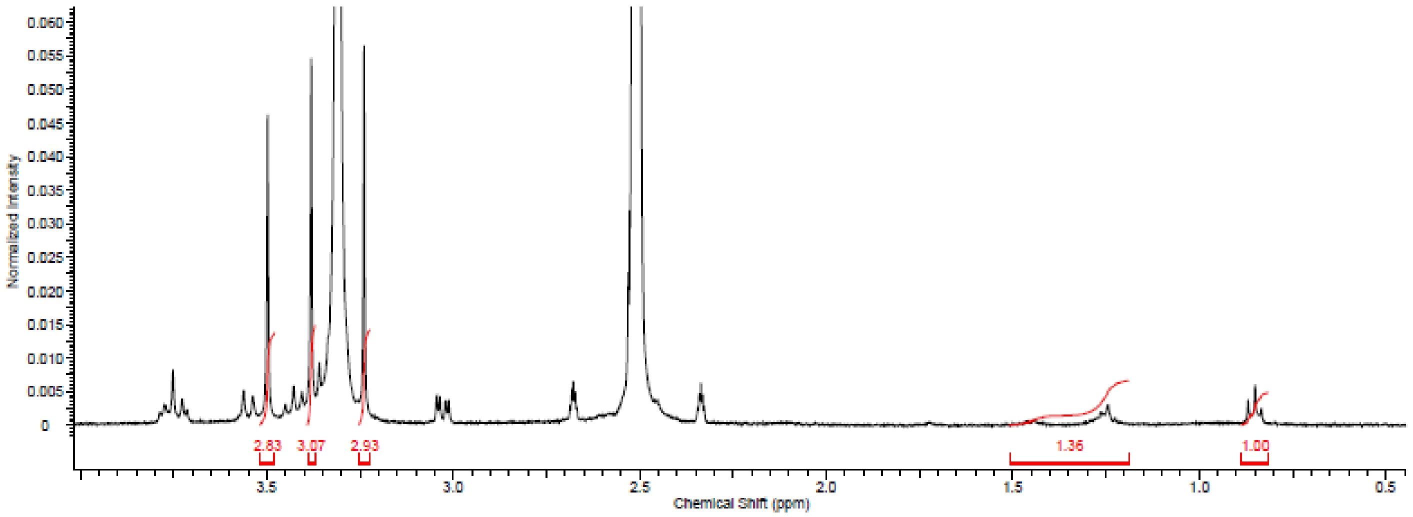

9.7.2) The FT-IR Spectrum of TMA·VAL

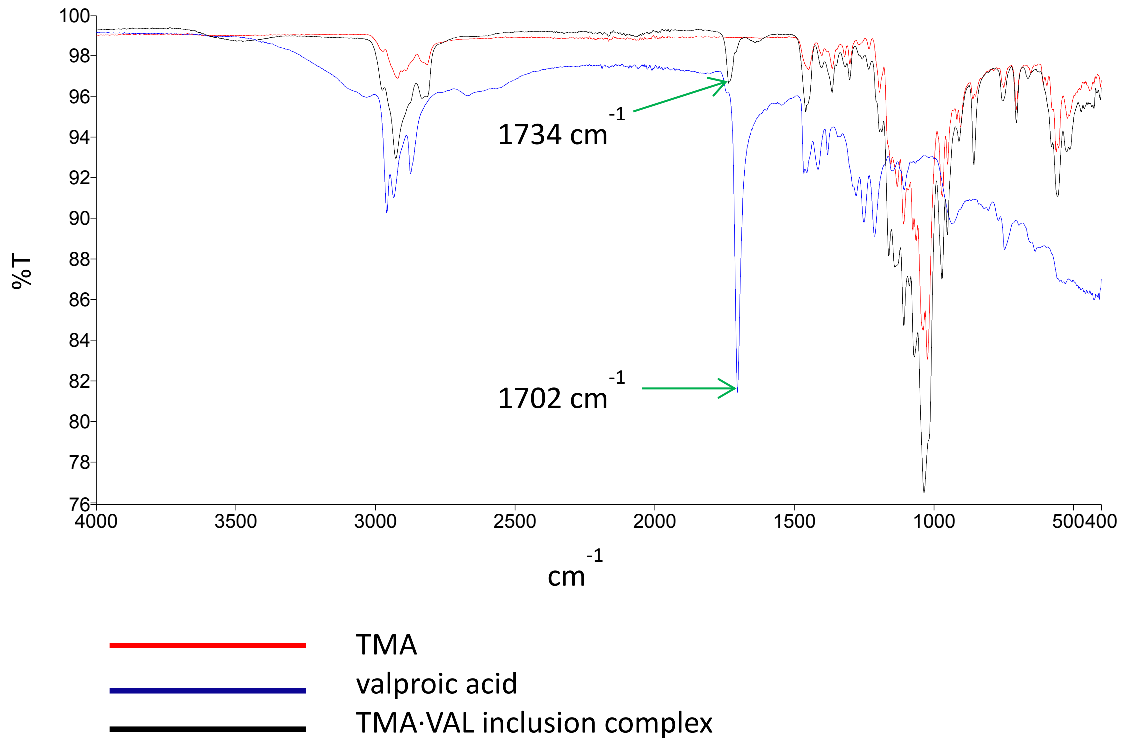

9.7.3) Calculation for determining the stoichiometry of the anhydrous TMA·VAL inclusion complex (from the TGA analysis)

Total percentage mass loss of valproic acid: 9.9 ± 0.7 %

Ratio of valproic acid to an equimolar anhydrous inclusion complex:

$$\frac{M(Valproic\ acid)}{M(Valproic\ acid) + M(TMA)}$$

$$\frac{144.211}{144.211 + 1225.32} \times 100 = \ 10.5\ \%$$

9.7.4) Calculation of the number of water molecules in TMA·VAL·nH$_2$O, and the number of water molecules per TMA molecule (from the TGA analysis).

$$1.5\ \% = \frac{MW(Water)n}{MW(TMA) + MW(Valproic\ acid) + MW(Water)n}$$

$$0.015 = \frac{18.016n}{1225.32 + 144.211 + 18.016n}$$

$\boldsymbol{n = 1.2\ water\ molecules}$

Therefore there are 1.2 water molecules per TMA molecule.

10.1) References

1) James, S. L.; Adams, C. J.; Bolm, C.; Braga, D.; Collier, P.; Friščić, T.; Grepioni, F.; Harris, K. D. M.; Hyett, G.; Jones, W.; Krebs, A.; Mack, J.; Maini, L.; Orpen, A. G.; Parkin, I. P.; Shearouse, W. C.; Steed, J. W.; Waddel, D. C. *Chem. Soc. Rev.,* **2012**, *41*, 413.
2) Engel, E. R. Supramolecular Modification of Selected Antiretroviral Drugs. MSc Thesis, University of Cape Town, South Africa, 2011.
3) Frömming, K.; Szejtli, J. *Cyclodextrins in Pharmacy*; Kluwer Academic Publishers: London, 1994.
4) Pubchem. *6-Thioguanine*. <https://pubchem.ncbi.nlm.nih.gov/compound/6-Thioguanine> (Accessed 16 June 2016).
5) Gaidamauskas, E.; Norkus, E.; Butkus, E.; Crans, D. C.; Grincienė, G. *Carbohydr. Res.,* **2009**, *344*, 250.
6) Jiménez, V.; Alderete, J. B.; Delgado, E. J.; Belmar, J.; Gavín, J. *Struct. Chem.,* **2006**, *17*, 217.